Christoph von Hagke

Coupling between Climate and Tectonics?

Low temperature thermochronology and structural geology applied to the pro-wedge of the European Alps

Coupling between Climate and Tectonics?

Low temperature thermochronology and structural geology applied to the pro-wedge of the European Alps

Dissertation zur Erlangung des Doktorgrades

im Fachbereich Geowissenschaften

an der Freien Universität Berlin

Christoph von Hagke

Berlin, 2012

1. Gutachter: Prof. Dr. Onno Oncken

      Freie Universität Berlin

      Helmholtz-Zentrum Potsdam Deutsches GeoForschungsZentrum GFZ

2. Gutachter: Prof. Dr. Mark Handy

      Freie Universität Berlin

Tag der Disputation: 27.06.2012

Erklärung

Hiermit versichere ich, dass die vorliegende Dissertation ohne unzulässige Hilfe Dritter und ohne Benutzung anderer als der angegebenen Literatur angefertigt wurde. Die Stellen der Arbeit, die anderen Werken wörtlich oder inhaltlich entnommen sind, wurden durch entsprechende Angaben der Quellen kenntlich gemacht. Diese Arbeit hat in gleicher oder ähnlicher Form noch keiner Prüfungsbehörde vorgelegen.

Berlin, Mai 2012

HARNISCHSTRIEMEN, Faltenachsen,

Durchstich-

punkte:

dein Gelände.

An beiden Polen

der Kluftrose, lesbar:

dein geächtetes Wort.

Nordwahr. Südhell.

SLICKENSIDES, fold-axes,

rechanneling-

points:

your terrain.

On both poles

of the cleftrose, legible:

your outlawed word.

Northtrue. Sunbright.

Paul Celan 1967 (Atemwende), translated by Pierre Joris (Breathturn)

Table of content

APPENDIX

1 Thermochronological approach to the late stage evolution of the Molasse basin and the Interaction between climate and tectonics

1.1 General Introduction and Summary

Continental collision results in telescoping of Earth's crust and the consequent formation of orogens with a complex internal structure, a characteristic mechanical configuration and resulting complex kinematics. Orogenic fronts mark the foremost position of active deformation, thus forming the linkage between the orogen and its foreland basin and therefore registering the spatiotemporal history of the two. Resolving this history contributes to our understanding of the kinematic history of orogens and consequently enables an assessment of the contribution of the driving forces behind mountain building; the results of which provide insights on the interactions between climate and tectonics, a topic which has been and continues to be heavily debated (Molnar and England, 1990; Willett, 1999; e.g. Beaumont et al., 2001; Whipple and Meade, 2006; Whipple, 2009).

A suitable study area to investigate these interactions between climate and tectonics are the Central European Alps, due to the unparalleled amount of geological and structural data and the well studied present day kinematics. Additionally, countless studies document the uplift and erosion history (e.g. Ratschbacher et al., 1989; Pfiffner et al., 1990; Lammerer and Weger, 1998; Frisch et al., 2000; Bistacchi et al., 2001; Malusa and Vezzoli, 2006; Genser et al., 2007; Kuhlemann, 2007; Champagnac et al., 2009; Vernon et al., 2009a; Norton et al., 2010b; Glotzbach et al., 2011b). Like the inner Alps, the foreland basin has been the focus of numerous studies, and so both basin stratigraphy and tectonic setting are well resolved (e.g. Ganss and Schmidt-Thomé, 1953; Trümpy, 1980; Homewood et al., 1986; Pfiffner, 1986; Müller et al., 1988; Schlunegger et al., 1997a; Sinclair, 1997b; a; Sissingh, 1997; Kuhlemann and Kempf, 2002; Pfiffner et al., 2002; Berge and Veal, 2005; Berger et al., 2005a; Berger et al., 2005b).

Accordingly, the Central Alps can serve as a natural laboratory for resolving the complex system of coupled processes that are responsible for deformation and surface response. The

potential of similar coupling processes are reported from other orogens all over the world, for example the Olympic Mountains (e.g. Montgomery and Brandon, 2002), Taiwan (e.g. Fuller et al., 2006)and the Himalayas (e.g. Whipple, 2009) and may therefore be discussed in a similar way. In this thesis I focus on the North Alpine pro-wedge and scrutinize the potential driving forces of tectonic activity. The key questions I try to answer are:

- Is it possible to constrain further the timing and amount of deformation (i.e. shortening) in the foreland fold and thrust belt of the European Alps, in particular in Late Neogene times?
- What does this timing and magnitude of deformation tell us about the kinematics of late stage exhumation and the relation between the Alps and their foreland?
- Can we evaluate the influence of climate (or climate changes) on timing and magnitude of deformation within the foreland fold and thrust belt?

To address these questions, I combine low temperature thermochronology (in particular apatite fission track and apatite (U-Th-Sm)/He dating) with critical taper analysis and try to extrapolate the present day kinematic situation into the past; thus providing an instrument to understand wedge dynamics through time.

The following sub-chapters give a general overview over the working area and the applied thermochronological methods. Chapter 2 demonstrates the application of low temperature thermochronology to the foreland basin of the Central Alps and reveals that the Subalpine Molasse in Switzerland was tectonically active in Neogene times. It is shown that this tectonic activity is coeval with tectonic activity in internal parts of the orogen, as well as with the more external Jura Mountains. This chapter was submitted to *Tectonics*. Chapter 3 is supplementary information to Chapter 2, showing methodological details. Chapter 4 focuses on the Alps as an orogenic wedge and shows that critical taper theory is applicable for the Central Alps. Detailed analysis of surface and detachment slopes reveals variations in effective coefficient of friction of the basal detachment between the foreland and the more internal parts of the orogen. Exceedingly weak detachments are found also within pelitic horizons, which cannot be solely attributed to elevated pore pressures. Chapter 5 combines the two approaches (low temperature thermochronology and critical wedge analysis) in

order to constrain Alpine wedge dynamics through time. Additional thermochronological data from a profile crossing the Subalpine Molasse east of the Jura Mountains show that the Neogene tectonic activity is a regional feature. Shortening rates in the west and the east of the Central Alps have been similar since at least the Late Miocene. I combine the thermochronological data from the Subalpine Molasse with data from the External Crystalline Massifs and restore the Late Miocene wedge geometry of the Central Alps. It becomes obvious that the taper of the Central Alps has not changed significantly since 10 Ma. Accordingly, the Central Alps have been in steady state since then. Consequently, this study shows the tectonic contribution to the Late Miocene-to-present orogenic evolution. This thesis shows that we have no evidence that Miocene to Pliocene climatic events influenced the wedge stability and kinematics on the northern flank of the Central Alps, and therefore primarily plate boundary or mantle-induced processes controlled the tectonics of the Neogene-to-Recent foreland thrusting. Chapter 6 summarizes the results of the individual chapters.

1.2 Allgemeine Einführung und Zusammenfassung

Die Kollision zweier Kontinente führt zur Bildung von Gebirgen mit einer komplexen internen Struktur, einem individuellen mechanischen Bau und daraus resultierender komplexer Kinematik. Orogenfronten bilden den äußersten Rand aktiver Verkürzung und gleichzeitig die Verbindung zwischen dem Gebirge und seinem Vorland. Sie archivieren deswegen deren raumzeitliche Entwicklung. Erkenntnisse über die Entwicklung von Orogenfronten tragen maßgeblich zum Verständnis der Kinematik von Gebirgen bei und erlauben Rückschlüsse auf die Kräfte, die für Gebirgsbildung verantwortlich sind. Deswegen bieten sich Orogenfronten auch für die Untersuchung von potentiellen Wechselwirkungen zwischen Klima und Tektonik an – eine Fragestellung, über die bereits seit über 20 Jahren heftig diskutiert wird (Molnar and England, 1990; Willett, 1999; e.g. Beaumont et al., 2001; Whipple and Meade, 2006; Whipple, 2009).

Die europäischen Zentralalpen sind ein geeignetes Untersuchungsgebiet, um unterschiedlich gesteuerte Prozesse zu verstehen, da es aus diesem Raum eine beispiellose Menge an geologischen und strukturellen Daten vorhanden ist und die Kinematik bereits detailliert beschrieben wurde. Zusätzlich dokumentieren zahllose Studien die Hebungs- und Abtragungsgeschichte der Zentralalpen (z.B. Ratschbacher et al., 1989; Pfiffner et al., 1990; Lammerer and Weger, 1998; Frisch et al., 2000; Bistacchi et al., 2001; Malusa and Vezzoli, 2006; Genser et al., 2007; Kuhlemann, 2007; Champagnac et al., 2009; Vernon et al., 2009a; Norton et al., 2010b; Glotzbach et al., 2011b).

Wie die Alpen selbst, so ist auch das Vorland im Detail untersucht worden und die Stratigraphie des Beckens sowie der derzeitige tektonische Aufbau sind gut bekannt (z.B. Ganss and Schmidt-Thomé, 1953; Trümpy, 1980; Homewood et al., 1986; Pfiffner, 1986; Müller et al., 1988; Schlunegger et al., 1997a; Sinclair, 1997b; a; Sissingh, 1997; Kuhlemann and Kempf, 2002; Pfiffner et al., 2002; Berge and Veal, 2005; Berger et al., 2005a; Berger et al., 2005b).Die europäischen Zentralalpen sind also ein „natürliches Versuchslabor", das sich in besonderem Maße für die Untersuchung der mutmaßlichen Kopplung von klimatischen

und tektonischen Prozessen eignet, welche für Deformation sowie die daraus resultierenden Reaktionen des Gebirgskörpers verantwortlich sein könnte.

In dieser Doktorarbeit wird der Pro-Keil der nördlichen Alpen betrachtet und Kräfte, die für die Gebirgsbildung verantwortlich sein können, eingegrenzt. Die Schlüsselfragen sind:

- Kann man den Zeitpunkt und die Magnitude der Deformation (Verkürzung) im Vorlandüberschiebungsgürtel der Europäischen Alpen genauer bestimmen, insbesondere die Verkürzung vom Neogen bis heute?
- Was sagt das Ergebnis dieser Bestimmung bezüglich der Gebirgskinematik während der späten Exhumierungsgeschichte aus und was können wir für Rückschlüsse bezüglich der Verbindung zwischen Alpen und Vorland ziehen?
- Was ist der Einfluss des Klimas (bzw. von Klimaschwankungen) auf den Deformationszeitraum und -magnitude?

Um diese Fragen zu beantworten wird Niedrigtemperatur—Thermochronologie (genauer Apatit Spaltspur und (U-Th-Sm)/He Datierung) mit der Theorie der kritischen Keilform kombiniert und die heutige kinematische Situation in die Vergangenheit extrapoliert. Dabei werden Verfahren entwickelt, mit denen es gelingt, Gebirgsbildung und deren Entwicklung über die Zeit besser zu verstehen. Die vorgestellte Methodik ist für alle ähnlich strukturierten Gebirge anwendbar, in denen ebenso potentielle Interaktionen zwischen Oberflächenprozessen und Tektonik beschrieben wurden, wie z.B. den Olympic Mountains (USA) (z.B. Montgomery and Brandon, 2002), Taiwan Fold and Thrust Belt (z.B. Fuller et al., 2006) oder im Himalaya (z.B. Whipple, 2009).

Die Doktorarbeit ist wie folgt gegliedert: Kapitel 2 beschreibt die Anwendung von Niedrigtemperatur-Thermochronologie auf das Vorland der Zentralalpen und zeigt dass, entgegen vorheriger Theorien, die Subalpine Molasse auch im Neogen aktiv deformiert wurde. Es wird aufgezeigt, dass diese Deformation zeitgleich mit Deformation im gebirgsinneren und im externen Jura Überschiebungsgürtel stattfand. Dieses Kapitel wurde bei *Tectonics* zur Veröffentlichung eingereicht. Kapitel 3behandelt methodische Details, die als zusätzliche Informationen für Kapitel 2 dienen. Kapitel 4 betrachtet die Alpen als

kritischen Keil und stellt dar, dass die Theorie des kritischen Keils auf das Untersuchungsgebiet anwendbar ist. Eine detaillierte Analyse des basalen Abscherhorizonts und des Oberflächenwinkels zeigt variable Reibungskoeffizienten entlang des Décollements. Extrem niedrige Reibungskoeffizienten können nicht nur in salz-, sondern auch in tonreichen Einheiten nachgewiesen werden. Es kann gezeigt werden, dass dies nicht ausschließlich auf überhöhte Porendrücke zurückzuführen ist. Dieses Kapitel wurde bei *G³* zur Veröffentlichung eingereicht. Kapitel 5 kombiniert die beiden Ansätze (Thermochronologie und Theorie des kritischen Keils). Zusätzliche thermochronologische Daten von einem Profil über die Subalpine Molasse zeigen dass die tektonische Aktivität, die im Schweizer Teil des Beckens entdeckt wurde, kein lokales Phänomen ist. Die Verkürzungsraten im Westen und im Osten der Zentralalpen sind seit mindestens dem späten Miozän vergleichbar. Die gesamten thermochronologischen Daten aus dem Vorland werden mit Daten aus den Externen Massiven verglichen. Es zeigt sich, dass der Orogenkeil sich seit etwa 10 Millionen Jahren nicht verändert hat und sich die Zentralalpen im kinematischen Gleichgewicht befinden. Diese Doktorarbeit zeigt dementsprechend den tektonischen Anteil an der Gebirgsbildung. Diese Doktorarbeit zeigt dass keine offensichtliche Korrelation zwischen klimatischen Ereignissen und tektonischer Aktivität besteht. Deswegen werden Plattentektonik oder Mantelprozesse als treibende Kraft der Überschiebungsaktivität postuliert. Kapitel 6 fasst die Ergebnisse zusammen.

Die zur Veröffentlichung eingereichten Teile der Doktorarbeit wurden von mir geschrieben und von den Mitautoren korrekturgelesen. Die detaillierte geologische Karte im Entlebuch basiert auf Arbeit von Fritz Schlunegger (Kapitel 2.5, Abbildung 2-3). Die Spaltspuralter, die mit der Externen Detektor-Methode (EDM) bestimmt wurden (Kapitel 2.7.1), hat Meinert Rahn zur Verfügung gestellt. Das bilanzierte Profil entlang der Bregenzerach wurde von Silvia Aichholzer und Hugo Ortner konstruiert (Kapitel 5.3, Abbildung 5-2).

1.3   The Molasse Basin

1.3.1   Geographic setting

The Molasse basin extends along the northern flank of the Alpine orogen, reaching a length of more than 1000 km. It can be followed from south of Geneva across the Swiss "Mittelland", the German and Austrian "Alpenvorland" into the western foreland of the Carpathians. The Jura Mountains in Switzerland, the Swabian and Franconian Alb and the Bohemian massif form its northern fringe. Its width changes markedly along strike. East of Munich it reaches a width of more than 130 km, but tapers out towards its eastern and western limits. In the east it is linked with the Vienna Basin.

1.3.2   Pre-Tertiary Basin Evolution

The basement of the basin consists of gneisses and variscan granites of the down-going European Plate. They can be found in outcrop in the Black Forest and the Bohemian Massif and have also been encountered in numerous wells in the Molasse Basin (Bachmann et al., 1987). The external massifs of the Alps are also part of the European basement, which has been brought to surface by thrusting and are thus now in a par-autochthonous position. They are one of the major source areas for Tertiary sediments of the Molasse. Following the Variscan orogeny, SW-NE striking grabens and half-grabens developed in the area of the basin; the thickness of the sediments within these local troughs is not known so far (Bachmann et al., 1987). Their subsidence has been related to late Palaeozoic wrench faulting, which transsected the Variscan fold belt and its European foreland (Arthaud and Matte, 1977). The distribution of these troughs can only be mapped on the basis of seismic and sparse well data. Therefore it is very likely that some remain undiscovered, which must be taken into account when balanced cross-sections are constructed. For example the Entlebuch Trough was recognized on reflection seismic data and was also encountered in the Entlebuch-1 deep drilling (Vollmayr and Wendt, 1987). Based on seismic data, the total thickness of Permo-Carboniferous sediments in the Entlebuch Trough was estimated to reach more than 1500m (Bachmann et al., 1987).
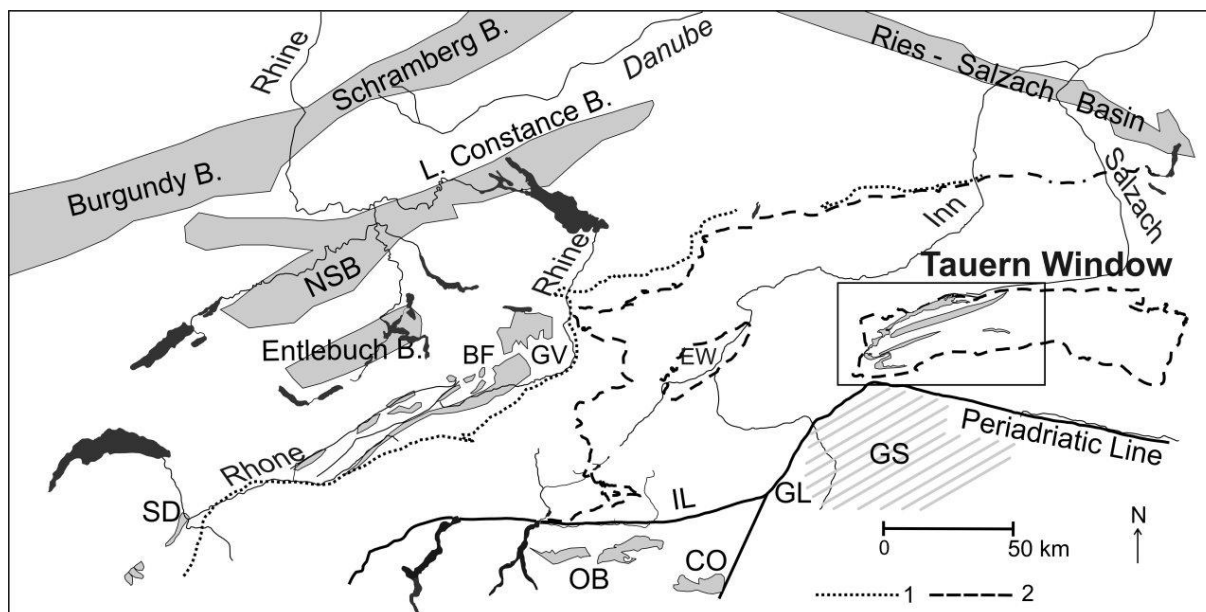
Figure1-1: Post-Variscan basins in Central Europe (mostly Permo-Carboniferous) taken from Vesela et al. (2008). 1- Penninic und Helvetic thrust-front, 2- Austroalpine-Penninic thrust-front, SD – Sal Salvan-Dorénaz Basin, BF – Bifertengrätli Basin, GV – Glarner Verrucano Basin, IL – Insubric Line, OB – Orobic Basin, CO – Collio Basin, GL – Judicarien Line, GS – Grödner Sandstone Basin, EW – Engadin Window

During the Mesozoic, a sequence of clastic and calcareous sediments was deposited on top of a late Palaeozoic unconformity. Starting with Upper Buntsandstein redbeds, the Triassic is mainly represented by Muschelkalk and Keuper sequences, which contain marine carbonates, evaporites and clastic sediments (Trümpy, 1960; 1980). Communications of the Germanic inland sea with the Tethys were seldom or lacking during Middle Muschelkalk (Ziegler, 1990). This resulted in the deposition of evaporites, the "Anhydrite Group", in a SW-NE trending depression in the northern and eastern parts of the Swiss Jura (Trümpy, 1980). These units serve as décollement horizon for most of the Swiss Jura, whereas further west this role is also taken by the Keuper evaporites (Laubscher, 1977; Philippe, 1994).

The Jurassic sequence is of special interest for hydrocarbon exploration because it has both source rocks and oil producing sandstones, and consequently is well studied. The early Jurassic deposits are dark pelites, which locally contain intercalations of shallow marine sand- and limestones. An important horizon is the Toarcian Posidonia Shale, which is widely distributed, features a rich nektonic and planktonic fauna, and is oil producing. During Middle Jurassic the Jura platform differentiates into two realms which stay separate until the Late Jurassic. Sedimentation in the north-west is characterized by a shallow-marine facies

which features for example platform carbonates, oolitic limestones and reef carbonates, whereas in the Swabian realm a more muddy sedimentation under a low-energy regime prevails (Trümpy, 1980). Eventually, the Helvetic facies developed, which reflects a relatively deep, sub-euxinic outer shelf depositional environment (Bachmann et al., 1987). Late Jurassic series crop out in the Helvetic nappes of western Austria and Switzerland.

During latest Jurassic to earliest Cretaceous a eustatically induced regression affected Western Europe (Ziegler, 1990). This caused a rapid shallowing of the South German shelf areas and led to the establishment of a land-bridge between the seas bordering the Tethys and those of northern Germany and north-eastern England (Trümpy, 1980; Bachmann et al., 1987). Cretaceous sedimentation is governed by eustatic sea level changes and repeated erosion phases. Mostly marine conditions prevailed throughout the area of the Molasse basin; predominant lithologies are marls, limestones and, during late Cretaceous series, sandstones. However, Cretaceous sediments play only a minor role in the basin evolution and are only preserved at its fringes (Trümpy, 1980).

1.3.3 Tertiary Basin Evolution

With the Adriatic plate advancing from the south, the down-going European plate underwent flexural bending (Pfiffner, 1986). This resulted in the formation of a characteristic wedge-shaped foreland basin. During Tertiary time, rivers originating in the rising Alps and partly in the Bohemian Massif shed huge amounts of sediment into the evolving basin (Trümpy, 1980). Along-strike of the orogen, several river systems which terminate in characteristic fans can be distinguished. Examples of these are the Napf-Fan in Central Switzerland, the Hörnli- or the Nesselburg-Fan in Bavaria. Close to the orogenic front, Molasse sediments can reach a thickness of 4000-5000 metres, in some places even more (e.g. Matter et al., 1980). Often organic material can be found in the Molasse sediments and several coal, oil and gas deposits have been reported (e.g. Trümpy, 1960; Vollmayr and Wendt, 1987; Schegg et al., 1999).

The North foreland Basin of the Alps is classically subdivided into five lithostratigraphic units, for which (by convention) the German abbreviations are used (Kempf et al., 1999). From

oldest to youngest: North Helvetic Flysch (NHF), Lower Marine Molasse (UMM), Lower Freshwater Molasse (USM), Upper Marine Molasse (OMM), and Upper Freshwater Molasse (OSM). Based mainly on magneto-stratigraphy and fossil record (e.g. Schlunegger et al., 1996), absolute depositional ages can be postulated:

North Helvetic Flysch (NHF), c. 40-34 Ma

Lower Marine Molasse (UMM), c.34-28 Ma

Lower Freshwater Molasse (USM), c. 28-22 Ma

Upper Marine Molasse (OMM), c.22-16 Ma

Upper Freshwater Molasse (OSM), c. 16-5 Ma

In the two regressive cycles of UMM + USM and OMM + OSM respectively, fine-to-coarse-grained clastics were deposited in deep marine, deltaic, shelf and beach environments (e.g. Matter et al., 1980; Lemcke, 1984). The sedimentary succession starts with turbidity current deposits, which are observed in both the Fischschiefer in Switzerland and the Deutenhausener beds which are mostly present in the Austrian and Bavarian part of the basin (Füchtbauer, 1967).

1.3.3.1 North Helvetic Flysch

The North Helvetic Flysch overlies neritic sediments of Eocene age (e.g. Herb, 1988; Sinclair, 1997b). It is a classic flysch sequence, which developed in orogen-parallel troughs (Homewood and Caron, 1982; Caron et al., 1989). A striking feature is the abundant occurrence of andesitic material in the basal formations (in the Central Alps mostly the Taveyannaz and Altdorf Sandstones) (e.g. De Quervain, 1928; Trümpy, 1980; Homewood, 1983; Sinclair, 1997a).This makes them important target rocks for thermochronological sampling, as they mostly contain apatite.

1.3.3.2 Lower Marine Molasse (UMM), Rupelian

The Lower Marine Molasse Group (UMM) forms the transition from the under-filled to the over-filled stage of basin evolution (Schlunegger et al., 2001). Sediments were deposited in a shallow marine environment that extended to the Carpathians in the East. Lithologies

preserved are fine grained sandstones, clay stones and marls. The transition from Flysch to Molasse sedimentation is witnessed by various (calci-) turbidites (Matter et al., 1980). A typical marine fauna, with shark teeth, shells etc. developed throughout the whole basin in that period. The Alps were not a high orogen at this time, therefore only small deltas of coarse clastic material could be formed at the southern fringe of the basin (Matter et al., 1980).

1.3.3.3 Lower Freshwater Molasse (USM), Chattian to Aquitanian

Contemporaneous with backthrusting along the Insubric Line (Schmid et al., 1996) and advance of the orogenic wedge (Milnes and Pfiffner, 1977; 1980), the first USM strata were deposited (Schlunegger et al., 1997b).The first alluvial fans developed, including the Rigi, Napf and Pfänder. They comprise sedimentary and crystalline material from Penninic and Austroalpine units (Füchtbauer, 1967). The USM deposits form the bulk of the Molasse sedimentary succession, with local maxima of up to 5000 m thickness (Walter, 1995). Farther from the Alpine front, lacustrine and fluviatile deposits dominate the western Molasse basin, whereas in the east mostly brackish conditions prevail (e.g. Schlunegger et al., 1996; Schlunegger et al., 1997a; Schlunegger et al., 1997b; Berger et al., 2005b). In the brackish and fresh-water deposits, coal-bearing beds can be found, which were mined in the Bavarian part of the basin (Balthasar et al., 1975).

1.3.3.4 Upper Marine Molasse (OMM), Burdigalian

Corresponding to a global sea-level rise, the foreland basin was flooded and marine sediments were deposited (Berger et al., 2005b). Lammerer (2008) related basin subsidence in the east to the rise of the Tauern Window. Alternatively, a decrease of sediment discharge from the orogen into the basin resulted in basin underfill and consequently could have caused a transition to marine conditions (Schlunegger et al., 1997b).Shallow marine conditions prevailed again for c. 6 Ma (e.g. Schlunegger et al., 1996). The sedimentation of the Napf and Hörnli Fans (central Switzerland) continued. Sand and clay was deposited basin wide. During the Lower Miocene, parts of the northern Alps and of the Carpathians were flooded by the Molasse Sea (Trümpy, 1980). At a late stage of OMM deposition, a sea cliff developed along the northern basin margin, probably during the Ottnangian sea-level

highstand (Kuhlemann and Kempf, 2002). The end of OMM sedimentation is marked by brackish deposits from the early Karpatian (upper Burdigalian) (Kuhlemann and Kempf, 2002).

1.3.3.5 Upper Freshwater Molasse (OSM), Serravallian

During the Upper Freshwater Molasse, the sea finally retreated. The build up of alluvial fans and palaeo-river systems continued and sedimentary thicknesses locally exceed 1500 m (Walter, 1995). Farther in the basin, mostly sandstones and marls are preserved; at the fringes volcanic activity occurred (e.g. Rahn and Selbekk, 2007). The topmost OSM deposits have been removed by erosion (Schegg, 1992; Schegg and Leu, 1998; Cederbom et al., 2004; Mazurek et al., 2006; Willett and Schlunegger, 2010; Cederbom et al., 2011).

Figure 1-2: Flysch and Molasse in outcrop. Top Left: NHF from Altdorf, Switzerland, top right: UMM beds clay sand intercalations; Griesigen, Switzerland, bottom left: Sandstone of the USM, Peißenberg; Bavarian Molasse (photo by Thomas Weinfurtner), bottom right: OMM sandstone in Lucerne "the most mournful and moving piece of stone in the world" (Mark Twain, 1880 in "A Tramp Abroad"). What he did not know: this piece of stone has been moving since c. 20 Ma.

1.3.3.6 Heterogeneities of deposition along strike

The sedimentary facies vary along strike such that in the east of the basin the regressive cycles are less pronounced than in the west (e.g. Fuchs, 1976; Ortner et al., 2011). In the eastern part of the basin, only one regressive cycle is deposited and marine conditions prevail until the late Burdigalian, when they are superseded by the sediments of the OSM (Jin et al., 1995; Burkhard and Sommaruga, 1998a; Schlunegger, 1999; Piller et al., 2004). Some of these rock units include other facies than what their formal name suggests, and time equivalent series contain different lithological suites, varying over short distances (Matter et al., 1980; Sissingh, 1997). The influence of these heterogeneities on the tectonics will be discussed in section 1.3.4.

1.3.4   Tectonic Setting

The Molasse basin, together with the Jura fold and thrust belt, forms the most external part of the Alpine chain (Burkhard, 1990). At the southern fringe of the basin, sediments were incorporated into the Alpine wedge shortly after deposition, leading to the formation of the Subalpine Molasse (Vollmayr and Wendt, 1987; Müller et al., 1988; Schlunegger et al., 1997a; Kempf et al., 1999). The Subalpine Molasse separates the Alpine nappe stack from the weakly deformed to flat lying Plateau Molasse and thus form the northern margin of the Alps as defined by Müller et al. (1988).

Since the southern limits of the basin are overthrusted and partly hidden from direct observation, it is difficult to restore the original basin width. Unfolding the Subalpine Molasse leads to an original basin width of at least 10 km but potentially more than 30km (Matter et al., 1980). Thus the present day Molasse basin is only a small remnant of a formerly much larger basin (Burkhard and Sommaruga, 1998b).

Heterogeneities in foreland mechanical stratigraphy (facies changes, the presence of basement palaeo-highs or older deformation structures) influence displacement patterns, particularly in the Western Alps (Lickorish et al., 2002). Furthermore, for the foreland basin of the Central and Eastern Alps these differences serve as pre-deformational conditions controlling the local structural style of the Subalpine Molasse (Ortner et al., 2009; Hinsch and Linzer, 2010). However, they do not influence the observed amount of shortening (Ortner et al., 2011).

In most parts of the basin the Subalpine Molasse has the structure of a triangle zone (e.g. Müller et al., 1988). This was undiscovered until the borehole Sulzberg-1 was drilled in the late 1980s. In comparison with the Alberta Foothills, the wedge which is thrust into the autochthonous foreland was described for the first time (Müller et al., 1988) and has later been revealed in more detail on high resolution seismic profiles (Berge and Veal, 2005). Growth structures show that the frontal structure propagated towards the foreland until at least the deposition of the youngest preserved sediments at c. 9 Ma (Ganss and Schmidt-Thomé, 1953; Eberhard, 1986; Ortner et al., 2009).

1.4 Methods

1.4.1 Principles of Thermochronology

Thermochronology is, amongst other applications, widely used for the reconstruction of thermal and structural histories of mountain belts. A range of thermochronometers is commonly applied, each sensitive to a different temperature (Figure 1-3), which Dodson (1973) termed the "closure temperature". Since temperature increases with crustal depth, this temperature can be translated into depth under the assumption of a geothermal gradient. The basic principle behind thermochronology is the decay of different radioactive isotopes and the thermally controlled accumulation of the decay products (e.g. Braun et al., 2006; Reiners and Brandon, 2006). Radio-isotopic production is a function of time and accordingly a thermochronometer reports the last point in time when a certain mineral within a rock experienced a certain temperature; hence thermochronology is suitable for deciphering timing and rate of crust removal. It is particularly useful for recognizing late reheating events, which is common in sedimentary basins. Applying different thermochronometers to one sample provides additional information as it further constrains the exhumation history. Only minerals which can incorporate radioactive isotopes into their crystal lattice are suitable for dating. The most common minerals used are zircon, titanite, monazite, apatite, hornblende, biotite, muscovite and K-feldspar. Many of these minerals are suitable for more than one thermochronological method. For instance zircon can be used for (U-Th)/Pb, fission track and (U-Th)/He dating (Figure 1-3).

The concept of closure temperature

Dodson (1973) defines the closure temperature T_c as "*its temperature at the time corresponding to its apparent age*". It is the point in time at which a completely mobile daughter product of radioactive decay becomes completely immobile (Dodson, 1973).
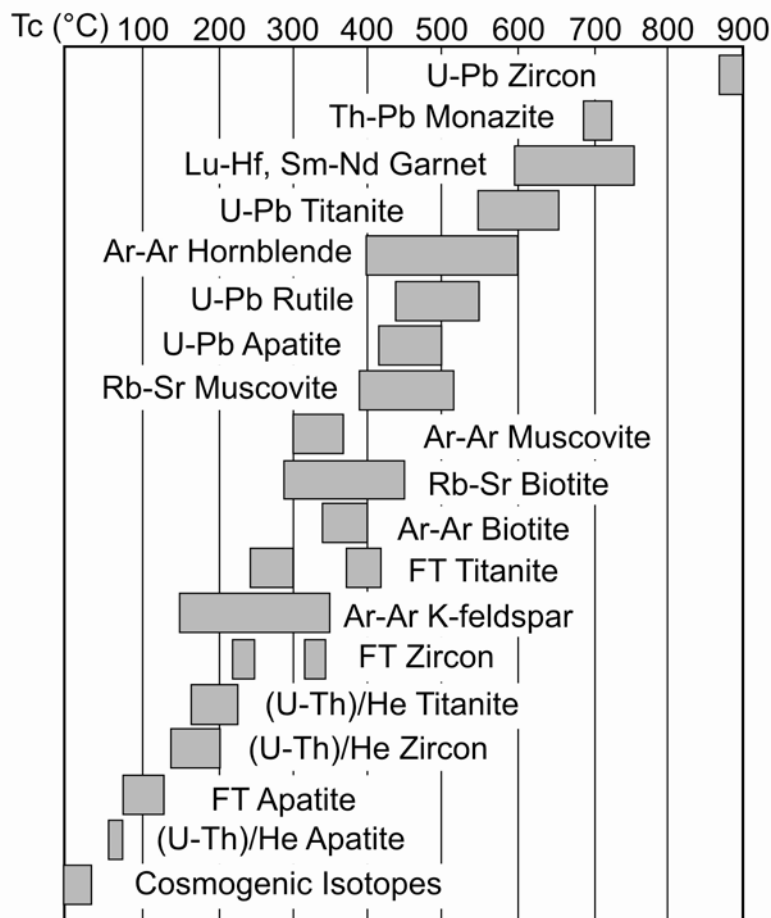
Figure 1-3: Thermochronometers commonly used to disclose exhumation histories of minerals and rocks (after http://su-thermochronology.syr.edu/). Closure Temperatures taken from the compilation by Reiners et al. (2005).

However, the concept of closure temperature has certain caveats which we can see if we follow the original derivations by Dodson (1973). The entire concept is based on diffusion of daughter isotopes within the crystal (the retentivity of the crystal respectively) and can thus be expressed by the Arrhenius equation:

$$D = D_0 \times e^{\left(-\frac{E}{RT}\right)} \tag{1-1}$$

where *D* denotes the diffusion coefficient with the dimension m²/s, *T* the absolute temperature in °K, *R* the gas constant, *E* the activation energy and D_0 the diffusion coefficient at an infinitely high temperature. As diffusion is strongly temperature dependent, for a cooling history Dodson (1973) introduces a time constant τ, which describes the diffusion-coefficient decrease during cooling. This changes the formula to:

$$D = D_0 \times e^{\left(-\frac{E}{RT_0} - \frac{t}{\tau}\right)} \qquad \text{(1-2)}$$

Here, T_0 denotes the temperature at $t=0$. The dimension of τ is time and is equal to the time span needed to diminish D by a factor of e^{-1} or to increase E/RT by 1. Mathematically expressed this is

$$\tau = -\frac{RT^2}{E\left(\frac{dT}{dt}\right)} \qquad \text{(1-3)}$$

Together with (1-2) this means that the diffusion coefficient decreases exponentially with time and temperature. At some point the diffusion becomes so slow that the production rate of daughter isotopes is higher than the loss rate and eventually the daughter isotopes are immobile and accumulated in the crystal. Dodson shows that the closure temperature is given by:

$$T_c = \frac{E}{R * \ln\left(A\tau\frac{D_0}{a^2}\right)} \qquad \text{(1-4)}$$

A denotes a numerical, dimensionless constant depending on the geometry (i.e. the surface-to-volume ration) of the crystal (A = 27 for a cylinder and 55 for a sphere) and a is a characteristic dimension of the system, such as the radius of a cylinder or a sphere. Hence the closure temperature is dependent on the shape of the crystal and the cooling rate. For reheated samples additional complexity is added, as diffusivity is a function of magnitude and duration of the heating event, which means that the closure temperatures listed in (Figure 1-3) may have no significance (e.g. Reiners et al., 2005).

A general limitation of the closure temperature concept is that it is based on thermal diffusion only, whereas in many rocks fluid-assisted recrystallization may govern isotope exchange rates (Villa, 1998). For low-temperature thermochronometers however, thermal diffusion is usually the primary control on daughter isotope retention (Baxter, 2010).

In this study, apatite fission track and apatite (U-Th-Sm)/He dating are combined, which are two low temperature thermochronometers with similar T_c. These have been calibrated independently in numerous studies (e.g. Gleadow and Duddy, 1981; Green et al., 1989; Wolf et al., 1996; Carlson et al., 1999; Farley, 2000; Stockli et al., 2000) Combining particularly these two methods proved to yield good constraints on time-temperature histories within depths between 1 and 5 km, (e.g. Armstrong et al., 2003; Ehlers et al., 2003; Ehlers, 2005; Stockli, 2005; Fitzgerald et al., 2006; Foeken et al., 2007).

1.4.2 Fission track formation and fading

Fission tracks in apatite develop when a heavy, unstable ^{238}U nucleus splits spontaneously into two fragments and creates a damage trail as these fragments are travelling at high velocity through their surrounding medium (Tagami and O'Sullivan, 2005). Two models for track formation exist. One is the "ion explosion spike" model, which explains track formation with electrostatic displacements due to the massive positive charge of the fragments (Fleischer et al., 1975). Alternatively, in the "thermal spike" model, thermal activation and conduction results in crystal lattice defects as the energetic particles are passing through the medium (e.g. Bonfiglioli et al., 1961). Also both, thermal and ion explosion spike may be present to different degrees in a "compound spike" (Chadderton, 2003). In general, the tracks represent a cylindrical shape with a length between 10 and 20 µm (c. 16 µm for apatite) and a diameter of 6-10 nm (Wagner and Van den haute, 1992; Tagami and O'Sullivan, 2005). The created tracks are latent but can be enlarged by chemical etching, and inspected under an optical microscope. Figure 1-4 shows spontaneous tracks in an apatite crystal after etching.

Fission tracks are unstable and will start to shorten progressively at elevated temperatures (Green et al., 1986). This annealing is the re-crystallization of the amorphous core of the track (Tagami and O'Sullivan, 2005). During early stages of annealing, the tracks shrink from both ends, which makes track length a function of temperature (Donelick et al., 1999). The annealing behaviour is dependent on the kinetics of the respective apatite grain (Carlson et al., 1999; Donelick et al., 1999). A measure of the annealing kinetics is the Dpar value, which is the arithmetic etch pit figure diameter parallel to the crystallographic c-axis (Donelick et

al., 2005) (Figure 1-4). This parameter is correlated with the chemical composition of the apatite, but cannot be used as a proxy for it, as it is also controlled by factors such as accumulated α-particle damage or the temperature of formation (Carlson et al., 1999; Donelick et al., 2005). Apatites with low Dpar values (< 1.75 μm) are more sensitive to annealing (Carlson et al., 1999). These apatites are quite common and also most of the apatites in this study have Dpar values below 1.75 μm. Some general statements about the nature of Dpar with respect to the chemical composition of the apatite can be synthesized from Carlson et al. (1999) and Donelick et al. (2005):

- If the apatite has a low Dpar, it is a Ca-rich F-apatite and its Cl wt% content is low
- Not every Ca-rich F-apatite features a low Dpar value
- If the apatite is chlorine rich (> 0.5 wt%), it anneals slowly
- Apatites with low Dpar values are also low in FeO, OH and Mn

Annealing of fission tracks is also dependent on their orientation with respect to the crystallographic c-axis. Fission tracks at high angles to c-axis undergo systematic accelerated annealing (Donelick et al., 1999).
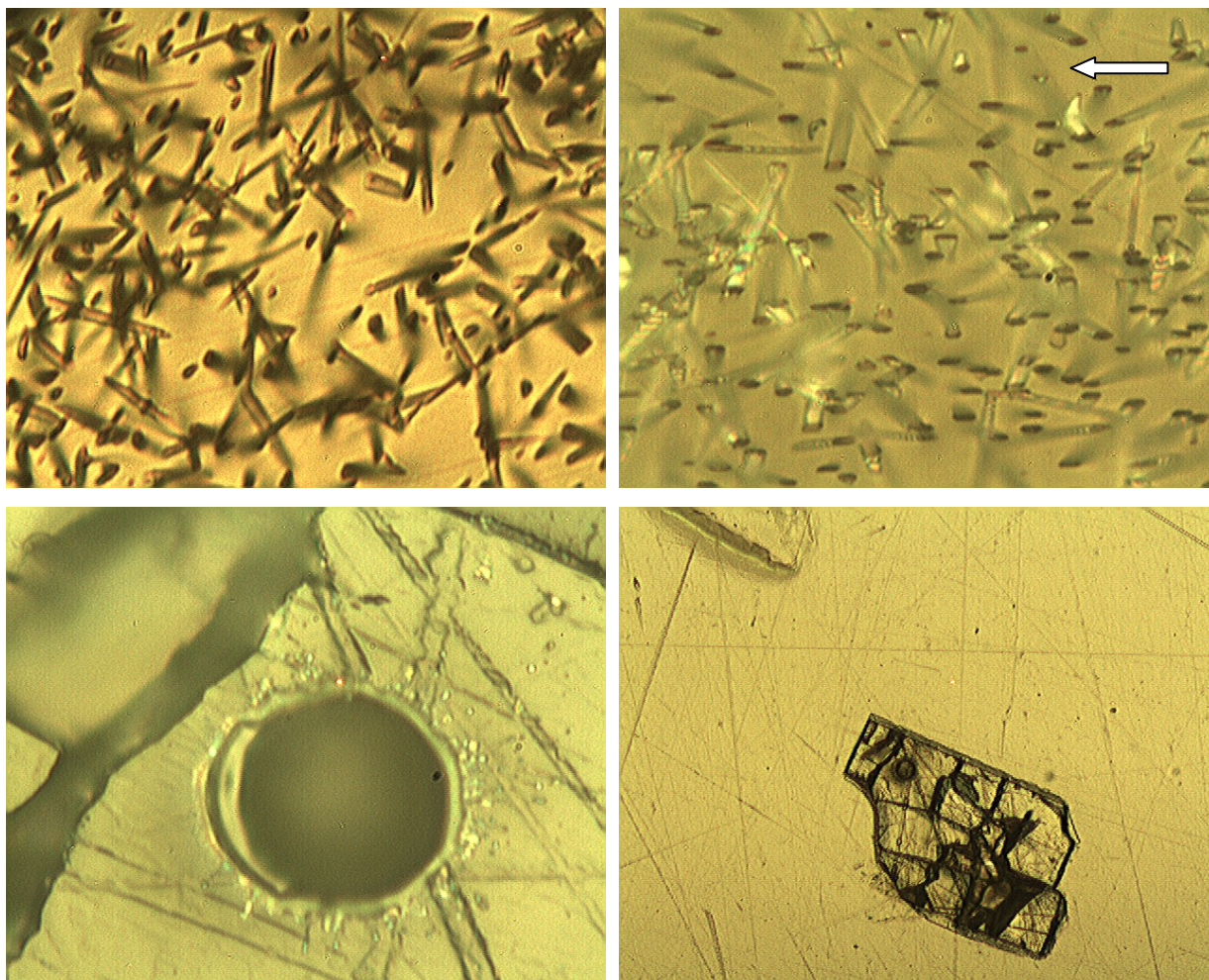
Figure 1-4: Top left: spontaneous fission tracks on a polished and etched surface of apatite. Magnification is 2000x. Note the confined tracks bottom left of the picture. Note also that some tracks appear long and thin, whereas others are short and thick. This can depend on different grades of annealing as well as on their angle to c-axis (tracks parallel to c-axis are longer). Top right: spontaneous tracks under reflected light. The etch figures are very clear and all aligned parallel to the c-axis of the crystal (indicated by the white arrow). Magnification is 2000x. Bottom left: Pit created during laser spot analysis of the apatite. Bottom right: mounted and polished apatite grain. Magnification is 1600x. Note the laser spot top left of the grain.

The temperature range in which track annealing occurs is called the Partial Annealing Zone (PAZ). This temperature range is dependent on apatite chemistry but usually falls in the range between c. 60 and 110 °C. It is clearly visible in vertical age-elevation profiles in relatively stable thermo-tectonic environments (Gleadow and Duddy, 1981). Rapid denudation at a certain point in time leads to a cooling pulse and can exhume the PAZ, halting the annealing process (Fitzgerald et al., 2006) (Figure 1-5). This pattern can become more complicated when multiple thrusts or thrusting phases offset the exhumed PAZ or when the isotherms are not flat lying but are perturbed due to relief.
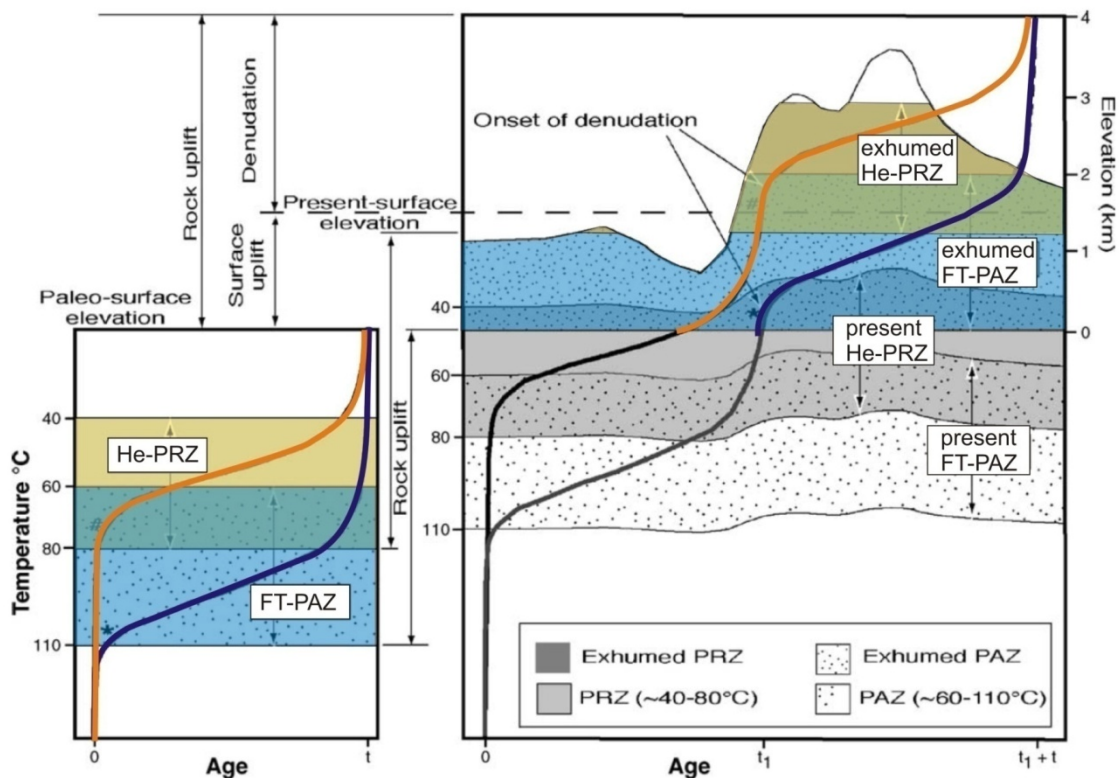
Figure 1-5: The concept of the present day and fossil partial annealing and the partial retention zone after Fitzgerald (2006). A rapid cooling and exhumation event at t_1 is observed as a break in slope of the elevated age-elevation profile. This one dimensional pattern can become much more complex when 2D or 3D effects are accounted for.

1.4.3   Fission track age determination

The fission track age is a function of the relative abundance of parent and daughter isotopes within the apatite. The measure for daughter isotopes is the track density, which is determined under an optical microscope simply by counting the amount of tracks within a selected area. In this study, the amount of parent isotopes was determined with the Laser Ablation Inductively Coupled Mass Spectrometry (LA-ICP-MS) method, which measures ^{238}U in situ (Hasebe et al., 2004). Therefore, the apatite grain must be ablated with a pulsing laser beam, which is drilling an approximately 13 μm deep and c. 10 μm wide pit into each grain where track density was previously determined. Figure 1-4 shows such a pit and the respective grain. A disadvantage of this method is that, as the grain is destroyed, recounting is impossible. Additionally, the pit is assumed to be representative for the entire grain, which is problematic for grains with multiple age zones, inclusions or unevenly distributed parent isotopes. However, to some degree, the pulsing measurement of the laser ablation is able to

detect zoning within the grain. The method also allows the direct determination of ^{238}U (Donelick et al., 2005), in contrast to the indirect counting of fission track maps as done when applying the "classical" external detector method (Gleadow and Duddy, 1981). Moreover, LA-ICP-MS dating is faster and cheaper than the classical approach, since the samples do not have to be irradiated after counting.

After Donelick (2005), the LA-ICP-MS AFT age of a single apatite grain is given by

$$t_i = \frac{1}{\lambda_d} ln\left(1 + \lambda_d \zeta_{MS} g \frac{\rho_{s,i}}{P_i}\right)$$

<div align="right">(1-5)</div>

Where λ_d is the decay constant of ^{238}U, ζ_{MS} is the calibration factor, g is a geometry factor (= 0.5 for tracks intersecting the analyzed area from bottom and top), P_i is the (^{238}U/^{43}Ca) for apatite grain i, and $\rho_{s,i}$ is the density of spontaneous tracks (tracks per counted area). As the dating is a statistical method, 40 grains were dated if possible. They can be pooled into one age that is representative for a sample with a uniform cooling history and comparable annealing kinetics. The equation after Donelick (2005) is then

$$t_{pooled} = \frac{1}{\lambda_d} ln\left(1 + \lambda_d \zeta_{MS} g \frac{\sum N_{s,i}}{\sum P_i \Omega_i}\right)$$

<div align="right">(1-6)</div>

Where $N_{s,i}$ denotes the number of spontaneous tracks counted over the area Ω_i. However, in this study, most samples are sedimentary rocks and hence potentially comprise a variety of different apatites. In addition, reheating occurred in the Subalpine Molasse, which was not always substantial enough to anneal the tracks completely. In this case, the pooled age has no geological meaning but can be used for general age trends. A geologically meaningful sample would comprise of single grain age populations (peak ages), which can be determined statistically. A first impression of whether a sample has more than one population can for instance be gained from probability density plots. Figure 1-6 shows the probability density plots for different samples of this study. It becomes clear that many samples must have more than one single grain age population and that hence the pooled age is not geologically meaningful. Alternatively, LA-ICP-MS AFT ages can be analyzed with

radial plots (Vermeesch, 2009). I also applied this method, as it is able to determine single grain age populations much more precisely. How this is done and a more detailed description how AFT dating was performed in this study is given in sections 2.4 and 3.2.
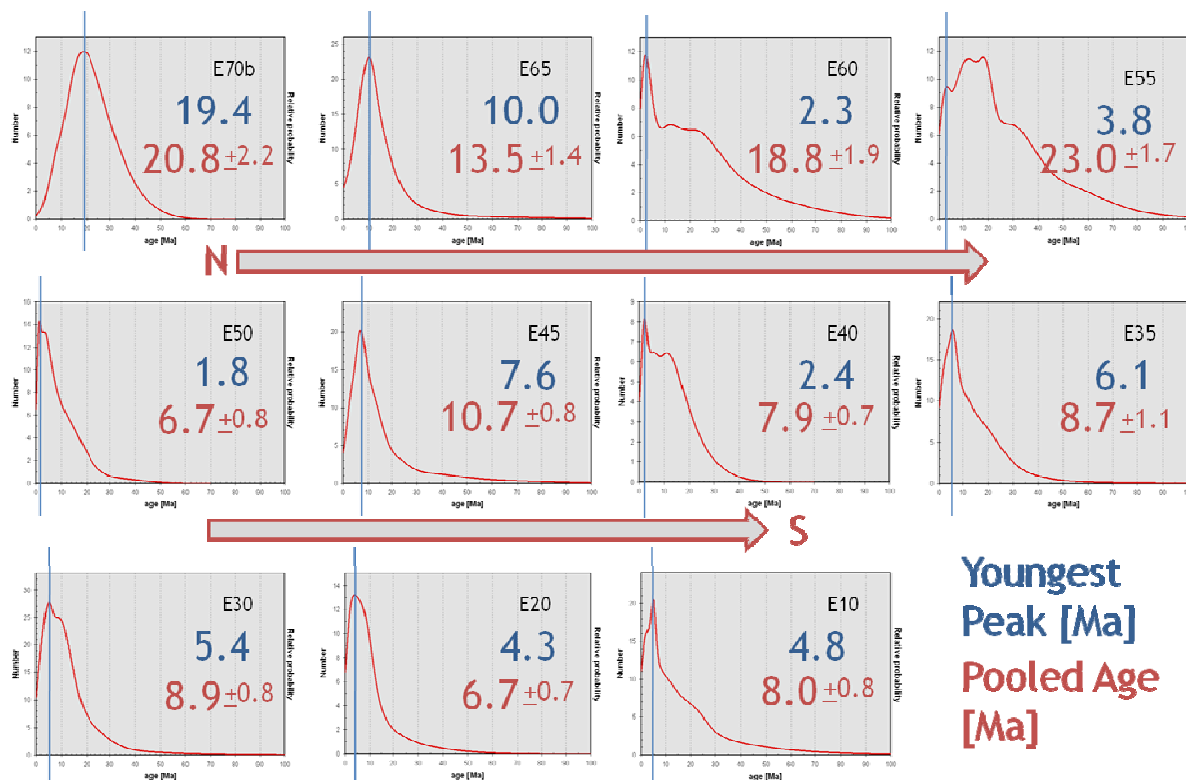
Figure 1-6: Probability density plots for samples from the Entlebuch in the Subalpine Molasse. Axes of the individual plots are relative probability vs. age. For samples which feature just one grain age population, one single and sharp peak would be expected. The youngest peaks were determined manually and have hence no error bars (blue lines). The pooled age is calculated according to equation (1-6).In many of these samples the youngest peak and the pooled age differ significantly, indicating the presence of more than one grain age population.

1.4.4   (U-Th-Sm)/He dating

Apatite is able to retain [4]He in its crystal lattice. This makes it suitable for (U-Th-Sm)/He dating. Helium is produced within the crystal mainly by [238]U, [235]U, [232]Th and to a minor degree by[147]Sm. Typically, apatites have a Sm age contribution of 0.1-10% (Belton et al., 2004b). Still, unless the Sm/ (U+Th) is unusually high, the Sm-contribution is rather small (Foeken et al., 2007).The generalized exact age equation, which includes Samarium is after Vermeesch (2008)

$$[He] = \left(8\frac{137.88}{138.88}\left(e^{\lambda_{238}t} - 1\right) + \frac{7}{138.88}\left(e^{\lambda_{235}t} - 1\right) \right)[U]$$

$$+ 6\left(e^{\lambda_{232}t} - 1\right)[Th] + 0.1499\left(e^{\lambda_{147}} - 1\right)[Sm]$$

(1-7)

Which is equal to the helium production rate *P* after Dunai (2005):

$$P = \sum_{j=1}^{4} \frac{p_j}{\lambda_j}\left(e^{\lambda_j t} - 1\right)$$

(1-8)

with

$p_1 = 8\,\lambda_1\,[^{238}U];$ $\lambda_1 = 1.55125 \times 10^{-10}a^{-1}$

$p_2 = 7\,\lambda_2\,[^{235}U];$ $\lambda_2 = 9.8485 \times 10^{-10}a^{-1}$

$p_3 = 6\,\lambda_3\,[^{232}Th];$ $\lambda_3 = 4.9475 \times 10^{-11}a^{-1}$

$p_4 = \lambda_4\,[^{147}Sm];$ $\lambda_4 = 6.539 \times 10^{-12}a^{-1}$

where $\lambda_{238} = \lambda_1$, $\lambda_{235} = \lambda_2$, $\lambda_{232} = \lambda_3$ and $\lambda_{147} = \lambda_4$ and denote the decay constants of ^{238}U, ^{235}U, ^{232}Th and ^{147}Sm respectively.

[4]He is rapidly transported out of the crystal by diffusion processes at temperatures higher than their closure temperature (effective closure temperature after Flowers et al. (2009)). This temperature depends on the cooling rate and the amount of parent isotopes present (Flowers et al., 2009). Similarly to AFT dating, the system is not closing instantly but in a transient fashion over a temperature range. Analogously, this zone is called the Partial Retention Zone (PRZ). Typically, the PRZ ranges between c. 80 and c. 40 °C (Figure 1-5). In the middle of the PRZ, He ages are extremely sensitive to temperature (Farley and Stöckli, 2002). At even lower temperatures, nearly all daughter isotopes are accumulated within the crystal (Wolf et al., 1998). However, helium-diffusivity is not only a function of temperature. It also scales with the inverse square of grain size (Farley, 2000), depends on the grain shape

(Farley, 2000; Reiners and Farley, 2001) and is sensitive to defects within the crystal lattice such as fission tracks or radiation damage (Shuster et al., 2006; Flowers et al., 2009).

For age determination, suitable crystals have to be selected, which are preferably idiomorphic and unbroken. This can be a major challenge, especially for sedimentary samples. The selected grains are degassed by laser heating and later dissolved to analyze parent isotope content on the ICP-MS. The resulting ages have to be corrected for α particle ([⁴He]) ejection (Farley and Stöckli, 2002). α particles travel approximately 20 μm through the crystal (Ehlers and Farley, 2003). Therefore parent isotopes that are located close to the fringes of the measured apatite grain have a certain probability to eject the α particle into the surrounding medium, which leads to erroneously young age determinations. This effect becomes more important, the bigger the surface volume ratio is. Apatites with a diameter of less than 75 μm do not yield trustworthy (U-Th-Sm)/He ages (Ehlers and Farley, 2003), (Figure 1-7). To overcome this effect, all measured (raw) ages are corrected by a factor F_T, which defines the fraction of parent isotopes that are able to implant all their daughter isotopes within the crystal (Farley and Stöckli, 2002). Farley et al. (1996)define it as

$$F_T = 1 - 0.75 \left(\frac{s}{r}\right) + 0.0625 \left(\frac{s}{r}\right)^3 \qquad \text{(1-9)}$$

where s is the stopping distance and r is the grain radius. They calculate the corrected age t_{corr} by increasing the raw age t:

$$t_{corr} = t \left(\frac{1}{F_T}\right) \qquad \text{(1-10)}$$

This correction implies that no helium is implanted into the grain from external sources and that the parent isotopes are evenly distributed within the grain (Farley et al., 1996; Farley and Stöckli, 2002; Ehlers and Farley, 2003).
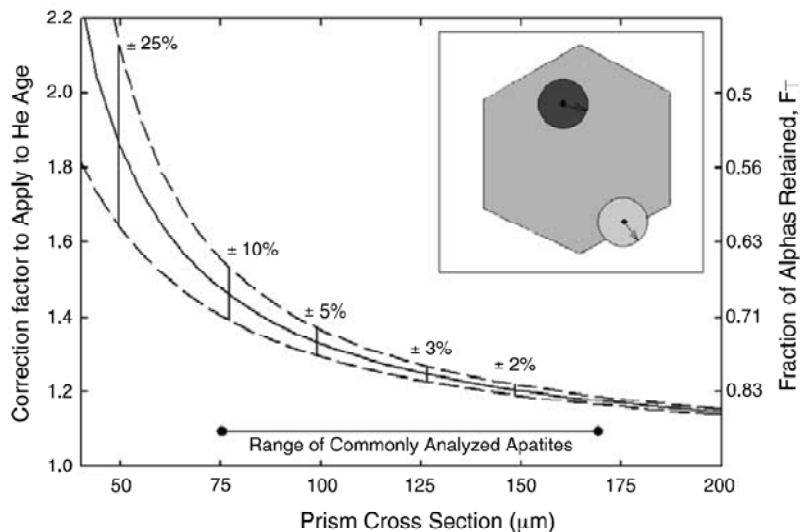
Figure 1-7: The influence of α particle ejection and the correction needed on the raw age (Ehlers and Farley, 2003). Dashed lines indicate the 1 σ uncertainty on the correction factor F_T. The inset shows a schematic cross section through an apatite grain and the potential ejection of α particles when the parent isotope is located less than 20 μm from the fringe of the grain.

A common phenomenon observed in (U-Th-Sm)/He dating is single grain age variation, which can have different causes. Grain age variations which are a consequence of methodological uncertainties, such as grain zonation, U- or Th-rich inclusions, imprecise F_T correction or implanted helium are geologically meaningless. In contrast, samples which contain grains with different chemical composition, reside for a long time in the PRZ or cool relatively slowly (< 3 °C/Ma) often display geologically meaningful single grain age variations (Fitzgerald et al., 2006). To detect whether a grain is geologically meaningful, Vermeesch (2008) proposed the additional method to plot helium production rate against measured helium. This should result in a straight line through the origin and all grains which fall off that line are potentially wrong. Such plots for all samples of this study are given in the appendix. A description how (U-Th-Sm)/He dating was applied in this study is given in chapter 2.4.

2 Resolving the latest uplift and erosion history of the Northern Alpine Foreland Basin with low temperature thermochronology

Von Hagke, C., Cederbom, C.E., Oncken, O., Stöckli, D.F., Rahn, M.K., Schlunegger, F.

Submitted to Tectonics

Abstract

The Subalpine Molasse forms a transition zone between the Alps and its undeformed foreland and therefore provides information about the late orogenic evolution of the Alps and the foreland basin itself. However, its latest uplift and erosion history is poorly understood due to the lack of late Miocene to Pliocene sediments. We constrain the late Miocene to Pliocene history of this transitional zone with apatite fission track and (U-Th)/He data. We used Laser ablation-ICP-MS for apatite fission track dating and compare these with previously published and unpublished EDM fission track data. Two investigated sections across tectonic slices show that the Subalpine Molasse was tectonically active after the onset of folding of the Jura Mountains. This is much younger than hitherto believed. Thrusting occurred at 10, 8, 6-5 Ma and potentially thereafter. This is contemporaneous with reported uplift of the external crystalline massifs in the Alps. We find that the Jura Mountains and the Subalpine Molasse used the same detachments as the external massifs and are therefore kinematically coupled. Estimates on the amount of shortening corroborate this idea. Considering the Subalpine Molasse as part of a readjusting critical wedge offers a possible explanation for the thrusting.

2.1 Introduction

The Alps and its adjacent northern foreland basin are among the best studied areas in the world, but we know little about the latest uplift and erosion history. This is mostly due to the lack of preserved sediments spanning the time interval between the Late Miocene and the Pliocene, which were removed by erosion (Kuhlemann and Kempf, 2002; Cederbom et al., 2004; Cederbom et al., 2011; Schlunegger and Mosar, 2011). In contrast, the orogenic evolution of the Alps until the Middle Miocene is well known from the well-preserved

sedimentary record in the foreland basin (Pfiffner, 1986; Schlunegger et al., 2007). Based on this record, feedback mechanisms between crustal shortening, surface erosion and exhumation of upper crustal material have been elaborated in several recent studies (Schlunegger and Simpson, 2002; Willett et al., 2006).

Recent low temperature thermochronology studies partly unveiled the Pliocene and Quaternary evolution of the orogen and the foreland basin. Based on apatite and zircon fission track (FT) as well as apatite (U-Th-Sm)/He dating, Reinecker et al. (2008), Vernon et al. (2009b) and Glotzbach et al. (2010) constrained the exhumation histories of the Gotthard, Aar, and Mont Blanc massifs which are located in the centre of the orogen. Exhumation rates accelerated after 10 and 5 Ma. However, the mechanisms, which lead to this increase, are not clear. They may be related partly to increased rock uplift rates and partly to an acceleration of glacial scouring (Reinecker et al., 2008; Glotzbach et al., 2011a; Valla et al., 2011). For the Molasse Basin, an increase in erosion rate since 5 Ma has been postulated (Kuhlemann, 2000). Also, apatite FT data from boreholes (Cederbom et al., 2004; 2011) indicate rapid erosion starting at 5 Ma, which the authors attribute to a combination of climatic, tectonic, and geodynamic causes. However, the mechanisms leading to this phase of rapid erosion are a matter of debate (Cederbom et al., 2011; Schlunegger and Mosar, 2011). This in mainly due to the poor understanding of the late tectonic evolution of the external Alps.

To overcome this situation, we here explore the kinematic evolution of the proximal part of the Molasse Basin – the so-called Subalpine Molasse – at high resolution. To this end, we analyze vertical and horizontal sections for patterns of low-temperature thermo-chronometric ages. Emergent active thrusts may be visible as offsets in thermo-chronometric ages. We sampled two sections across the border between the Helvetic thrust nappes, the Subalpine Molasse and the flat-lying Plateau Molasse. We made a special effort to sample at a high spatial resolution, particularly in both the hanging and footwall of faults. Possible offsets in ages allow to bracket the age when these faults experienced deformation. Here, we combine apatite FT and apatite (U-Th-Sm)/He analyses to better constrain the timing, rate and style of exhumation in the Subalpine Molasse. Based on these data we

propose a new model that explains differential exhumation of the Subalpine Molasse in the light of the Alps as a critical wedge.

2.2 Regional geologic context

The North Alpine Foreland Basin (NAFB) extends c. 700 km from Haute Savoie, France in the west through Switzerland and Bavaria to the Linz-Vienna area of Austria in the east. It is a classic peripheral foreland basin whose Stratigraphy, structure and formation have been studied for over a hundred years (e.g. Äppli, 1897; Heim, 1919; Cadisch, 1928) and for which many geodynamic concepts have been tested (e.g. Ganss and Schmidt-Thomé, 1953; Trümpy, 1980; Homewood et al., 1986; Pfiffner, 1986; Schlunegger et al., 1997a; Sinclair, 1997b; a; Sissingh, 1997; Kuhlemann and Kempf, 2002; Pfiffner et al., 2002; Berger et al., 2005a; Berger et al., 2005b).

The formation of the basin is attributed to progressive flexural bending of the down-going European Plate adjacent to the approaching uprising Alps in Miocene time (Pfiffner, 1986; Burkhard and Sommaruga, 1998a; Pfiffner et al., 2002; Schlunegger et al., 2007). Consequently, the northern boundary of the wedge-shaped basin propagated northward through time, while the southernmost (and oldest) deposits were continuously incorporated into the Alpine orogen (Homewood et al., 1986). Together with the Jura fold and thrust belt the Molasse Basin forms the most external part of the Alpine chain (Burkhard, 1990) (Figure 2-1).

Starting in the Palaeogene, the complex collision history of the Alps was dominated by the foreland-directed propagation of the Alpine front (e.g. Delacou et al., 2004). However, the outward propagation of deformation is not uniform and single-staged along the strike of the orogen. In the Western Swiss Molasse, deformation jumped from a proximal position in the Subalpine Molasse (SM) across most of the basin to the more distal Jura Mountains (Figure 2-1). This is in contrast to the Eastern Alps, where distal deformation remained fixed along the SM. Some have argued that thrusting in the Western Swiss Molasse basin ceased at c. 12 Ma in conjunction with that jump to Jura thrusting (Burkhard and Sommaruga, 1998a). In the Jura Mountains, deformation proceeded until at least late Pliocene time (Liniger, 1964;

Mosar, 1999; Ustaszewski and Schmid, 2007). It may even continue at very slow rates today involving the basement blocks in thick-skinned deformation (Mosar, 1999; Ustaszewski and Schmid, 2007; Madritsch et al., 2008; Madritsch et al., 2010).
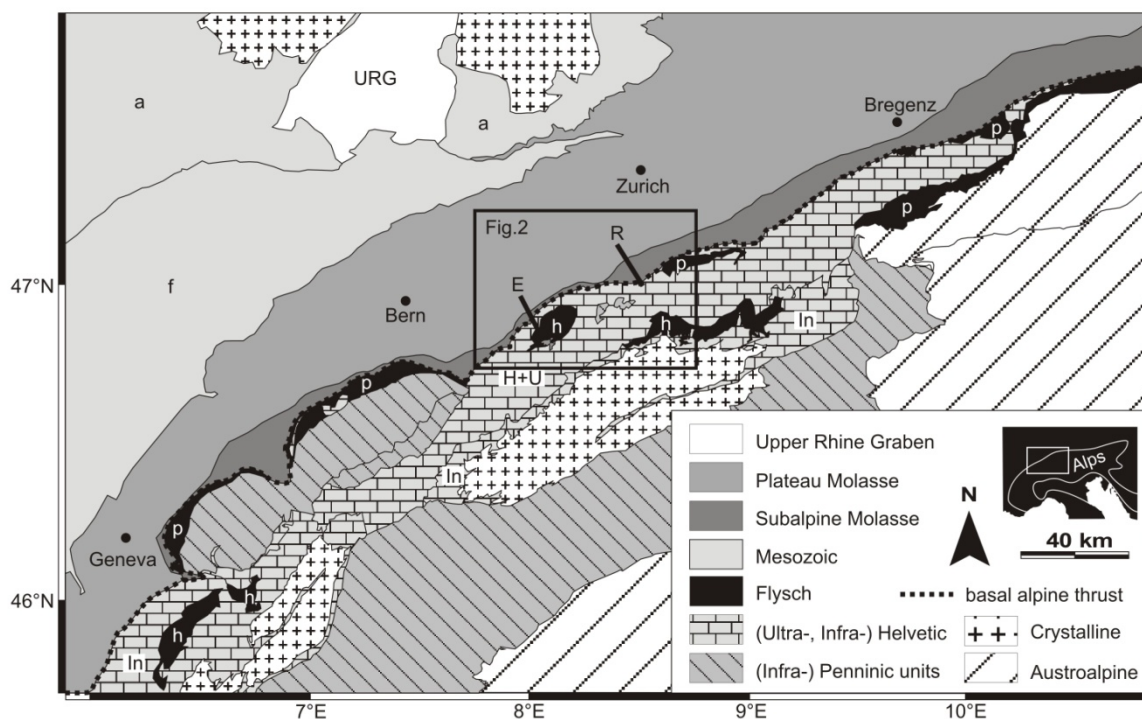
Figure 2-1: Tectonic map of the Northern Central Alps and the adjacent foreland based on Spicher (1980). URG - Upper Rhine Graben, a – autochthonous Jura, f – folded Jura, p – Penninic Flysch, h – Helvetic Flysch, H – Helvetics, U – Ultrahelvetics, In – Infrahelvetics, E – trace of Entlebuch profile and R – trace of Rigi profile indicated by black line.

Tertiary basin evolution

Sedimentation in the Molasse Basin started in Palaeocene-Eocene time with deposition of flysch and continued until Late Eocene to Early Oligocene times (Matter et al., 1980; Homewood et al., 1986; Ruffini et al., 1997; Sinclair, 1997a; b; Kempf and Pfiffner, 2004). This was followed by at least two major regressive cycles from marine- to fresh-water deposits (Matter et al., 1980). Deposition of Molasse sediments prograded northwards between the Early Oligocene and the Late Miocene. Accumulation of Molasse deposits probably continued until the Pliocene, when the Molasse Basin was uplifted and eroded (Cederbom et al., 2011).

The Swiss Molasse stratigraphic sequence is subdivided into four litho-stratigraphic units (Figure 2-1): the Lower Marine Molasse (UMM) and the Lower Freshwater Molasse (USM), which together form the first regressive cycle. It is followed by the Upper Marine Molasse (OMM), and the Upper Freshwater Molasse (OSM), which is of late Miocene age and comprises the second regressive cycle. By convention, the German abbreviations are used for these different litho-stratigraphic units (Matter et al., 1980). For a more detailed description of the stratigraphy of the Swiss Molasse Basin, the reader is directed to Matter et al. (1980) and Schlunegger (1999).

A sub-Quaternary unconformity truncates the Molasse deposits because of extensive erosion during the Pliocene, as revealed by vitrinite reflectance and previously published apatite FT studies in the Swiss part of the basin (Schegg, 1992; Mazurek et al., 2006; Cederbom et al., 2011). Hence, the complete stratigraphic record of the foreland basin covers the time range from c. 35 (including the Helvetic Flysch units into the foreland sequence), to 11.5 Ma (Rahn and Selbekk, 2007). The timing of the end of deposition, the timing of onset of erosion and the amount of removed section remain speculative (Schlunegger and Mosar, 2011). Remnants of younger deposits at the distal edge of the basin are preserved only in synclines of the Jura (Kälin, 1997).

The morphology of the basin was overprinted by glacial erosion, which peaked around 0.8 Ma (Haeuselmann et al., 2007). Today, rivers draining the Alps cover wide parts of the basin with Quaternary sediments.

2.3   The Subalpine Molasse

The Subalpine Molasse comprises a group of inclined slices of sediments north of the basal Alpine thrust. These were accreted into the Alpine wedge in early Miocene times (Schlunegger et al., 1997a; Kempf et al., 1999). During the Miocene, a triangle zone developed in parts of the basin, separating the overthrusted Subalpine Molasse from the weakly deformed to flat-lying Plateau Molasse (Vollmayr and Wendt, 1987). The structure of the triangle zone is constrained by borehole and seismic data (Müller et al., 1988; Berge and Veal, 2005).

Because the southern limits of the basin are hidden beneath tectonically higher units, it is difficult to restore the original basin width. Unfolding the Subalpine Molasse yields shortening of at least 10 km, but total shortening could be as large as 50 km (Burkhard and Sommaruga, 1998a). For the eastern Swiss Molasse basin, Kempf et al. (1999) estimated 28 km of shortening.

We present two detailed cross-sections located close to the sampling transects across the Rigi and Entlebuch areas. The Rigi cross-section has only minor modifications with respect to the balanced profile published by Burkhard (1990). The Entlebuch cross section, which is located approximately 30 km farther west, is a new construction and based on previous work by Trümpy (1980), Burkhard (1990), Pfiffner (2010), as well as on our own mapping and includes the projected Entlebuch-1 drilling mud log (Vollmayr and Wendt, 1987). The well is situated approximately 10 km east of the sampling profile. Both cross-sections cover all relevant tectonic structures in the study area.

General overview of the discussed cross sections

The thrust pattern of both profiles can be simplified to four structural domains (Figure 2-2), which are separated by thrusts observed in both profiles. Additionally, domains of local faulting and closely spaced thrusts exist in the Entlebuch. Tectonic Slice (TS)-1 represents all analyzed units south of the basal Alpine thrust. The northern limit of TS-2 is the basal UMM thrust, which also forms the southern limit of the triangle zone. TS-3 is the triangle zone itself and TS-4 represents the Plateau Molasse with 4a being the folded and tilted proximal part and 4b the tectonically undisturbed flat-lying part (Figure 2-2).

One important difference between the two profiles as seen in map view is the greater apparent thickness of the UMM in Entlebuch, which is almost entirely absent in the Rigi area, even though the sediment thickness of the UMM increases south- and eastward (Kuhlemann and Kempf, 2002). This indicates that the Molasse at the Entlebuch section was more deeply eroded and/or exhumed from deeper levels. We collected thermochronometric samples in similar structural positions along both profiles (Figure 2-2 & Figure 2-3).
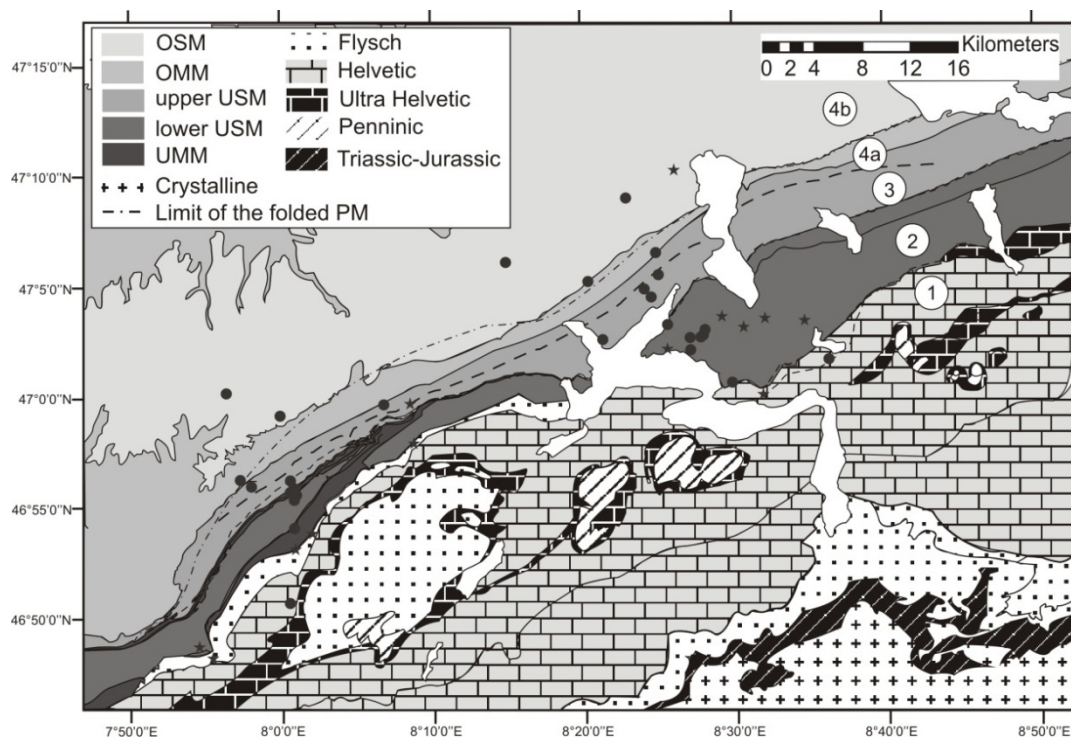

Figure 2-2: Detailed geological map of the study area with sample locations indicated. Black dots denote sampling localities for AFT and (U-Th-Sm)/He data analyzed by CvH, black stars denote sample points of AFT data analyzed by MR. Four tectonic slices (1-4) are indicated as discussed in the text. TS-4b represents the flat lying part of the Plateau Molasse.

2.4 Fission Track and (U-Th-Sm)/He Principles and Methods

The FT and (U-Th-Sm)/He dating methods are based on two different physical processes and cover different temperature intervals. The apatite FT technique records cooling in the range of c. 120-60°C (Carlson et al., 1999) whereas the (U-Th-Sm)/He method detects cooling events in the range of c. 80-40°C (Wolf et al., 1996; Flowers et al., 2009). Note that all presented ages are cooling ages, thus representing the point in time, when an apatite grain within the sample passed through its individual closure temperature. Rapidly cooled samples will feature similar fission track and (U-Th-Sm)/He ages. In areas experiencing slower cooling, the two thermochronometer ages will differ (e.g. Fitzgerald et al., 2006). Combined, the two techniques provide a powerful means to decipher low-temperature cooling histories (Armstrong et al., 2003; Stockli, 2005). For more detailed information about the methods and their application, the reader is referred to the supplementary information section.

We performed LA-ICP-MS AFT analyses on 31 samples. Where possible, we produced 40 single grain ages for every sample. Age and standard measurements are summarized in Table 2-1. From three sampling locations, we chose several boulders of potentially different origin that experienced a common post-depositional time-temperature history.

For the vertical sections and some locations in the basin, ages produced with the EDM-method were added to the data set, and compared to the LA-ICP-MS data set (see chapter 2.7.2). We took previously published data from Cederbom et al. (2004). Unpublished EDM ages were counted by M. Rahn and are listed in Table 2-2. A short description of the sampling strategy and the age-dating procedure is given in the supplementary information.

We present the so-called peak FT and the central ages, which represent either the age of a grain age population obtained by RadialPlotter (Vermeesch, 2009) or the whole-sample-age, respectively (Galbraith, 2005). For completely annealed samples, the peak age and the central age are identical; for samples with more than one grain age population, the central age provides information about trends within the data set and is statistically robust. Grain age populations are defined by minimising the Bayesian information criterion (BIC) (Vermeesch, 2009). Radial plots for all dated AFT samples are presented in the supplementary information.

In addition, we present 18 mean (U-Th-Sm)/He ages. For all samples three to six aliquots were analyzed (Table 2-3). Raw (U-Th-Sm)/He ages were corrected for alpha ejection at the crystal surfaces. In this study, we use the weighted mean age. Mean age and error calculation are discussed in the supplementary information.

2.5 Sampling Strategy

We collected samples along two horizontal profiles that span the entire folded and thrusted proximal part of the Molasse Basin, from the Flysch units in the south to the tectonically undisturbed, flat-lying Plateau Molasse in the north (Figure 2-3 & Figure 2-5). We sampled according to thrust spacing along river profiles and, as far as possible, at a similar elevation. In the Entlebuch horizontal profile, sampling started in the south in the "Globigerinenschiefer" (Südelbach-series, upper Eocene), followed the NS-striking, deeply incised Waldemme Valley and reached the Napf OSM alluvial fan conglomerates (11-7 Ma, Schlunegger (2010)) in the north. We collected samples at an approximate elevation of 800 m. In the Rigi horizontal section, the sampling strategy was similar to Entlebuch, ranging from the North Helvetic Flysch (Altdorfer Sandstone, lower Oligocene) in the south to the OSM fluvial deposits of Tortonian age in the north. We collected samples at an approximate elevation of 500 masl. A sub-vertical sampling profile was taken at the west face of the Rigi Mountain. Where possible, we selected granitic or sedimentary boulders in order to minimize effects of different time-temperature histories prior to deposition into the Molasse basin.

All samples from the Entlebuch vertical profile were separated from cuttings from the Entlebuch-1 borehole. Because of little available material, each sample represents 15-20 m of well section.

Generally, boulders and immature sandstones with crystalline rock fragments were preferentially sampled. We extracted and concentrated the apatite crystals by using a standard combination of heavy liquid- and magnetic separation techniques (see supplementary information).

Figure 2-3: Detailed maps of the Entlebuch and Rigi areas and their corresponding thermochronology data. Figure 2-3A: mean (U-Th-Sm)/He ages in the Entlebuch, Figure 2-3B: central AFT ages from the Entlebuch area, Figure 2-3C: mean (U-Th-Sm)/He ages from the Rigi Mountain, Figure 2-3D: central AFT ages from the Rigi area.
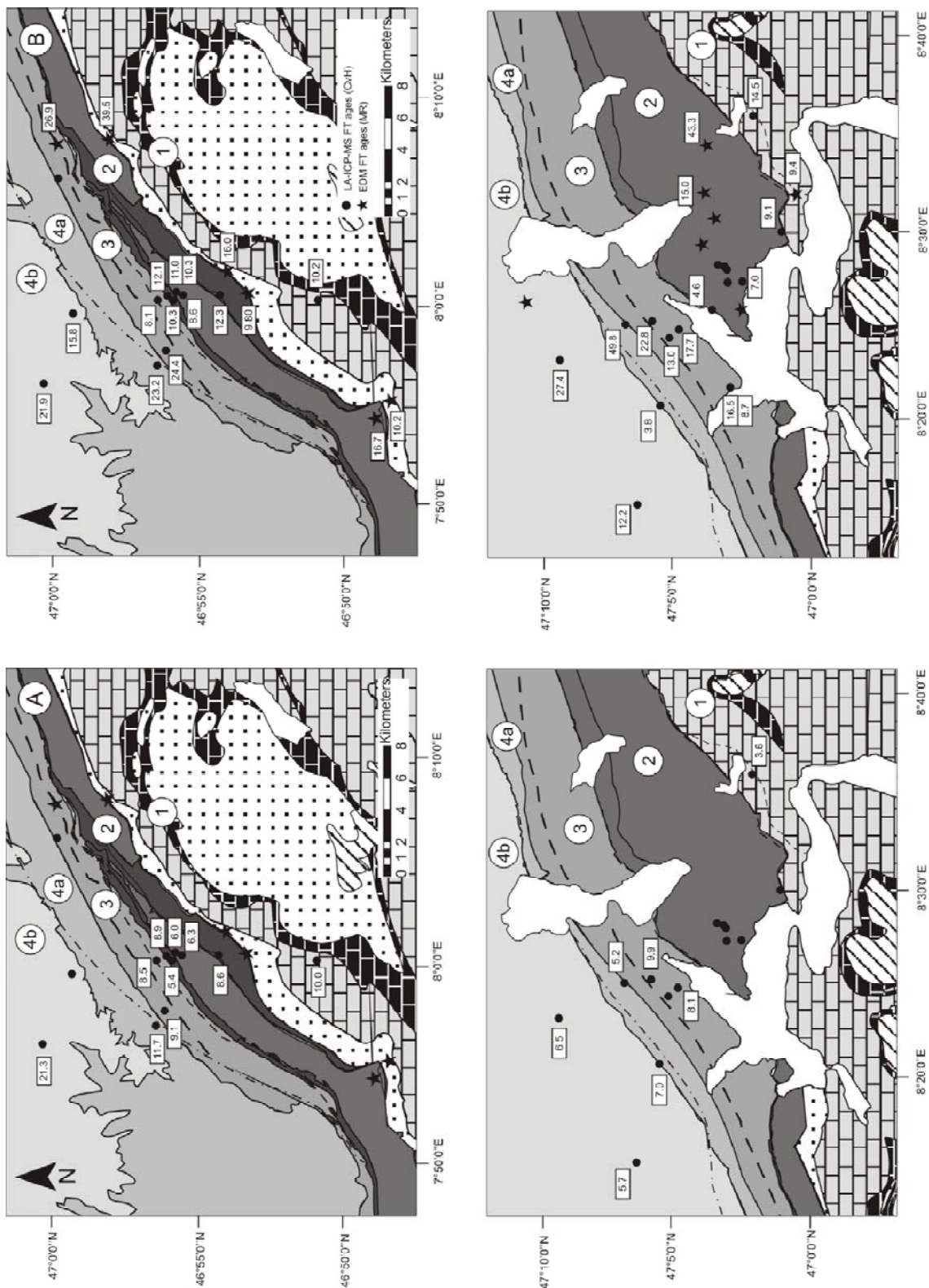
2.6 Thermal Modelling of the data

We constrained thermal histories from forward and inverse modelling of the AFT and (U-Th-Sm)/He data with the HeFTy v1.7.0 software (Ketcham, 2005). Where available, models are based on single-grain fission track (including up to four Dpar measurements per counted grain) and single grain (U-Th-Sm)/He data. For the (U-Th-Sm)/He ages, we added a 10% error to the analytical error to account for inaccurate α-ejection corrections. Inverse models were run until 100 statistically good paths (goodness of fit (GOF > 0.5) were achieved. If this was not possible, at least 10,000 independent t-T-paths were calculated.

We base our (U-Th-Sm)/He models on the Flowers et al. (2009) approach that yields in the calibration of the kinetic properties. Stopping distances for α-particles were calculated following Ketcham (2009) and we used the redistribution option for α-calculation, accounting for potentially zoned grains. Age α-correction was performed following Ketcham (2009). We applied the annealing model of Ketcham et al. (2007a) for assessing the model parameters for the fission track ages, and the Ketcham et al. (2007b) approach for the projection of the c-axis. We did not make any assumptions about the pre-depositional part of the cooling history. Likewise, no constraints were set for the cooling history in the basin. For burial histories, we used published sedimentation rates and thrust loading rates as maximum values, where available (Caron et al., 1989; Sinclair, 1997a).

We set the end of the t-T path to present day annual average temperatures, which was obtained from the Atlas of Switzerland (2004). We took temperature at the time of deposition from Mosbrugger et al. (2005). To allow for rapid exhumation in the hinterland until shortly before re-burial (i.e. accounting for minimal lag-times) the stratigraphic age and the hinterland history may overlap. For the basin history, we assumed temperatures not higher than 140 °C at any time after burial. This temperature is significantly higher than that required for resetting of the systems used in this study.

By using both inverse and forward modelling, we tested different cooling pulses derived from first order observations in the data set (i.e. 10 Ma), as discussed in literature (i.e. 5 Ma, (Cederbom et al., 2004; Cederbom et al., 2011)) and a glacial to post-glacial cooling (i.e. 2 Ma or later). We estimated the maximum and minimum amounts of cooling for each event.

Furthermore, we tested constant cooling over a period of a few million years (as opposed to transient / fast cooling) due to a potentially high and constant background erosion rate.

2.7 Results

Here, we present the LA-ICP-MS (Table 2-1), the EDM (Table 2-2), the U-Th-Sm/He data (Table 2-3) and the peak ages of the FT data (Table 2-4) in individual chapters. We then compare the two data sets and present cooling histories generated by inverse modelling of the two data sets combined.

2.7.1 AFT age distribution

Entlebuch horizontal section

Figure 2-3A is a detailed map of all sample locations and their corresponding central AFT age. Figure 4 presents the central age and the corresponding stratigraphic age along the horizontal section. For quality control, we produced AFT ages for two separate samples from the same location. Samples E30 and E35 were collected close to the northern fringe of TS-2, south of a minor thrust (Figure 2-3B), within an area where at least partially annealed samples are expected based on previous studies (Cederbom et al., 2004; Cederbom et al., 2011). The central ages obtained are 10.3 ± 2.2 Ma and 11.0 ± 3.5 Ma respectively, reproducing well within error. One single grain age population is sufficient for minimising the BIC for both samples.

However, not all single grain ages plot within the 2-sigma-error bars, indicating the potential presence of more than one population. Decomposing the grain ages into two populations results in peak ages of 12.1 Ma and 6.0 Ma (E30), and 15.5 Ma and 6.6 Ma (E35), respectively. In sample E30, Dpar values range from 1.11 to 1.68 μm. There is no direct correlation between single grain age and Dpar value. Modelling the data with HeFTy confirms the potential presence of the two peak ages. Based on Dpar measurements, the single grain ages can be divided into two monokinetic populations that both pass the χ²-test and reproduce the peaks: Single grain ages, which statistically belong to the older peak, have Dpar values higher than 1.52 μm, whereas all others have 1.49 μm or lower. Likewise, the

peaks in sample E35 can be corroborated by Dpar values; the younger peak is accordingly assigned to Dpar values of 1.27 µm or lower, the older peak to values of 1.33 µm or higher. The similarity in peak ages for samples E30 and E35 indicate that both samples have been strongly partially annealed since deposition and experienced similar cooling histories.

AFT ages within domains TS-1 to TS-3 (samples E05-E35) range between 8.1 to 12.3 Ma. These southern samples are all much younger than the corresponding stratigraphic age, and accordingly must have experienced at least temperatures within the PAZ after deposition. In the northern part of the section, AFT ages are older than the corresponding stratigraphic age. The potential low temperature boundaries of the exhumed fossil PAZ are located at the northern termination of the triangle zone (Figure 2-4).

The analyses of the grain age distributions by radial plots (E05-E50) yields young grain age populations for some of specimens. In E05, the youngest peak age is similar to the central age (10.2 Ma and 10.1 Ma, respectively), indicating strong partial or total annealing. In E10, two grain age populations are identified, yielding ages of 20.9 and 5.1 Ma respectively. The two age populations correlate with Dpar, the grains of the older peak having Dpar ≥ 2.2 µm, and the younger grains being associated with Dpar ≤ 1.5 µm.

Sample E20 (TS-2) has only one grain age population and a central age of 8.6 ± 1.8 Ma, indicating total annealing. E40, as the northernmost sample of TS-2, suggests two grain age populations of 12.7 Ma and 2.9 Ma respectively. The youngest peak age, however, is based on one single grain age and this age is much younger than the corresponding (U-Th-Sm)/He-age. Removing this grain from the data set results in a central age of 12.1 ± 3.8 Ma. All samples in TS-1 and TS-2 have been strongly or totally annealed since deposition, and two samples have a youngest population that is of Pliocene age.

For sample E45 (TS-3), collected just north of the basal UMM thrust, three distinct grain age populations are observed, one of which is older than its stratigraphic age. Single grain ages do not correlate with Dpar values (1.0 to 1.6 µm). Sample E40, immediately south of the UMM basal thrust, features two age populations that are significantly younger than its stratigraphic age. Hence, the single grain age distribution suggests that sample E45 has not

been totally annealed and has not experienced temperatures as high as sample E40 south of the basal thrust of the Subalpine Molasse.

At the northern fringe of TS-3, sample E50 yields a central age of 8.1 ± 3.0 Ma, which is slightly younger than ages farther to the south. Two grain age populations are 14.2 Ma and 3.5 Ma, respectively. A weak correlation between Dpar and single grain ages in E45 and no such correlation in E50 suggest that sample E50 is closer to being totally annealed and has hence probably experienced higher temperatures than E45.

In TS-4, AFT ages (samples E55-E70b; Figure 2-4) are significantly older than in the other tectonic units. They are as old as or only slightly younger than their corresponding stratigraphic age, indicating partial annealing. All samples except E70, which is a granitic boulder, are associated with two distinct grain age populations. Within the fossil partial annealing zone, small changes in elevation may have a large impact on AFT ages. This potentially explains why no uniform trend of younger central AFT ages is observed northwards in TS4, although the stratigraphic ages become younger.

Table 2-1: Results of apatite fission track dating from the Subalpine Molasse, Switzerland, using the LA-ICP-MS method for ^{238}U analysis. Dpar is the arithmetic mean maximum diameter of fission-track etch figures, Ns is the number of spontaneous tracks counted, P = ^{238}U/^{43}Ca and Ω = area for a single apatite grain, ζMS is the zeta value for LA-ICP-MS dating, and Q is the χ^2 probability. Central ages were calculated using the RadialPlotter software by Vermeesch (2009).

Sample	Grains	Dpar	Ns	Area Analyzed	Σ (P*Ω)	1σ Σ (P*Ω)	ζMS	1σ ζMS	^{43}Ca	^{238}U	Q	Central age	1σ	age dispersion
		(mm)		(cm^2)	(cm^2)	(cm^2)			bkg:sig	bkg:sig		(Ma)	(Ma)	(%)
E05	15	1.24	56	2.09E-04	0.65755	1.06E-02	192608	5.78E-01	216.78	23.57	0.00	10.2	2.75	34.6
E10	34	1.40	123	6.67E-04	1.4791	3.70E-02	192140	8.08E-01	239.49	76.55	0.00	12.3	2.25	24.6
E20	32	1.26	93	9.18E-04	1.2717	1.51E-02	189357	7.61E-01	215.57	18.31	0.55	8.6	0.90	0.0
E30	32	1.40	163	1.30E-03	1.6831	2.30E-02	188361	1.64E+04	234.27	33.49	0.04	10.3	1.11	12.6
E35	19	1.24	71	3.80E-04	0.80586	1.52E-02	193111	8.24E-01	217.56	41.03	0.06	11.0	1.76	14.2
E40	19	1.23	551	3.85E-04	1.178	3.59E-02	193825	8.36E-01	271.53	94.31	0.00	10.3	1.91	14.4
E45	27	1.32	210	8.90E-04	1.8422	2.54E-02	186681	1.08E+04	214.94	21.76	0.00	12.1	1.76	23.0
E50	24	1.18	88	6.69E-04	1.2643	1.35E-02	195509	8.64E-01	219.41	17.10	0.00	8.1	1.49	30.1
E55	27	1.26	249	6.03E-04	1.1395	2.01E-02	196480	8.81E-01	207.99	86.96	0.00	24.4	3.23	13.9
E60	23	1.25	123	4.47E-04	0.63711	8.28E-03	194631	8.50E-01	230.19	520.92	0.00	23.2	3.92	17.7
E65	55	1.30	265	1.87E-03	2.01	3.60E-02	192693	9.42E-01	261.68	426.53	0.00	15.8	1.64	16.1
E70b	40	1.42	522	6.00E-04	2.3632	1.95E-02	188950	1.84E+04	252.05	26.54	0.00	21.9	1.24	6.3
RH05	37	1.28	113	7.24E-04	1.1488	1.51E-02	185959	8.33E-01	239.23	143.75	0.00	14.5	3.50	31.4
RH10	39	1.18	25	1.11E-03	0.55854	5.95E-03	190315	5.88E-01	283.77	46.48	0.84	9.1	1.75	0.0
RH15	16	1.32	10	2.37E-04	0.37926	9.91E-03	190907	5.85E-01	255.18	205.76	0.19	7.0	2.52	25.2
RH25	6	1.14	3	1.01E-04	0.19965	7.50E-03	191408	7.96E-01	203.92	6.65	0.12	4.6	3.93	70.1
RH30a	26	1.29	198	4.30E-04	1.5115	3.19E-02	189618	5.91E-01	244.96	75.60	0.00	16.5	1.35	5.7
RH30b	25	1.17	148	4.63E-04	2.187	3.30E-02	188615	5.95E-01	220.58	53.81	0.00	8.7	1.02	16.0
RH35	11	1.40	33	1.89E-04	0.23082	4.41E-03	211879	5.85E-01	275.75	181.76	0.00	17.7	5.15	17.6
RH40	13	1.28	8	2.78E-04	0.11016	3.08E-03	211879	5.85E-01	266.01	465.53	0.03	13.0	5.35	10.4
RH45	40	1.25	331	1.28E-03	1.8253	2.20E-02	189796	2.12E+04	235.95	108.21	0.00	22.8	2.93	19.4
RH50	27	1.38	150	5.54E-04	0.39386	6.88E-03	187571	1.37E+04	221.40	40.81	0.00	49.8	9.62	20.3

RH60c	6	1.16	4	1.28E-04	0.12542	3.21E-03	190053	7.73E-01	223.49	11.00	1.00	3.8	1.83	0.0
RH65	16	1.29	118	5.43E-04	0.56082	2.11E-02	188633	1.73E+04	246.11	189.92	0.11	27.4	4.83	9.1
RH70	34	1.39	214	1.26E-03	1.8217	2.03E-02	189373	1.98E+04	213.98	48.65	0.00	12.2	1.43	16.9
RV15	12	1.10	31	1.73E-04	0.092727	2.08E-03	190401	7.79E-01	198.89	21.77	0.00	27.9	12.80	22.4
RV20	21	1.18	120	4.32E-04	0.34426	7.90E-03	189111	5.93E-01	318.74	39.08	0.00	17.6	7.30	32.2
RV25	18	1.24	7	2.65E-04	0.086605	1.40E-03	190968	7.88E-01	223.56	166.00	0.96	17.1	6.15	0.0
RV30a	30	1.23	151	7.63E-04	0.88886	1.68E-02	191393	5.83E-01	284.55	176.40	0.00	15.6	4.46	36.1
RV30b	27	1.50	191	5.95E-04	0.83113	1.16E-02	192006	5.81E-01	265.85	40.12	0.00	17.5	4.82	39.8
RV30c	27	1.39	159	3.47E-04	0.68695	8.31E-03	185364	6.34E-01	221.89	24.29	0.00	23.0	3.61	19.7

Table 2-2: Results of apatite fission track dating from the Subalpine Molasse, Switzerland, using the external detector method (EDM) for U analysis. Ns and Ni are the numbers of spontaneous and induced tracks counted, respectively, rhoD is the density of tracks on the dosimeter glass mica (corresponding to 12 ppm U), and P (χ^2) is the value indicating whether the data show extra Poissonian variations (i.e. if they are over-dispersed due to experimental or geological factors (Tagami and O'Sullivan, 2005). For age calculation, a ζ (CN5) of 343 ± 5 (MR) was used.

Sample	location	Grains (dmnls)	Ns (tracks)	Ni (tracks)	rhoD (10E6t/cm³)	P (χ^2)	Central age (Ma)	age dispersion (%)
MR P179	Flühli	23	53	982	1.061E+06	0.46	9.80±1.4	0
MR P198	Fischenbach	40	769	5014	1.025E+06	0.28	26.9±1.2	0

Table 2-3: Apatite (U-Th-Sm)/He dating results from the Subalpine Molasse, Switzerland. [eU] is the effective uranium concentration, which weights the decay of the parents for their alpha productivity (Flowers et al., 2009); [Ft] is the α-ejection correction factor, [series] denotes the lab in which the grains were analyzed, [excluded ages] have not been taken into account for the geological interpretation for reasons given in the text and in supplementary information.

sample	elevation (masl)	mass (µg)	U ppm	Th ppm	eU	Sm ppm	4He (nmol/g)	Ft	raw age	corrected age	Error (Ma)	series	excluded age	Mean age	error
E05-1	1140	12.68	98.69	70.29	115.22	70.21	7.11	0.78	11.38	14.62	0.88	(B)			
E05-2		2.28	16.11	15.91	20.56	157.94	3.05	0.68	26.66	39.25	2.35		e		
E05-3		4.28	61.85	9.87	64.94	162.59	2.19	0.73	6.19	8.46	0.51			10.01	7.22
E05-4		1.86	381.77	207.99	726.12	59293.54	102.15	0.67	20.59	30.94	16.72		e		
E05-5		2.83	74.44	637.79	222.24	196.99	8.67	0.68	7.07	10.33	0.08		e		
E10-1	845	1.48	49.26	373.62	137.79	504.58	2.50	0.69	3.35	5.01	0.11	(A)			
E10-2		5.09	56.60	460.41	164.81	445.13	4.96	0.77	5.53	7.37	0.11				
E10-3		4.97	23.01	1377.17	342.74	541.33	3.75	0.78	1.99	2.63	0.04		e		
E10-4		9.60	20.10	3.69	21.45	101.29	0.78	0.80	6.85	8.55	0.17			6.65	1.91
E30-1	800	4.15	19.66	150.49	54.71	82.06	1.32	0.70	4.37	6.25	0.37	(A)			
E30-2		2.12	10.89	61.87	25.29	32.41	0.56	0.65	4.03	6.18	0.37				
E30-3		5.72	16.82	102.46	41.03	125.78	1.09	0.74	4.81	6.47	0.39			6.30	0.39
E35-1	785	8.66	20.03	36.43	29.07	130.99	0.75	0.82	4.82	5.95	0.11	(B)		5.95	0.11
E40-1	772	10.96	51.90	36.22	61.15	183.64	3.04	0.81	9.29	11.53	0.20	(A)			
E40-2		1.89	173.74	41.26	185.05	361.24	4.29	0.70	4.32	6.19	0.12				
E40-3		5.87	11.15	29.40	19.36	287.47	0.42	0.79	4.23	5.42	0.11				
E40-4		31.42	7.98	20.23	13.06	84.71	0.27	0.88	3.88	4.45	0.07				
E40-5		12.45	21.96	18.16	27.44	260.52	0.63	0.82	4.36	5.32	0.09			5.37	2.35
E45-1	758	2.28	28.19	58.25	42.56	192.12	1.24	0.65	5.29	8.10	0.49	(B)			
E45-2		2.76	40.14	41.27	49.84	39.04	1.66	0.69	6.11	8.86	0.53				
E45-3		2.08	57.13	27.14	64.10	143.08	2.42	0.67	6.94	10.33	0.62			8.92	0.78
E50-1	745	6.06	0.09	0.05	0.10	0.02	0.00	0.79	0.00	0.00	na	(A)	e		
E50-2		6.66	25.90	34.09	35.95	440.44	1.10	0.80	5.91	7.42	0.12				
E50-3		7.17	10.69	8.35	13.66	209.58	0.51	0.80	7.27	9.18	0.22				

E50-4		8.09	41.25	7.24	44.10	236.07	2.06	0.79	8.82	11.19	0.21			8.53	2.29
E55-1	800	5.93	20.15	28.21	27.75	222.15	0.88	0.79	6.02	7.68	0.15	(A)			
E55-2		8.74	2.68	55.33	15.64	45.10	2.78	0.82	32.52	40.68	0.66		e		
E55-3		5.99	21.42	22.54	28.09	295.56	1.37	0.79	9.38	11.90	0.21			9.05	3.92
E60-1	970	5.27	34.41	7.27	36.47	77.13	1.71	0.78	8.76	11.30	0.22	(A)			
E60-2		6.91	22.55	38.57	32.51	216.68	2.88	0.79	16.73	21.28	0.33				
E60-3		5.16	7.47	16.77	12.10	155.27	0.33	0.78	5.20	6.72	0.15				
E60-4		2.95	21.83	25.65	28.42	136.98	1.88	0.73	12.39	17.16	0.32				
E60-5		7.02	12.11	19.66	17.00	73.23	1.32	0.80	14.54	18.35	0.29			11.68	28.80
E65-1	773	5.72	0.22	7.77	2.03	2.59	2.93	0.77	259.86	348.96	7.15	(A)	e		
E65-2		3.30	68.93	16.55	76.17	686.03	0.00	0.77	0.00	0.00	na		e		
E65-3		5.57	33.49	11.85	37.35	227.01	2.24	0.80	11.34	14.20	0.25				
E65-4		1.50	12.43	14.11	16.40	144.23	0.89	0.63	9.76	15.49	0.93				
E65-5		4.62	0.16	1.16	0.44	1.67	0.01	0.72	2.08	2.87	0.17		e		
E65-6		3.63	29.17	12.68	32.72	126.66	2.27	0.72	12.68	17.61	1.06				
E65-7		3.12	25.76	17.93	30.71	165.48	2.16	0.71	12.76	17.90	1.07				
E65-8		3.19	26.89	18.03	31.30	51.53	2.34	0.71	13.74	19.43	1.17			14.80	1.92
E70b-1	1325	1.10	87.24	73.73	104.76	109.39	10.55	0.60	18.51	30.86	1.85	(B)	e		
E70b-2		1.18	87.43	76.97	106.04	177.88	7.81	0.61	13.52	22.05	1.32				
E70b-3		0.98	49.18	90.88	70.87	153.64	4.67	0.56	12.03	21.46	1.29				
E70b-4		3.71	81.57	72.51	99.07	160.19	8.33	0.73	15.44	21.26	0.30			21.31	1.32
E3-1-1	420-435	3.32	31.00	6.04	32.84	89.44	0.86	0.71	4.82	6.75	0.40	(B)			
E3-1-2		1.80	31.32	50.98	43.53	94.64	1.22	0.65	5.13	7.86	0.47				
E3-1-3		1.06	14.81	39.57	25.02	218.89	0.70	0.57	4.97	8.71	0.52			7.61	0.65
E3-2-1	1210-1230	1.10	52.29	9.92	55.04	93.46	0.58	0.62	1.95	3.17	0.19	(B)			
E3-2-2		1.93	61.61	55.75	74.95	101.71	2.08	0.66	5.11	7.69	0.46				
E3-2-3		2.00	5.08	21.46	10.40	76.07	0.34	0.65	5.84	8.96	0.54			4.32	4.59
E3-2.5-1	1415-1435	1.01	41.35	94.42	63.77	136.04	1.33	0.56	3.80	6.78	0.41	(B)			
E3-2.5-2		1.01	99.36	84.06	119.43	144.33	1.35	0.59	2.08	3.53	0.21				

Sample	Depth											(B)	e		
E3-2.5-3		0.97	33.40	47.95	44.87	86.51	0.37	0.57	1.49	2.61	0.16			3.27	1.36
E3-3-1	1615-1635	2.56	24.0	26.1	30.2	49.1	1.09	0.7	4.03	6.0	0.48	(B)			
E3-3-2		5.78	48.8	36.6	57.4	42.4	0.75	0.8	2.65	3.3	0.27				
E3-3-3		4.10	17.6	7.9	19.6	44.4	0.45	0.3	0.93	3.5	0.28			3.76	0.80
E3-4-1	1820-1840	0.97	54.6	121.7	82.8	33.3	2.23	1.3	6.23	5.0	0.40	(B)			
E3-4-2		1.94	1.2	2.0	1.7	0.5	1.70	270	######	##########	########		e		
E3-4-3		2.24	41.7	66.0	57.3	80.3	1.58	0.1	0.05	0.5	0.04		e	4.97	0.40
E3-5-1	2110-2130	1.96	24.05	42.05	33.97	47.61	0.35	0.66	1.88	2.85	0.17	(B)			
E3-5-2		1.54	59.66	79.60	78.80	164.65	0.62	0.63	1.43	2.27	0.14				
E3-5-3		4.11	21.70	9.13	24.00	39.92	0.73	0.73	5.63	7.77	0.47		e	2.49	0.08
RH05-1	620	3.52	8.91	223.65	60.66	52.65	0.71	0.69	2.11	3.05	0.18	(B)			
RH05-2		1.73	30.12	67.68	46.48	156.83	0.57	0.62	2.25	3.63	0.22				
RH05-3		1.11	29.94	345.87	110.12	111.50	1.66	0.58	2.73	4.73	0.28			3.57	0.40
RH12-1	735	9.81	36.3	160.8	73.6	58.5	1.3	0.79	3.29	4.2	0.33	(B)			
RH12-2		9.14	41.2	167.5	80.1	65.3	1.5	0.78	3.45	4.4	0.35				
RH12-3		5.29	0.7	0.8	0.9	0.2	4.3	0.75	827.10	1103.3	88.26		e	4.29	0.35
RH17-1	461	2.10	122.1	43.5	132.5	71.4	4.2	0.68	5.92	8.7	0.70	(B)			
RH17-2		1.30	11.2	376.9	98.3	50.4	1.0	0.60	1.81	3.0	0.24				
RH17-3		1.68	19.7	108.2	45.0	67.4	0.6	0.63	2.24	3.5	0.28			3.59	1.89
RH23-1	383	2.10	7.5	39.7	16.8	20.6	1.0	0.65	10.94	16.8	1.34	(B)	e		
RH23-2		3.08	4.2	11.2	7.0	39.9	0.1	0.70	3.80	5.4	0.43				
RH23-3		4.91	8.5	16.2	12.4	27.3	0.3	0.73	4.64	6.3	0.51			5.80	0.51
RH35-1	562	3.47	14.71	38.50	23.85	57.23	0.95	0.71	7.24	10.25	0.61	(B)			
RH35-2		2.28	31.18	44.64	41.61	31.15	1.12	0.67	4.93	7.37	0.44				
RH35-3		3.30	19.96	44.02	30.37	55.28	0.90	0.71	5.41	7.64	0.46			8.08	1.27
RH45-1	535	3.71	43.95	81.04	63.27	133.00	2.19	0.71	6.32	8.94	0.54	(B)			
RH45-2		6.19	136.19	11.87	139.43	102.01	17.24	0.78	22.85	29.47	1.77		e		
RH45-3		5.91	62.03	10.42	64.91	95.36	2.48	0.77	7.05	9.15	0.55				
RH45-4		3.34	105.16	16.10	109.37	98.95	17.45	0.73	29.45	40.39	2.42		e		

RH45-5		6.61	59.57	24.41	65.72	105.39	3.73	0.77	10.46	13.50	0.81			9.86	2.98
RH50-1	740	2.09	5.50	25.71	11.64	44.46	0.52	0.65	8.00	12.36	0.74	(B)			
RH50-2		2.06	88.48	289.36	155.47	74.83	3.62	0.66	4.25	6.45	0.39				
RH50-3		0.89	67.78	65.45	84.29	288.87	2.05	0.58	4.44	7.65	0.46			7.69	3.77
RH60c-1	465	1.05	17.09	144.31	52.09	356.10	2.48	0.57	8.47	14.86	0.89	(B)	e		
RH60c-2		2.70	9.56	92.75	32.31	280.91	0.95	0.67	5.20	7.71	0.46				
RH60c-3		1.99	9.41	126.06	40.37	388.06	0.96	0.65	4.17	6.46	0.39			6.97	6.97
RH65-1	450	2.37	2.69	9.85	5.64	136.49	0.10	0.66	3.12	4.72	0.28	(B)			
RH65-2		2.34	87.27	30.09	94.58	76.78	2.72	0.68	5.32	7.80	0.47				
RH65-3		1.65	5.47	13.56	9.16	113.34	0.87	0.63	16.70	26.35	1.58		e		
RH65-4		0.80	16.01	60.81	30.68	134.89	0.45	0.55	2.67	4.88	0.20				
RH65-5		3.95	16.97	40.85	26.71	67.03	0.88	0.72	6.00	8.32	0.18			6.49	6.49
RH70-1	523	2.73	25.61	32.05	33.10	20.81	0.88	0.69	4.87	7.03	0.42	(B)			
RH70-2		2.77	25.09	39.05	34.62	107.72	0.67	0.69	3.50	5.06	0.30				
RH70-3		2.79	22.36	35.83	30.87	51.68	0.67	0.69	3.96	5.72	0.34			5.73	0.57
RV10b-1	1520	5.05	150.21	111.69	204.92	5799.02	0.38	0.75	0.31	0.42	0.03	(B)	e		
RV10b-2		1.28	30.95	81.23	80.14	6098.94	0.17	0.61	0.31	0.51	0.03		e		
RV10b-3		5.07	0.85	1.53	1.24	7.74	0.18	0.74	25.57	34.35	2.06			34.35	1.00
RV15-1	1405	2.23	24.65	134.95	57.74	404.00	1.68	0.67	5.20	7.81	0.47	(B)			
RV15-2		1.26	14.40	59.38	30.06	398.67	0.80	0.61	4.69	7.74	0.46				
RV15-3		2.16	13.74	46.84	27.41	577.83	1.32	0.66	8.28	12.53	0.75			7.78	0.75
RV25-1	1335	2.97	2.63	102.66	26.45	37.75	0.51	0.68	3.49	5.09	0.31	(B)			
RV25-2		5.14	2.04	3.00	2.89	30.78	0.10	0.75	6.22	8.32	0.50			5.97	2.06
RV30c-1	1040	1.22	13.19	55.29	26.33	84.12	0.71	0.59	4.86	8.25	0.50	(B)			
RV30c-2		2.15	43.40	53.42	56.12	82.70	1.62	0.66	5.31	8.06	0.48				
RV30c-3		3.25	33.25	78.61	51.44	18.71	1.87	0.70	6.66	9.47	0.57			8.51	0.57
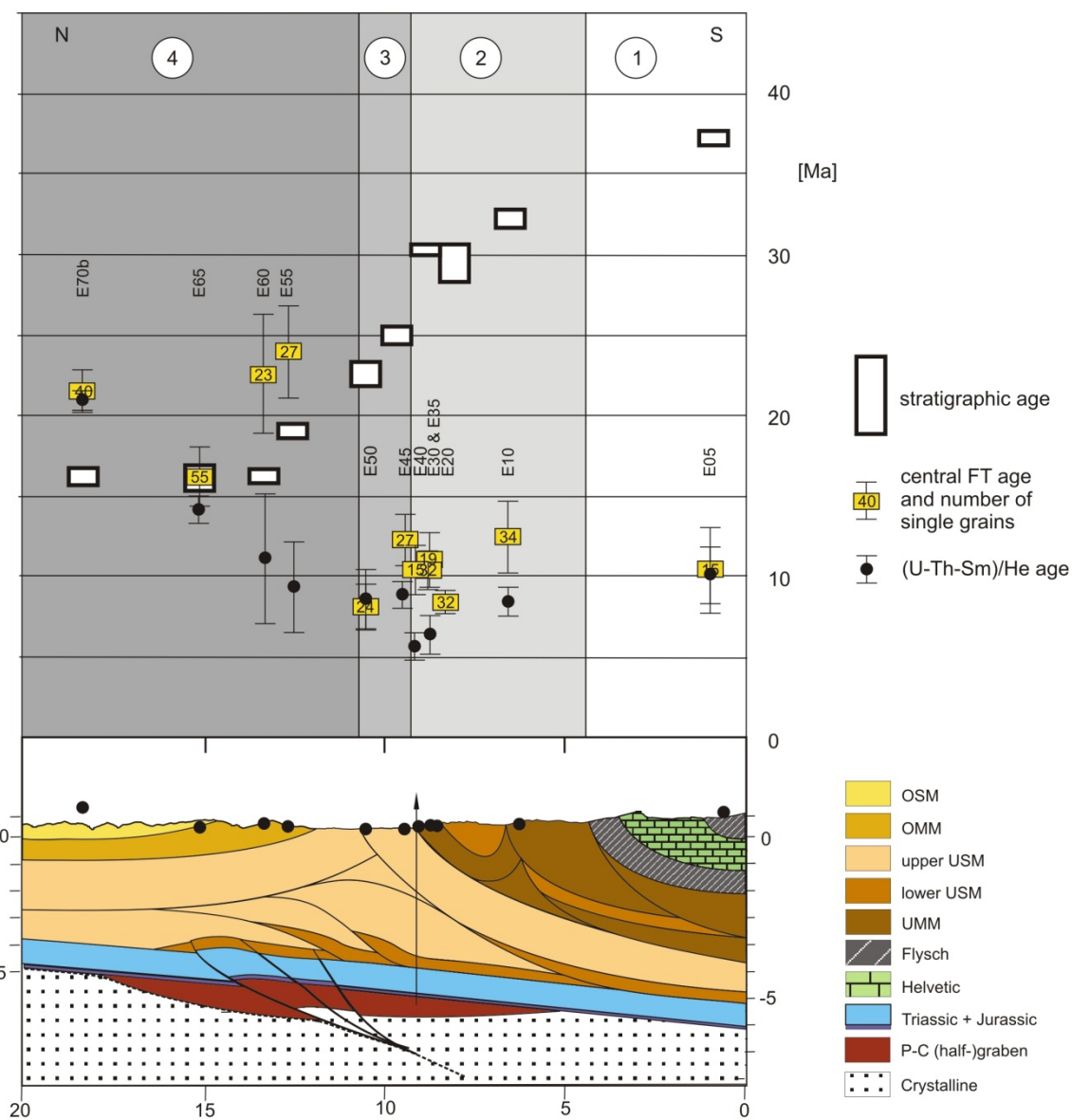
Figure 2-4: Profile across the Subalpine Molasse in the Entlebuch area, Switzerland. For location, see Figure 2-1. Black dots indicate the projected data points. The tectonic slices are taken from Figure 2-2. In the south, all thermochronology ages are significantly younger ages than the samples' stratigraphic ages, whereas in the north the opposite is true. Hence, an exposed palaeo-PAZ and PRZ lies in the tectonic slices south of TS-4.

Entlebuch vertical section

The well Entlebuch-1 is located at the boundary between UMM and USM, i.e. within the triangle zone (TS-3). EDM fission track data of this vertical section have been published and discussed in more detail in Cederbom et al. (2011). They show a younging trend of central

AFT ages below c. 1500 m depth. Furthermore, an offset in the PAZ within the youngest grain age population exists (Figure 2-6), which Cederbom and co-workers interpreted as an indication of thrust-reactivation during late cooling. This vertical section provides information about the shape and the location of the exhumed fossil PAZ.

Rigi horizontal section

Figure 2-3B shows a detailed map of sampling localities and corresponding central AFT ages. Again, central ages are presented together with corresponding stratigraphic age along the vertical transect (Figure 2-5). The central AFT ages in TS-1 and TS-2 are considerably younger than their corresponding stratigraphic age. Sample RH05 has a central age of 14.5 ± 7.0 Ma. Two grain age populations can be distinguished, and they do not relate to differences in Dpar. This indicates that the sample is partially, but not totally annealed. In the adjacent TS-2, the southernmost sample (RH10) has only one grain age population with a central age of 9.1 ± 3.5 Ma. In addition, grains with the highest Dpar values also have young single grain ages. Therefore, sample RH10 is regarded as totally annealed.

Continuing northwards to the basal Rigi thrust, samples RH15 and RH25 show successively younger central AFT ages. The single grain AFT ages in each sample belong to a single population indicating that both samples are totally annealed (Table 2-1).

Within the triangle zone (TS-3), ages are older than in TS-2, but still younger than their corresponding stratigraphic ages (RH30a to RH45; Figure 2-5). Samples RH30a to RH40 are totally or strongly partially annealed. All samples except RH35 contain only one grain age population. The northernmost sample RH45 has a central age of 22.8 ± 5.9 Ma, which is similar to its stratigraphic age. Moreover, it is associated with three grain age populations, two of which are older than the stratigraphic age. Hence, sample RH45 has probably experienced lower temperatures and less partial annealing than the samples farther south.
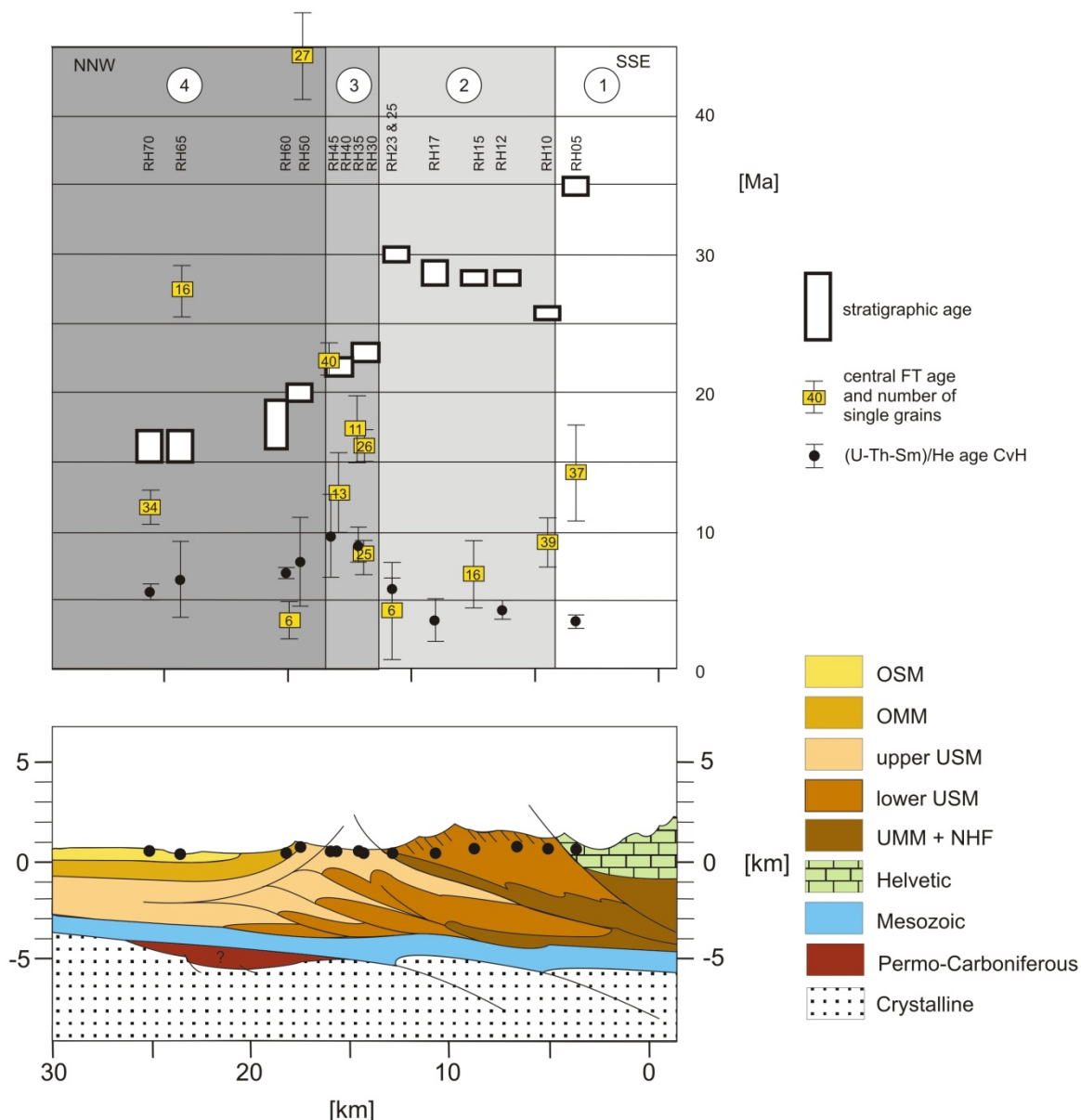
Figure 2-5: Profile across the Subalpine Molasse in the Rigi area, Switzerland. For location, see Figure 2-1. Colour coding is the same as in Figure 5. Note that in contrast to the Entlebuch profile, the (U-Th-Sm)/He and AFT ages experienced some reheating in the basin also north of the triangle zone.

In TS-4a, sample RH50 has a very old central age (45 Ma), with the youngest grain age population being older than the stratigraphic age. Evidently, the sample did not experience much heating after deposition. Sample RH60 is younger than its stratigraphic age but is based on six single grain ages only and therefore not reliable. Sample RH65 has a central age of 27.4 ± 5.0 Ma, which is much older than the stratigraphic age. Accordingly, the sample did not experience enough reheating in the basin to significantly reduce the AFT age. RH70 in contrast shows a central age of 12.2 ± 1.4 Ma, which is slightly younger than its

corresponding stratigraphic age. In addition, its grain age distribution decomposes into two peak ages, which are 6.1 and 16.1 Ma. They are younger than, and as old as the stratigraphic age respectively. This indicates post-depositional heating. Note that the corresponding sample in the Entlebuch section (E70) does not feature any indications of post depositional heating above 40°C. Additionally, the topmost sample in well Hünenberg-1, which is located 3km north of sample RH70, has not experienced any significant reheating since deposition (Cederbom et al., 2011).

Rigi vertical section

A sub-vertical profile from the western flank of Rigi Mountain (TS-2) is complemented by published EDM AFT ages from a sub-vertical section on the eastern Rigi flank and by subsurface ages from the Weggis well (EDM ages from Cederbom et al. (2004)).

From the new LA-ICP-MS data, RV10b will not be considered further. From 21 grains, only four have sufficient uranium for a meaningful age, and most of them have zero spontaneous tracks.

Sample RV15 yields a central age of 27.9 Ma at 1405 masl. At the base of the Rigi Mountain (630 masl), sample RH15 has a central age of 7.0 Ma. All new central AFT ages are plotted in Figure 2-6, together with the previously published central AFT data. Together they illustrate a trend of decreasing ages from top to bottom. The age pattern corresponds to an exhumed fossil PAZ (Cederbom et al., 2004).

Independent evidence for a fossil PAZ at Rigi is derived from the radial plots (supplementary information). At an elevation of 1040 masl, three samples (RV30a, RV30b and RV30c) were collected. Samples RV30a and -b originate from calcareous sandstone, whereas RV30c is a sandstone boulder. Their central ages reproduce within 1sigma error and samples RV30a and RV30b decompose into two similar grain age populations. The younger grain age populations (9.9 Ma and 9.3 Ma, respectively) are significantly younger than the corresponding stratigraphic age. A positive correlation exists between peak age and Dpar value in RV30b.
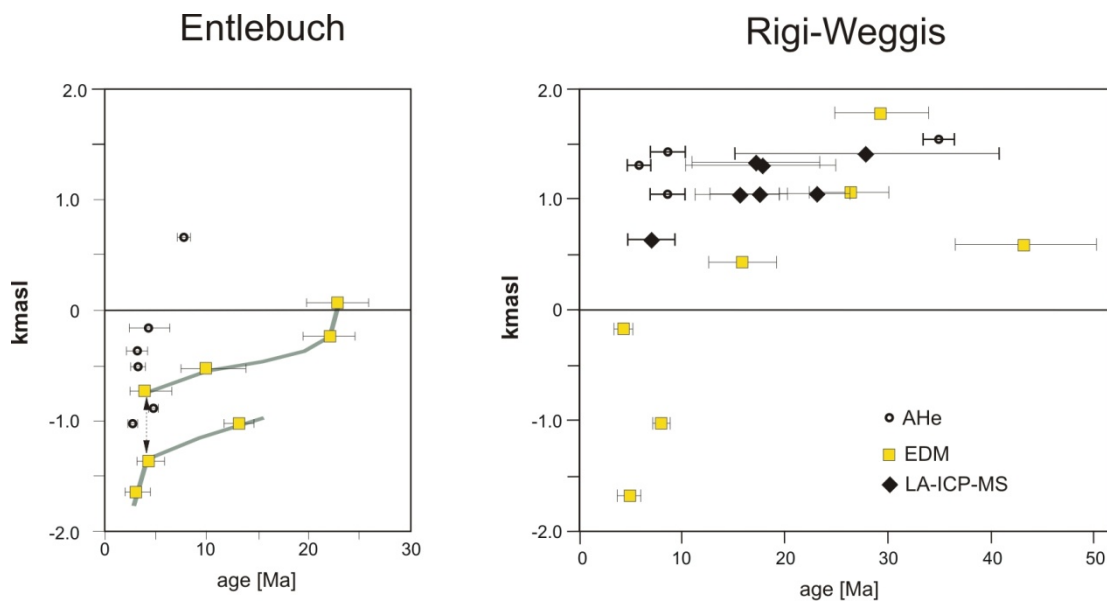
Figure 2-6: Vertical age profiles along the Entlebuch well (left) and the Rigi Mountain and Weggis well (right) with previously published and new data. Note the exhumed PAZ/PRZ within both profiles and the offset between them. For Details and comparisons between LA-ICP-MS and EDM data, see discussion in the text.

2.7.2 Comparison of EDM and LA-ICP-MS AFT results

At Entlebuch, a sample pair suitable for comparing the two dating methods lies in the southern part of the section (E10 and MRP 179), within the southernmost units of the Subalpine Molasse (Figure 2-3B, Table 2-1and Table 2-2). Both samples have undergone strong to total annealing. For sample MRP 179, track length measurements show complete resetting of the sample. The obtained AFT ages are 12.3 ± 2.3 Ma and 9.8 ± 1.4 Ma for LA-ICP-MS and EDM dating respectively, thus reproducing within error.

Sample pair E55 and MRP 198 was collected in the tilted part of the Plateau Molasse within the USM units (Figure 2-3B, Table 2-1 and Table 2-2). Sample E55 was collected 15 km west of sample MRP 198. The central AFT ages are 24.4 ± 3.3 Ma and 26.9 ± 1.2Ma, and again overlap within uncertainty.

Within the two sections on both flanks of the Rigi Mountain (Figure 2-3D & Figure 2-6), the fossil PAZ is evident. Even though the ages reproduce mostly within 1sigma error, a slight trend towards younger ages may be inferred for the LA-ICP-MS data set (for discussion, see supplementary information).

Sample	No. of grains	peak 1 (Ma)	grain portion %	peak 2 (Ma)	grain portion %	peak 3 (Ma)	grain portion %
E05	15	10.1	84.4	43.4	15.6		
E10	34	5.1	36.7	20.9	63.3		
E20	32	8.6	100				
E30	32	6.0	21.1	12.1	78.9		
E35	19	6.6	38.1	15.5	61.9		
E40	19	2.9	13.2	12.7	86.8		
E45	27	7.8	57.0	16.9	34.3	48.8	8.7
E50	24	3.5	40.7	14.2	59.3		
E55	27	17.6	50.9	38.1	49.1		
E60	23	8.2	25.4	32.4	74.6		
E65	55	11.0	68.3	30.8	31.7		
E70b	40	22.2	100				
RH05	37	9.6	72.2	51.1	27.8		
RH10	39	9.1	100				
RH15	16	6.9	100				
RH25	6	3.5	100				
RH30a	26	16.6	100				
RH30b	25	9.4	100				
RH35	11	8.6	43.6	29.5	56.4		
RH40	13	13.8	100				
RH45	40	14.4	52.1	30.0	39.4	121.0	8.5
RH50	27	30.0	72.4	176.0	27.6		
RH60c	6	3.8	100				
RH65	16	22.8	100				
RH70	34	6.1	29.9	16.1	70.1		
RV15	12	14.5	76.5	87.2	23.5		
RV20	21	7.5	74.8	71.0	25.2		
RV25	18	17.1	100		0.0		
RV30a	30	9.9	76.8	76.4	23.2		
RV30b	27	9.3	69.5	81.0	30.5		
RV30c	27	14.1	55.7	46.4	44.3		

2.7.3   (U-Th-Sm)/He age distribution

Entlebuch horizontal section

We performed (U-Th-Sm)/He analyses for all those samples (except E20) dated with the LA-ICP-MS AFT dating technique. Data are presented in Table 2-3 and plotted in Figure 2-3A & Figure 2-4. The general trend is similar to the AFT data: young ages are obtained in the southern part of the Subalpine Molasse, whereas ages become successively older northwards, including age trends within tectonic slices.

The southernmost sample, E05, has a mean (U-Th-Sm)/He age of 10.0 ± 2.0 Ma. Since the sample is significantly younger than its corresponding stratigraphic age, complete resetting of the (U-Th-Sm)/He system can be inferred, in line with strong partial or total annealing of the FT system. Following the profile northwards, ages become progressively younger in TS-1 and TS-2.

A clear jump in age is observed when crossing the basal UMM thrust into TS-3. Sample E45 and E50 have significantly younger stratigraphic ages (20-25Ma), but their mean (U-Th-Sm)/He ages are significantly older than farther south. Complete resetting of the (U-Th-Sm)/He system after deposition is probable in TS-3, since the single grain ages reproduce within uncertainty.

In TS-4, the (U-Th-Sm)/He ages for sample E55 to E65 are younger that their stratigraphic ages, but show a spread in single grain ages, which cannot be explained only by methodical factors (see supplementary information). Instead, partial resetting is likely. In TS-4, the (U-Th-Sm)/He ages become older towards the north. The northernmost sample (E70b) has a (U-Th-Sm)/He age older than its corresponding stratigraphic age (Figure 2-4). Hence, the grains have not been significantly reheated in the PRZ after deposition.

Entlebuch drill hole section

At a depth of 425 m below surface, an age of 7.6 ± 1.5 Ma is measured, which is significantly younger than its stratigraphic age. Towards greater depths, ages become younger. An offset

in this trend is observed between sample E3-3 and E3-4 (Figure 2-6). This offset coincides with the offset in central AFT ages (chapter 2.7.1).

Rigi horizontal section

(U-Th-Sm)/He analyses (Table 3, Figs. 3C and 5) were performed for most of the samples dated by LA-ICP-MS AFT technique. In TS-2, however, AFT and (U-Th-Sm)/He ages come from different samples. In general, all ages are young in comparison to the stratigraphic age and the oldest (U-Th-Sm)/He ages recorded in TS-3 (Figure 2-5).

Similar to Entlebuch, the ages display characteristic age patterns within the tectonic slices. In TS-1 and TS-2, the (U-Th-Sm)/He ages are identical within error. At the northern end of TS-2, an age of 5.8 ± 1.2 Ma is slightly older than the samples farther south (Figure 2-5). All ages are significantly younger than the corresponding stratigraphic ages, suggesting complete reset of the (U-Th-Sm)/He-system.

Older (U-Th-Sm)/He ages are observed in TS-3. Samples RH35 and RH45 have mean (U-Th-Sm)/He ages of 8.1 ± 1.6 Ma and 9.9 ± 2.0 Ma, respectively, thus reproduce within error. Their corresponding stratigraphic ages are significantly younger than those in TS-2.

In TS-4, the (U-Th-Sm)/He ages are generally younger than in TS-3, and they become successively younger towards north. Again, the age of the northernmost sample (RH70) is younger than the stratigraphic age of the sample, so the sample must have experienced post-depositional heating.

In summary, very young (U-Th-Sm)/He ages exist south of the triangle zone, while the oldest ages are found within the triangle zone. In the Plateau Molasse, the ages are generally young, but only slightly younger than their stratigraphic ages. Similar to the Entlebuch, an age offset occurs across the basal UMM thrust.

Rigi vertical section

With one exception (RV10b), (U-Th-Sm)/He ages were measured for all samples with LA-ICP-MS AFT data (Figure 2-6 and Table 2-3). The topmost sample (RV10b) from 1520 masl, has a (U-Th-Sm)/He age that is older than the stratigraphic age (however, with only one grain dated successfully). The relatively old age, if indeed representative, indicates that the sample was not fully reset and is located within or above the palaeo-PRZ. At 1405masl, the mean (U-Th-Sm)/He age is 8.5 ± 1.7 Ma. At 1335 masl, the sample yields an age of 6.0 ± 1.2 Ma. At 1040 masl the obtained age is 8.5 ± 1.7 Ma again. All these ages are significantly younger than the corresponding stratigraphic age, suggesting strong to complete resetting of the apatite (U-Th-Sm)/He system.

2.7.4 Comparison of apatite (U-Th-Sm)/He and AFT results

Both thermochronometers indicate significant cooling in Mio-Pliocene times. Combining the two data sets provides additional information about the cooling histories.

At Entlebuch (Figure 2-4), AFT ages in TS-1 and TS-2 are rather uniform. Corresponding (U-Th-Sm)/He ages in contrast become successively younger northwards, or towards the basal UMM thrust. For the southernmost sample E05, AFT and (U-Th-Sm)/He ages are very similar, indicating rapid cooling at c. 10 Ma. Farther north, the rapid cooling signal disappears. In samples E10 to E40, the (U-Th-Sm)/He ages become successively younger while the central AFT ages remain constant, resulting in a systematic divergence between He and AFT data in TS2.

Across the basal UMM thrust in Figure 2-4we observe a distinct increase in (U-Th-Sm)/He ages and a change from strongly to weakly annealed AFT ages. Within TS-3, the AFT ages and the number of grain age populations decrease northwards, while the (U-Th-Sm)/He ages remain constant. At the northern tip of the triangle zone (TS-3), both thermochronometers yield an age of c. 8 Ma.

North of the triangle zone (TS-4), the (U-Th-Sm)/He ages record significant post-depositional cooling, while the AFT ages are only partially annealed. A distinct increase in AFT ages is

observed between TS-3 and TS-4, whereas the mean (U-Th-Sm)/He ages are similar. Farther north, the mean (U-Th-Sm)/He ages increase again and become older than their corresponding stratigraphic age. Ages of the two thermochronometers overlap, indicating rapid uplift of the provenance region.

At Rigi, a different pattern emerges (Figure 2-5). For the southernmost sample (RH05), AFT and (U-Th-Sm)/He ages differ strongly. Hence, the rapid cooling at 10Ma found in the southernmost Entlebuch area is not discernible in the Rigi area. There the AFT ages are successively younger in TS-1 and TS-2 towards the north, but the corresponding (U-Th-Sm)/He ages are uniform or increase slightly. At the northern end of TS-2 along both sections, the ages of both thermochronometers overlap within error.

North of the basal UMM thrust, we find a clear offset in both AFT and (U-Th-Sm)/He ages, which is in line with the findings from the Entlebuch. In TS-3, most of the ages are still younger than or equal to the stratigraphic age, indicating that they cooled from elevated temperatures after deposition.

In TS-4 along the Rigi section, AFT ages scatter substantially while the (U-Th-Sm)/He ages decrease northwards. For sample RH60, the (U-Th-Sm)/He and AFT ages are inverted. This phenomenon is also known from other studies and usually attributed to annealing kinetics and radiation damage (Flowers et al., 2009). However, this holds only true for slowly cooled samples, which is not the case in our study. The AFT age is based on six single grain ages only and is therefore not considered reliable.

In TS-4, the AFT ages are older, while the (U-Th-Sm)/He ages are younger than the stratigraphic ages. A weak younging trend northwards coincides with a decreasing gap between stratigraphic and (U-Th-Sm)/He ages (Figure 2-5).

2.7.5 Modelled burial and exhumation histories

Figure 2-7 shows the modelling results. A summary of the modelling statistics can be found in the supplementary information. Modelling shows that all samples in TS-1 and TS-2 have

undergone total or near total resetting of the AFT system. Post-depositional heating still affected all samples in TS-3. In the Entlebuch, the samples must have reached temperatures of at least 110 °C. In the Rigi area, heating to c. 90 °C still produces good fits with the data. In TS-4, the influence of the source areas is significant and the ages are eventually detrital, meaning that they have not been reheated above c. 40 °C after deposition. Despite similarities between the Rigi and the Entlebuch cross sections, differences in their uplift histories are also discernible.

In TS-1 of the Entlebuch profile, the sediments were heated to temperatures of at least 110°C after deposition. A strong signal at c. 10 Ma is required, which cools the sample to at least 40°C. At lower temperatures, the range of possible t-T-paths becomes variable. Accordingly, the cooling from 40 °C to the present day temperature may have taken place at any point in time between 10 and 0 Ma, and is beyond thermochronological resolution. Modelling also shows that the thermochronological data cannot be explained by constant cooling.

In the southern part of TS-2 (sample E10), a rapid cooling pulse at c. 8 Ma can be observed, thus postdating the cooling event in TS-1. This signal must account for at least 70 °C of cooling. Crossing a local thrust within the tectonic slice, less rapid cooling starting at c. 10 Ma is observed, which also must account for 60-70°C of cooling. At the northern fringe of TS-2 (sample E40), a rapid cooling signal of at least c. 60°C at c. 6 Ma is required to explain the obtained thermochronology ages.

In TS-3 (E45), models predict rapid cooling between 12 and 10 Ma, i.e. at the same time as TS-1, and earlier than TS-2. This illustrates that no uniform trend in cooling from south to north is present. Moreover, this late Miocene pulse must account for at least c. 70 °C of cooling. After c. 7Ma, modelling solutions show a wider spread, allowing for either constant uplift since then, or short cooling pulses. At the northern end of TS-3, AFT and (U-Th-Sm)/He ages are identical within error (E50). Modelling corroborates a strong cooling signal at c. 8 Ma, coeval to cooling in TS-2.

In TS-4, an increasing hinterland-influence on the samples is clearly seen in the modelling. The samples close to TS-3 (E55 & E60) experienced post-depositional heating, but were not completely reset. Accordingly, in this area the fossil PAZ-PRZ is exposed at the surface. Farther north in the basin (samples E65 & E70), no significant reheating occurred. Instead, a strong hinterland signal becomes visible, showing rapid uplift of the source area at c. 20 Ma.

In the Rigi area, the rocks of TS-1 experienced temperatures in excess of PAZ/PRZ temperatures. Subsequent cooling, however, differs from the observations made for the southernmost Entlebuch area. A cooling pulse at c. 10 Ma may have occurred, but cannot account for the entire cooling from temperatures of at least 110°C. Instead, two alternative cooling scenarios are consistent with the observed ages at surface; (i) additional rapid cooling at c. 7 Ma and/or after 2 Ma or; (ii) more or less constant cooling since 10 Ma at a rate of 11°C/Ma.

In TS-2, (U-Th-Sm)/He and AFT ages are measured at different samples. Accordingly, the models are less well constrained. All samples have undergone total annealing/resetting after deposition, and cooling started after 10 Ma. In addition, all samples allow for cooling starting after 5 Ma.

In TS-3 (sample RH30a – RH40), all samples indicate cooling starting around 10 Ma. The southernmost samples (RH30a & b), however, allow also for rapid cooling shortly thereafter. Generally, cooling of TS-3 occurred earlier than the rapid cooling in northernmost TS-2.

In TS-4 (RH50 – RH70), the samples experienced minor post-depositional heating, affecting mostly the (U-Th-Sm)/He-system. The AFT ages are older than (or as old as) their stratigraphic ages. As in the Entlebuch area, the hinterland signals are increasingly important with increasing northward distance from the triangle zone. Accordingly, the fossil PAZ/PRZ are exposed at surface in the same structural position as in the Entlebuch section. Only RH70 shows significant reheating to temperatures between 100 and 120°C. Modelling suggests that this sample started cooling from this temperature between 11 and 5 Ma.
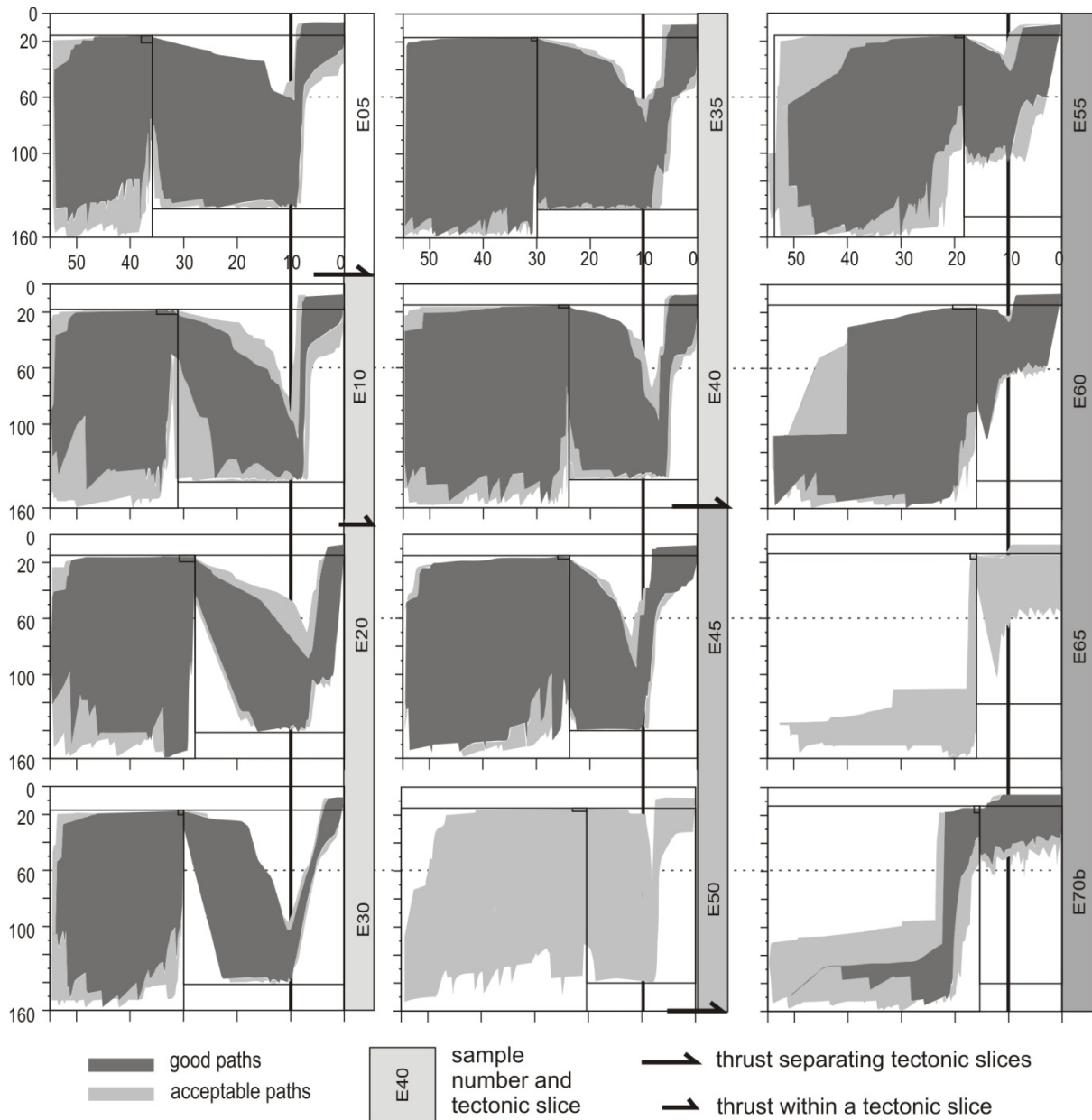
Figure 2-7A: HeFTy models for all Entlebuch samples discussed in the text. Plotted is temperature versus age in Ma. Tectonic slices are indicated by colour bars to the right of the modelling diagrams. Large thrust signs mark tectonic slice boundaries; small thrust signs denote local thrusts. Dark grey colours represent good fits (GOF > 0.5); light grey represents acceptable fits (GOF > 0.05) to the data. Different uplift pulses are visible within different samples, which are c. 10, c. 8 and c. 6-5 Ma. No general trend from north to south is observed. See text for detailed discussion.

In summary, modelling corroborates the observations derived from first order data inspection, which is rapid cooling in distinct time windows. The data require rapid cooling at c. 10 Ma, c. 8 Ma, c. 6-5 Ma, and allow for cooling after 2 Ma, in the different tectonic slices. The < 2 Ma cooling signal may be related to glacial erosion (Valla et al., 2010). Forward models show that the glacial contribution to the cooling signal cannot exceed c. 40 °C and is at the limits of resolution of low-temperature thermochronology. Therefore, we disregard it in our interpretation of thrust activity in late Miocene to Pliocene time. A discussion about the impact of glacial erosion on the data can be found in the supplementary material.

In addition, modelling shows that the two sections have undergone similar cooling histories, with minor differences. Both sections show strong reheating in the southern part of the basin and age offsets across identical thrusts. Differences in cooling histories between the sections are most pronounced for the southernmost samples. Finally, timing of these observed cooling signals within the different TS does not show any propagation direction along the profile (for instance getting younger towards north or south).
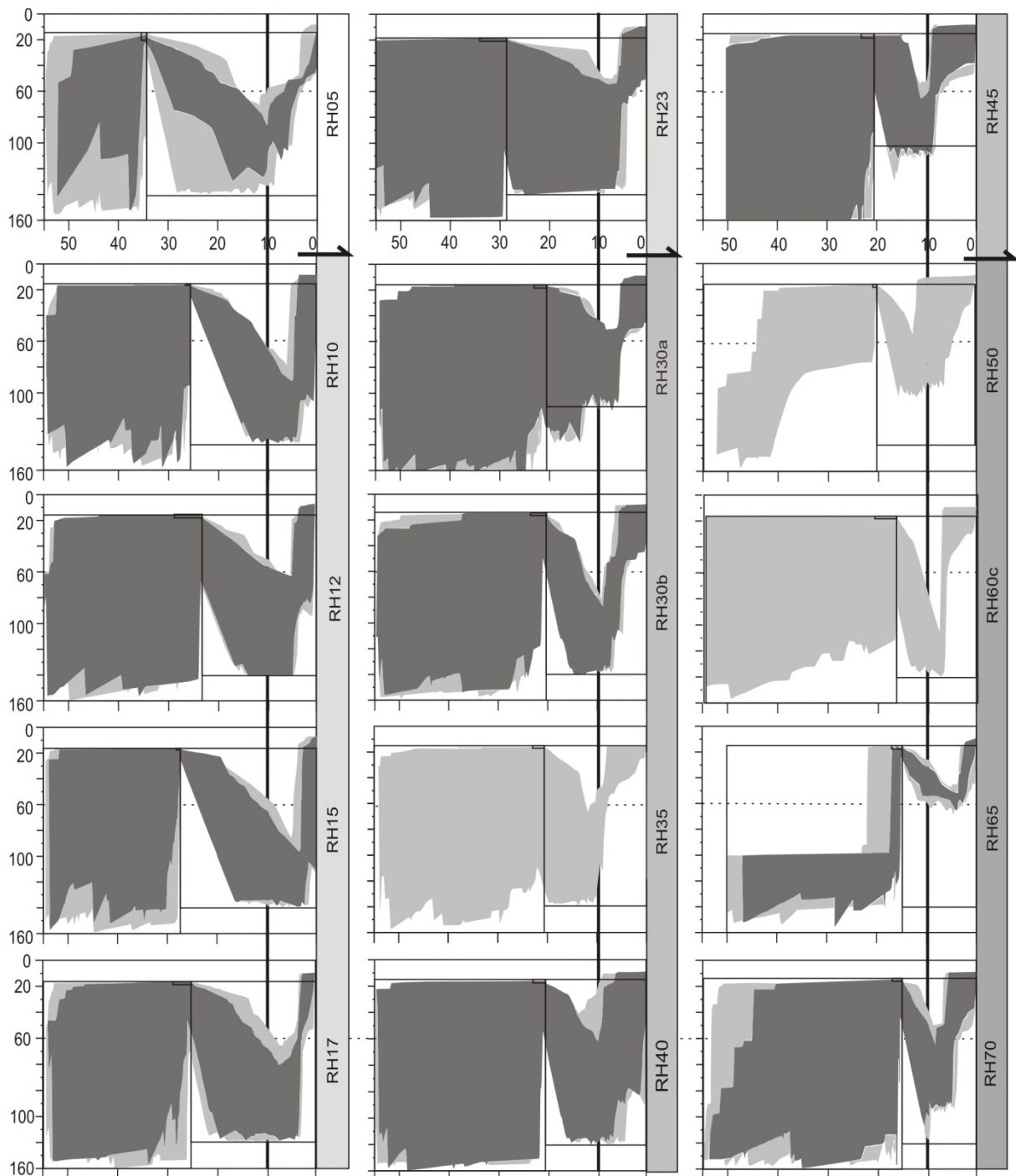
Figure 2-8B: HeFTy models for all Rigi samples discussed in the text. Legend and interpretation as in Figure 2-7.

2.8   Discussion

The locations of individual thrusts coincide with abrupt changes in observed pattern of low-temperature thermochronology ages along the Alpine border. Additionally, cooling pulses derived from modelling are more pronounced in samples that are located next to a thrust

(Figure 2-7). The observed age pattern and the modelled thermal histories strongly support the interpretation of late-stage tectonic activity in the Subalpine Molasse that was argued for Cederbom et al. (2011). Accordingly, we discuss the results in the light of thrust activity.

2.8.1 Thermochronology age pattern across thrusts

Figure 2-9 illustrates the expected thermochronological ages at surface, if an emergent thrust (i.e. a fault reaching the surface) moves rapidly starting at t_1. We assume an arbitrary (but uniform) primary age pattern (segment denoted with A). We chose rapid exhumation along the entire section at t_1. Accordingly, all AFT and (U-Th-Sm)/He ages are identical and show an age of t_1. In the case of slow exhumation (i.e. with more separated (U-Th-Sm)/He- and AFT ages) the expected age pattern that is affected by the thrust does not change. At t_2, rapid exhumation occurs along the thrust hanging walls. Samples from below the base of the PAZ that are now at surface, will show similar AFT and (U-Th-Sm)/He ages (segment B). They do not have an inherited age but will indicate the age of thrusting, i.e. t_2. Strictly speaking, the measured t_2 corresponds to a minimum age for thrust activity, i.e. the thrust was at least active until t_2, (but thrusting may have started earlier). With increasing distance from the thrust on its internal side, rocks that were lying within the PAZ at t_2 will be exposed (segment C), showing partially annealed AFT ages (becoming successively older with increasing distances to the thrust), but (U-Th-Sm)/He ages identical to t_2. At a certain distance from the thrust, rocks from within the PRZ are exposed and (U-Th-Sm)/He ages become progressively older than t_2 (segment D). At this point, both systems are not reset but still show evidence of post-depositional heating. Even farther away from the thrust, rocks from above the PAZ but within the PRZ will follow. Accordingly, the (U-Th-Sm)/He ages still show evidence of elevated temperatures, whereas the AFT-system is already unaffected by the thrust (segment E). Eventually, both thermochronometers will only display the primary age pattern again (segment A).
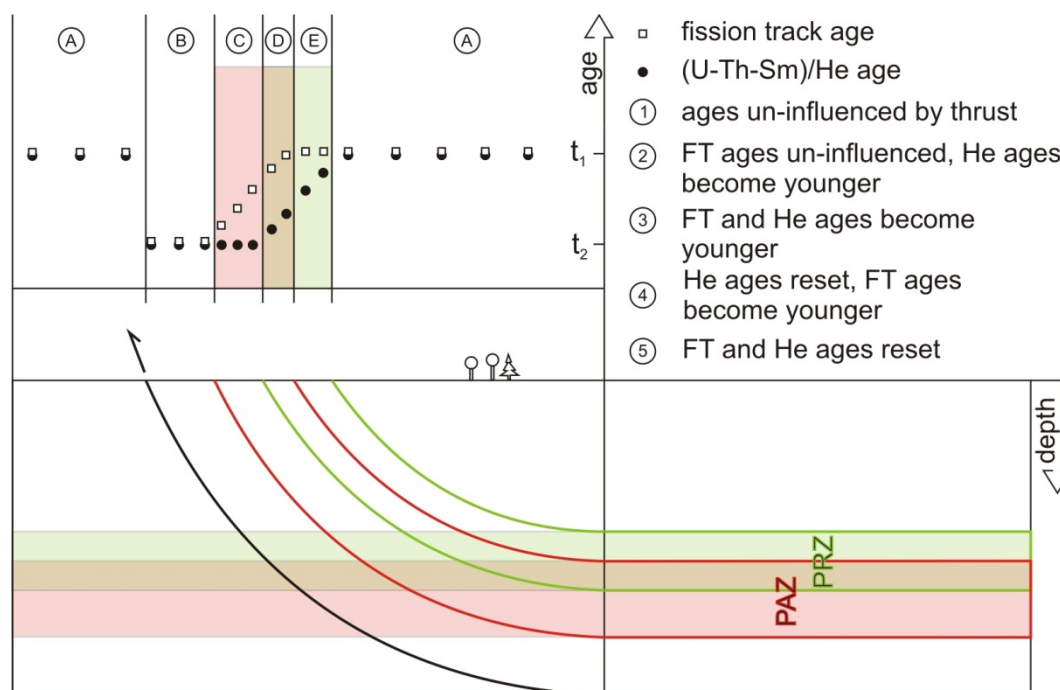
Figure 2-9: Conceptual sketch of the age evolution in a sample profile across a moving thrust. Different age relationships between the two thermochronometers are derived, depending on the distance to the fault. In segment E, the fission track ages stay uniform, but the (U-Th-Sm)/He ages become younger (as seen in TS-1 & TS-2 of the Entlebuch profile). In segment C, the (U-Th-Sm)/He ages stay uniform but the fission track ages become younger (as seen in TS-1 & TS-2 of the Rigi profile and in TS-3 of the Entlebuch profile).

In summary, exhumation decreases with distance from an emergent thrust in the case where there are splays from a shallow-dipping to sub-horizontal detachment fault with a stratigraphic cut-off angle of near 0° – as is the case for the Northern Alps. Note that with a simple movement along the thrust, different age-relationships of the two thermochronometers are expected. In segment B, the AFT ages are uniform and the (U-Th-Sm)/He-ages decrease, whereas in segment D, the (U-Th-Sm)/He ages are uniform and the AFT ages decrease. In this simple sketch, age relations in the hanging wall are only dependent on the distance from the sample to the thrust or the location of the thrust with respect to the positions of the PAZ and PRZ. In a more complex geological setting, temporal variations in heat flux across the thrust, others than flat lying isotherms, repeated movements along the thrust or irregular thrust geometry may further influence the age pattern. We expect both processes to be of minor importance in this part of the NAFB. Hence the present-day heat flow pattern can be used as a reliable source for an assessment of the palaeo-thermal regime (Rybach and Bodmer, 1980; Rybach, 1984; Deichmann and Rybach, 1989; Vedova et al., 1995; Schegg and Leu, 1998; Nagra, 2002; Schärli and Rybach,

2002; Mazurek et al., 2006; Cederbom et al., 2011). The supplementary material provides a discussion about heat flow variations in space and time in the NAFB. According to these findings, changes in heat flow pattern should be related to thrust activity. In the following section, we therefore discuss therefore the temperature field in the Molasse and its reaction to thrust activity.

2.8.2   Heat flow across active thrusts

The thermal effects and the consequences for the correct interpretation of cooling ages has been the focus of previous studies (e.g. Stüwe et al., 1994; Moore and England, 2001; Braun, 2002). In general the authors conclude that heat advection across active thrusts has to be taken into account for evaluating the amount of section removed and the exhumation rate. Thrusting causes heat flux above the thrust plane and can hence be described by the general heat equation (e.g. Braun et al., 2006). Exhumation due to thrusting leads to higher temperature gradients and upwards deflected isotherms near the surface in the respective area.

2D and 3D numerical models can predict the age patterns along a moving thrust by solving the heat equation (e.g. Braun et al., 2006; Lock and Willett, 2008). Warping of the isotherms and the accordingly varying thermochronological ages depend on décollement depth, fault dip and fault slip rate. Minimum ages occur next to the emerging fault ramp and ages increase above the flats. A minor offset by cooling of the hanging wall next to the fault plane can be observed in the models by Lock and Willett (2008). A clear jump to older ages is seen across the fault. Numerical models fit well with the qualitative reasoning and predictions.

2.8.3   Tectonics in the Subalpine Molasse

Both first order data inspection and subsequent modelling show that discrete cooling pulses at c. 10, 8, and 6-5 Ma can be derived from the data set. An apparent discrepancy within age trends is discovered - the (U-Th-Sm)/He ages remain constant while the AFT ages show a younging trend in some parts and an increasing trend in other parts.

In the Entlebuch, TS-1 and TS-2 show a pattern that is similar to segment (E) in Figure 2-9. Modelling shows rapid uplift at different periods for different samples. Accordingly, tectonic activity at a thrust between TS-1 and TS-2 and at the thrust just north of E10 is suggested at c. 10 and c. 8 Ma respectively. The offset between TS-2 and TS-3, which is the basal USM thrust, is evident from the (U-Th-Sm)/He ages, the single grain AFT ages as well as from modelling. Thrusting must have been active until at least c. 6-5 Ma. TS-3 shows a thermochronological age pattern which is similar to the segments (C) and (B) in Figure 2-9. Again supported by large offsets in the data set between TS-3 and TS-4, the topmost structure of the triangle zone was tectonically active until at least c. 8 Ma.

In the Rigi section, the interpretation of the age patterns is complicated by the fact that for some samples either (U-Th-Sm)/He or AFT data exist. The age patterns of TS-1 and TS-2 are similar to the segments (D) and (C) of Figure 2-9, showing rotation along the basal UMM thrust. (U-Th-Sm)/He and AFT ages reproduce at c. 6 Ma, which is in line with the findings for Entlebuch. North of the basal UMM thrust, AFT data do not show a clear trend, but within the (U-Th-Sm)/He data of TS-4, a trend towards younger ages exists. (Re-)Activation of a thrust within the triangle zone and consequent back thrusting of the Plateau Molasse over the underlying duplex is able to explain this trend. This implies thrusting between TS-3 and TS-4, as observed at Entlebuch. The movement must have taken place at c. 8 Ma (and could have continued thereafter).

In sum, data and modelling illustrate thrust activity within both profiles along the same thrusts at the same time and additional local faulting at Entlebuch. The corresponding age/elevation profiles corroborate these findings: Cederbom et al. (2004; 2011) observe thrusting between the Weggis and the Entlebuch well (i.e. between TS-2 and TS-3, along the basal UMM thrust). In addition, they find an offset within the vertical sections, which we also see in our (U-Th-Sm)/He data in the Entlebuch well (Figure 2-6). This offset may have occurred at any time after the uplift of the fossil PAZ and PRZ (i.e. after 6-5Ma).

2.8.4 The link to the inner Alps

Thrusting within the Subalpine Molasse must be accommodated by thrusting within the Alps because of kinematic linkage via common detachments. Figure 2-10 shows the link of the

Subalpine Molasse to the orogen. The thrusts of the Subalpine Molasse connect to the Alpine sole thrust and hence to the base of the Aar Massif (Boyer and Elliott, 1982; Burkhard, 1990; Pfiffner et al., 1990; Burkhard and Sommaruga, 1998a). This kinematic link with all reactivated thrusts implies synchronous uplift of the two. The uplift of the Aar and Gotthard Massifs are constrained by several recent studies (Reinecker et al., 2008; Vernon et al., 2009b; Glotzbach et al., 2010). Vernon et al. (2009b) argue for a suite of exhumation events in the Aar massif and the Lepontine Dome with high rates at 9-7 Ma and 5-3 Ma, respectively. Glotzbach et al. (2010) and Reinecker et al. (2008) argue for nearly constant exhumation since c. 14 Ma but see also slightly accelerated uplift rates between 10 and 7 Ma. Moreover, Glotzbach et al. (2011a) use patterns of length distributions of apatite fission tracks to infer a steady-state exhumation of the Western Alps since 10 Ma. The thrusting pulses detected in the Subalpine Molasse are hence synchronous with uplift of related structures within the orogen correspond reasonably well to the exhumation events detected by Vernon et al (2009b).

In addition, the amount of shortening observed in the Subalpine Molasse and Jura Mountains must be balanced by shortening within the orogen itself. Total shortening within the Molasse Basin, which is mostly taken up in the Subalpine Molasse, is at least 35 km but can be as large as 50 km (Burkhard and Sommaruga, 1998a). Shortening related to thrust reactivation must hence be smaller. Our data provide an estimate of horizontal shortening related to the late stage deformation based on thrusts dip, amount of cooling, and an assumption of the (palaeo-) geothermal gradient based on Schegg and Leu (1998). A description of the procedure is found in the supplementary information. Accordingly, each event, which brings the sample from temperatures above the base of the PAZ to less than 40 °C (i.e. the temperature at which the (U-Th-Sm)/He-system is not sensitive anymore) requires c. 4 km of shortening. For the three detected cooling pulses derived from the data, this sums up to a total of at least c. 12 km of late Miocene shortening within the Subalpine Molasse, which is distributed over different thrusts. Contemporaneous shortening in the Jura is approximately 5-7 km (Burkhard, 1990; Philippe et al., 1996). Shortening within the Aar Massif is difficult to constrain, since the number of imbricates within the massif is unknown (Vollmayr and Wendt, 1987; Burkhard, 1990). However, Schmid et al. (1996) estimate at least 15 km of post 19 Ma shortening for the Aar Massif. Accordingly, both

timing and amount of shortening derived from our data are corroborated by results of previous studies.
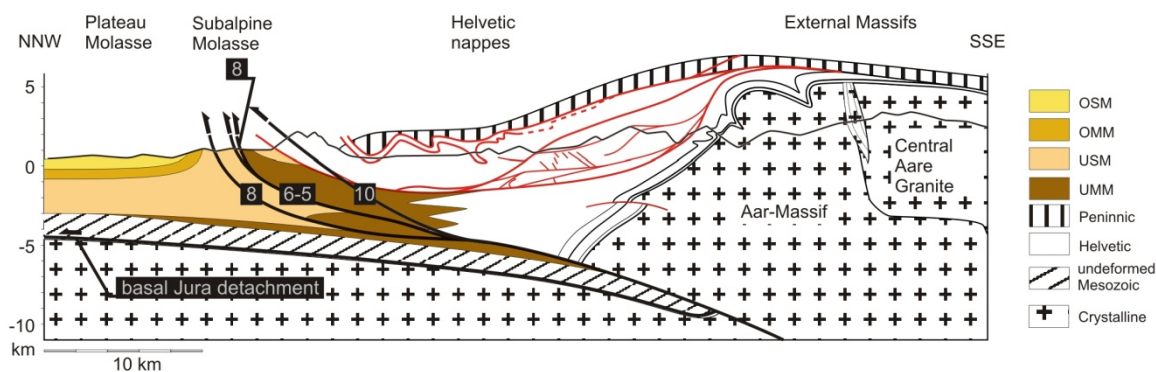
Figure 2-10: Tectonic link of the Subalpine Molasse to the inner Alps. The profile is based on Pfiffner (2010) and is located between the Rigi and Entlebuch profiles. Active structures within the Subalpine Molasse are marked with thick black lines. Numbers in black boxes indicate the time of thrust activity (in Ma). Note that the southernmost active thrust must be linked to the Alpine sole thrust, as the basal Helvetic thrust is deformed by up-doming of the Aar Massif.

2.8.5 The link to the Jura Mountains and critical taper theory

It is commonly inferred that thrusting in the Subalpine Molasse ceased with the onset of Jura folding, which started around 12 Ma (Burkhard and Sommaruga, 1998a). Cederbom et al. (2011) observed thrusting in the Subalpine Molasse around 5 Ma, which is roughly coincident with the cessation of thin-skinned thrusting and onset of erosion in the Jura Mountains (Ustaszewski and Schmid, 2006; Willett and Schlunegger, 2010). Recent tectonic activity within the Jura Mountains related to deep, intra-basement detachment underneath the basin has been suggested by Mosar (1999) based on uplift and seismicity data. In agreement with that, Ustaszewski & Schmid (2007) found a late Pliocene change from thin- to thick-skinned tectonics at the northern fringe of the Jura fold and thrust belt. The inferred strain rates are $2*10^{-16}$ s^{-1}, which is low. Finally, Madritsch et al. (2010) recorded largely aseismic recent deformation of the Mesozoic cover of the Jura mountains, and seismogenic faulting within the underlying basement.

These partly contrasting differences in the interpretation of a link between deformation of the Jura, the external massifs and the Subalpine Molasse are mainly based on a lack of high-

resolution exhumation data from the proximal basin border. The new data presented in this study show that thrusting within the Subalpine Molasse occurred at different thrusts in certain time windows and at least until 6-5 Ma. This is contemporaneous with folding of the Jura Mountains and uplift of the Aar Massif, which are all probably linked through common detachments (Figure 2-10). If the Alps (including the Jura Mountains) are considered to be a critical wedge, then thrusting in the SM is equivalent to tectonic activity behind the orogenic front. Our data show that the wedge must have been unstable in its inner parts also in mid to late Neogene times. Both case studies from other orogens (e.g. Zhang et al., 2004; Simoes and Avouac, 2006) and analogue models (Lohrmann et al., 2003), show that advancing wedges tend to re-adjust in order to maintain a critical taper.

Alternatively, wedge-internal thrusting and associated surface uplift can result in a supercritical wedge whose front propagated towards the foreland. Mosar (1999) suggested such a scenario for the Alpine external massifs by invoking a newly forming detachment linking the footwall ramp below the Aar Massif and the northern front of the Jura Mountains. In addition to readjusting of the wedge, overthrusting of a detachment ramp may cause thrusting behind the orogenic front (Robert et al., 2009). Steps in the basement-cover contact below the Molasse basin, caused by Permo-Carboniferous (half) grabens may have served as ramps (Burkhard and Sommaruga, 1998a) and therefore provide an alternative explanation for internal thrusting.

2.9   Conclusions

In this study, we show that the Subalpine Molasse was tectonically active at c. 10, c. 8 and c. 6-5 Ma. The individual active thrusts can be pinpointed for every time window. We find that thrusting is neither foreland nor hinterland propagating. Tectonic activity can be traced back into the orogen, where the external crystalline massifs were exhumed at the same time. Thrusting is also coeval with and potentially linked to the deformation of the Jura Mountains. The data presented here bridge the gap between the so far assumed cessation of thrusting in the Subalpine Molasse at 12 Ma and the reported thrusting at c. 5 Ma. In particular, we claim that 1) the Subalpine Molasse was active until recent times, and 2) that it can be considered as part of a wedge that encompassed the entire section between the

external massifs and the Jura fold-and-thrust belt, and 3) that it was deformed in order to maintain critical taper conditions. The identification of Holocene tectonic activity of the Subalpine Molasse lies beyond the resolution of the applied thermochronometers. However, late stage cooling can be as much as 30-40 °C, which would translate into c. 1 km of (potentially glacial) erosion.

2.10 Acknowledgements

3 Supplementary information to "Resolving the latest uplift and erosion history of the Northern Alpine Foreland Basin with low temperature thermochronology"

3.1 Density and magnetic separation techniques applied

All samples from the horizontal profiles were crushed using a roller mill. For borehole cuttings, samples were crushed by hand in a mortar. The samples were sieved into different size fractions (< 500, 355, 250 µm) and the < 250 µm fraction was processed further. For cleaning, distilled water was used and the samples were decanted manually. After drying, the sample was separated into magnetic and non-magnetic fractions, using the Frantz magnetic separator at 1.45A, a slope of 15° and a tilt of 15°. For heavy liquid separation, bromoform and diiodomethane were used and the samples were dried with acetone. The percentage of apatite in the samples was often far less than 5%.

3.2 Apatite fission track dating and its application

3.2.1 Theoretical background

Fission tracks are trails of damage in the crystal lattice of a mineral that are created by spontaneous fission of ^{238}U (Reiners et al., 2005). Fission tracks are produced continuously through time, but anneal immediately at high temperatures. Below a certain temperature, fission tracks start to accumulate. The amount of spontaneous tracks is proportional to the time that has elapsed since the grain cooled into the so-called Partial Annealing Zone (PAZ). The PAZ is the transition zone in which tracks are accumulated while fission tracks are still shortened. An apatite that cools quickly through the PAZ will have a geologically meaningful AFT age, while an apatite that cools slowly through the PAZ or experiences reheating, records an AFT age that may be geologically meaningless. Reheating of grains due to burial in a sedimentary basin may lead to partial or total annealing of fission tracks and, hence, a loss of the detrital information in the apatite grain.

The temperature range at which partial annealing occurs is mainly dependent on duration of heating and chemical composition of the individual grain (Green et al., 1986). The annealing properties of apatite are therefore important when interpreting the AFT ages and the single grain age distribution. Fluorine-rich apatites are less resistant to annealing than chlorine-rich

apatites (Carlson et al., 1999; Barbarand et al., 2003a; Barbarand et al., 2003b), but additional parameters affect the annealing kinetics. In order to constrain the combined effect on the annealing properties for each grain, the so-called Dpar value is used (Carlson et al., 1999; Ketcham et al., 1999). The Dpar value is the width of an etched fission track crossing the polished grain surface that is being analyzed in a grain mount. By standard, a mean value of four measurements taken parallel to the c-axis is used as representative Dpar for each apatite crystal (Donelick et al., 2005).

Apatite grains of different provenance are likely to have different detrital FT ages and potentially also different annealing kinetics. If so, a spread in single grain ages will be observed in samples that are not totally annealed. Moreover, the differences in single grain AFT ages will be pronounced in samples that have spent long periods of time within the PAZ. For a detailed description of the fission track method, the reader is referred to Donelick et al. (2005) and Tagami & O'Sullivan (2005).

3.2.2   Application of the fission track method

Following separation, the apatite concentrates were mounted using the epoxy-only method (Donelick et al., 2005) and polished manually. Apatite mounts were etched with 5.5M HNO_3 at 21°C for 20s, following Carlson et al. (1999). Fission track counting was carried out by C. von Hagke with an optical microscope using un-polarized, transmitted and reflected light at 1600× or 2000× magnification (100× dry objective, 1.25× projection tube, 12.5× or 16× oculars, respectively) in the AtoZ laboratory in Idaho, USA.

To analyze uranium concentration, we used laser ablation inductively coupled plasma mass spectrometry (LA-ICP-MS). Samples were ablated with a New Wave UP-213 laser ablation system; elements were analyzed in solution with a Finnigan Element2, a high-resolution single collector ICP-MS. All LA-ICP-MS analyses were performed at the GeoAnalytical Lab of Washington State University, USA.

Given the assumption that the ^{43}Ca is directly related to the volume of apatite ablated during a given LA-ICP-MS session, the ratio of $^{238}U/^{43}Ca$ gives a relative measure of the uranium

concentration in apatite (Donelick et al., 2005). AFT ages were calculated using the modified zeta calibration approach (Donelick et al., 2005). This zeta calibration factor is determined for each sample analyzed (Table 2-1).

Analyst bias during the age dating process is probably the biggest source of error during the whole dating procedure. There is a human tendency to be influenced and ultimately biased by expectations and/or preliminary results (Donelick et al., 2005). Therefore, during microscope work, samples were renamed and analyzed in arbitrary order.

However, the apatite content was low in some samples. Note that counting of too few grains may lead to undiscovered grain age populations. In theory, dating at least 117 randomly selected grains from each sample is necessary to constrain the total age probability density pattern, the number and relative abundance of age populations, and the presence and age of potentially limiting, minor populations (Vermeesch, 2004; Andersen, 2005). This is of course impossible to achieve, but two conclusions should be drawn from this: first, even if only one grain has a different age from all others, it may not be a contamination but a meaningful age, and second, even if samples appear to be fully annealed, it is not certain that they really are. However, even with 20 counted grains, a population which makes up only 10% of the separate, will be detected with 85% percent likelihood (Andersen, 2005).

Statistical analysis of grain age populations within a sample is crucial for a correct interpretation of the fission track data. Applying a central age (i.e. a weighted geometric mean of all single grain ages) is only appropriate, if the spread in single grain ages can be related to one common age (i.e. if the data is not over-dispersed (Galbraith and Laslett, 1993)). If the grains do not have a common age, the central age is geologically meaningless and only provides information about trends within the data set. However, since extraction of grain age populations is a statistical method, it often remains problematic to decide how many distinct age components are present in one sample (Galbraith, 2005).

A common practice for detecting several populations is to apply the statistical χ^2-test (Galbraith, 2005). A failure of the χ^2-test may indicate that the single grain AFT ages do not belong to one single population. If a sedimentary sample contains several single grain age

populations, it generally implies that the sample has not been totally annealed since deposition.

The χ² test, with a cut-off at 5 %, works reasonably well for fission track dating with the conventional external detector method (EDM). However, it is not applicable for ages generated with the LA-ICP-MS method, because the precision of uranium measurements is much higher and the single grain age error becomes much smaller than with the traditional EDM.
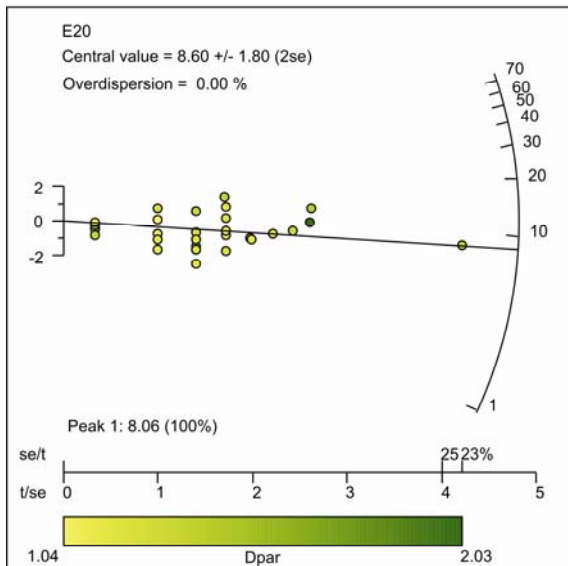
Failure of the χ²-test was regarded of minor significance for our samples. Instead all fission track ages were statistically analyzed with the software RadialPlotter (Vermeesch, 2009), which is specially designed for LA-ICP-MS data. The detection of different grain age populations is based on a minimisation of the Bayesian Information Criterion (BIC). Assuming that the single grain ages are independent and identically distributed, the BIC distinguishes between competing scenarios (i.e. number of grain age populations) based only on the maximum likelihood (Liddle, 2007). The resulting radial plot simultaneously visualizes a measured single grain age and its precision (Vermeesch, 2009).

For radial plots generated with RadialPlotter, the single grain age measurements must be log-transformed, which is impossible for grains with zero spontaneous tracks (Ns). Therefore, a value for Ns of 0.5 was assigned to these grains. This still accounts for natural variability of U-concentrations and has only minor effects on the mixture model algorithm. For central ages, the effect is negligible. An assessment of the error introduced can be found in chapter 3.3.

Galbraith (2005) points out that, in practice, it is wise not to rely solely on statistics, but to be aware that several different scenarios may provide an equally good fit to the same data and that, therefore, the geological context has to be included when interpreting the data. Grains that have less than 2 ppm uranium content have been excluded in the analysis because of the large uncertainty they are associated with. This is due to the age equation, where the uranium content is inverse proportional to the fission track age whereas in the error calculations the uranium concentration is directly proportional to the age and
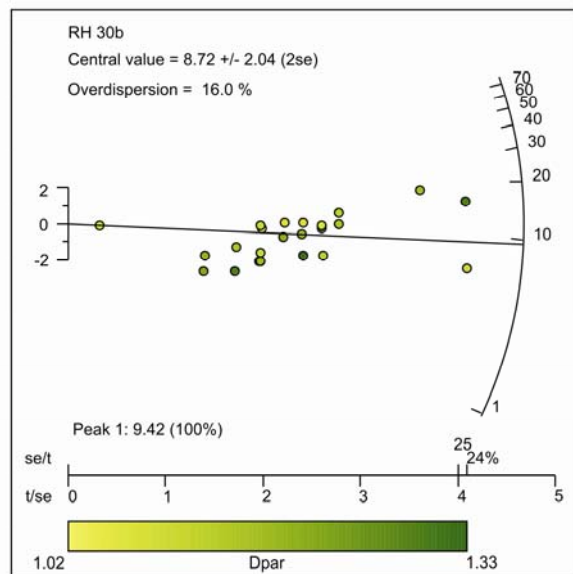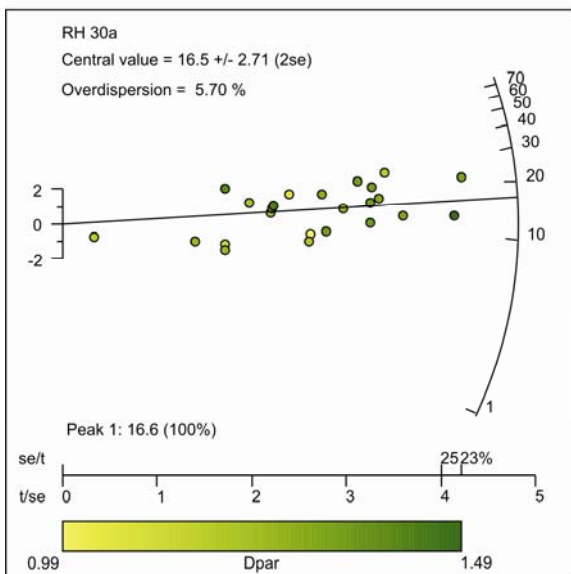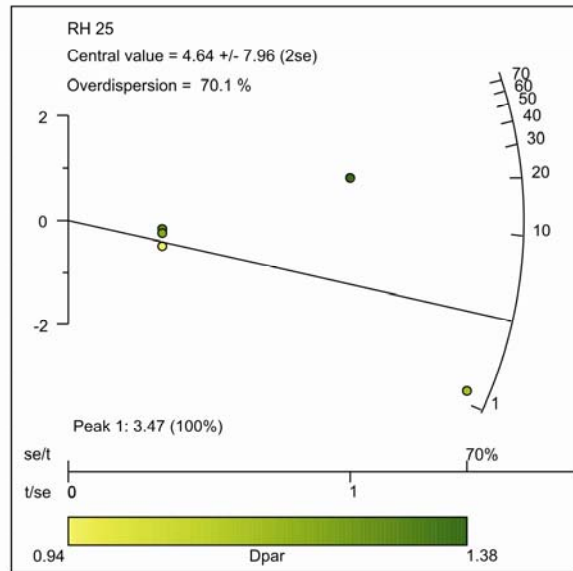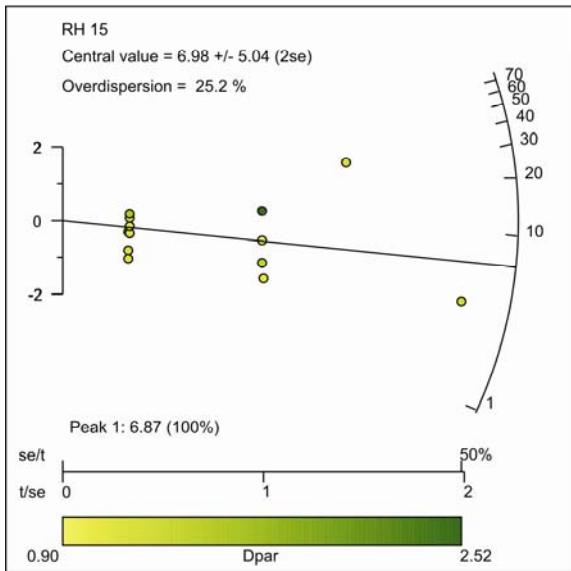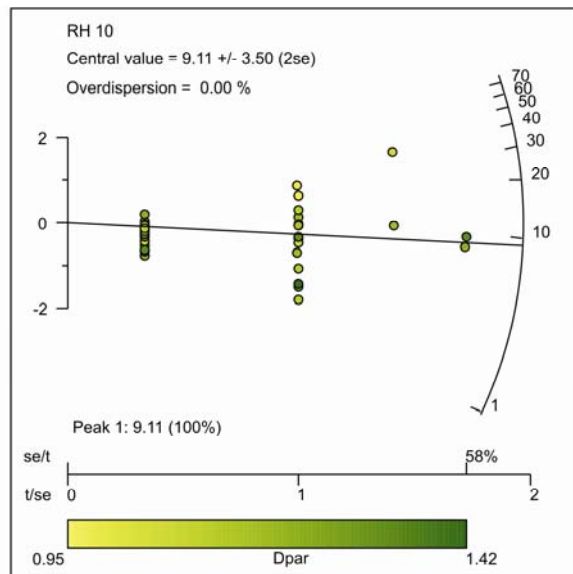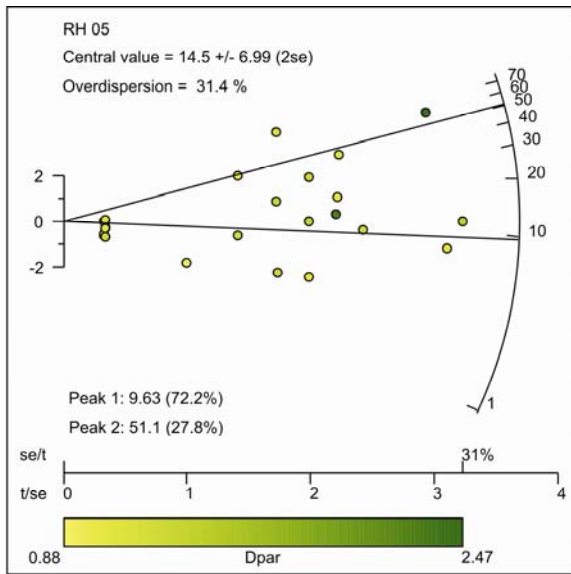
increases quadratically (Donelick et al., 2005). Hence grains with very low uranium have oftentimes very young fission track ages and errors of several hundred Ma or even Ga. We use the cut-off of 2 ppm as this is the lower limit of a typical uranium concentration for apatite (Harrison and Zeitler, 2005).
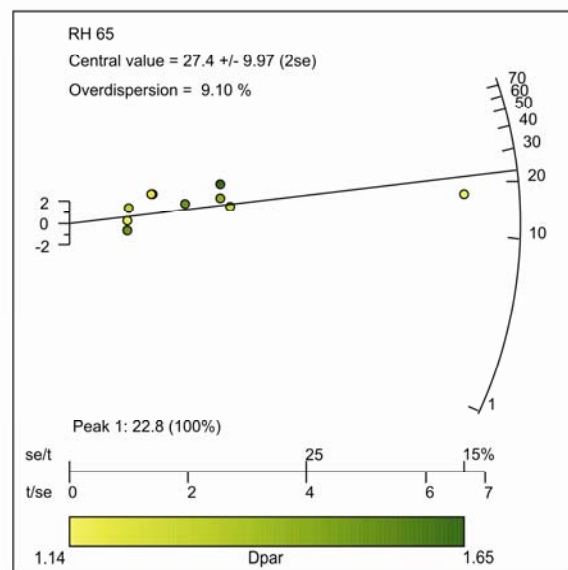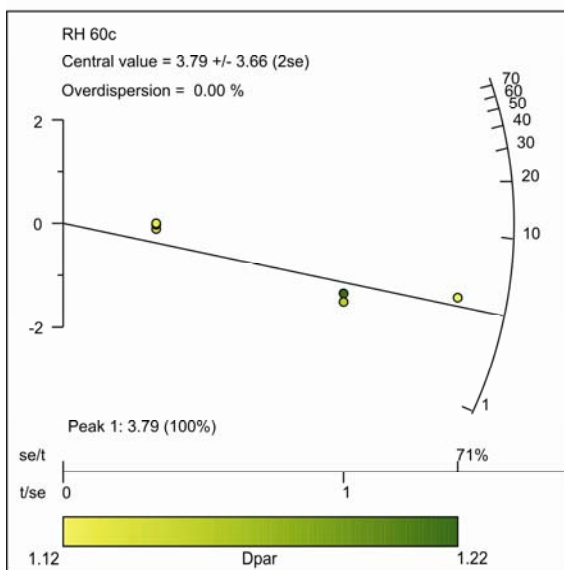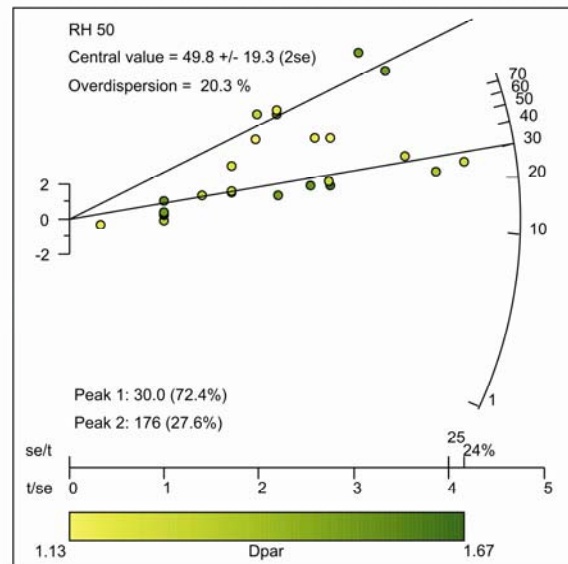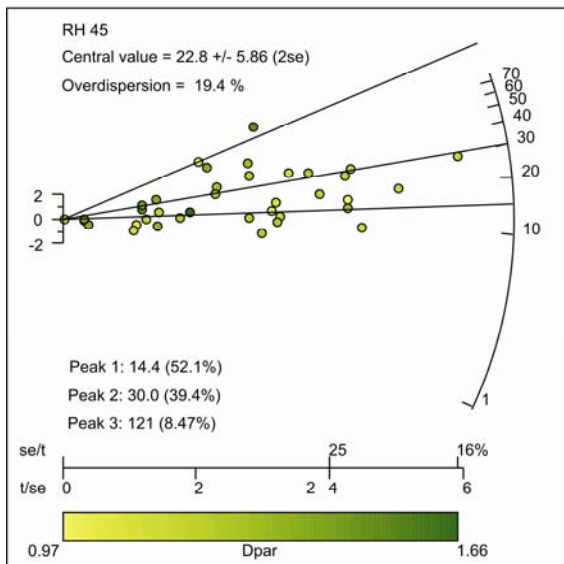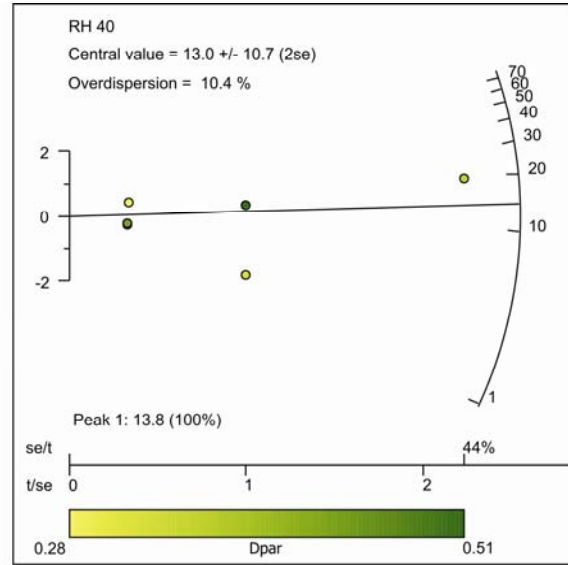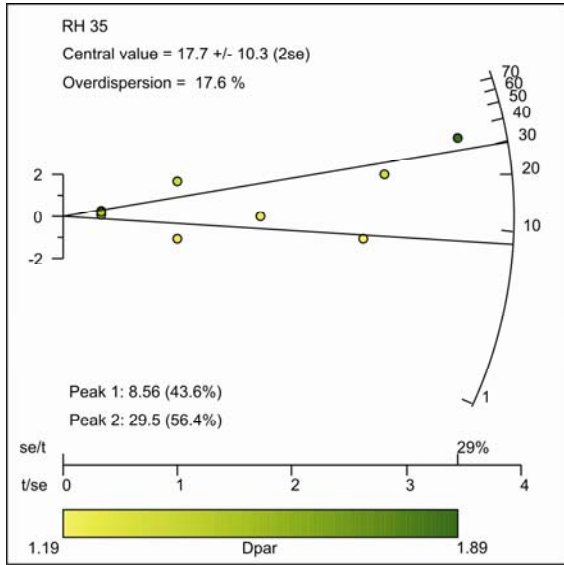
A: Radial plots Entlebuch

B: Radial plots Rigi

RH 35
Central value = 17.7 +/- 10.3 (2se)
Overdispersion = 17.6 %

Peak 1: 8.56 (43.6%)
Peak 2: 29.5 (56.4%)

RH 40
Central value = 13.0 +/- 10.7 (2se)
Overdispersion = 10.4 %

Peak 1: 13.8 (100%)

RH 45
Central value = 22.8 +/- 5.86 (2se)
Overdispersion = 19.4 %

Peak 1: 14.4 (52.1%)
Peak 2: 30.0 (39.4%)
Peak 3: 121 (8.47%)

RH 50
Central value = 49.8 +/- 19.3 (2se)
Overdispersion = 20.3 %

Peak 1: 30.0 (72.4%)
Peak 2: 176 (27.6%)

RH 60c
Central value = 3.79 +/- 3.66 (2se)
Overdispersion = 0.00 %

Peak 1: 3.79 (100%)

RH 65
Central value = 27.4 +/- 9.97 (2se)
Overdispersion = 9.10 %

Peak 1: 22.8 (100%)

Figure 3-1: Radial plots for Entlebuch (A) and Rigi (B) showing the precision of the single grain ages and the determined peak ages (black lines).
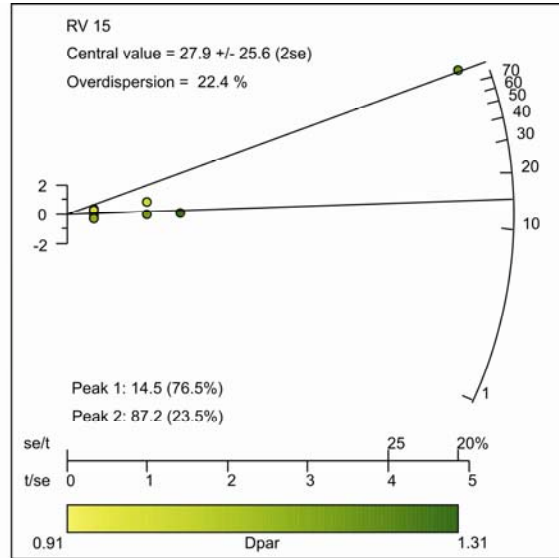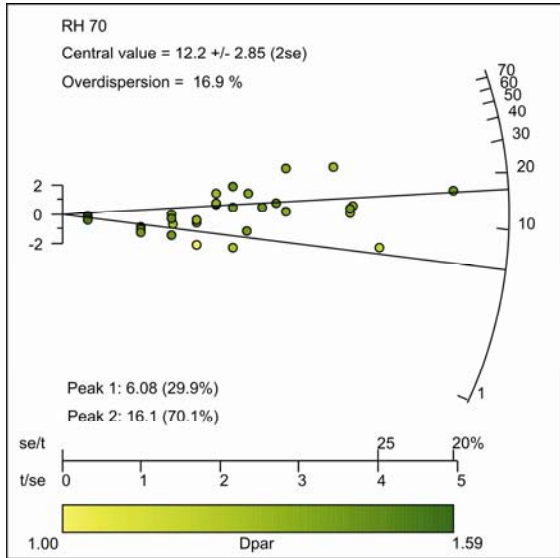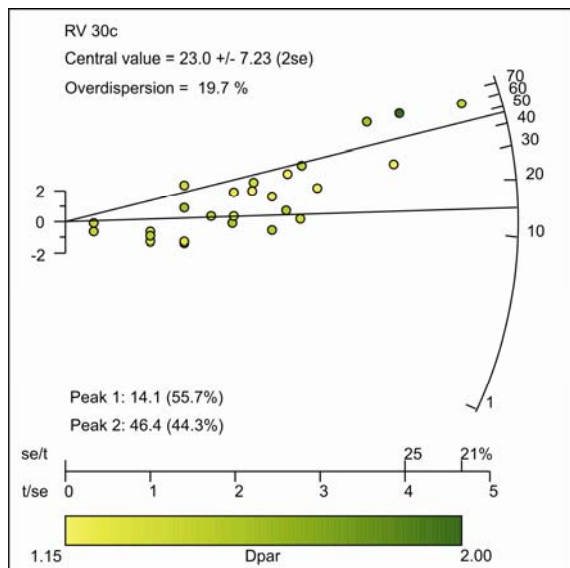
3.3   Assumption of Ns = 0.5

Table 3-1: error introduced by assuming Ns=0.5. Max age denotes the calculations for Ns = 0.9, Min age denotes calculations for Ns = 0.1. Difference is Max age minus Min age. #Ns = 0 denotes the number of dated grains within that sample that have zero spontaneous tracks. 1σ denotes the error of the central age.

Sample	Max age	Min age	Difference	#Ns=0	1σ
E05	9.8	9.4	**0.4**	3	2.75
E10	8.6	8.0	**0.5**	12	2.25
E20	7.1	6.8	**0.3**	6	0.90
E30	9.1	9.0	**0.1**	6	1.11
E35	9.0	8.8	**0.2**	3	1.76
E40	46.2	45.8	**0.3**	6	1.91
E45	10.8	10.7	**0.1**	2	1.76
E50	6.9	6.7	**0.2**	4	1.49
E55	23.2	23.0	**0.2**	6	3.23
E60	19.3	18.9	**0.4**	4	3.92
E65	11.6	11.5	**0.1**	11	1.64
E70b	20.8	20.8	**0.0**	0	1.24
RH05	10.2	9.5	**0.6**	11	3.50
RH10	7.4	4.6	**2.8**	20	1.75
RH15	5.4	3.1	**2.3**	10	2.52
RH25	2.7	1.6	**1.1**	4	3.93
RH30a	13.8	13.7	**0.1**	2	1.35
RH30b	8.0	8.0	**0.0**	1	1.02
RH35	15.0	13.7	**1.3**	4	5.15
RH40	9.2	7.5	**1.7**	9	5.35
RH45	16.8	16.7	**0.2**	5	2.93
RH50	35.9	35.7	**0.2**	3	9.62
RH60c	4.7	3.0	**1.7**	3	1.83
RH65	16.0	16.0	**0.0**	4	4.83
RH70	10.8	10.7	**0.1**	4	1.43
RV15	41.6	34.6	**6.9**	8	12.80
RV20	31.5	27.9	**3.6**	15	7.30
RV25	14.1	8.6	**5.4**	12	6.15
RV30a	23.3	21.9	**1.4**	16	4.46
RV30b	22.8	22.3	**0.6**	6	4.82
RV30c	22.3	22.1	**0.2**	2	3.61

For assessing the error introduced into by assuming Ns = 0.5, all ages were calculated also with Ns = 0.1 and Ns = 0.9, leading to a maximal and a minimal age for that sample. Results are given in Table a3-1. For all ages, the error introduced is most of the times negligible and in any case by far smaller than the error of the central ages.

3.4 EDM sampling strategy and age dating procedure

EDM dating was performed by M. Rahn. Samples for EDM FT analysis were obtained from Flysch and Molasse sandstones, epiclastic greywackes (Taveyanne greywacke), and minor quartzitic sandstones and crystalline basement rocks. Apatites were extracted from 10-35 kg rock samples using standard crushing and mineral separation techniques. Grains were mounted in epoxy, polished and etched for 20s in 5M HNO_3 at 20 °C. Samples, together with CN5 standard glass dosimeters were irradiated in the highly-thermalized (cadmium ratio (thermal/epithermal + fast neutrons) > 200) RISØ reactor, Denmark. The external detector method was used and muscovite mica detectors were etched for 45min in 40% HF at 20°C. Tracks were counted and lengths measured using optical microscopes with magnifications of 1250x and 1600x. To minimize apatite compositional effects grains with fat tracks, i.e. large etch pits typically assigned to Cl-rich apatite, were excluded. Central ages (Galbraith & Laslett 1993) were calculated using the IUGS-recommended zeta calibration approach (Hurford & Green 1983). Statistical χ^2 tests were applied to search for internal variation assuming the single grain ages of mono-population samples to be Poissonian distributed. Failure of this test may indicate a lack of age resetting during the Alpine thermal overprint.

3.5 Differences between LA-ICP-MS and EDM data

The fact that all these samples are from sediments with various provenance histories and that they are located within a partial annealing zone where age variations are normal, might alone be enough for explaining the slight differences. However, a systematic variation between the two data sets may also be an explanation, which would then provide additional information about the shape of the fossil PAZ. As the data sets come from the western and eastern mountain flanks respectively, this would imply that the base of the PAZ is higher in the west than in the east. As this variation occurs along strike within one tectonic slice, it could be attributed to variations in heat flow or differences in glacial erosion.

Data density of heat flow is too poor to carry out quantitative studies, but from the Bavarian Subalpine Molasse and from the Swiss Plateau Molasse, temperature variations along strike of 1 °C/km are not exceptional (e.g. Schärli and Rybach, 2002). Taking the 4 km distance between the eastern and western flank of Rigi, results in a respective temperature

difference of 4 °C. Using the present day geothermal gradient of 30 °C (Schegg and Leu, 1998), c. 130 m of offset of the Partial Annealing Zone is possible.

Differences in glacial erosion on the eastern and western flank of Rigi Mountain may also play a role. The surface gradient of the glacier was lower on the western side of the Rigi Mountain during the last glacial maximum (Bini et al., 2009), resulting in slower ice velocities. However, both sides have been covered with thick ice sheets and present day morphology suggests that the glacial erosion efficiency was similar on both mountain flanks.

Generally, these rough calculations should only point out that the two data sets reproduce within error with a possible offset towards younger ages at the western Rigi Mountain flank (where ages were determined with Laser Ablation).

3.6 Apatite (U-Th-Sm)/He dating and its application

3.6.1 Theoretical background

During radioactive decay of ^{238}U, ^{235}U, ^{232}Th and ^{147}Sm radiogenic ^{4}He is produced in the crystal lattice. At high temperatures ^{4}He is transported rapidly out of the crystal by diffusion, but at lower temperatures diffusion becomes less efficient and He is retained and enriched in the crystal lattice. The amount of ^{4}He can therefore be translated into a cooling age. Again, there is a transition zone where both mechanisms (retention and diffusion) are significant, the so-called partial retention zone (PRZ).

The temperature range in which partial retention takes place varies depending on several parameters. Helium diffusivity scales with the inverse square of grain size (Farley, 2000). Radiation damage associated with U and Th decay has to be accounted for (Flowers et al., 2009), because damage trails within the crystal are acting as traps for helium atoms and increase retentivity. Zonation within the grain may also affect the diffusion rate and, hence, the temperature interval of the PRZ.

Samples that cooled relatively quickly through the PRZ have less variation in single grain ages, whereas samples that cooled relatively slowly (< 3 °C/Ma) or resided within the PRZ prior to later cooling have a comparatively greater variation in (U-Th-Sm)/He ages (Fitzgerald et al., 2006).

It must be noted, that even if separation from their host sediment would be a strictly random process, the selection of grains for analysis may be skewed towards a certain grain age population, as not every grain is suitable for (U-Th-Sm)/He analysis. Preferably, big, inclusion-free, and idiomorphic crystals were picked.

Ideally, the single grain ages reproduce within error. However, often a spread in ages is observed in the data set, as a result of undiscovered crystal or fluid inclusions, cracks, grain zonation and implanted helium from external sources. In order to avoid influences leading to geologically meaningless ages, those grains with a necessary re-extract on the helium line, with very low uranium content and with erroneously high ages, were excluded from further

interpretation (Table 2-3). More information about why an individual grain was rejected is given in chapter 3.7.

However, a spread in ages can also be geologically meaningful and may simply reflect sampling of an incompletely annealed sedimentary sequence where single detrital apatite grains carry their own partial or complete thermal history and have no direct geological relationship with one another (Redfield, 2010). Moreover, a spread can be produced if grains with different properties remain in the partial retention zone for a longer time period, which then provides information about the rate of cooling (Fitzgerald et al., 2006). A discussion about variations in single grain (U-Th-Sm)/He ages is given in Fitzgerald (2006).

As discussed for the fission track data, most of the samples in this study have been reheated substantially after deposition. In case of a complete resetting of the (U-Th-Sm)/He system, the mean age is more reliable, because it balances out undetectable wrong single grain age measurements, caused for instance by zoned grains (Fitzgerald et al., 2006). In addition, the typically dated grain is not a perfect crystal but a fragment. Dating broken grains leads to an inappropriate Ft-correction, i.e. too young or old (U-Th-Sm)/He ages. In such case a mean age has shown to be most reliable (Brown et al., 2011). Finally, especially in the case of rapid cooling, the youngest age and the weighted mean age will be similar and provide a good approximation of the "true" age.

Even if the samples are not fully reset, the weighted mean age provides good information about age trends, analogous to shifts in central fission track ages. Detecting different populations within the (U-Th-Sm)/He data sets would be unlikely, as routinely only 3 to 6 single grains are measured.

3.6.2 Application of the (U-Th-Sm)/He method

A first set of grains (set A) was examined and checked for inclusions at the GFZ Potsdam, Germany with a Zeiss SteREODiscovery V12 microscope with a Plan S 1.0x objective. A second set of grains (set B) was inspected at Kansas University (KU) with a Nikon SMZ-U stereomicroscope. Both microscopes are equipped with cross-polarizer, rotating stage and plane-polarized darkfield illumination at 100x. Precise grain dimension measurements were conducted from digital photomicrographs in order to make precise alpha-ejection corrections. Set (A) was loaded into Nb-tubes and analyzed at the Arizona Radiogenic Helium Dating Laboratory. Set (B) was loaded into Pt-tubes and analyzed in the KU (U-Th-Sm)/He laboratory. Single grains were degassed by laser heating, dissolved and analyzed with ICP-MS to quantify the amount of U, Th and Sm. For a detailed description of the individual lab procedures, the reader is directed to Stockli (2006), Reiners & Nicolescu (2006) and Reiners (2007), respectively.

3.7 Excluding single (U-Th-Sm)/He ages

Table 3-2: Why was which He-age rejected?

sample	cause for excluding
E05-2	re-extract
E05-4	re-extract
E05-5	very high Th; possible auth coating/overgrowth?
E10-3	very high Th; possible auth coating/overgrowth?
E50-1	U content too low
E55-2	U content too low
E65-1	U content too low
E65-2	U content too low
E65-5	U content too low
E70b-1	re-extract
E3-4-2	zircon
E3-4-3	no He measured
E3-5-3	inclusion
RH12-3	zircon
RH23-1	re-extract
RH45-2	re-extract
RH45-4	re-extract
RH60c-1	re-extract
RH65-3	re-extract
RV10b-1	ICP-data bad
RV10b-2	ICP-data bad

Few grains must be rejected from the data set because of lacking uranium or re-extracts on the helium line. An additional method for discovering erroneous ages was proposed by Vermeesch (2008). Plotting helium production rate P versus measured helium concentration for a sample, should result in a straight line going through the origin (see Appendix). All ages that do not plot on that line have too high or too low helium values, which must result from inclusions, helium implantation or wrong Ft corrections and should therefore be rejected. After the careful analysis of the single grain ages (see Appendix), the weighted mean age can be calculated e.g. after Grossman et al. (1983).

3.8   The weighted mean (U-Th-Sm)/He age

The weighted mean is calculated with

$$\tau = \frac{\sum_{i=1}^{n} w_i * x_i}{\sum_{i=1}^{n} w_i}$$

3-1

with

n = number of single grains

x_i = measured age

w_i = weighting of x_i = $1/\sigma^2$

and the respective error is given by

$$\sigma_{\tau}^{2} = \frac{\sum_{i=1}^{n} w_i * (x_i - \tau)^2}{\sum_{i=1}^{n} w_i}$$

3-2

This means that not only the mean age is dependent on the error but also the error of the mean age is dependent on the single grain ages. So if the single grain ages reproduce very well (or if only one grain was dated successfully), the error of the mean age is null. For instance sample E30 has three successfully dated grains which are 6.3 ± 0.4, 6.2 ± 0.4 and 6.5

± 0.4 Ma. The resulting mean age and respective error based on the calculations above is 6.3 ± 0.01 Ma. This is of course much smaller than the error on the ages is in reality.

The opposite is true for ages which do not reproduce nicely, may it be caused by partial resetting of the sample or by reset samples, where only broken grains could be dated. In that case, the error on the mean age will increase tremendously, to values which are geologically meaningless. For example sample E10 has two successfully dated grains, which have ages of 14.6 ± 0.9 and 8.5 ± 0.5 Ma. The mean age is 10.0 ± 7.1 Ma. This would mean that the grains have the same likelihood to have a mean age of 3Ma, as they have to have an age of 10 or 17 Ma. It is easy to see that, based on the single grain ages this sample cannot have cooled below its PRZ at 3 Ma, so the error is enormously overestimated. If anything, the youngest possible time the sample can have cooled below its PRZ would be the youngest age minus its error, which would in this case be at 8 Ma. And this minimum value does not account for the older grains at all. Accordingly, we chose to use an error of 20 % on all the mean ages. This is probably still an overestimation of the "true" error of the grain but much more reasonable.

3.9 Modelling the data

Table 3-3: Modelling results for apatite thermochronology data from the Subalpine Molasse, Switzerland, including the number of totally modelled as well as obtained good and acceptable paths. The higher the good/accurate and the good/created ratio, the easier the modelling of the sample.

sample	good	accurate	created	good/accurate	good/created
E05	100	524	60273	0.19	0.002
E10	51	684	100000	0.07	0.001
E20	100	197	5631	0.51	0.018
E30	101	260	28863	0.39	0.003
E35	372	1333	85385	0.28	0.004
E40	100	632	52404	0.16	0.002
E45	100	225	42249	0.44	0.002
E50	0	86	100000	0.00	0.000
E55	100	715	10666	0.14	0.009
E60	122	315	83040	0.39	0.001
E65	0	288	100000	0.00	0.000
E70b	100	291	10199	0.34	0.010
RH05	10	196	115029	0.05	0.000
RH10	100	167	5807	0.60	0.017
RH12	100	110	3821	0.91	0.026
RH15	100	189	3106	0.53	0.032
RH17	100	477	20354	0.21	0.005
RH23	100	213	3241	0.47	0.031
RH25	100	277	6483	0.36	0.015
RH30a	95	206	100296	0.46	0.001
RH30b	100	179	14180	0.56	0.007
RH35	0	138	100000	0.00	0.000
RH40	100	183	1451	0.55	0.069
RH45	117	324	93215	0.36	0.001
RH50	0	55	100000	0.00	0.000
RH60c	0	115	100000	0.00	0.000

3.10 Heat and fluid flow in the NAFB

Heat flow variations may influence the cooling signal of a sample, and result in an incorrect translation into erosion or tectonic activity. Tectonic activity may itself change the temperature field, resulting in heat patterns which may wrongly be interpreted as variation in heat flow. Fluid flow along thrusts may as well be responsible for locally restricted heating of the adjacent rocks, independent of thrust activity. Therefore a careful assessment of the

origin of a thermal regime and the expected patterns is necessary to discern between different scenarios.

To calculate present-day conductive heat flow densities, the corrected geothermal gradient is multiplied with the rocks' thermal conductivity (Rybach and Bodmer, 1983). The latter is hard to quantify, leading to uncertainties of up to 20 % for heat flow values. However, data density in the NAFB is good, and present-day geothermal gradients are known from various wells in the Molasse Basin (Rybach and Bodmer, 1980; Rybach, 1984; Schegg and Leu, 1998; Schärli and Rybach, 2002). Based on these, a reliable map for present-day heat flow in the Plateau Molasse is available (Nagra, 2002). Generally, the heat flow decreases gradually from north to south within the flat lying part of the Molasse basin (Schärli and Rybach, 2002). For the proximal folded and thrusted basin, data density is too low to construct reliable heat flow density maps.

A study of the present-day geothermal regime of the Molasse Basin along a traverse Basel-Lucerne revealed a notable linear increase of temperature with depth in all investigated deep drillings below 400 m (Rybach and Bodmer, 1980). These authors conclude that below 400m depth, hydrologic effects, which change the temperature gradient, can be excluded. That means that the present-day Molasse basin is in most parts a conductive heat transfer environment. These findings are corroborated by thermal gradients measured in bore holes and several hot springs (Deichmann and Rybach, 1989).

Only in very limited zones, advective heat transfer is probable, which is expressed by high anomalies in the heat flow pattern (Vedova et al., 1995; Nagra, 2002). An interesting observation is that the locations of up-welling of hot water are related to the position of boundary faults of the underlying Permo-Carboniferous troughs. Such zones are only found in the distal parts of the basin and in restricted areas. Thus, no change in heat flow is expected for the proximal part of the basin.

The assessment of the palaeo heat flow plays a paramount role for the correct interpretation of thermochronological ages. This is a major concern, as the palaeo-geothermal field evolves temporally and spatially during Alpine orogenesis and foreland

basin evolution. The palaeo-geotherm at the time of sedimentary deposition is not commonly recoverable, and it is not likely to remain constant throughout denudation (Redfield, 2010). Vitrinite reflectance data provide an independent proxy for palaeo-heat flow. A comprehensive discussion about the palaeo-geothermal gradient and its uncertainties based on published and unpublished VR data is given in Mazurek et al. (2006) and in Cederbom et al. (2011). The authors conclude that the heat flow did not change significantly during the last 10 Ma in the Swiss part of the Molasse and was probably not higher than today. Accordingly, estimates of removed section derived from the cooling ages are minimum values.

Independent evidence for little lateral variations and changes in palaeo-heat flow (at least for part of the study area) are the small age differences between sample E55 and sample MRP 198, which were collected at a distance of 15 km (Figure 3). The central AFT ages are 24.4 ± 3.3 Ma and 26.9 ± 1.2 Ma, respectively, and their agreement within error is in line with the minor variation of present-day heat flow (Schärli and Rybach, 2002). To summarize, this means that both, changes in geothermal gradient and fluid flow seem to have been limited and did not affect the study area significantly.

3.11 Glacial erosion in the NAFB

Glacial activity is an important factor for the Quaternary evolution of the Molasse basin. Originally incised by rivers, the valleys are today over-deepened, witnessing the dramatic overprinting of the foreland morphology by glaciers (Pfiffner et al., 1997b). In the Aare valley of the North Alpine Foreland Basin incision possibly increased by a factor of 10 after the onset of local glaciation (Haeuselmann et al., 2007).

The Aare glacier is comparable to the glaciation at Rigi in terms of ice thickness and surface gradient (Bini et al., 2009). The Entlebuch area was less affected by glaciers (Bini et al., 2009). Glacial overprinting, in turn, results in rapid fluvial erosion. The rivers reshape the over-steepened landscape, rock uplift in these areas accelerates and overall, more mass is removed (Norton et al., 2010a). Similarly, Champagnac et al. (2009) concluded that the Pleistocene to present sediment production, transport and storage strongly depends on the

glacial inheritance of the landscape, resulting in different erosion rates in the glaciated and non-glaciated areas. However, due to dropping base levels in the Holocene, the Entlebuch is currently undergoing incision, thus also affected by increased post-glacial processes. In any case, the post 2 Ma cooling signal may be related to glacial erosion (Valla et al., 2010) and possibly large volumes of sediment have been removed since the Pleistocene, mainly after 0.8-1.0 Ma (Haeuselmann et al., 2007).

For every sample, we evaluated the maximum amount of cooling which may have occurred within the last 2 Ma, using forward modelling with the HeFTy software. It is not possible to explain more than c. 40°C of cooling by glacial erosion, even in those areas affected most strongly by glaciation. This is a maximum value, as we allow for zero lag times of the orogen.

3.12 Calculation of shortening based on thermochronology

For calculating the amount of shortening, the dip angle of the thrust is taken from the cross sections and the depth of the sample is calculated using the geothermal gradient and the minimum temperature, the sample must have reached in the basin Figure 3-2. These input parameters contain errors. First, the dip angle is not always well constrained but may vary within some degree. Second, the thrusts are not planar but steep close to the surface and flat at depth. A change in dip angle of c. 5° results in an error of c. 10 %. Third, the temperature of resetting is ill defined and may vary between 110 °C and 100 °C, depending on annealing kinetics. The best proxy for this is the Dpar value. The standard Durango has a Dpar value of 2.2 μm and anneals completely at c. 110 °C (dependent on cooling velocity). Fitzgerald et al. (2006) use a closure temperature T_c c. 100 °C because they observe small Dpar values ranging between 1.3 and 1.6 μm. Cederbom et al. (2011) assume a T_c of 110 ± 5 °C for Dpar values between 1.5 and 1.8 μm. Despite some exceptions, all apatites in this study have a Dpar value of 1.7 or lower. Accordingly, we use a T_c of 100 °C, if all Dpars are below 1.5 μm, a T_c of 105 °C for values below 1.8 μm and a T_c of 110 °C for all values above 1.8 μm. However, the assumed T_c has only little effect on the shortening estimates (Table 3-4). The top of the PAZ is usually assumed at temperatures of 40 °C. Using a closure temperature of 100 °C and the 30 °C present day geothermal gradient of Rigi (Schegg and Leu, 1998), the resulting displacement on the thrust is 4.4 km. The error introduced by this

uncertainty can also be as big as 10 %. Third, an error is introduced with the geothermal gradient (see discussion above). In sum, shortening varies between 3.7 and 5.0 km for the individual thrusts.

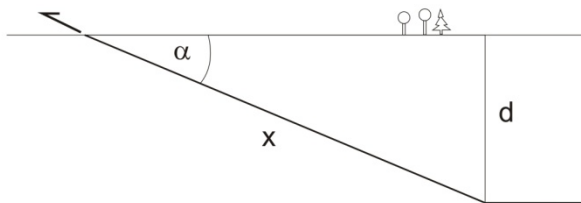**Figure 3-2: amount of throw on thrusts derived from thermochronology**

Figure 3-2 shows a schematic sketch how the throw on the thrust x is calculated. Input parameters are 1) dip of the fault α and 2), depth d from which the sample has been brought from the FT closure temperature to less than 40 °C (i.e. the temperature when the AHe system is not sensitive anymore). d is calculated by using an assumed geothermal gradient. The throw on the thrust is then calculated with:

$$x = d/\sin \alpha \qquad \text{3-3}$$

The dip of the main Rigi thrust is 27° (Hantke, 2006). The steeper dips in the Entlebuch (c. 30°) would decrease shortening estimates.

Table 3-4 shows different calculations for the estimated throw on the thrusts. The 4 km, which we use for assessment of shortening, is a minimum estimate.

Table 3-4: different calculations for amount of thrusting, using geothermal gradients of Rigi and Entlebuch, different closure temperatures and different thrust dips

geotherm	depth top PAZ	Tc AFT system	thrust dip	throw on thrust
30	1.33	100	30	4.00
30	1.33	105	30	4.33
30	1.33	110	30	4.67
30	1.33	100	27	4.41
30	1.33	105	27	4.77
30	1.33	110	27	5.14
28	1.43	100	30	4.29
28	1.43	105	30	4.64
28	1.43	110	30	5.00
28	1.43	100	27	4.72
28	1.43	105	27	5.11
28	1.43	110	27	5.51

4   Critical taper analysis of the Central Alps reveals variations in detachment strength.

von Hagke, C., Oncken, O. submitted to G³

Abstract

Although evidence for very weak detachments underlying foreland thrust belts is growing, very little is known about the lateral variations in effective friction coefficients, as well as the geological nature of such variations. Using critical taper analysis, we show that a detailed and systematic measurement of surface slope of the Central European Alps reveals variations in effective friction coefficients along the décollement, based on the argument that the Alps are at critical state. We show that the basal décollement is very weak close to the deformation front but strong below the more internal units. The transition from effective friction coefficients of the basal décollement of < 0.05 to ≥ 0.4 is related to a switch of the detachment lithology in the sedimentary cover sequences into the metamorphic basement. Very low effective friction coefficient values of < 0.1 and even 0.05 not only occur within evaporites but also within shale sequences in Triassic (west) or Upper Cretaceous/Lower Tertiary units (east) used by the Alpine sole décollement. These very low values found in the shales - comparably low values are reported from other orogens – are caused partly by slightly elevated pore pressures ($\lambda \approx 0.54$) but require additional mechanisms of dynamic weakening.

4.1   Introduction

Recent studies have shown that the basal décollements beneath active thrust wedges may be extremely weak. The strength of such a basal detachment is usually estimated using various strategies based on critical wedge theory (Davis et al., 1983; Dahlen et al., 1984; Dahlen, 1990) as well as from numerical analysis. Several studies have shown that it is possible to estimate the coefficient of basal friction by applying mechanical models of wedges. Davis and von Huene (1987) apply the critical Coulomb wedge model (Dahlen et al., 1984) using the hangingwall fault geometry at the Aleutian Trench and infer a weak detachment, which they ascribed to elevated pore pressure. Schott and Koyi (2001) use an elastic wedge model (Yin, 1993; Mandal et al., 1997) and calculate the coefficient of basal

friction for the Makran and Nankai wedges from fault geometry and material properties and find values of μ_b = 0.16 and 0.2 respectively, which is very low. Recently, Suppe (2007) used the example of the Taiwan wedge and the toe of the Niger delta to show that it is possible to constrain effective friction coefficients of the detachments (detachment strength in his nomenclature) by a simple measurement of surface and detachment slope. Also effective friction coefficient variations along and across strike have been reported from various orogens and analyzed in sandbox and numerical models (e.g. Calassou et al., 1993; Baby et al., 1995; Macedo et al., 1999; Schreurs et al., 2001; Calais et al., 2002; Couzens-Schultz et al., 2003; Bose et al., 2009). These studies focus on a (both, transient or sharp) change from brittle to ductile behaviour but little is known about effective friction coefficient variations within a single brittle detachment. In particular, the regional variability of the low effective friction coefficient values increasingly reported, or their relationship with the detachment lithology remain poorly known. In this study, we closely follow the approach by Suppe (2007) and show that the equations he has derived can be used to reveal effective friction coefficient variations along one single brittle detachment.

The European Alps provide a unique laboratory to investigate variations in effective friction coefficients in a natural system, because of the availability of high-resolution geologic and tectonic maps for the entire orogen. Additionally, various orogen-scale balanced cross sections based on high quality geophysical data provide control on the 3D architecture and the depth of the detachment horizons, their stratigraphic position and lithologies involved (e.g. Schmid et al., 1996; Escher and Beaumont, 1997; Pfiffner et al., 1997a; Burkhard and Sommaruga, 1998a; Schmid et al., 2004; Pfiffner, 2005; Lüschen et al., 2006; Lammerer et al., 2008; Pfiffner, 2010).We chose to concentrate on the central part of the orogen, because along strike variations in deep structure and timing of metamorphic events of this segment are minor (e.g. Pfiffner et al., 1997c; Gebauer, 1999; Thöny, 1999; Schmid and Kissling, 2000; Schmid et al., 2004). This suggests that wedge dynamics did not vary significantly along strike.

4.2 Geological framework

The Central European Alps are the result of the convergence and collision of the African and European plates (e.g. Trümpy, 1960; Frisch, 1979; Stampfli et al., 2001; Schmid et al., 2004). Following southward subduction of the Penninic Ocean, the continents collided at c. 35 Ma, incorporating continental and oceanic fragments of the Penninic domain into the orogenic wedge (e.g. Handy et al., 2010). Ongoing convergence resulted in northward thrusting of the European passive margin (Helvetics) and downward flexing of the European Plate. This entails the formation of the North Alpine Foreland Basin and the subsequent deposition of two regressive cycles of marine and fresh water sediments (e.g. Pfiffner, 1986; Sinclair and Allen, 1992; Schlunegger et al., 1997a; Sinclair, 1997b; Berger et al., 2005b; Willett and Schlunegger, 2010). The southern part of the foreland basin was folded and thrusted shortly after deposition, and today forms the Subalpine Molasse (Homewood et al., 1986). After c. 15 Ma, folding of the Jura Mountains started, which forms now, together with the North Alpine Foreland Basin, the most external part of the Alpine chain (e.g. Burkhard, 1990; Burkhard and Sommaruga, 1998a). Shortening within the Subalpine Molasse and Jura Mountains is transferred southwards to below the External Massifs (Pfiffner et al., 1997d). The latter consist of accreted European basement now overlying the recent Alpine basal décollement, and today form the northern drainage divide of the Central Alps (Figure 4-1). Uplift of the External Massifs commenced around 13 Ma, underlining the common kinematic coupling with the external thrust systems (Fügenschuh and Schmid, 2003), (Figure 4-1B). This kinematic link via a common detachment allows us to consider the entire suite of tectonic units from the External Massifs through the Subalpine Molasse and Jura Mountains as part of a single orogenic wedge.

Critical taper theory predicts that a wedge will evolve towards force equilibrium (the critical state) characterized by being at the verge of failure internally and at the base. Force equilibrium means that the detachment parallel component of gravitational body force and the resulting overburden pressure together with the basal shear traction equal the compressive push (Davis et al., 1983). Hence, a central requirement of the wedge theory is that the system is actively converging, which we will discuss below. Equilibrium is reflected by a wedge with a stable surface taper (α) and detachment dip (β) over time (Davis et al., 1983; Dahlen, 1984; Dahlen et al., 1984). Critical wedges react instantaneously to changes in

stress regime. For instance the Taiwan fold and thrust belt, which serves as a classic example for a critical wedge, has been shown to react with internal deformation only because of air pressure lowering due to seasonal typhoons (Liu et al., 2009). However, on longer time scales orogens react with a certain response time to perturbations, which is dependent on post-perturbation erosion efficiency but also on wedge size and convergence velocity (Whipple and Meade, 2006; Whipple, 2009). For the European Alps the response time was estimated to be c. 5.5 Ma, which implies that short term perturbations such as the Pleistocene glaciations will not affect orogen-scale wedge dynamics (Tomkin and Roe, 2007).

The Alps provide an exceptional data set to infer that they are at the verge of failure: in addition to natural phenomena like erosion, the human impact and resulting disturbances of the stress field is abundant and distributed across the entire mountain range (Figure 4-2). In many regions of the Alps, water reservoir impoundment induced seismic activity. Famous examples in the Central and Western Alps are Monteynard, France, where an earthquake of magnitude M_L 4.9 was triggered shortly after filling a reservoir (Rothé, 1970; Gupta et al., 1972), the Lake of Salanfe, Switzerland, where abnormally high seismicity after reservoir filling triggered thermal springs at a distance of c. 15 km (Bianchetti et al., 1992), or the Verzasca Dam, Switzerland, where several hundred local earthquakes occurred after filling (Süsstrunk, 1968; Gupta et al., 1972). A few events have been attributed to the Swiss dams of Linth-Limmern and Lac Hongrin (Fäh et al., 2011). Drilling of the Gotthard Base Tunnel in the Central Alps triggered a series of 112 earthquakes with a maximum magnitude of M_L 2.4 (Husen et al., 2012). Fluid injection in a geothermal drilling in Basel stimulated several earthquakes in 2006 and 2007 with a maximum magnitude of M_L 3.4 (Häring et al., 2008; Deichmann and Ernst, 2009; Ripperger et al., 2009; Bachmann et al., 2011). In addition, rainfall and resulting variations in water table caused seismic activity in the Central Alps. Deichmann et al. (2006) and Husen et al. (2007) show that a heavy rainfall event in 2005 caused abnormally high seismicity and Roth (1992) sees a correlation between intense precipitation coupled with seasonal snow melt and shallow seismicity in the eastern Swiss Alps. In addition to these transient effects, seismicity in the Central Alps and their north-western foreland is well distributed (Figure 4-2). Moreover, the fan shape of the maximum horizontal stresses perpendicular to the Alpine arc exhibits an identical, strike-slip dominated, kinematic pattern within the orogen as well as in its foreland.
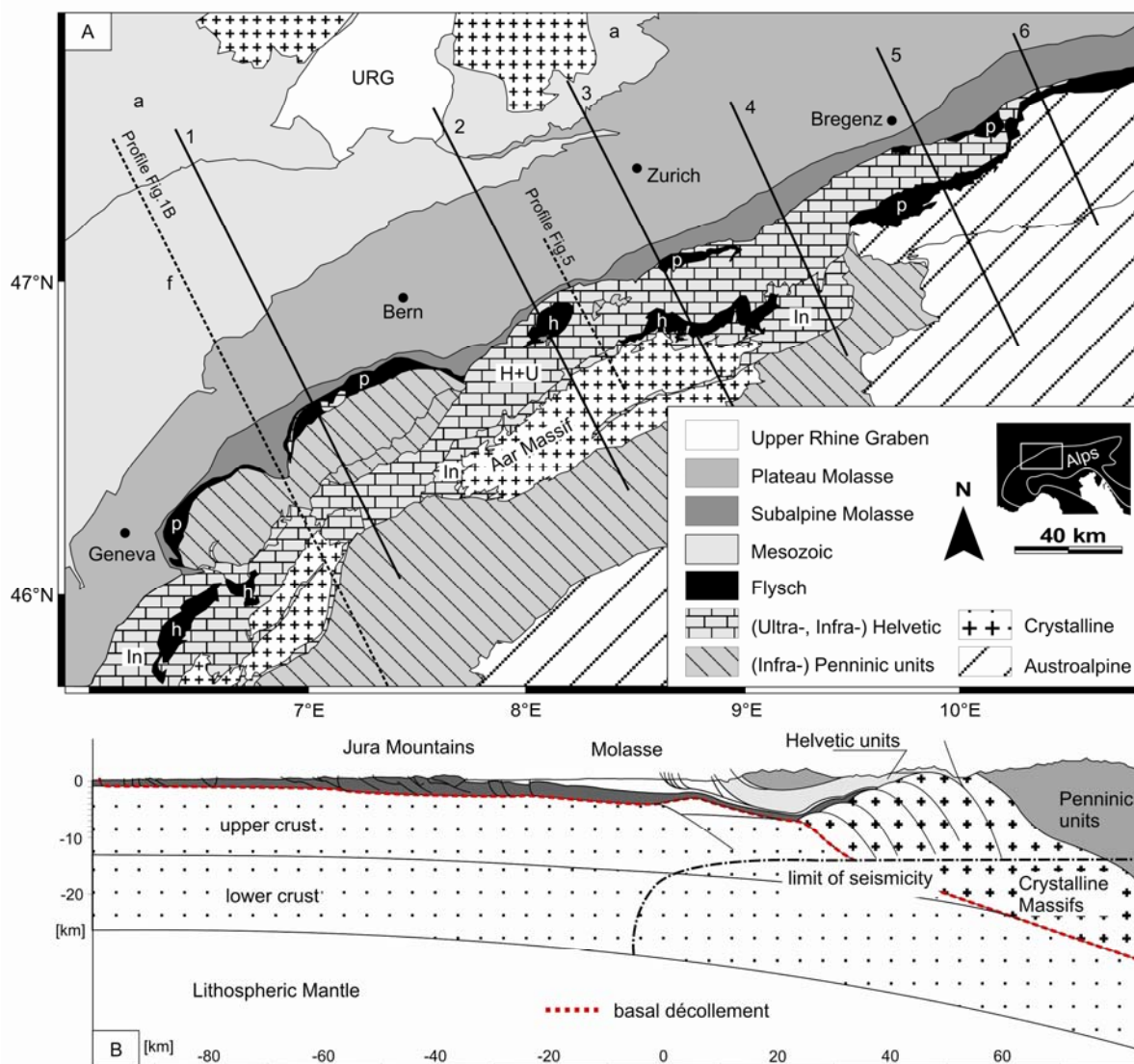
Figure 4-1A: Tectonic map of the Northern Central Alps and the adjacent foreland based on Spicher (1980). URG – Upper Rhine Graben, a – autochthonous Jura, f – folded Jura, p – Penninic Flysch, h – Helvetic Flysch, H – Helvetics, U – Ultrahelvetics, In – Infrahelvetics, – traces of analyzed profiles indicated by black lines. Note the crystalline bodies within the Alps, the External Massifs (including the Aar Massif). Figure 4-1B is a cross section through the Central Alps, modified after Burkhard and Sommaruga (1998a), showing all major tectonic units. The origin of the x-axis is located at the northernmost thrust of the Subalpine Molasse. The limit of seismicity coinciding with the 300-350 °C isotherm is based on Okaya et al. (1996). In red the basal décollement is indicated.

That the system is actively deforming also on longer time scales is indicated by active fault scarps in Eastern Switzerland, which were probably active already in pre-glacial times (Persaud and Pfiffner, 2004). In summary, this suggests that the Central Alps are close to failure equilibrium.

To apply critical taper theory, i.e. to accommodate the assumption of force equilibrium, the basal detachment must also be at the verge of failure. This appears probable, as the foreland is seismically active above and below the detachment horizon (Fäh et al., 2011). In addition, the maximum horizontal stress (S_H) above and below the detachment is identical within statistical error (Heidbach, 2012, personal communication based on Deichmann and Marschall, 2002; Kastrup et al., 2004; Valley and Evans, 2009; Deichmann, 2010). In the eastern Central Alps, neo-tectonic activity shows that the basal detachment is still active (Persaud and Pfiffner, 2004). In the western Alps Mosar (1999) has argued for a newly developing mid crustal detachment underneath the Molasse Basin (see also Lacombe and Mouthereau, 2002) and a change from thin- to thick-skinned tectonics in the Jura Mountains (Giamboni et al., 2004; Ustaszewski et al., 2005; Ustaszewski and Schmid, 2006; Madritsch et al., 2008; Madritsch et al., 2010). However, this mid-crustal décollement is only incipient and has probably not yet developed into a through-going tabular fault able to modify and control surface taper (Mosar, 1999). We therefore do not consider it to be in force equilibrium yet and therefore largely irrelevant for present-day wedge dynamics.
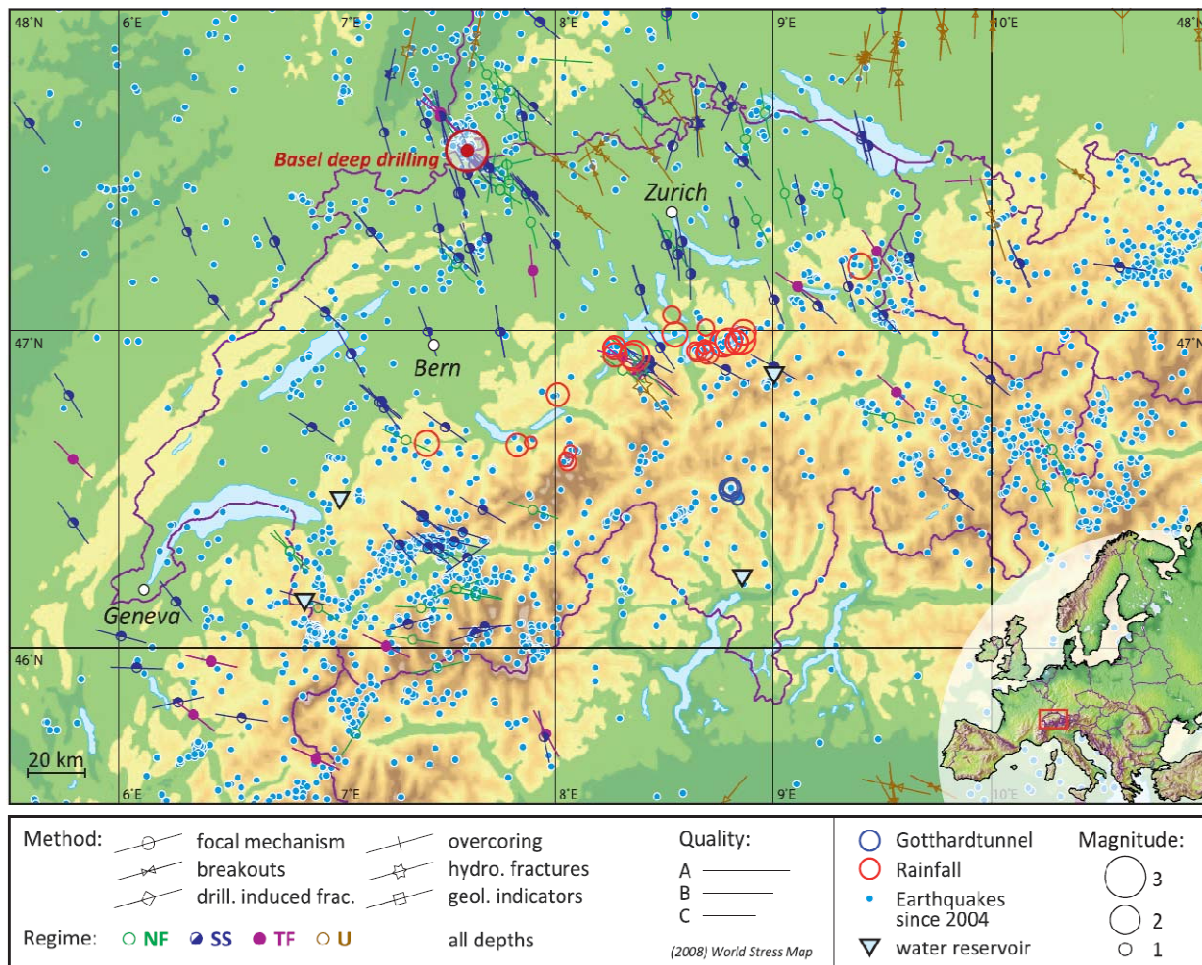
Figure 4-2: Seismic activity in the Central Alps is distributed all over the orogen. For optical clarity, we chose the arbitrary interval from 2004 to 2009 from the SED catalogue (Fäh et al., 2011). The dots represent the respective epicentres, not magnitude. Seismic events triggered by human impact are indicated, the stress indicators are taken from the World Stress Map (Heidbach et al., 2008). See text for further explanations.

To maintain critical taper ($\alpha + \beta$), the amount of denudation (i.e. the decrease in $\alpha + \beta$) must be balanced by accretionary flux. To quantify this amount of shortening, we use a simple 2D area balancing approach. Champagnac et al. (2009) model preset day denudation rates [mm/a] along a cross section in the Central Alps based on the data from Wittmann et al. (2007) and Norton et al. (2008). We use these predicted denudation rates at every knick point along our respective topographic section (profile 2) and can calculate the area A, which is representative for denudation per year along this profile (Figure 4-3).We will discuss below how we come to the representative topography (and consequently α). We then feed the area A back into the section to calculate shortening per year S. This is the height of the trapezoid that is defined by the area A, one of the parallel sides c, which is the depth to detachment and the two adjacent angles, which are 90° + surface slope α_s and 90° +

detachment dip β_s (Figure 4-3). The height of a trapezoid is defined as *S = 2A / (a + c)*, where *a* in our case is given by *a = c + S* (tan α_s + tan β_s)*. We can hence write

$$2A = S\left(2c + S(\tan\alpha_s + \tan\beta_s)\right)$$
(4-1)

which reformulates into

$$S^2(\tan\alpha_s + \tan\beta_s) + 2Sc - 2A = 0$$
(4-2)

and hence

$$S = \frac{-2c + \sqrt{4c^2 + 8A(\tan\alpha_s + \tan\beta_s)}}{2(\tan\alpha_s + \tan\beta_s)}$$
(4-3)

where *c* denotes the depth to detachment (18 km, Pfiffner (2010)) and α_s and β_s denote the surface slope and detachment dip at the rear of the wedge. Using the topographic slope of 1° and a detachment slope of 22°, the present day shortening rate required to maintain critical taper is then 1.9 mm/a. Note that the shortening rate estimate is mainly dependent on *c*; changes in α_s and β_s hardly change the results. However, this calculation is valid only for the orogen being exactly at critical state and only includes the northern flank of the orogen. As shortening-related uplift may not replace the entire eroded material, this is a maximum value. If, for instance, only 80 % of the eroded area were accommodated by deformation, only 1.5 mm/a of shortening are required. A lower limit for shortening might be < 1 mm/a, which was calculated by Champagnac et al. (2009) for the entire Central Alps cross section from rotation of the Adriatic plate around an Euler pole located in the Po Basin. These values range below the resolution of continuous GPS measurements and would therefore escape detection by geodetic methods. Also, note that these calculations are independent of surface uplift, as they only depend on maintaining the critical taper $\alpha + \beta$. In any case, from ongoing shortening along the Alpine basal décollement, we conclude that the basal décollement is close to the verge of failure, too.
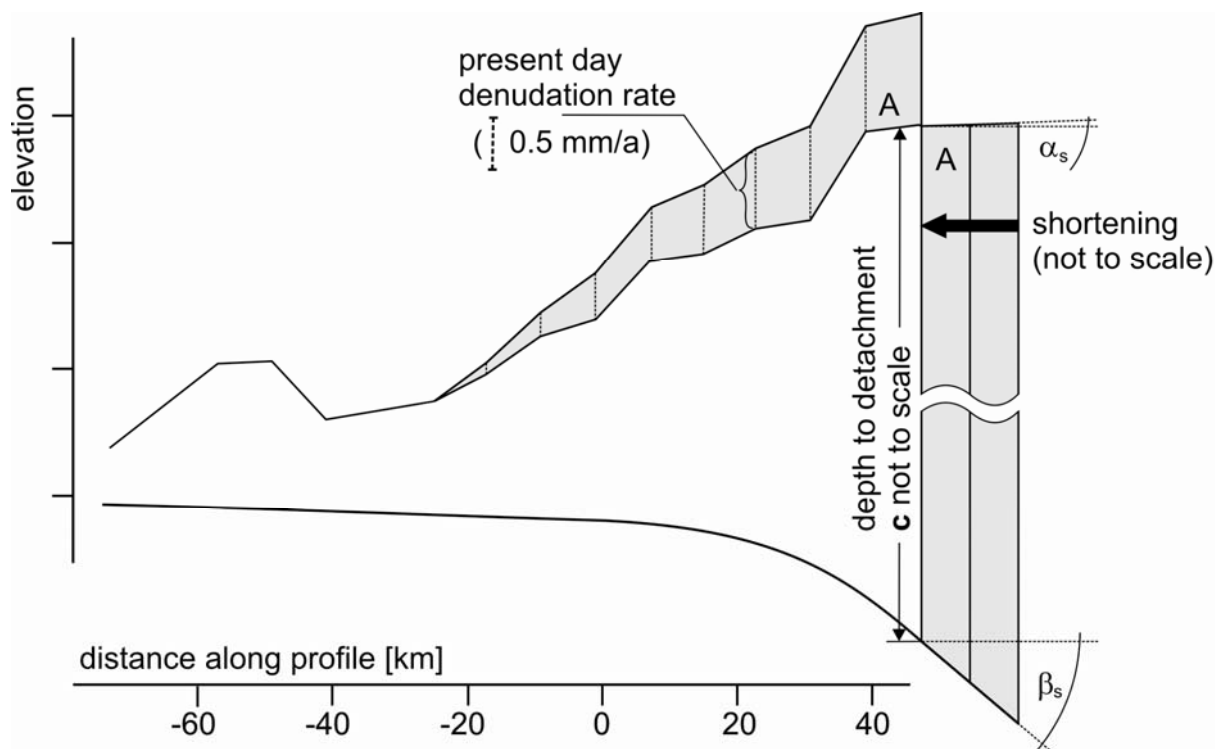
Figure 4-3: Area balancing to estimate the amount of shortening along profile 2 (Figure 4-1 and Figure 4-4). The denudation rate values are taken from Champagnac (2009). To maintain critical taper, the denuded area A is the sum of the small trapezoids determined for every surface slope bin and must be equal to the area fed back into the cross section by accretionary flux.

4.3   Critical taper analysis

In the case of a mechanically homogenous wedge, the critical taper equation using the small angle approximation of Dahlen (1990) is

$$(\alpha + \beta) \approx \frac{(1 - \rho_f/\rho)\beta + \mu_b(1 - \lambda_b) + S_b/\rho g H}{(1 - \rho_f/\rho) + 2(1 - \lambda)\left(\frac{sin\phi}{1 - sin\phi}\right) + C/\rho g H} \tag{4-4}$$

Where ρ_f is the density of the fluid above the wedge (water or air), ρ is the mean density of rock, μ_b is the basal friction coefficient, λ_b is the pore fluid pressure at the base, S_b is basal cohesion, C is compressive wedge strength, ϕ is the angle of internal friction and H is wedge thickness. In simple terms, the critical taper angle ($\alpha + \beta$) is dependent on the ratio of basal fault strength and wedge internal strength. Suppe (2007) collects all wedge-strength terms as

$$W = 2(1 - \lambda)[sin\phi / (1 - sin\phi)] + C/\rho gH \qquad \text{(4-5)}$$

This is equal to the normalized differential stress at failure (Dahlen, 1990; Suppe, 2007)

$$W = (\sigma_1 - \sigma_2)/\rho gH \qquad \text{(4-6)}$$

This is a dimensionless parameter, which is useful because it assesses the wedge strength independent of the amount of overburden. It is giving a measure of horizontal to vertical stress at failure.

Furthermore, Suppe (2007) collects all fault strength terms as

$$F = \mu_b(1 - \lambda_b) + S_b/\rho gH \qquad \text{(4-7)}$$

This is the normalized basal shear traction at failure of the detachment (Dahlen, 1990; Suppe, 2007)

$$F = \sigma_\tau/\rho gH \qquad \text{(4-8)}$$

As F is (analogous to W) dimensionless and a function of μ_b, we term it effective coefficient of friction in the following.

Suppe (2007)reformulates the critical taper equation (4-4) with (4-5) and (4-7) into

$$\alpha + \beta = \frac{\beta(1 - \rho_f/\rho) + F}{(1 - \rho_f/\rho) + W} \qquad \text{(4-9)}$$

and after some algebra to

$$F = \alpha(1 - \rho_f/\rho) + (\alpha + \beta)W \qquad \text{(4-10)}$$

As the Central Alps are a subaerial wedge, ρ_f / ρ (air density over rock density) will be negligible and we can substitute $(1- \rho_f / \rho) \cong 1$ (Suppe, 2007) and can write for the Central Alps

$$F = \alpha + (\alpha + \beta)W \qquad \text{(4-11)}$$

Equation (4-11) yields all possible pairs of F and W that satisfy critical taper theory. This is a linear equation, whose (positive) slope is the critical taper ($\alpha + \beta$) and whose intercept is the surface slope. This allows us to calculate the basal detachment strength only from determination of α and β, under the assumption of the finite wedge strength parameter W (Suppe, 2007).

4.4   The Central Alpine critical wedge

For our analysis of the Central Alps, we use a variable, systematically determined topographic slope α and corresponding variable detachment dip β. We determined α and β along six profiles, reaching from the undeformed foreland basin to beyond the drainage divide within the orogen, thus covering the whole pro-wedge of the Central Alps (Figure 4-1). It is noteworthy that the results of this analysis are only valid for this part of the orogen (i.e. between the six profiles), where force balance is required. Criticality of the pro-wedge is independent of criticality of the retro-wedge, which might as well be at stable or super-critical state (e.g. Graveleau et al., 2012). It is not possible to extrapolate them for instance to the Western or Eastern Alps without further in depth analysis. The analysis we perform is also only valid for the present day wedge geometry.

We took β from published crustal scale profiles (Schmid et al., 1996; Pfiffner, 2010) (Figure 4-4), which are based on reflection seismic data or have adjacent balanced cross sections. We measured the corresponding α from topographic swath profiles based on the SRTM 3-arc second digital elevation model. Each swath has a width of c. 15 km. We defined one representative α for segments of 7.5 km length along the profiles. We determined this value empirically. It is the best fit that represents variations in α but smoothes out topographic effects caused by recent glacial erosion (Figure 4-4). To account for effects of peak uplift in

response to glacial relief production we used the 95th percentile of the topographic data. Additionally, this value is still big enough so that local particularities will average out. We assume mechanical homogeneity for each segment.

Figure 4-4 shows the results of the topographic analysis for the six profiles. The origin of the horizontal axis in all plots is located at the surface expression of the most external thrust within the Subalpine Molasse. The depth to the underlying detachment is not to scale. Profiles 1-3 reach from the Jura Mountains in the north to the External Massifs in the south. South of the topographic step at the southern fringe of the Jura Mountains, the topography rises quite steadily from the Molasse to the south of the Helvetic units (coloured in green). As most obvious in profiles 2 and 3, α decreases thereafter in the basement units. Note the deeply incised Rhone Valley in profile 1. In the south of Profiles 4-6, Helvetic and Austroalpine nappes still cover the crystalline basement. A similar pattern as observed in profiles 1-3 emerges but the decrease in α appears to be less abrupt.

To calculate the effective coefficient of friction of the décollement F with the retrieved α- and their corresponding β-values according to equation (4-11), we need to constrain the wedge internal strength parameter W. For a cohesionless dry sand wedge as used in analogue experiments, the internal friction $tan\,\Phi$ is c. 0.58 (Davis et al., 1983; Suppe, 2007), which corresponds to a wedge strength parameter of 1.9 (Suppe, 2007). Using a maximum value of 0.85 for crustal strength according to Byerlee's law (Byerlee, 1978) and hydrostatic conditions (λ = 0.4) which preferentially persist in continental crust to depths of as much as 12 km (Townend and Zoback, 2000; Zoback and Townend, 2001) and are measured in drillings in the Molasse until depths close to the basal detachment (Müller et al., 1988), the maximum plausible value for W is 2.2 (Suppe, 2007). However, a more applicable value for European basement might be taken from the German KTB deep drilling (Brudy et al., 1997), where the corresponding W is 1.0 ± 0.2 (Suppe, 2007).
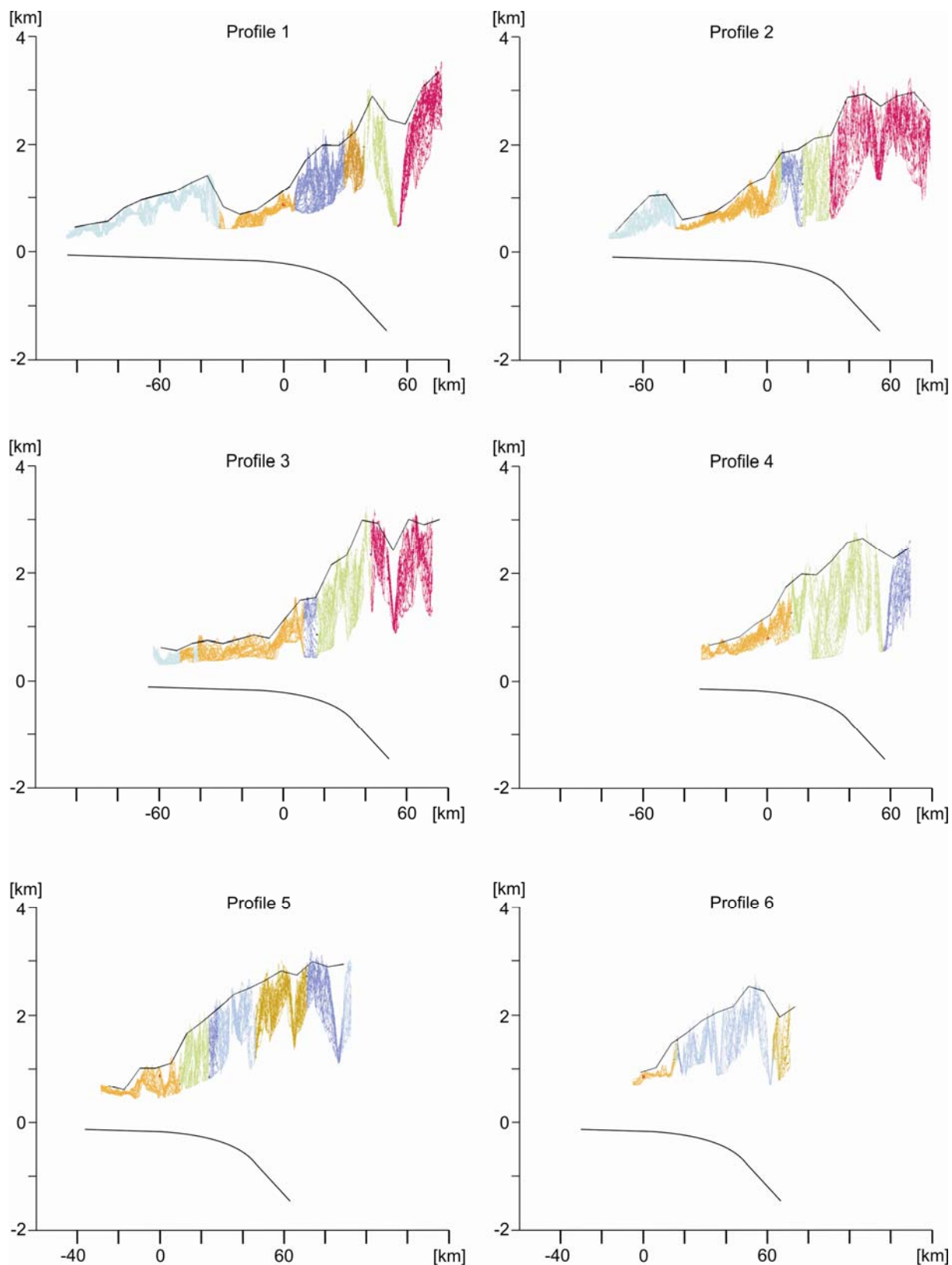
Figure 4-4: Swath profiles of the six cross sections. See Figure 1 for location. Colours represent different geological units of the single profiles within the swath. Light blue = Jura Mountains, yellow = Alps, lavender = Penninic, brown = Ultra-Helvetic, green = Helvetic, red = External Massifs. For profiles 5 & 6: powder-blue = Austroalpine and gold = Silvretta units. Black lines show the binning of the swath, which we used for α determination. Note the good fit, which is only slightly perturbed by major glacial valleys.

Figure 4-5 shows the results of the calculations of F along the six investigated profiles (Figure 4-1, Figure 4-4). The origin of the x-axis is (in analogy to Figure 4-4) located at the most external thrust of the Subalpine Molasse. In plot A we use a uniform wedge strength parameter of $W = 1.0$. The striking result is that a significant increase in F from north to south along all profiles is required. In the frontal part of the wedge, the values of effective basal friction are below 0.2, which is very low. The negative F-values in profile 1 result from the negative α-values at the southern fringe of the Jura Mountains. An increase in detachment strength occurs south of the Subalpine Molasse and eventually the values seem to reach a plateau at basal friction coefficients around 0.4 to 0.5.

However, variations of the wedge-internal strength parameter are likely to occur because of lithological differences, different degrees of compaction, lithification or metamorphic overprint or different porosities and fluid pressures. Generally, W is predicted to increase towards more internal units through an increase in cohesion (Fletcher, 1989; Dahlen, 1990; Suppe, 2007; Buiter, 2012). In the case of the Central Alps, it is therefore reasonable to assume a lower W for the more external parts where it is composed of sedimentary rocks (as opposed to the more internal crystalline massifs). The sedimentary western Taiwan wedge has a value of $W = 0.6$ (Suppe, 2007), - a value also found in wells drilling sedimentary sequences (Zoback and Townend, 2001) - which we use to test the influence of variations in wedge strength parameter. Plot B of Figure 4-5 shows that with variable W, the difference in effective friction coefficient F between the frontal and the back part of the wedge is slightly more pronounced. Thus, the general pattern of a strong internal detachment and a weak external detachment is a robust feature, independent of how well constrained our assumptions of W are. Our topographic analysis (Figure 4-4) provides independent support for increased W in the inner part of the orogen. The observed decrease in α in the internal units at constant β results in a decrease of taper, which is clear evidence for wedge strength increase (Zhao et al., 1986; Fletcher, 1989).
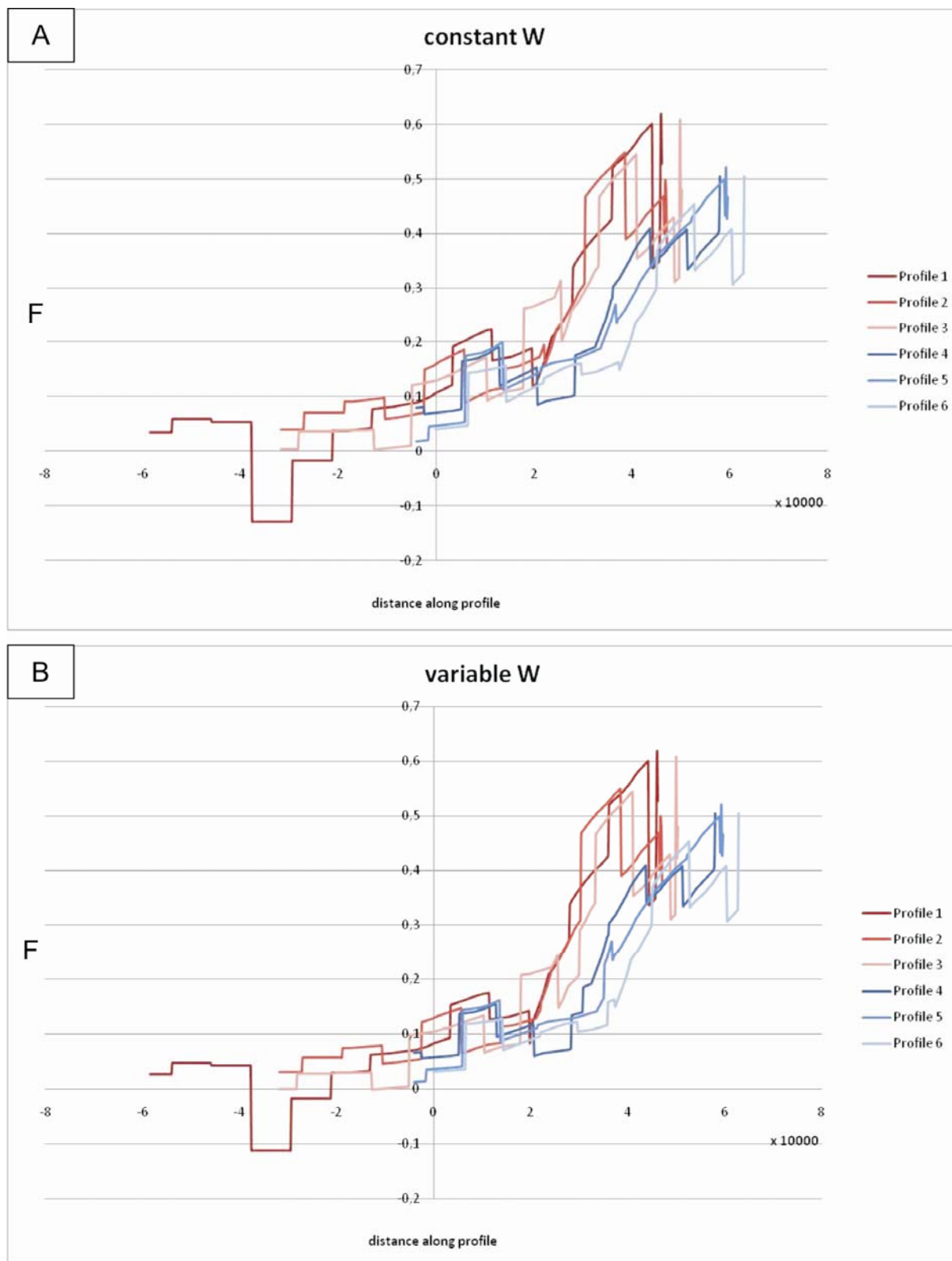
Figure 4-5: F-W plots of all six profiles. Origin of the x-axis is the surface expression of the most external thrust within the Subalpine Molasse. In panel A, W is set to 1 for all calculations. In panel B, W is 0.6 for the parts of the wedge which are composed of sedimentary rocks (the northern part of the wedge, until c. 20 km south of the x-axis origin in all profiles).

Since glacial erosion may have affected α and the state of wedge criticality, we next explore its potential influence quantitatively. Increased erosion might have lowered α (or β if the erosion would be fully compensated by isostasy, as suggested by Wittmann et al. (2007)) and consequently the wedge might have been pushed from critical into the sub-critical state. At present day, the difference of erosion rate between the high crystalline Alps and the foreland is 0.63 ± 0.16 mm/a, which is probably a long-term feature (Wittmann et al., 2007). The distance between the surface expression of the most external thrust within the Subalpine Molasse and the drainage divide is c. 50 ± 5 km (Figure 4-4). This results in a reduction of the critical taper of 0.72 ± 0.25 °/Ma (using small angle approximation, which gives a maximum value). This in turn results in reduction of F of 0.013 ± 0.004 Ma^{-1}. This is negligible for our analysis as it is well within the margin of uncertainty and lower than the observed short-distance variations (Figure 4-5).
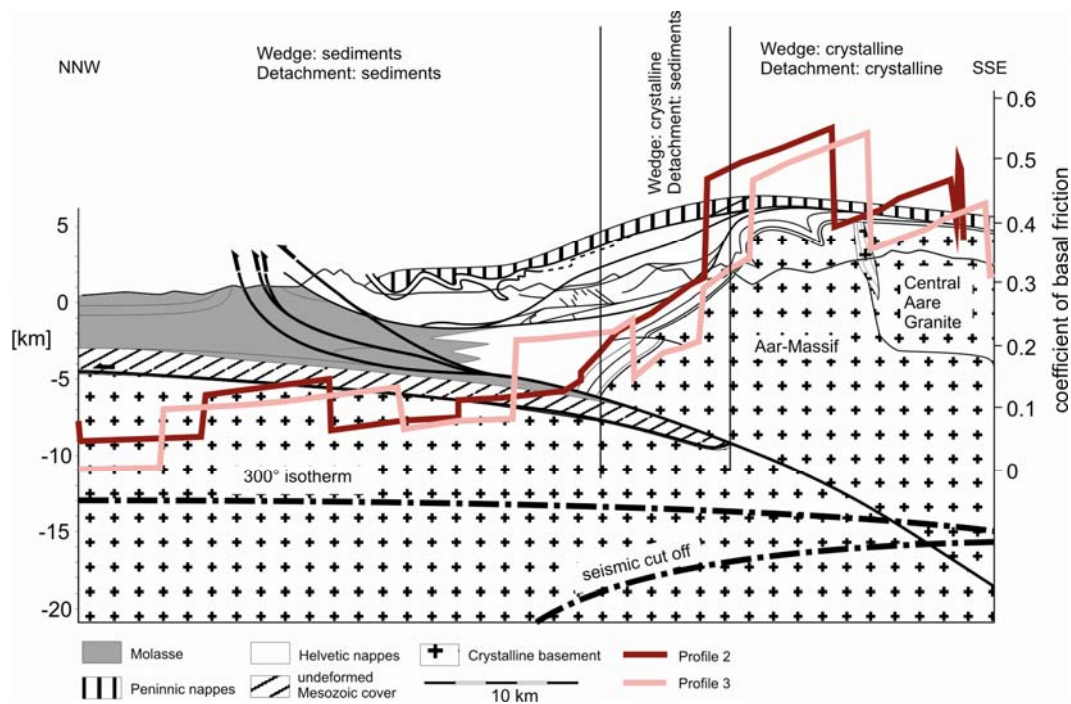
Figure 4-6: Geological cross section through the Central Alps modified after Pfiffner (2010). For exact location, see Figure 4-1. The overlay is the result of the adjacent swath profiles. Note the strong dependence of detachment strength on wedge and fault geology. In the frontal part, where sediments slide over sediments, the fault strength is very low. The deduced increase in detachment strength coincides with the area where crystalline basement successively over-thrusts sedimentary units. Where the detachment runs exclusively through crystalline rocks, fault strength is ± constant and comparatively high.

4.5   Correlation of wedge mechanics and observed geology

We next investigate the relationship between inferred F-values and lithology. Figure 4-6 shows a cross section through the central part of the study area (modified after Pfiffner, 2010) and the two adjacent analyzed profiles 2 and 3. The area of very low basal friction (< 0.2) coincides with the area where the detachment is cutting through sedimentary rocks and the overlying wedge likewise consists of sediments. The rapid increase in basal friction occurs in the part of the wedge, where metamorphic basement at the tip of the hangingwall ramp is sliding on top of sedimentary rocks forming the footwall flat. Southwards, a surprisingly exact correlation between the area where the detachment cuts through metamorphic basement down to the footwall ramp and the "plateau" of high values of basal friction (between 0.4 and 0.5) becomes obvious. Independent support for this scenario is given by calculations of the present day stress field within the North Alpine Foreland Basin (Figure 4-2), where the observed pattern requires a strong detachment within the orogen and a weak detachment in the foreland (Heidbach, personal communication 2012). In the area south of the Massifs, the basal friction does not seem to increase anymore. However, this may also be an artefact of a change from brittle to ductile conditions, which occurs on the footwall ramp approximately at a depth of 15 km (Figure 4-1B), the present day cut-off of crustal seismicity (Okaya et al., 1996) and depth range of the 300-350 °C isotherm.

The link to lithology also becomes obvious when looking at the data in map view (Figure 4-7). As expected from previous studies (e.g. Philippe, 1994; Letouzey et al., 1995; Sommaruga, 1999), the friction values are lowest (< 0.05) below the Jura Mountains and the western Plateau Molasse, where the detachment is running in Triassic evaporites. These salt deposits pinch out towards east and south (Philippe, 1994; Sommaruga, 1999). In the central part of the study area, the massive salt deposits are lacking (Figure 4-7), but at the detachment depth, intercalations of anhydrite and shales are reported from the Entlebuch deep drilling (Vollmayr and Wendt, 1987). These shale-sulphate multi-layers may also become exceedingly weak (Jordan and Nüesch, 1989). The southward continuation of this inter-layering is not fully known, but the Triassic sequence in the hangingwall cover of the Aar Massif does not show any evaporite remnants apart from some cargneule with a thickness of less than 2 m (Krayenbuhl and Steck, 2009). This suggests a south- to south-eastward disappearance of evaporites and a predominance of shales, marls and limestones

at the detachment level. The Triassic sequences further to the southwest (external Massifs in the French Alps) contain more abundant remnants of cargneule and evaporites.
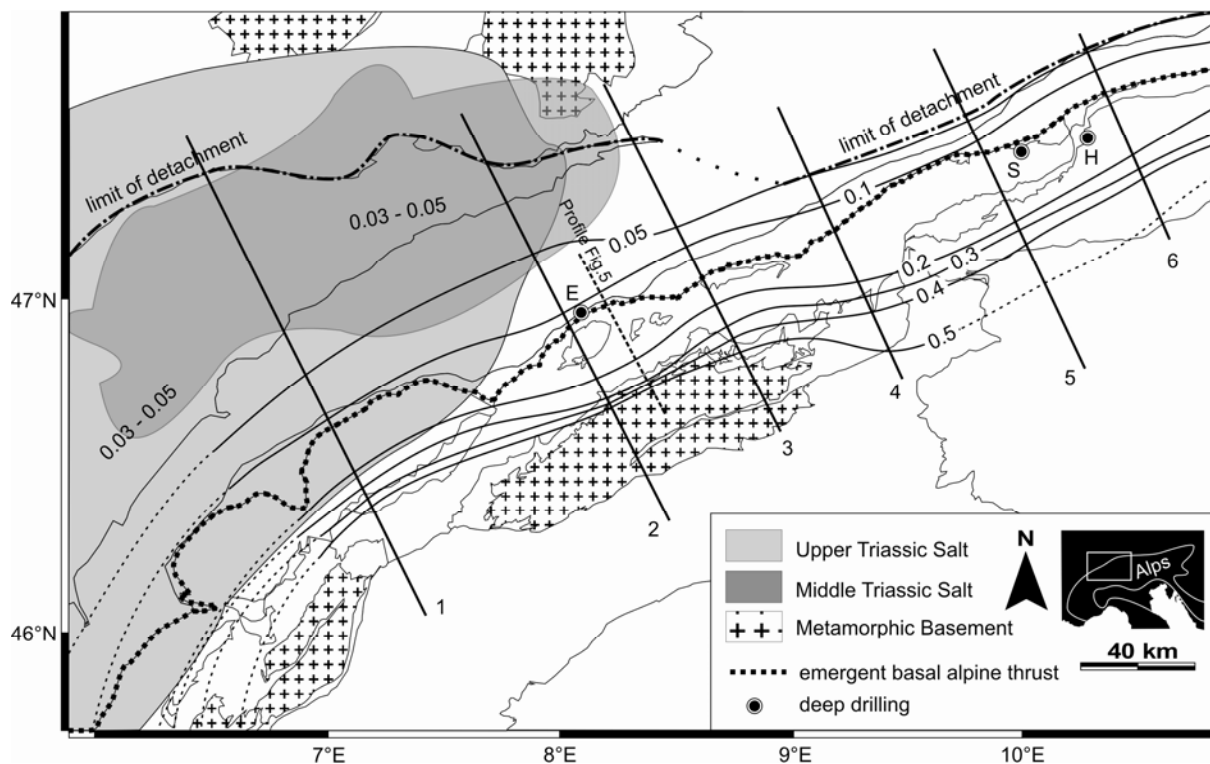

Figure 4-7: Map of basal detachment strength. Where the detachment is running through the salt deposits, the strength is lowest (< 0.05), as is known from previous studies. Note the rapid increase in detachment strength at the front of the External Crystalline Massifs. Limit of the detachment taken from Spicher (1980). The transition between Jura and the eastern Subalpine Molasse is only poorly constrained. Salt distribution is taken from Philippe et al. (1996). Black lines are the profile traces as in figure 4-1A.

In the eastern part of the study area, where the detachment rises stratigraphically to separate Upper Cretaceous/Tertiary pelites in the footwall and Triassic marls in the hangingwall (e.g. Bachmann and Müller, 1981; Auer and Eisbacher, 2003; Berge and Veal, 2005), the values, surprisingly, are comparably low (c. 0.1). These very low effective coefficients of basal friction independent of the existence of evaporites are also reported from the Makran and the Nankai wedge (Schott and Koyi, 2001) or from Taiwan (Suppe, 2007). They are much lower than values obtained in laboratory experiments (Byerlee, 1978). Yet, they clearly demonstrate that a shale-dominated sequence may exhibit extremely low effective coefficients of friction. While this is generally attributed to high pore fluid pressures in such sequences, Suppe (2007) notes that no excess pore pressures were found in a well drilling the Taiwan detachment. In the eastern part of our study area, slightly elevated pore

fluid pressures are reported from the deep drillings Sulzberg-1 and Hindelang-1 (Müller et al., 1988). The Sulzberg-1 drilling reaches the basement and penetrates the basal thrust at a depth of 4280 m below surface, after drilling exclusively through Molasse sediments (Herrmann et al., 1985). At detachment depth, the pore fluid pressure is c. 570 bar (Müller et al., 1988) rising from a near hydrostatic pressure gradient in the hangingwall to an elevated gradient of 2-2.4 bar/10m approaching the detachment. Using typical values for the density of the Molasse sediments of 2.5 g/cm³ (e.g. Schärli and Rybach, 2002), the corresponding lithostatic pressure is 1070 bar. This results in a λ-value of 0.53, which is only slightly higher than hydrostatic (0.4) and far less than lithostatic. The drilling Hindelang-1 does not reach the basement or the basal detachment but includes the Helvetic detachment – the detachment formed prior to the current Alpine sole décollement. The pore fluid pressure again rises towards this level and reaches c. 740 bar (Müller et al., 1988). Using typical density values for limestone of 2.7 g/cm³ dominating the hangingwall, the corresponding lithostatic pressure is 1375 bar, and λ is 0.53. Hence, elevated pore pressures in shale-dominated lithologies may contribute to the low detachment strength, but are insufficient to explain the very low values observed. Therefore, either excess pore pressures may be a transient feature only during seismic rupture or a rapid creep event or other ill-defined aspects related to dynamic weakening in shales play a key role.

4.6   Summary and conclusions

In this study we extended the wedge mechanical approach by Suppe (2007) and showed that it is possible to detect variations in effective coefficient of friction of the basal décollement from detailed analysis of wedge geometry. We proposed a way to obtain surface slope values, for which so far no standardized method is used. We applied this theoretical approach to the Central Alps and found the detachment in the frontal part of the wedge to have an effective coefficient of basal friction of below 0.2 (in shale-dominated sediments) or even below 0.1 (evaporites). Fluids are only mildly over-pressured, insufficient to explain the very low values. In contrast, we found that in more internal units (metamorphic basement under brittle conditions), a comparatively high coefficient of basal friction of between 0.4 and 0.5 is required. These observations corroborate a lithological control of F along the

detachment. The method described here is a powerful approach to gain further insights on wedge kinematics and to map detachment characteristics.

4.7 Acknowledgements

5 Have the Central Alps been in tectonic steady state since 10 Ma? Results from low temperature thermochronology and critical wedge considerations

In preparation for submission to the Swiss Journal of Geosciences

von Hagke, C., Oncken, O., Ortner, H., Cederbom, C.E., Aichholzer, S.

Abstract

In the European Alps, Late Neogene tectonic activity has been reported but the responsible mechanism is still debated. Here we present new apatite fission track and apatite (U-Th)/He data from the Alpine orogenic front, the Subalpine Molasse. We show that the cooling signal reported from the Swiss part of the basin since 10 Ma is also present farther east and hence independent of thrusting within the Jura Mountains. By reconstructing the Alpine wedge at 10 Ma, we show that the taper of the Central Alps has not varied significantly and presumably remained at or close to the critical state since then. The present day shortening rate ranges between 1.0 and 2.0 mm/a and has been constant since at least the Late Miocene. This is interpreted to indicate that the Central Alps have been at kinematic steady state since 10 Ma. In conjunction with the observations of repeated out-of-sequence thrusting in the Subalpine Molasse, the static deformation front, constant shortening and erosion rates and the constant taper, we argue that the mass flux is also at steady-state and that climate events therefore have not influenced wedge stability and kinematics on the northern flank of the orogen during the last 10 Ma.

5.1 Introduction

Although the foreland basin of the European Alps is one of the most studied foreland basins in the world, our understanding of its late Miocene to present tectonic history is incomplete, mostly because sediments of that time have been eroded away (Cederbom et al., 2004). The same holds true for the kinematic history of the orogenic front, since reconstruction of the latter usually hinges on foreland deposits. Recently, several studies have attempted to resolve this late stage development, aiming at understanding the reported erosion signal and the imprint of climate change before and up to the Pliocene-Pleistocene boundary

(Cederbom et al., 2004; Cederbom et al., 2008; Ortner et al., 2009; Rosenberg and Berger, 2009; Willett and Schlunegger, 2009; Cederbom et al., 2011; Schlunegger and Mosar, 2011). One of the key results implies that the folded and thrusted southern part of the Swiss Molasse basin (the Subalpine Molasse, Figure 5-1), was tectonically active after 5 Ma (Cederbom et al., 2008; Cederbom et al., 2011) but also during times when the more external Jura Mountains were actively deformed (von Hagke et al., in review) in contrast to previous thinking, which assumed that the Alpine front had been extinct tectonically since the Late Miocene. Whether this erosion and thrusting signal is a consequence of active shortening at the orogen scale, of mantle processes or of climatically forced erosion changes remains debated (e.g. Mosar, 1999; Willett and Schlunegger, 2009; Cederbom et al., 2011; Schlunegger and Mosar, 2011).

These various mechanisms presumably cause differences in the orogenic response, in particular in the magnitude and lateral extent of the shortening and erosion signal. For example, since the Jura Mountains are kinematically related to the Subalpine Molasse (Pfiffner et al., 1997d), it remains to be tested (i) whether the tectonic signal in the Subalpine Molasse is a local anomaly or observable along strike the orogen (i.e. east of the Jura Mountains), (ii) whether the shortening is synchronous using the same detachment system or not, (iii) whether the lateral wavelength of the reported signal has a relationship with the lateral extent of climate induced changes or mantle associated processes. This knowledge is a requirement for understanding the kinematics of the orogen and a key for elucidating the mechanism behind the erosion signal.

In this paper, we report thermochronological data from a profile south of Lake Constance, crossing the entire Subalpine Molasse into the undeformed foreland basin (Bregenzerach, Austria, Figure 5-2). We combine this new data set with previously published thermochronology data from the basin farther west (Cederbom et al., 2004; Cederbom et al., 2011; von Hagke et al., in review) and from the structurally related hinterland (Hurford et al., 1989; Reinecker et al., 2008; Vernon et al., 2009b; Glotzbach et al., 2010; Glotzbach et al., 2011b; Weisenberger et al., 2012). We use these data to reconstruct the kinematic evolution of the Central Alpine wedge since 10 Ma. Finally, we use wedge mechanical considerations to understand the exhumation and erosion history of the Central Alps since

Late Miocene times. Based on the comparison between the eastern and western data sets we will discuss mechanisms of late Neogene forcing on the Alpine wedge.
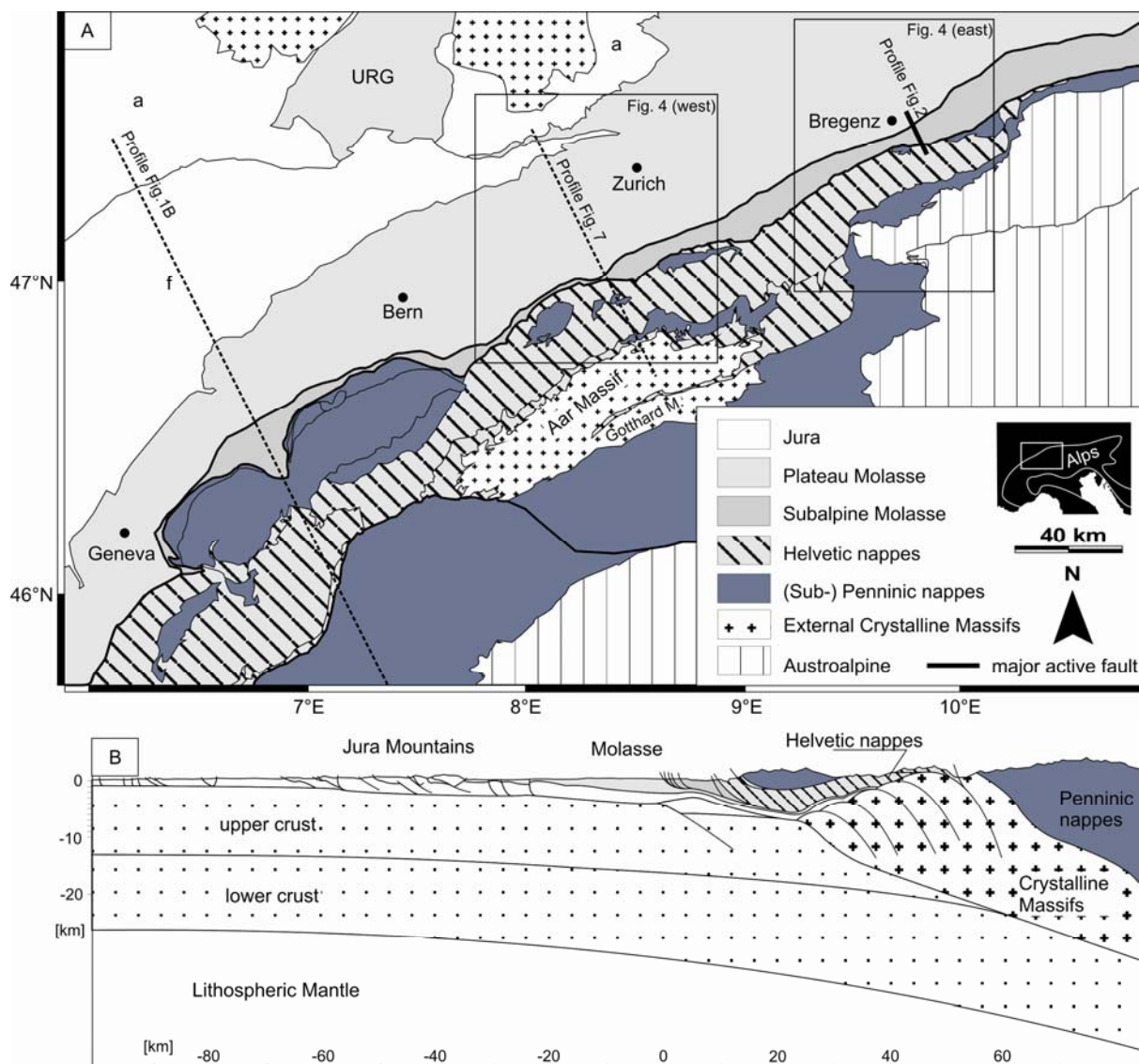

Figure 5-1A: Tectonic map of the Central Alps, the foreland basin and the Jura Mountains. Figure 1B is a cross section through the Central Alps, modified after Burkhard and Sommaruga (1998a), showing all major tectonic units. The origin of the x-axis is located at the northernmost thrust of the Subalpine Molasse.

5.2 Geological framework

The European Alps are the consequence of telescoping of the crust as a result of convergence and collision of the African and the European Plates (e.g. Trümpy, 1960; Frisch, 1979). The Molasse basin evolved as a classical orogenic foredeep due to flexural bending of the European plate by the advancing orogenic wedge (Pfiffner, 1986). In the Western and

Central Alps, the Molasse sedimentation can be subdivided into the Rupelian Lower Marine Molasse (UMM), Chattian to Aquitanian Lower Freshwater Molasse (USM), Burdigalian Upper Marine Molasse (OMM) and the Burdigalian to Serravallian Upper Freshwater Molasse (OSM). At the southern fringe of the basin, incorporation of these sediments into the Alpine wedge started shortly after deposition, around 22 Ma (Pfiffner et al., 1997a). This led to formation of the folded and thrusted Subalpine Molasse and a characteristic triangle zone (Müller et al., 1988; Berge and Veal, 2005), (Figure 5-2). At c. 10 Ma, folding of the Jura Mountains in an external position started in the western Central Alps (e.g. Burkhard, 1990; Bollinger et al., 1993; Burkhard and Sommaruga, 1998a), coeval with the onset of uplift and exhumation of the External Crystalline Massifs (Fügenschuh and Schmid, 2003), (Figure 5-1). From this coeval exhumation, section balancing and seismic lines, the Jura Mountains, the Subalpine Molasse and the External Massifs are interpreted to be linked via a common detachment underlying the late stage northern flank of the Central Alpine orogenic wedge (Pfiffner et al., 1997a).

5.3   Tectonic slices in the Subalpine Molasse

In the western part of the Subalpine Molasse four structural domains have been identified (von Hagke et al., in review). The limits of these tectonic slices are thrusts which run parallel to the Alpine front over long distances, whereas faults within these tectonic slices are of local importance. The same tectonic slices are present in the Bregenzerach area that we focus on in this study (Figure 5-2). Tectonic slice 1 (TS-1) represents the area south of the southernmost thrust of the Subalpine Molasse. The northern limit of tectonic slice 2 (TS-2) is the basal UMM thrust and forms the southern limit of the triangle zone. The northern limit of tectonic slice 3 (TS-3) is the surface rupture of the triangle zone and tectonic slice 4 (TS-4) represents the flat lying Plateau Molasse and its north-dipping southern fringe. Figure 5-2 shows a new balanced cross section across the Subalpine Molasse east of the Bregenzerach stream. We selected the Bregenzerach stream for thermochronological age dating because it is one of the few profiles which provides excellent outcrops in all stratigraphic units of the Molasse.
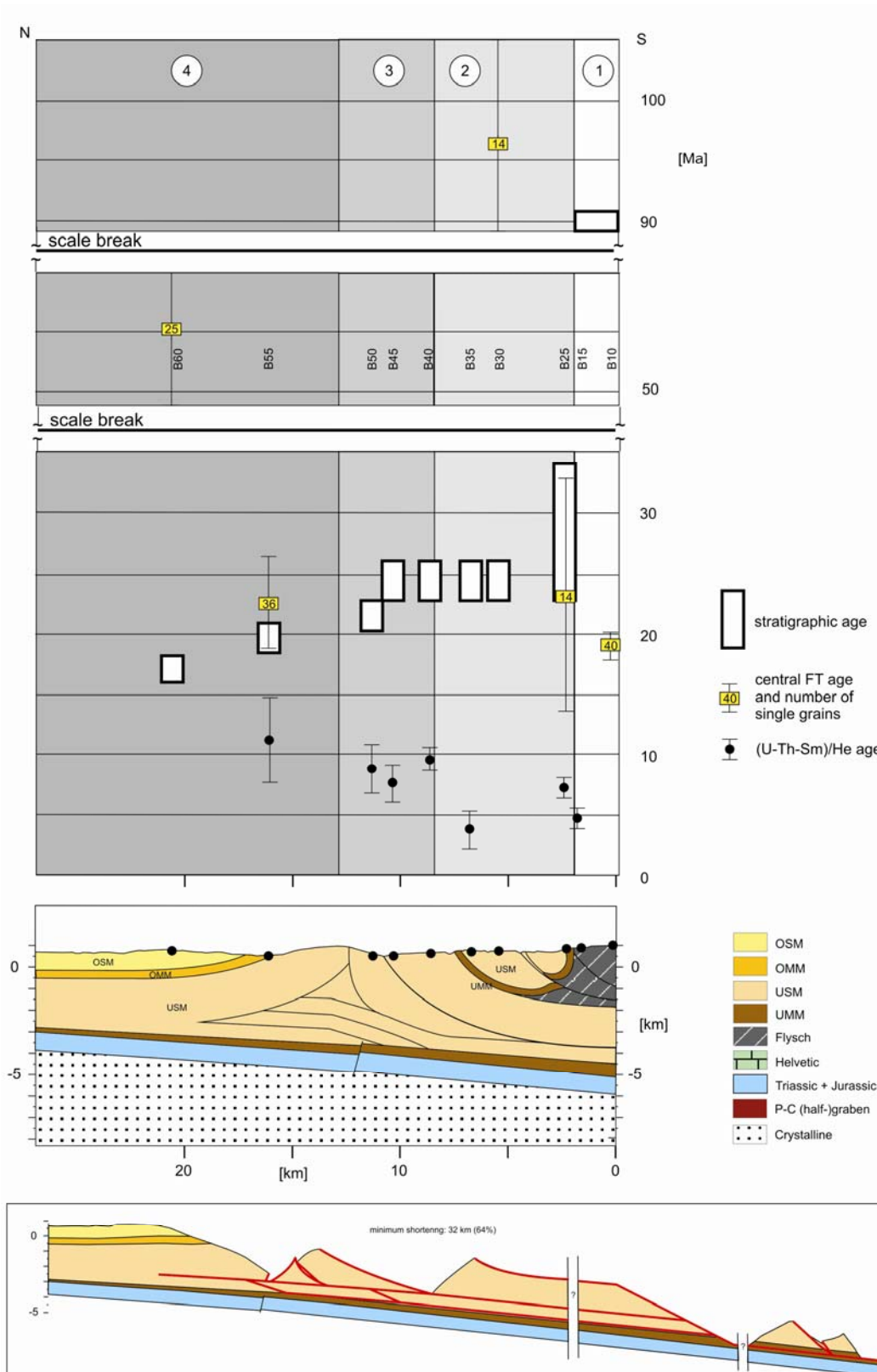
Figure 5-2: Balanced cross section across the SM south of Bregenz, Austria (see Figure 1). Black dots indicate the projected data points. We sub-divided the Subalpine Molasse into four tectonic slices, bound by thrusts that can be followed along-strike over tens of kilometres. Note the offsets in AHe ages across the thrusts between TS-1 and TS-2.

5.4   Thermochronological Methods

Apatite fission track (AFT) and apatite (U-Th-Sm)/He (AHe) dating allow reconstructing the tectono-thermal history of the topmost few kilometres of the earth's crust. A combination of these two methods has proven to be a powerful means for deciphering low-temperature cooling histories (Armstrong et al., 2003; Stockli, 2005), especially when syn-tectonic sediments are missing due to late stage erosion as is the case in the North Alpine Foreland Basin. These dating methods are sensitive to cooling intervals between c. 120-60 °C and 80-40 °C, respectively (Wolf et al., 1996; Carlson et al., 1999). These temperature intervals are termed the partial annealing zone (PAZ) for the AFT system and partial retention zone (PRZ) for the AHe system, respectively. Reheating of an apatite grain after deposition during burial to temperatures higher than the base of the PAZ or PRZ causes a resetting of the thermochronological clock and a loss of information from the hinterland. Within the PAZ and PRZ, partial resetting occurs, i.e. thermochronology ages become successively younger. When apatites have different annealing kinetics due to different chemical composition, they will be reset at different temperatures. The differentiated annealing results in different grain age populations (e.g. Galbraith, 2005), which can be estimated statistically for the fission track ages. Thermochronological ages which are older than their stratigraphic ages are detrital ages and provide information about the cooling of the hinterland only. However, as they have not been reheated substantially after deposition they carry information about the maximum temperature reached in the basin. For a detailed description of the methods, the reader is referred to Donelick (2005) for fission track dating and Farley & Stöckli (2002) for (U-Th-Sm)/He dating.

Sample preparation for AFT dating was carried out according to the methods described by Donelick et al. (2005). To analyze uranium concentration, we used laser ablation inductively coupled plasma mass spectrometry (Hasebe et al., 2004; Donelick et al., 2005). Samples were ablated with a New Wave UP-213 laser ablation system; elements were analyzed in solution with a Finnigan Element2, i.e. a high-resolution single collector ICP-MS. We performed all laser ablation analyses at the GeoAnalytical Lab of Washington State University, in the USA. Central and peak ages were calculated with the RadialPlotter software (Vermeesch, 2009). We determined Dpar for all single grains. This is a measure of

the annealing kinetics, with lower Dpar values indicating that the grain is sensitive to annealing (Carlson et al., 1999; Ketcham et al., 1999).

For AHe analysis, apatites were analyzed with a SteREODiscovery V12 microscope with a Plan S 1.0x objective. The microscope is equipped with cross-polarizer, rotating stage and plane-polarized darkfield illumination at 100x. We selected at least three grains for every sample. The grains were degassed and analyzed for parent isotope content in the laboratory of the University of Kansas. Raw AHe ages were corrected for alpha ejection at the crystal surfaces. We present the weighted mean ages.

5.5   New thermochronological data

Thermochronology ages were obtained from all four tectonic slices in the Subalpine Molasse. Figure 5-2 shows a projection of the sampling locations into the cross section (black dots) and the respective ages above the profile. We produced AFT ages for five samples (Table 5-1). Peak ages are reported in Table 5-2. AHe ages were obtained from seven samples (Table 5-3). For two samples (B25 & B 55), we applied both methods. We present the weighted mean AHe ages, accounting for broken grains and consequent uncertainties of the Ft corrections (Fitzgerald et al., 2006; Brown et al., 2011). Mean and single grain ages are given in Table 5-3.

In TS-1, all samples originate from Cretaceous Flysch units. The obtained central AFT age (sample B10) is 18.6 ± 1.7 Ma thus considerably younger than its corresponding stratigraphic age. This requires substantial reheating after deposition. AHe dating in TS-1 (sample B15) yields a weighted mean age of 5.0 ± 0.7 Ma. This sample is located immediately south of the Subalpine Molasse (Figure 5-2). In TS-2, the southernmost sample (B25), which stems from the UMM, yields a central AFT age of 23.5 ± 9.7 Ma. This is as old as, or slightly younger than its corresponding stratigraphic age. The single grain ages can be decomposed into two grain age populations (Table 5-2), one being older and one younger than the stratigraphic age of the sample, indicating partial resetting. Further north, sample B30 yields a central fission track age of 96.4 ± 17.7 Ma with a youngest peak age of 35.1 Ma, thus still older than the corresponding stratigraphic age. The AHe ages of TS-2 in contrast are younger than the

corresponding stratigraphic ages. In the south, sample B25 yields an age of 7.6 ± 0.57 Ma, which is older than the age of the adjacent sample B15, south of the thrust. In the north, sample B35 yields an age of 4.3 ± 1.5 Ma, thus comparably young as the AHe age of sample B10. Crossing the basal UMM thrust into TS-3, a clear jump in AHe ages can be observed. Samples B40, B45 and B50 yield ages of 9.1 ± 0.7, 7.2 ± 2.0 and 8.6 ± 2.5 Ma, respectively, thus all reproducing within error at an age which is significantly younger than the corresponding stratigraphic ages and significantly older than the ages obtained in TS-2. Note that sample B40 is only based on one grain (table 5-3). In TS-4, the central fission track ages and all peak ages are older than their corresponding stratigraphic age (samples B55 and B60). The AHe age obtained from B55 is 10.8 ± 4.2 Ma and younger than its corresponding stratigraphic age. However, the broad spread in single grain ages as observed here may indicate partial resetting of the sample. All measured Dpar values for the AFT ages are lower than 1.4 µm, indicating complete annealing of fission tracks at temperatures of less than 100 °C (Carlson et al., 1999; Donelick et al., 1999).

Table 5-1: Results of apatite fission track dating from the Subalpine Molasse, Austria, using the LA-ICP-MS method for ^{238}U analysis. Dpar is the arithmetic mean maximum diameter of fission-track etch figures, Ns is the number of spontaneous tracks counted, P = ^{238}U/^{43}Ca and Ω = area for a single apatite grain, ζMS is the zeta value for LA-ICP-MS dating, and Q is the χ^2 probability. Central ages were calculated using the RadialPlotter software by Vermeesch (2009).

Sample	latitude	longitude	grains	Dpar (µm)	Ns	Ω (cm^2)	Σ (P*Ω) (cm^2)	1σ Σ (P*Ω) (cm^2)	ξMS	1σξMS	^{43}Ca bkg:sig	^{238}U bkg:sig	Q	central age (Ma)	error (1sigma) (Ma)
B10	9.83438	47.40654	40	1.34	203	7.17E-04	1.1889	1.18E-02	187071	1.21E+04	246.26	16.36	0.02	18.6	1.74
B25	9.89256	47.43156	14	1.36	36	2.25E-04	0.2323	6.10E-03	187682	1.41E+04	232.90	69.41	0.00	23.5	9.65
B30	9.87793	47.46024	14	1.24	110	1.45E-04	0.14303	2.18E-03	198293	9.11E-01	193.62	30.43	0.00	96.4	17.70
B55	9.83029	47.51075	36	1.35	242	7.99E-04	0.98399	1.37E-02	188105	1.55E+04	200.11	1187.10	0.00	23.5	3.77
B60	9.78322	47.53855	25	1.36	989	6.69E-04	1.0927	1.44E-02	197505	8.98E-01	229.77	137.69	0.00	55.4	10.8

Table 5-2: Peak ages for all new AFT ages from the Bregenzerach Profile. The presence of different grain age populations is not interpreted further but used as indication for (partial) resetting.

Sample	Grains	peak 1 [Ma]	grain portion [%]	peak 2 [Ma]	grain portion [%]	peak 3 [Ma]	grain portion [%]
B10	40	18,7	100,0				
B25	14	6,6	48,8	68,7	51,2		
B30	14	35,1	12,0	105,0	88,0		
B55	36	19,5	77,6	44,1	17,8	183,0	4,6
B60	25	41,0	77,2	191,0	22,8		

Table 5-3: Apatite (U-Th-Sm)/He dating results from the Subalpine Molasse, Austria. [eU] is the effective uranium concentration, which weights the decay of the parents for their alpha productivity (Flowers et al., 2009); [Ft] is the α-ejection correction factor, [excluded ages] have not been taken into account for the geological interpretation because of analytical errors or lack of uranium.

sample	elevation [masl]	mass [µg]	U[ppm]	Th [ppm]	Sm [ppm]	eU	4He [nmol/g]	Ft	raw age [Ma]	corrected age [Ma]	1 σ error [Ma]	excluded age	weighted mean	error
B15-1	560	7.75	78.9	298.2	149.2	148.3	4.1	0.77	5.05	6.6	0.52			
B15-2		4.95	6.2	158.7	24.4	42.9	0.9	0.73	3.77	5.2	0.41			
B15-3		3.39	72.9	242.7	74.5	129.2	2.1	0.70	3.00	4.3	0.34			
B15-4		23.67	2.4	171.1	21.8	42.0	0.9	0.83	3.98	4.8	0.38		4.97	0.54
B25-1	520	2.36	15.3	3.6	19.9	16.2	0.5	0.69	5.32	7.7	0.62			
B25-2		1.64	8.8	55.1	17.4	21.6	0.5	0.63	4.33	6.9	0.55			
B25-3		1.50	8.2	10.6	15.3	10.7	0.3	0.63	5.54	8.8	0.70		7.63	0.57
B35-1	480	9.46	13.0	235.4	57.2	67.5	2.4	0.78	6.45	8.3	0.66			
B35-2		9.88	11.5	128.5	45.5	41.3	0.6	0.78	2.71	3.5	0.28			
B35-3		8.34	29.0	146.5	63.9	63.1	1.3	0.78	3.71	4.8	0.38			
B35-4		16.68	15.6	132.4	32.3	46.2	4.3	0.82	16.67	20.4	1.63	e	4.36	2.12
B40-1	475	7.75	3.4	4.0	17.4	4.4	0.6	0.78	23.26	29.9	2.39	e		
B40-2		4.95	14.4	64.0	48.7	29.4	1.1	0.73	6.71	9.1	0.73			
B40-3		3.39	59.3	308.6	75.9	130.7	30.9	0.69	42.98	61.9	4.95	e	9.14	0.73
B45-1	460	4.05	6.5	16.3	30.3	10.4	0.3	0.72	4.46	6.2	0.49			
B45-2		3.34	8.4	156.0	25.0	44.5	1.0	0.70	4.18	6.0	0.48			
B45-3		7.23	50.6	131.6	56.0	81.2	4.0	0.77	8.99	11.7	0.94			
B45-4		3.08	6.7	7.4	18.3	8.5	0.3	0.70	6.90	9.8	0.79		7.19	4.04
B50-1	460	3.19	24.9	69.2	86.1	41.3	1.1	0.70	4.72	6.7	0.54			
B50-2		2.50	13.9	16.1	22.1	17.7	0.6	0.69	6.69	9.7	0.78			
B50-3		5.83	1.8	12.0	19.3	4.7	0.8	0.75	29.87	40.1	3.21	e		

B50-4		2.70	22.9	38.6	81.0	32.2	1.7	0.69	9.72	14.1	1.13		8.56	6.43
B55-1	640	5.22	38.1	45.2	47.9	48.7	3.3	0.73	12.28	16.9	1.35			
B55-2		2.76	29.6	26.9	53.4	36.1	1.1	0.69	5.79	8.4	0.51			
B55-3		2.29	132.0	92.4	75.3	153.6	12.3	0.67	14.80	21.9	1.32			
B55-4		7.59	59.8	2.3	29.9	60.5	2.7	0.79	8.23	10.5	0.84			
B55-5		4.75	148.0	68.1	158.8	164.5	35.1	0.75	39.28	52.5	4.20	e		
B55-6		3.42	0.6	0.6	0.0	0.7	0.0	0.71	-4.04	-5.7	-0.46	e	10.82	17.65

5.6 Thermal history

We have performed inverse modelling of time-temperature paths with the HeFTy software (Ketcham, 2005), using the depositional age (Zacher, 1995) and the respective surface temperature (Mosbrugger et al., 2005) as modelling constraints. The hinterland cooling, i.e. the time-temperature paths prior to deposition were not constrained. Where applicable (i.e. where the AFT ages are older than the corresponding stratigraphic ages), we set maximum temperatures within the basin to 80 °C, which is within the PAZ. For samples indicating total annealing (B10 & B15), a maximum temperature of 140 °C was set. This allows for total annealing at any time after deposition.

The achieved thermal histories are plotted in Figure 5-3. They corroborate the result that reheating within the basin is required for most samples. Modelling of sample B25 shows a distinct cooling pulse at c. 8 Ma. It is well constrained because for this sample both, AFT and AHe data exist. Sample B15 and B35 show a rapid cooling pulse at c. 5 Ma, whereas the samples B40, B45 and B50 (TS-3) as well as sample B55 (TS-4) do not require rapid exhumation.
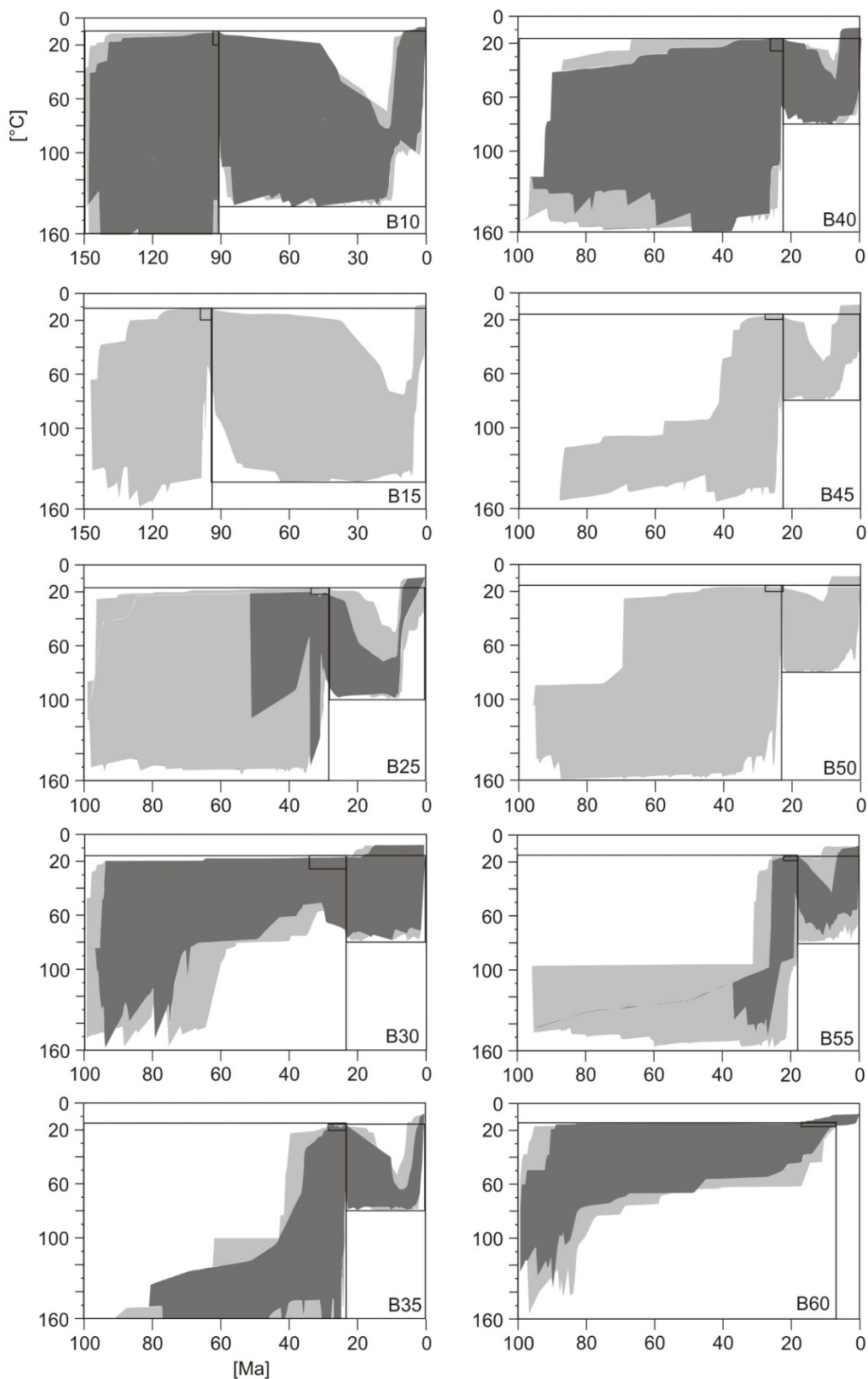
Figure 5-3: Cooling and exhumation histories derived from thermal models using HeFTy (Ketcham, 2005). All models were run without any constraints on hinterland cooling histories. Depositional ages were taken from Zacher (1995), depositional temperatures from Mosbrugger (2005). Light grey paths denote acceptable fits; dark grey paths denote good fits. Note the different time scale for samples B10 and B15.

5.7 Interpretation of the cooling signals

We detect a gradient in maximum palaeo-temperatures along the cross section. In TS-1, temperatures experienced where high enough to affect the AFT system substantially, as the AFT age is significantly younger than the corresponding stratigraphic ages. To produce good fits for the data with modelling, sample B10 must have been reheated to at least 80 °C. In TS-2, the AHe system is reset while the AFT system witnesses some reheating in the south (B25) but no reheating in the north (B30). The palaeo-temperature must have been at least 60 °C in the north and probably slightly higher in the south assuming similar annealing kinetics, which is reasonable due to similar Dpar values (Table 5-1). TS-3 also shows resetting of the AHe system (no FT data). TS-4 shows indications of partial resetting within the AHe system, thus requiring less than 60 °C of cooling. With a geothermal gradient of 30 °C, which is typical for the present day situation but was probably lower in the past (Schegg and Leu, 1998; Cederbom et al., 2011), and the assumption of constant heat flow, the cooling translates into at least 2.6 km of eroded section for TS-1, at least 2.0 km of eroded section in TS-2 and TS-3 and less than 2.0 km in TS-4. Furthermore, distinct offsets in AHe ages across the thrust between TS-1 and 2 and between TS-2 and TS-3 can be observed. No offset is recorded between TS-3 and TS-4. Two rapid exhumation pulses are detected; the first occurred at c. 8 Ma and a second one at c. 5 Ma. At least the 5 Ma ages seems to be structurally controlled, showing offsets at major faults, which means that the cooling signal relates to tectonic activity within the Subalpine Molasse. The 5 Ma age is a minimum age for thrusting. The widths of the PAZ and PRZ are only poorly constrained due to lack of a vertical age section. It is therefore impossible to resolve whether the activity started before 5 Ma or if we are looking at a tectonic pulse thereafter.

5.8 Lateral correlation of tectonic events

We can compare these findings with data and reported tectonic activity from the Swiss part of the basin (Cederbom et al., 2008; von Hagke et al., 2010; Cederbom et al., 2011; Schlunegger and Mosar, 2011; von Hagke et al., in review). Figure 5-4 shows an evaluation of the thermochronological results by von Hagke et al. (in review) in comparison with the new data presented in this study. We have estimated the amount of cooling for every AFT and AHe age. For totally annealed samples, we used the corresponding Dpar values to estimate

the maximum heating temperature. In this study, we use a resetting temperature of 100 °C for samples with Dpar values lower than 1.5 µm, samples with Dpar values between 1.5 and 2.0 µm are assumed to reset at 105 °C and for samples with Dpar values exceeding 2.0 µm, we use a resetting temperature of 110 °C, as discussed in von Hagke et al. (in review). Most samples have Dpar values lower that 1.7 µm in the Swiss part of the basin (von Hagke et al., in review) and below 1.4 µm in the east (Table 5-1). The estimated temperatures are minimum estimates, of the maximum palaeo-temperature. In contrast to the Bregenzerach data, the AFT system farther west in the basin was totally annealed. This results in a cooling deficit of c. 30 °C in the eastern compared to the western Molasse basin, which translates to c. 1 km difference of eroded section. Vitrinite reflectance studies in the Swiss part of the basin indicate that palaeo-heat flow was rather uniform and probably much lower than today (Schegg and Leu, 1998; Sachsenhofer, 2001; Schärli and Rybach, 2002). Hence, variations in palaeo-heat flow are too small to explain this difference. Additionally, this implies that the erosion estimates are minimum estimates. However, both data sets show that the structures in the Subalpine Molasse were tectonically active in Late Neogene times (Figure 5-4). In the west, tectonic activity is evident between tectonic slices 1 and 2, tectonic slices 2 and 3, as well as between tectonic slices 3 and 4 (von Hagke et al., in review). In the east, tectonic offset between tectonic slice 3 and 4 cannot be resolved with the thermochronological data and must, if present, lie within the error of the AHe ages. In any case, tectonic activity in the Subalpine Molasse during late Neogene times is probable east of the eastern termination of the Jura Mountains too. Hence, it is a regional feature, which is likely to be kinematically independent of the Jura fold and thrust belt.
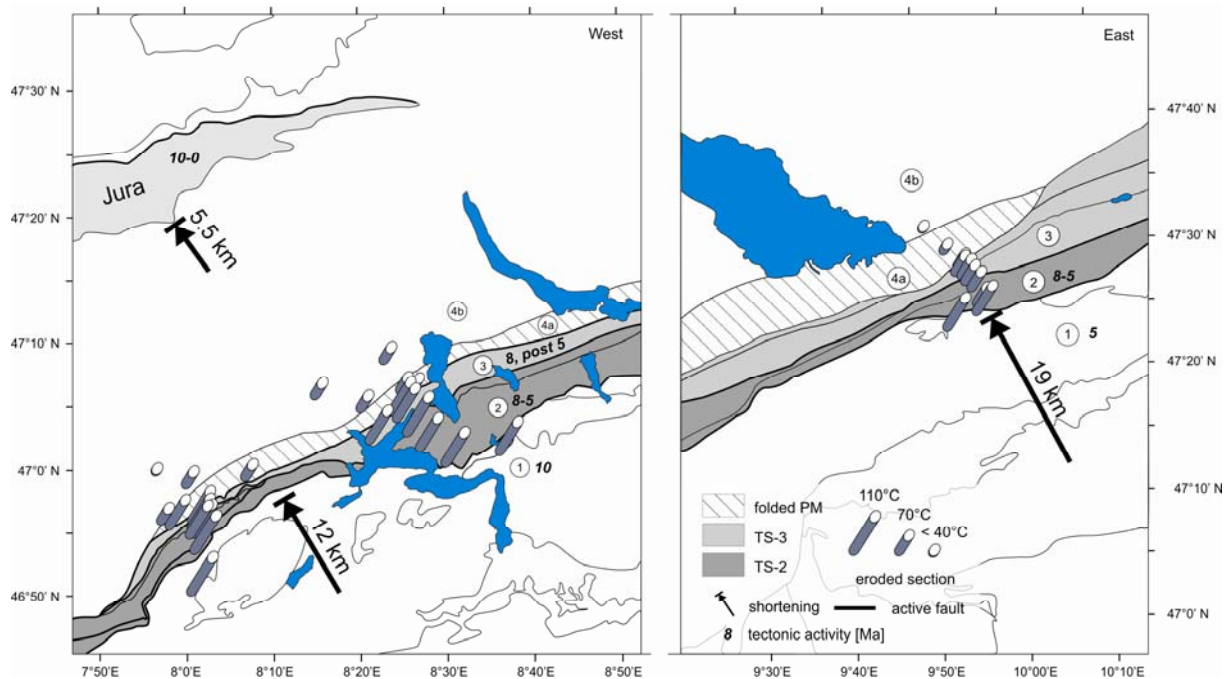
Figure 5-4: Comparison between thermochronological data in the Subalpine Molasse of the Central Alps. Tectonic slices as defined in Figure 2 are indicated. Left panel shows the data from von Hagke et al. (in review), right panel from this study. Note the similarities in thrust activity. Data from the Jura Mountains taken from Bollinger (1993) and Madritsch et al. (2010).

5.9 Post 10 Ma shortening in the Central Alps

Here we discuss shortening estimates from literature and make a shortening estimate for the Bregenzerach profile. Figure 5-5 shows a summary of Neogene shortening estimates for the Central Alps and the Jura Mountains. We choose to determine shortening for the last 10 Ma, because this is the oldest reported age of tectonically-related cooling in the Subalpine Molasse (von Hagke et al., in review). Von Hagke et al. (in review) estimate c. 12 km of shortening since 10 Ma within the western Subalpine Molasse based on AFT and AHe dating, uplift and erosion estimates and thrust dips from balanced sections. This translates to c. 13.5 km of movement along a thrust dipping 27°, which is reported from that area (Hantke, 2006).

Philippe et al. (1996) calculate a total shortening of 5.5 km since c. 13 Ma for the Jura Mountains in the prolongation of the data set. Assuming constant shortening through time, this corresponds to c. 4.2 km of shortening since 10 Ma. Assuming that shortening within the Jura Mountains stopped at c. 5 Ma (Willett and Schlunegger, 2010), shortening between 10

Ma and 5 Ma would be 3.4 km. Since the detachment of the Jura Mountains is only gently dipping (1-3°), shortening is almost equal to horizontal displacement of the Alpine body on this detachment. In summary, we estimate a minimum of 16.9 – 17.7 km of post 10 Ma displacement of the frontal Aar Massif on the basal décollement in the western Central Alps.

Additional shortening within the Helvetic domain is not likely, since these thrusts do not link with the current décollement but rather form a major klippen with an emergent décollement on both flanks. However, these estimates are minimum estimates, as minor shortening might be hidden in the gently folding of the Plateau Molasse as well as some fold tightening in the Helvetic domain.

In the east, it is impossible to quantify post 10 Ma shortening from the data because the AFT system is not fully reset and the AHe system witnesses only thrusting thereafter. However, from our section balancing of the Bregenzerach transect, we can deduce a minimum of 32 km of shortening since Late Burdigalian times (16 - 17 Ma). Assuming a constant shortening rate, this would require c. 20 - 19 km of post 10 Ma shortening. This estimate is consistent with shortening estimates from adjacent profiles; Schmid et al. (1996) calculate 15 km of post 19 Ma shortening along the NFP-20 East profile, in the eastern Central Alps (thus west of our transect) and Frisch et al. (1998) reconstruct 42 km of post Oligocene shortening in a profile east of our transect. In summary, the amount of shortening post 10 Ma is similar in the west and in the east of the Central Alps. Since the foreland deformation is kinematically linked with uplift and displacement of the Aar Massif, the amount of shortening within the Subalpine Molasse plus the shortening in the Jura Mountains in the west is counterbalanced by northward displacement of the Aar Massif on its basal detachment. We can hence restore the Late Miocene wedge geometry using the exhumation history of the Aar Massif.
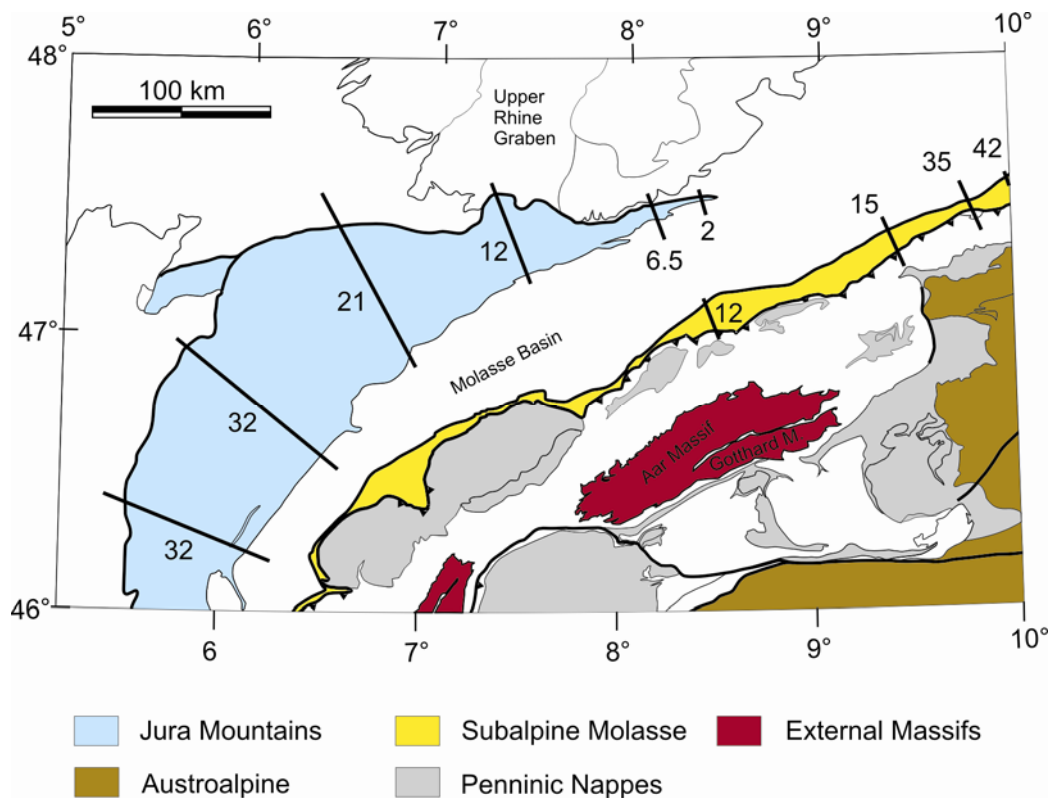
Figure 5-5: Neogene shortening within the Central Alps (based on Schmid et al., 2004). Shortening in the Jura taken from Philippe (1996), shortening within the Subalpine Molasse compiled from Schmid et al. (1996), Frisch et al. (1998)and v.Hagke et al. (in review).

5.10 Restoration of Late Miocene wedge geometry

We determine the former wedge geometry along the two profiles where thermochronology data of both, the foreland and the hinterland, is available. The first profile reaches from the Jura Mountains into the Aar Massif; the second profile is the southward prolongation of the profile discussed above, where the Aar Massif is still covered by Austroalpine nappes (Figure 5-1).

The exhumation of the Aar and Gotthard Massifs is constrained by several studies. Reinecker et al. (2008), report constant exhumation of 0.5 km/Ma at the northern flank of the Aar Massif since 10 Ma, which results in 5.0 km of exhumation, c.f. also Michalski and Soom (1990) and Weisenberger et al. (2012). Exhumation rates of 0.5 km/Ma since 10 Ma are also reported from different locations within the Aar Massif. Vernon et al. (2009b) and Glotzbach et al. (2010) report a phase of accelerated exhumation of c. 0.7 km/Ma for the Aar and Gotthard Massif between c. 10 and 7 Ma and subsequent exhumation at a rate of 0.5

km/Ma. This results in 5.6 km of exhumation. Valla et al. (2012) report even higher rates of 2-4 km/Ma for the time span of 8-10 Ma followed by rates of 0.3-0.5 km/Ma until present, which results in 6.4 to 12 km of exhumation. Assuming that exhumation rates are directly proportional to shortening rates, we can estimate the evolution of shortening rates through time on the base of the reported exhumation data. Figure 5-6 shows the individual shortening scenarios for the reported exhumation rates. For the scenario of constant exhumation (Michalski and Soom, 1990; Reinecker et al., 2008; Weisenberger et al., 2012), the corresponding shortening rate would be between 1.7 and 1.8 mm/a. For the exhumation scenario suggested by Glotzbach et al. (2010), shortening is between 2.2 and 2.1 mm/a from 10 to 7 Ma and thereafter between 1.6 and 1.5 mm/a. Following the scenario Valla et al. (2012) proposed, shortening is as high as 4.9-4.7 mm/a (using their minimum uplift estimates of 2 mm/a) and decreases to 0.9 mm/a for the time span from 8 Ma to present. In all scenarios shortening rates do not change significantly at least throughout the last c. 8 Ma and they are similar to present day rates (Champagnac et al., 2009; von Hagke and Oncken, submitted) (Figure 5-6).
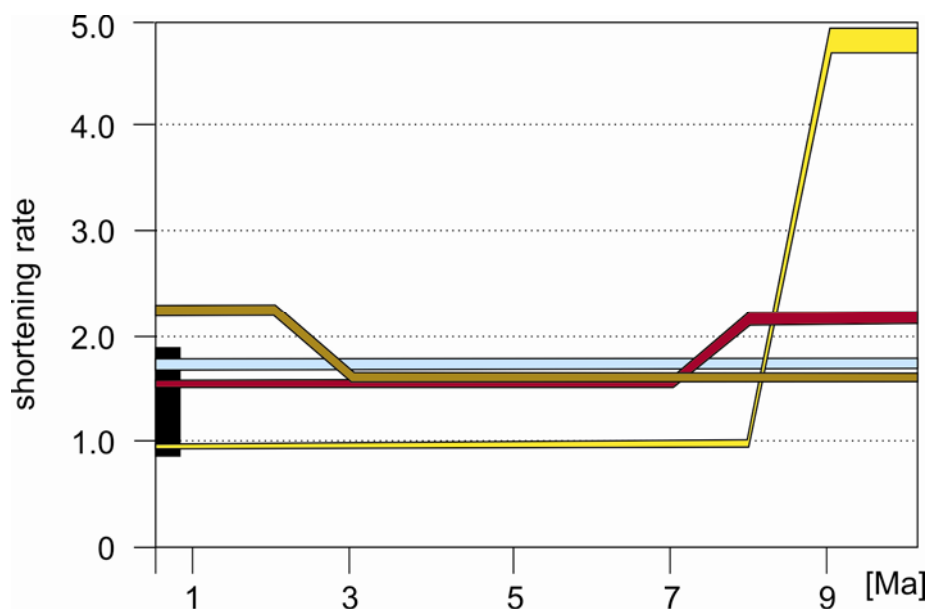
Figure 5-6: shortening rates through time. Calculations based on Michalski and Soom (1990), Reinecker et al. (2008) and Weisenberger et al. (2012) (blue), Valla et al. (2012) (yellow), Glotzbach et al. (2010) (red)and Hurford et al. (1989) (brown). The black rectangle denotes the possible range of present day shortening rates within the Central Alps (Champagnac et al., 2009; von Hagke and Oncken, submitted).

The goal of our wedge geometry restoration is to detect whether the orogenic taper varied substantially through time. For the western part of the wedge, we consider a material point in the Aar Massif and restore it by 16.9 – 17.7 km on a detachment ramp dipping 20° (taken from the balanced crustal scale cross section by Burkhard and Sommaruga (1998a)) and then restore the measured exhumation (Figure 5-7). The change in taper angle (Δα) since 10 Ma is the difference between present-day taper angle and the taper angle resulting from restoring the material point (Figure 5-7). It is a consequence of the difference in elevation between the present-day location of the material point and its location after restoration (Δh).

We first calculate the exhumation which brings the material point back to present-day elevation after restoring the shortening (shortening * sin (detachment dip)). Exhumation is 5.8 km for 16.9 km and 6.1 km for 17.7 km of shortening, respectively. Second, we calculate Δh by subtracting these values from reported exhumation values. Using small angle approximation (sin Δα ≈ Δα), the difference in taper Δα can be calculated measuring only the distance between the Subalpine Molasse and the External Massifs. This is a maximum estimate, because taking the distance between Jura Mountains and External Massifs would decrease Δα. For our calculations we use a distance of 50 ± 5 km. Negative Δh (and consequently negative Δα values) signify that the taper angle was lower 10 Ma ago.

The results are given in Table 5-4. All Δα values are (sometimes considerably) lower than 1.5°, despite for the calculations with 12 km of exhumation. We acknowledge that this is a maximum value which still fits the data of Valla et al. (2012) but compared to all other independent calculations, it does not seem to be geologically reasonable. This indicates that the taper in the Swiss Central Alps did not change significantly since 10 Ma.

Table 5-4: 5-4A shows Δα values based on exhumation values of the Aar Massif. Δα values are highlighted in red. In spite of the calculations with extremely high amounts of eroded section, all values are below 1.5°, indicating that the orogenic taper was stable since 10 Ma. Table 5-4B shows the analogous calculations for the eastern profile. Shortening values used are 19 and 20 km derived from our section balancing. The grey fields are calculated with a décollement dip of 18°, the red fields are calculated with a décollement dip of 23°. See text for further explanations.

Table 5-4A:

Measured exhumation [km]	Δ h	Distance along profile = 45 km	Distance along profile = 50 km	Distance along profile = 55 km
5	-0.78	-0.99	-0.89	-0.81
5	-1.05	-1.34	-1.21	-1.10
5.6	-0.18	-0.23	-0.21	-0.19
5.6	-0.45	-0.58	-0.52	-0.47
6.4	0.62	0.79	0.71	0.65
6.4	0.35	0.44	0.40	0.36
12	6.22	7.87	7.09	6.45
12	5.95	7.53	6.78	6.17

Table 5-4B:

Measured exhumation [km]	Δ h	Distance along profile = 45 km	Distance along profile = 50 km	Distance along profile = 55 km
5.4	-0.47	-0.60	-0.54	-0.49
5.4	-0.78	-0.99	-0.89	-0.81
5.4	-2.02	-2.58	-2.32	-2.11
5.4	-2.41	-3.07	-2.76	-2.51

We use the same approach for the eastern profile. Hurford et al. (1989) report a constant uplift of the Silvretta Nappe at a rate of c. 0.5 km/Ma from 35 to 2 Ma and slightly increased rates thereafter. With a rate of 0.7 km/Ma for Pleistocene to present rates, the exhumation

since 10 Ma would be 5.4 km. This results in constant shortening rates of 1.6 mm/a from 10 to 2 Ma and an increase thereafter to rates between 2.3 and 2.2 mm/a, which is similar to what we calculated for the western profile (Figure 5-6).

For restoration, we use the décollement dip from the adjacent NFP-20 East profile (Schmid et al., 1996). As it is not strictly balanced, we calculate Δα values based on décollement dips between 18 and 23°. This results in Δα values lower than 1° (décollement dip = 18°) or Δα values lower than 3° (décollement dip = 23°) (Table 5-4). As these changes refer to changes of the critical taper angle, which is surface slope plus décollement slope, variations of 3° over 10 Ma are still small. Given the uncertainties of exhumation rates and the similarities between the eastern and the western profile in thrusting rates, as well as timing and location of thrusting, we argue that the geometry of the Central Alps did not change within error since 10 Ma.
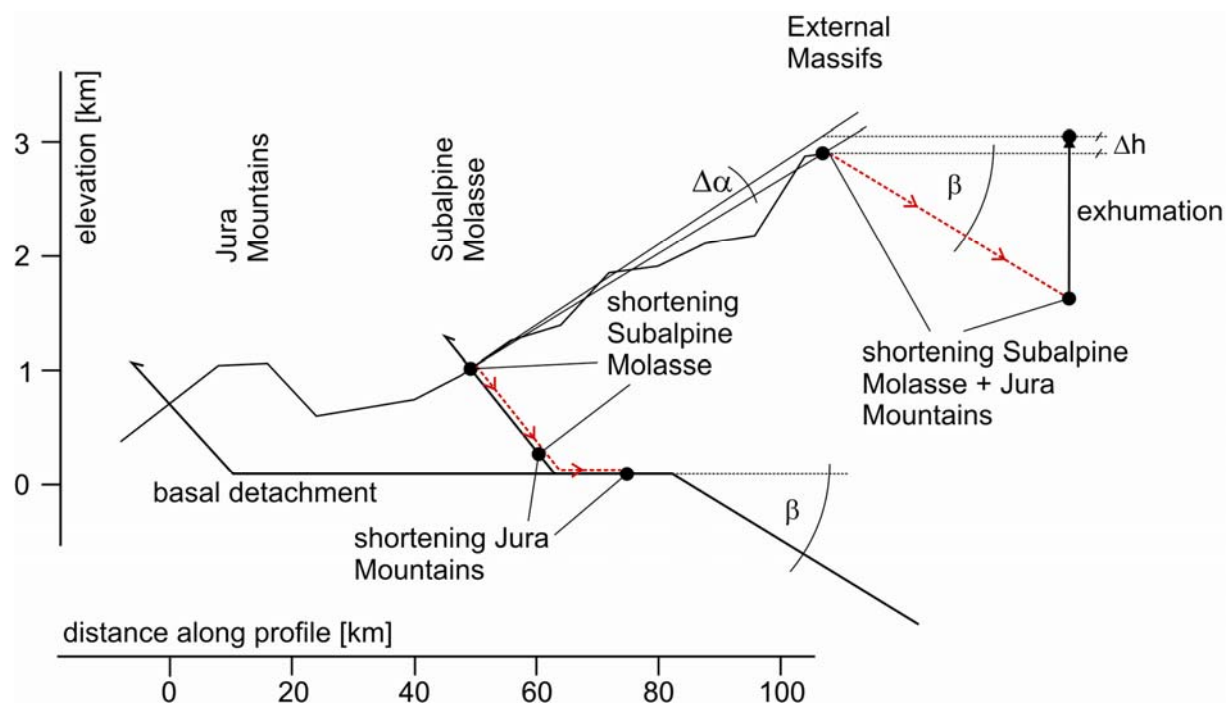
Figure 5-7: schematic sketch of the restoration of the wedge taper since 10 Ma. The kinematic link between the Subalpine Molasse and the External Massifs via the same basal décollement allows for restoration of palaeo-wedge with thermochronological data from both areas. Goal is the quantification of the change in taper, Δα. We use the shortening estimates from the Subalpine Molasse and the Jura Mountains, calculate the resulting exhumation and compare them with reported data from the External Massifs.

5.11 Discussion: Are the Central Alps in tectonic steady state since 10 Ma?

Critical taper theory predicts that an orogenic wedge deforms internally until a critical taper is attained, which is dependent on detachment strength and internal wedge strength (Davis et al., 1983). Recent seismic activity in the Central Alps triggered by climatic events or human activity as well as deformation on the basal detachment indicates that the Central Alps are at present at or close to critical state (von Hagke and Oncken, submitted). The finding that the Subalpine Molasse is repeatedly active during Neogene times, contemporaneous with deformation in the external Jura Mountains and in the more internal Crystalline Massifs shows that the Central Alpine wedge was at or close to the verge of failure internally and on the basal décollement throughout that time. This is indicative for criticality, which is corroborated by our finding that the taper of the Alps did not change significantly since the Late Neogene.

In the case of the Central Alps, the detachment and internal strength is lithologically controlled (von Hagke and Oncken, submitted). Since the most external element of the Alps, the Jura Mountains with their weak salt detachment, was already accreted into the wedge in the Late Neogene, major changes in lithologies which could have changed wedge properties cannot have occurred. If detachment strength and internal wedge strength remained constant, changes in taper and distribution of internal deformation/erosion must be ascribed to external mechanisms, such as mantle processes or climatically forced erosion changes. Accordingly, the constant taper we detect in conjunction with distributed deformation and constant shortening rates since at least 8 Ma shows that the Central Alps are in kinematic steady state within that time-frame.

Our and previously published thermochronological data in conjunction with tectonic studies in the Jura Mountains (e.g. Ustaszewski and Schmid, 2007; Madritsch et al., 2008; Madritsch et al., 2010) indicate that the orogenic front has been stationary since c. 10 Ma. Furthermore, our data and the data from von Hagke et al. (in review) show repeated out-of-sequence thrusting within the Subalpine Molasse. Additionally, Wittmann et al. (2007) report erosion rates from the Central Alps and show that the present day rates of 0.9 mm/a for the crystalline Central Alps and 0.27 mm/a for the foreland are long-term features that have been stable for more than 5 Ma. Together with our finding of constant shortening and

a constant taper, this requires that the mass-flux between erosion and accretion is also at steady-state.
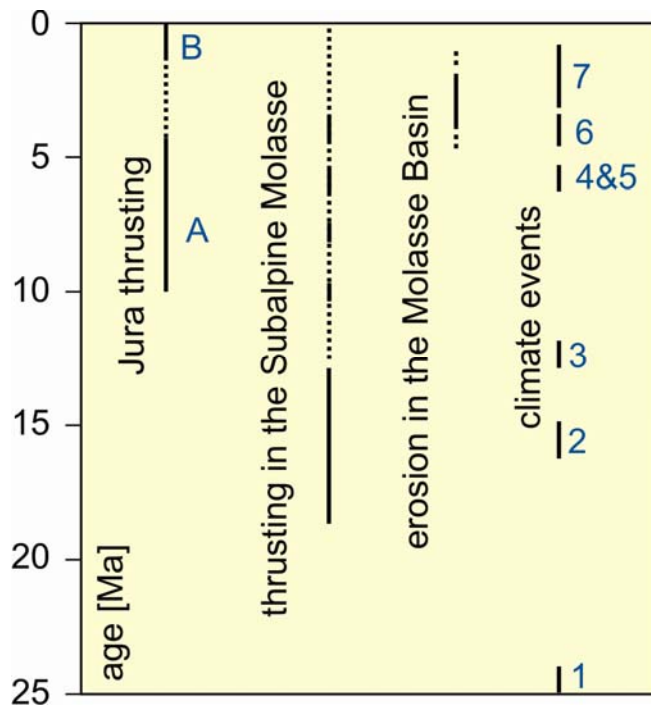
Figure 5-8: Timing of events in the Alpine foreland basin. A: thin-skinned Jura thrusting after Bollinger et al. (1993), B: thick skinned thrusting after Becker (2000), Madritsch (2008; 2010). Climate events: (1) Late Oligocene Warming (Mosbrugger et al., 2005), (2) Mid-Miocene Climatic Optimum (Mosbrugger et al., 2005), (3) East Antarctic Ice Sheet (Bruch et al., 2007), (4) Alpine glaciation at 6.26-5.50 (Hodell et al., 2001), (5) Messinian Salinity Crisis at 5.96-5.33 (Krijgsman et al., 1999; Hodell et al., 2001), (6) increased global climate perturbation since 3.8 Ma (Zhang et al., 2001; Molnar, 2004) and gradual increase in moisture supply in Europe due to closure of the Panama Isthmus from 4.6-3.2 Ma (Driscoll and Haug, 1998; Cederbom et al., 2004), (7) Northern Hemisphere Glaciation starting at 3.1-2.5 Ma and reaching its maximum at c. 1.0-0.8 Ma (Haug and Tiedemann, 1998; Haeuselmann et al., 2007). Erosion in the Molasse Basin after Cederbom et al. (2004; 2011) and Willett and Schlunegger (2010). Thrusting in the Subalpine Molasse after Trümpy (1980), Cederbom et al. (2011) and von Hagke et al. (in review).

This required balance between erosion and accretion allows considerations about the role of climate during the last 10 Ma. Figure 5-8 summarizes the timing of tectonic and climatic events in the Molasse Basin and the Jura Mountains. Several climatic events have been reported, which may have initiated erosion in the Molasse basin. As becomes obvious, tectonic activity in the Jura and the Subalpine Molasse does not correlate well with timing of known climatic events. This may be explained in different ways. First, as the youngest sediments from the Molasse have been eroded, it is possible that the local climate might

have been different from global trends but was dominated by orographic evolution in the nearby area (Mosbrugger et al., 2005). Second, the orogen might react to climatic signals with a certain response time. For the European Alps the response time was estimated to be c. 5.5 Ma, which implies that short term perturbations such as the Pleistocene glaciations will not affect orogen-scale wedge dynamics (Tomkin and Roe, 2007). However, our finding that the pro-wedge of the Central Alps is at steady-state through time suggest that none of these climatic events was able to perturb the kinematic equilibrium significantly, as previously suggested (e.g. Willett, 1999). We acknowledge that our considerations are only valid for the pro-wedge of the Alps. At the retro-wedge, the Messinian Salinity Crisis at 5.5 Ma seems to be linked to deactivation of thrusting, as visible from seismic imaging of Po Basin sediments (Willett et al., 2006). Moreover, our results are applicable for the Alpine pro-wedge, but are not able to explain the extensive erosion signal reported from the foreland Plateau Molasse (Cederbom et al., 2004; Willett and Schlunegger, 2010; Cederbom et al., 2011; Schlunegger and Mosar, 2011).

5.12 Conclusions

In this study we presented a new approach for constraining palaeo-taper of an orogen by using low temperature thermochronology combined with wedge dynamics. We show that

- the structures within the Subalpine Molasse were repeatedly active throughout the last 10 Ma, independent of kinematic coupling with the Jura fold-and-thrust belt

- the amount of post 10 Ma shortening within the Subalpine Molasse is similar along the strike of the orogen and at least 17-20 km

- the shortening rates for the northern flank of the Central Alps are constant since at least 8 Ma and fall between 1 and 2mm/a

- the taper angle of the Central Alps did not change more than 3° (probably less than 1.5°) since Late Neogene times

- the Central Alps are at kinematic steady state

- the mass flux between erosion and accretion is at steady state

- we have no evidence that Miocene to Pliocene climatic events influenced the wedge stability and kinematics on the northern flank of the Central Alps

5.13 Acknowledgements

6   Conclusions

The goal of this thesis was to constrain the timing and magnitude of thrusting within the orogenic front of the European Alps (the Subalpine Molasse), in order to gain insights on the kinematic history of the orogen and hence on the driving mechanisms responsible for mountain building. Several hypotheses for the driving mechanisms behind late Neogene erosion in the Alpine region have been argued for in the literature, in particular climate, tectonic and geodynamic forcing.

First, suitable profiles across the Subalpine Molasse were selected for applying low temperature thermochronology. Close sampling intervals assured that all potentially active thrusts were covered within the data set. Both, apatite (U-Th)/He and apatite fission track dating were applied to three horizontal transects and two complementary well transects across the Swiss and Austrian parts of the thrusted Molasse.47 fission track ages and 75 single grain (U-Th)/He ages have been produced and modelled with the HeFTy software with the aim to constrain the timing, location and magnitude of tectonic reactivation and erosion in the thrusted part of the basin and the adjacent units. The data set corroborates the previously detected strong Late Neogene erosion signal, but additionally shows that the Subalpine Molasse was tectonically active also during times when the more external Jura fold and thrust belt was deformed. Periods of thrusting occurred at 10, 8, 6-5 Ma and potentially thereafter.

In addition to the geological interpretation, the thermochronological data is interesting from a methodological perspective. Fission track analyses have been carried out using the relatively new LA-ICP-MS technique. For some sample pairs of neighbouring localities and identical tectonic origin, data were compared with conventional EDM dating results. Even though differences between two sampling points might result from changes in heat flow, differential tectonic uplift or variable glacial erosion, the data produced by different analysts with an independent method reproduces well within the error bars. This is the first applied study which offers this comparison and shows that the LA-ICP-MS method can be successfully applied also in settings with comparably young fission track ages.

Next, critical taper analysis of the Alpine pro-wedge was carried out in order to understand the thermochronological signal in the framework of Alpine kinematics. Here, a method was developed (based on an approach suggested by Suppe (2007)), which uses detailed analysis of the surface slope, α, in combination with analysis of the detachment slope to determine the strength of the basal décollement. This was applied along six profiles in the Central Alps, reaching from the undeformed foreland basin to beyond the drainage divide within the orogen. It could be shown that the décollement is exceedingly weak in the frontal part of the wedge but strong in more internal parts. The strength transition from effective coefficients of friction from < 0.05 to ≥ 0.4 is related to a switch of the detachment lithology from the sedimentary cover sequences into the metamorphic basement. The very low values found in the shales - comparably low values are reported from other orogens – are partly caused by slightly elevated pore pressures ($\lambda \approx 0.54$) but require additional mechanisms of dynamic weakening. The method developed is a powerful approach to gain further insights on wedge kinematics and to map detachment characteristics.

Finally, the results of these two methods were combined. An additional profile for thermochronological age dating was chosen to investigate whether tectonic activity of the structures of the Subalpine Molasse is a local phenomenon or independent of the Jura Mountains. It could be seen that the amount of erosion observed in the eastern part of the basin is less than in the west but the minimum amount of shortening post 10 Ma is similar. Using new and previously published thermochronological data in combination with critical wedge considerations, led to the finding that the pro-wedge of the Central Alps is at kinematic and mass-flux steady state since 10 Ma. This implies that observed climate changes did not influence the behaviour of the orogen since the Late Miocene.

7 References

Andersen, T. (2005) Detrital Zircons as Tracers of Sedimentary Provenance: Limiting Conditions from Statistics and Numerical Simulation. *Chemical Geology*, 216, 249-270.

Äppli, A. (1897) Aus Der Geschichte Der Erde. *Schweizerische Pädagogische Zeitschrift*, 7, 30-46.

Armstrong, P.A., Ehlers, T.A., Chapman, D.S., Farley, K.A. & Kamp, P.J.J. (2003) Exhumation of the Central Wasatch Mountains, Utah: 1. Patterns and Timing of Exhumation Deduced from Low-Temperature Thermochronology Data. *J. Geophys. Res.*, 108, 2172.

Arthaud, F. & Matte, P. (1977) Late Paleozoic Strike-Slip Faulting in Southern Europe and Northern Africa: Result of a Right-Lateral Shear Zone between the Appalachians and the Urals. *Geological Society of America Bulletin*, 88, 1305-1320.

Auer, M. & Eisbacher, G.H. (2003) Deep Structure and Kinematics of the Northern Calcareous Alps (Transalp Profile). *International Journal of Earth Sciences*, 92, 210-227.

Baby, P., Colletta, B. & Zubieta, D. (1995) Etude Géométrique Et Expérimentale D'un Bassin Transporté : Exemple Du Synclinorium De L'alto Beni (Andes Centrales). *Bulletin de la Société Géologique de France*, 166, 797-811.

Bachmann, C.E., Wiemer, S., Woessner, J. & Hainzl, S. (2011) Statistical Analysis of the Induced Basel 2006 Earthquake Sequence: Introducing a Probability-Based Monitoring Approach for Enhanced Geothermal Systems. *Geophysical Journal International*, 186, 793-807.

Bachmann, G.H. & Müller, M. (1981) Tiefbohrung Vorderriß 1, (Kalkalpen, Bayern) *Geologica Bavarica*, 81, 17-53.

Bachmann, G.H., Müller, M. & Weggen, K. (1987) Evolution of the Molasse Basin (Germany, Switzerland). *Tectonophysics*, 137, 77-92.

Balthasar, K., Geissler, P. & Heissbauer, H. (1975) *Die Oberbayerische Pechkohle*.

Barbarand, J., Carter, A., Wood, I. & Hurford, T. (2003a) Compositional and Structural Control of Fission-Track Annealing in Apatite. *Chemical Geology*, 198, 107-137.

Barbarand, J., Hurford, T. & Carter, A. (2003b) Variation in Apatite Fission-Track Length Measurement: Implications for Thermal History Modelling. *Chemical Geology*, 198, 77-106.

Baxter, E.F. (2010) Diffusion of Noble Gases in Minerals. *Reviews in Mineralogy and Geochemistry*, 72, 509-557.

Beaumont, C., Jamieson, R.A., Nguyen, M.H. & Lee, B. (2001) Himalayan Tectonics Explained by Extrusion of a Low-Viscosity Crustal Channel Coupled to Focused Surface Denudation. *Nature*, 414, 738-742.

Becker, A. (2000) The Jura Mountains — an Active Foreland Fold-and-Thrust Belt? *Tectonophysics*, 321, 381-406.

Belton, D.X., Lorencak, M., Carter, T.J., Norman, M., Kohn, B.P. & Gleadow, A. (2004b) Samarium in Apatite: Contributions to Radiogenic Helium and the Effect on (U-Th)/He Thermochronology. *10th International Fission Track Dating Conference*. P. Andressien. Amsterdam**,** 40.

Berge, T.B. & Veal, S.L. (2005) Structure of the Alpine Foreland. *Tectonics*, 24, TC5011.

Berger, J.P., Reichenbacher, B., Becker, D., Grimm, M., Grimm, K., Picot, L., Storni, A., Pirkenseer, C., Derer, C. & Schaefer, A. (2005a) Paleogeography of the Upper Rhine Graben (Urg) and the Swiss Molasse Basin (Smb) from Eocene to Pliocene. *International Journal of Earth Sciences*, 94, 697-710.

Berger, J.P., Reichenbacher, B., Becker, D., Grimm, M., Grimm, K., Picot, L., Storni, A., Pirkenseer, C. & Schaefer, A. (2005b) Eocene-Pliocene Time Scale and Stratigraphy of the Upper Rhine Graben (Urg) and the Swiss Molasse Basin (Smb). *International Journal of Earth Sciences*, 94, 711-731.

Bianchetti, G., Roth, P. & Vuataz, F.-D. (1992) Deep Groundwater Circulation in the Alps : Relations between Water Infiltration, Induced Seismicity and Thermal Springs : The Case of Val D'illiez, Wallis, Switzerland. *Eclogae Geol. Helv.*, 85, 291-305.

Bini, A., Buoncristiani, J.F., Couterrand, S., Eliwanger, D., Felber, M., Florineth, D., Graf, H.B., Keller, O., Kelly, M.A., C., S. & Schoeneich, P. (2009) Die Schweiz Während Des Letzteiszeitlichen Maximums. C. Schlüchter, Bundesamt für Landestopografie swisstopo. Wabern.

Bistacchi, Dal, P., Massironi, Zattin & Balestrieri (2001) The Aosta-Ranzola Extensional Fault System and Oligocene-Present Evolution of the Austroalpine-Penninic Wedge in the Northwestern Alps. *International Journal of Earth Sciences*, 90, 654-667.

Bollinger, T., Engesser, B. & Weidmann, M. (1993) Première Découverte De Mammifères Pliocènes Dans Le Jura Neuchâtelois. *Eclogae Geol. Helv.*, 86, 1031-1068.

Bonfiglioli, G., Ferro, A. & Mojoni, A. (1961) Electron Microscope Investigation on the Nature of Tracks of Fission Products in Mica. *Journal of Applied Physics*, 32, 2499-2503.

Bose, S., Mandal, N., Mukhopadhyay, D.K. & Mishra, P. (2009) An Unstable Kinematic State of the Himalayan Tectonic Wedge: Evidence from Experimental Thrust-Spacing Patterns. *Journal of Structural Geology*, 31, 83-91.

Boyer, S.E. & Elliott, D. (1982) Thrust Systems. *AAPG Bulletin*, 66, 1196-1230.

Braun, J. (2002) Quantifying the Effect of Recent Relief Changes on Age-Elevation Relationships. *Earth and Planetary Science Letters*, 200, 331-343.

Braun, J., Van der Beek, P.A. & Batt, G. (2006) *Quatitative Thermochronology: Numerical Methods for the Interpretation of Thermochronological Data*, first edn. Cambridge Univ. Press, New York.

Brown, R.W., Beucher, R., Gallagher, K., Persano, C., Stuart, F.M. & Fitzgerald, P.G. (2011) A New Approach to Deriving Thermal History Information from Apatite (U-Th)/He Analyses Which

Exploits the Natural Dispersion of Single Crystal Age Determinations. *Geophysical Research Abstracts*, 13, EGU2011-8194-2013,.

Bruch, A.A., Uhl, D. & Mosbrugger, V. (2007) Miocene Climate in Europe - Patterns and Evolution - a First Synthesis of Neclime. *Palaeogeography Palaeoclimatology Palaeoecology*, 253, 1-7.

Brudy, M., Zoback, M.D., Fuchs, K., Rummel, F. & Baumgärtner, J. (1997) Estimation of the Complete Stress Tensor to 8 Km Depth in the Ktb Scientific Drill Holes: Implications for Crustal Strength. *J. Geophys. Res.*, 102, 18453-18475.

Buiter, S.J.H. (2012) A Review of Brittle Compressional Wedge Models. *Tectonophysics*, 530–531, 1-17.

Burkhard, M. (1990) Aspects of Large-Scale Miocene Deformation in the Most External Part of the Swiss Alps (Subalpine Molasse to Jura Fold Belt). *Eclogae Geol. Helv.* , 83, 559-583.

Burkhard, M. & Sommaruga, A. (1998a) Evolution of the Western Swiss Molasse Basin: Structural Relations with the Alps and the Jura Belt. In: *Geological Society, London, Special Publications* (Ed. by A. Mascle, C. Puigdefabregas, H. P. Luterbacher & M. Fernandez), 134, 279-298.

Burkhard, M. & Sommaruga, A. (1998b) *Evolution of the Western Swiss Molasse Basin: Structural Relations with the Alps and the Jura Belt*.

Byerlee, J. (1978) Friction of Rocks. *Pure and Applied Geophysics*, 116, 615-626.

Cadisch, J. (1928) Das Werden Der Alpen Im Spiegel Der Vorlandsedimentation. *Geologische Rundschau*, 19, 105-119.

Calais, E., Nocquet, J.-M., Jouanne, F. & Tardy, M. (2002) Current Strain Regime in the Western Alps from Continuous Global Positioning System Measurements, 1996-2001. *Geology*, 30, 651-654.

Calassou, S., Larroque, C. & Malavieille, J. (1993) Transfer Zones of Deformation in Thrust Wedges: An Experimental Study. *Tectonophysics*, 221, 325-344.

Carlson, W.D., Donelick, R.A. & Ketcham, R.A. (1999) Variability of Apatite Fission-Track Annealing Kinetics: I. Experimental Results. *American Mineralogist*, 84, 1213-1223.

Caron, C., Homewood, P. & Wildi, W. (1989) The Original Swiss Flysch: A Reappraisal of the Type Deposits in the Swiss Prealps. *Earth-Science Reviews*, 26, 1-45.

Cederbom, C.E., Sinclair, H.D., Schlunegger, F. & Rahn, M.K. (2004) Climate-Induced Rebound and Exhumation of the European Alps. *Geology*, 32, 709-712.

Cederbom, C.E., Schlunegger, F., Sinclair, H.D. & Van der Beek, P.A. (2008) Late Neogene Climatic, Tectonic and Geodynamic(?) Forcing on the European Alps Recorded by the Erosion History of the North Alpine Foreland Basin *Geophysical Research Abstracts*, 10, EGU2008-A-01147.

Cederbom, C.E., Schlunegger, F., van der Beek, P.A., Sinclair, H.D. & Oncken, O. (2011) Rapid, Extensive Erosion of the North Alpine Foreland Basin at 5-4 Ma. *Basin Research*, 23, 528-550.

Chadderton, L.T. (2003) Nuclear Tracks in Solids: Registration Physics and the Compound Spike. *Radiation Measurements*, 36, 13-34.

Champagnac, J.D., Schlunegger, F., Norton, K., von Blanckenburg, F., Abbuhl, L.M. & Schwab, M. (2009) Erosion-Driven Uplift of the Modern Central Alps. *Tectonophysics*, 474, 236-249.

Couzens-Schultz, B.A., Vendeville, B.C. & Wiltschko, D.V. (2003) Duplex Style and Triangle Zone Formation: Insights from Physical Modeling. *Journal of Structural Geology*, 25, 1623-1644.

Dahlen, F.A. (1984) Noncohesive Critical Coulomb Wedges: An Exact Solution. *J. Geophys. Res.*, 89, 10125-10133.

Dahlen, F.A., Suppe, J. & Davis, D. (1984) Mechanics of Fold-and-Thrust Belts and Accretionary Wedges: Cohesive Coulomb Theory. *J. Geophys. Res.*, 89, 10087-10101.

Dahlen, F.A. (1990) Critical Taper Model of Fold-and-Thrust Belts and Accretionary Wedges. *Annual Review of Earth and Planetary Sciences*, 18, 55-99.

Davis, D., Suppe, J. & Dahlen, F.A. (1983) Mechanics of Fold-and-Thrust Belts and Accretionary Wedges. *J. Geophys. Res.*, 88, 1153-1172.

Davis, D. & von Huene, R. (1987) Inferences on Sediment Strength and Fault Friction from Structures at the Aleutian Trench. *Geology*, 15, 517-522.

De Quervain, F. (1928) Zur Petrographie Und Geologie Der Taveyannaz-Gesteine. *Schweizerische mineralogische und petrographische Mitteilungen*, 8, 1-87.

Deichmann, N. & Rybach, L. (1989) Earthquakes and Temperatures in the Lower Crust Below the Northern Alpine Foreland of Switzerland. In: *Properties and Processes of the Earth's Lower Crust* (Ed. by R. F. Mereu, S. Mueller & D. M. Fountain), 51, 197-213. American Geophysical Union, Geophysical Monograph.

Deichmann, N. & Marschall, I. (2002) Focal Mechanism Catalog of Earthquakes in Switzerland and Neighboring Countries, Compiled for Project Pegasos. *Swiss Seismological Service - ETH Zürich*.

Deichmann, N., Baer, M., Braunmiller, J., Husen, S., Fäh, D., Giardini, D., Kästli, P., Kradolfer, U. & Wiemer, S. (2006) Earthquakes in Switzerland and Surrounding Regions During 2005. *Eclogae Geologicae Helvetiae*, 99, 443-452.

Deichmann, N. & Ernst, J. (2009) Earthquake Focal Mechanisms of the Induced Seismicity in 2006 and 2007 Below Basel (Switzerland). *Swiss Journal of Geosciences*, 102, 457-466.

Deichmann, N. (2010) Earthquakes in Switzerland and Surrounding Regions 1996-2009 Version 2010.1. *Swiss Seismological Service - ETH Zürich*.

Delacou, B., Sue, C., Champagnac, J.D. & Burkhard, M. (2004) Present-Day Geodynamics in the Bend of the Western and Central Alps as Constrained by Earthquake Analysis. *Geophysical Journal International*, 158, 753-774.

Dodson, M.H. (1973) Closure Temperature in Cooling Geochronological and Petrological Systems. *Contributions to Mineralogy and Petrology*, 40, 259-274.

Donelick, R.A., Ketcham, R.A. & Carlson, W.D. (1999) Variability of Apatite Fission-Track Annealing Kinetics: Ii. Crystallographic Orientation Effects. *American Mineralogist*, 84, 1224-1234.

Donelick, R.A., O'Sullivan, P.B. & Ketcham, R.A. (2005) Apatite Fission-Track Analysis. *Reviews in Mineralogy and Geochemistry*, 58, 49-94.

Driscoll, N.W. & Haug, G.H. (1998) A Short Circuit in Thermohaline Circulation: A Cause for Northern Hemisphere Glaciation? *Science*, 282, 436-438.

Dunai, T.J. (2005) Forward Modeling and Interpretation of (U-Th)/He Ages. *Reviews in Mineralogy and Geochemistry*, 58, 259-274.

Eberhard, M. (1986) Litho- Und Biostratigraphie Im Oberen Süßwassermolasse-Fächer Der Adelegg (Südbayern). *Jahrbuch der Geologischen Bundesanstalt*, 129, 5-39.

Ehlers, T.A. & Farley, K.A. (2003) Apatite (U-Th)/He Thermochronometry: Methods and Applications to Problems in Tectonic and Surface Processes. *Earth and Planetary Science Letters*, 206, 1-14.

Ehlers, T.A., Willett, S.D., Armstrong, P.A. & Chapman, D.S. (2003) Exhumation of the Central Wasatch Mountains, Utah: 2. Thermokinematic Model of Exhumation, Erosion, and Thermochronometer Interpretation. *J. Geophys. Res.*, 108, 2173.

Ehlers, T.A. (2005) Crustal Thermal Processes and the Interpretation of Thermochronometer Data. *Reviews in Mineralogy and Geochemistry*, 58, 315-350.

Escher, A. & Beaumont, C. (1997) Formation, Burial and Exhumation of Basement Nappes at Crustal Scale: A Geometric Model Based on the Western Swiss-Italian Alps. *Journal of Structural Geology*, 19, 955-974.

ETHZ, I.f.K.u.G. (2004) Atlas Der Schweiz 2.0.2, Swisstopo. Zürich.

Fäh, D., Giardini, D., Kästli, P., Deichmann, N., Gisler, M., Schwarz-Zanetti, G., Alvarez-Rubio, S., Sellami, S., Edwards, B., Allmann, B., Bethmann, F., Wössner, J., Gassner-Stamm, G., Fritsche, S. & Eberhard, D. (2011) Ecos-09 Earthquake Catalogue of Switzerland Release 2011. Report and Database. Public Catalogue, Swiss Seismological Service ETH Zürich.

Farley, K.A., Wolf, R.A. & Silver, L.T. (1996) The Effects of Long Alpha-Stopping Distances on (U-Th)/He Ages. *Geochimica Et Cosmochimica Acta*, 60, 4223-4229.

Farley, K.A. (2000) Helium Diffusion from Apatite: General Behavior as Illustrated by Durango Fluorapatite. *Journal of Geophysical Research-Solid Earth*, 105, 2903-2914.

Farley, K.A. & Stöckli, D.F. (2002) (U-Th)/He Dating of Phosphates: Apatite, Monazite, and Xenotime. In: *Reviews of Mineralogy and Geochemistry, Phosphates: Geochemical, Geobiological, and Materials Importance* (Ed. by M. J. Kohn, J. Rakovan & J. M. Hughes), 48, 559-577.

Fitzgerald, P.G., Baldwin, S.L., Webb, L.E. & O'Sullivan, P.B. (2006) Interpretation of (U-Th)/He Single Grain Ages from Slowly Cooled Crustal Terranes: A Case Study from the Transantarctic Mountains of Southern Victoria Land. *Chemical Geology*, 225, 91-120.

Fleischer, R.L., Price, P.B. & Walker, R.M. (1975) *Nuclear Tracks in Solids*. University of California Press, Berkley.

Fletcher, R.C. (1989) Approximate Analytical Solutions for a Cohesive Fold-and-Thrust Wedge: Some Results for Lateral Variation of Wedge Properties and for Finite Wedge Angle. *J. Geophys. Res.*, 94, 10347-10354.

Flowers, R.M., Ketcham, R.A., Shuster, D.L. & Farley, K.A. (2009) Apatite (U-Th)/He Thermochronometry Using a Radiation Damage Accumulation and Annealing Model. *Geochimica Et Cosmochimica Acta*, 73, 2347-2365.

Foeken, J.P.T., Persano, C., Stuart, F.M. & ter Voorde, M. (2007) Role of Topography in Isotherm Perturbation: Apatite (U-Th)/He and Fission Track Results from the Malta Tunnel, Tauern Window, Austria. *Tectonics*, 26, TC3006.

Frisch, W. (1979) Tectonic Progradation and Plate Tectonic Evolution of the Alps. *Tectonophysics*, 60, 121-139.

Frisch, W., Kuhlemann, J., Dunkl, I. & Brügel, A. (1998) Palinspastic Reconstruction and Topographic Evolution of the Eastern Alps During Late Tertiary Tectonic Extrusion. *Tectonophysics*, 297, 1-15.

Frisch, W., Dunkl, I. & Kuhlemann, J. (2000) Post-Collisional Orogen-Parallel Large-Scale Extension in the Eastern Alps. *Tectonophysics*, 327, 239-265.

Fuchs, W. (1976) Gedanken Zur Tektogenese Der Nördlichen Molasse Zwischen Rhone Und March. *Jahrbuch der Geologischen Bundesanstalt*, 119, 207-249.

Füchtbauer, H. (1967) Die Sandsteine in Der Molasse Nördlich Der Alpen. *Geologische Rundschau*, 56, 266-300.

Fügenschuh, B. & Schmid, S.M. (2003) Late Stages of Deformation and Exhumation of an Orogen Constrained by Fission-Track Data: A Case Study in the Western Alps. *Geological Society of America Bulletin*, 115, 1425-1440.

Fuller, C.W., Willett, S.D., Fisher, D. & Lu, C.Y. (2006) A Thermomechanical Wedge Model of Taiwan Constrained by Fission-Track Thermochronometry. *Tectonophysics*, 425, 1-24.

Galbraith, R.F. & Laslett, G.M. (1993) Statistical Models for Mixed Fission Track Ages. *International Journal of Radiation Applications and Instrumentation. Part D. Nuclear Tracks and Radiation Measurements*, 21, 459-470.

Galbraith, R.F. (2005) *Statistics for Fission Track Analysis.*, Boca Raton, FL.

Ganss, O. & Schmidt-Thomé, P. (1953) Die Gefaltete Molasse Am Alpenrand Zwischen Bodensee Und Salzach. *Zeitschrift der Deutschen Geologischen Gesellschaft*, 105, 402-495.

Gebauer, D. (1999) Alpine Geochronology of the Central and Western Alps: New Constraints for a Complex Geodynamic Evolution. *Schweizerische mineralogische und petrographische Mitteilungen*, 79, 191-208.

Genser, J., Cloetingh, S.A.P.L. & Neubauer, F. (2007) Late Orogenic Rebound and Oblique Alpine Convergence: New Constraints from Subsidence Analysis of the Austrian Molasse Basin. *Global and Planetary Change*, 58, 214-223.

Giamboni, M., Ustaszewski, K., Schmid, S.M., Schumacher, M.E. & Wetzel, A. (2004) Plio-Pleistocene Transpressional Reactivation of Paleozoic and Paleogene Structures in the Rhine-Bresse Transform Zone (Northern Switzerland and Eastern France). *International Journal of Earth Sciences*, 93, 207-223.

Gleadow, A. & Duddy, I.R. (1981) A Natural Long Term Annealing Experiment for Apatite. *Nuclear Tracks and Radiation Measurements*, 5, 169-174.

Glotzbach, C., Reinecker, J., Dani, ík, M., Rahn, M., Frisch, W. & Spiegel, C. (2010) Thermal History of the Central Gotthard and Aar Massifs, European Alps: Evidence for Steady State, Long-Term Exhumation. *J. Geophys. Res.*, 115, F03017.

Glotzbach, C., Bernet, M. & van der Beek, P. (2011a) Detrital Thermochronology Records Changing Source Areas and Steady Exhumation in the Western European Alps. *Geology*, 39, 239-242.

Glotzbach, C., van der Beek, P.A. & Spiegel, C. (2011b) Episodic Exhumation and Relief Growth in the Mont Blanc Massif, Western Alps from Numerical Modelling of Thermochronology Data. *Earth and Planetary Science Letters*, 304, 417-430.

Graveleau, F., Malavieille, J. & Dominguez, S. (2012) Experimental Modelling of Orogenic Wedges: A Review. *Tectonophysics*, 538–540, 1-66.

Green, P.F., Duddy, I.R., Gleadow, A.J.W., Tingate, P.R. & Laslett, G.M. (1986) Thermal Annealing of Fission Tracks in Apatite: 1. A Qualitative Description. *Chemical Geology*, 59, 237-253.

Green, P.F., Duddy, I.R., Laslett, G.M., Hegarty, K.A., Gleadow, A.J.W. & Lovering, J.F. (1989) Thermal Annealing of Fission Tracks in Apatite: 4. Quantitative Modeling Techniques and Extension to Geological Timescales,. *Chemical Geology*, 79, 155-182.

Grossman, J., Grossman, M. & Katz, R. (1983) *Averages: A New Approach*. Archimedes Foundation, Rockport, Massachusetts.

Gupta, H.K., Rastogi, B.K. & Narain, H. (1972) Common Features of the Reservoir-Associated Seismic Activities. *Bulletin of the Seismological Society of America*, 62, 481-492.

Haeuselmann, P., Granger, D.E., Jeannin, P.-Y. & Lauritzen, S.-E. (2007) Abrupt Glacial Valley Incision at 0.8 Ma Dated from Cave Deposits in Switzerland. *Geology*, 35, 143-146.

von Hagke, C., Cederbom, C.E., Lindow, J., Oncken, O. & Schlunegger, F. (2010) Post 5ma Thrusting in the Northern Alpine Foreland Basin - Insights from Structural Geology and New (U-Th)/He and Fission Track Data. *Geophysical Research Abstracts*, 12, EGU2010-8858-2011.

von Hagke, C., Cederbom, C.E., Oncken, O., Stockli, D.F., Rahn, M. & Schlunegger, F. (in review) Linking the Northern Alps with Their Foreland: The Latest Uplift and Erosion History Resolved with Low Temperature Thermochronology. *submitted to Tectonics*.

von Hagke, C. & Oncken, O. (submitted) Critical Taper Analysis of the Central Alps Reveals Lithological Control of Variations in Detachment Strength. *G³*.

Handy, M.R., Schmid, S.M., Bousquet, R., Kissling, E. & Bernoulli, D. (2010) Reconciling Plate-Tectonic Reconstructions of Alpine Tethys with the Geological-Geophysical Record of Spreading and Subduction in the Alps. *Earth-Science Reviews*, 102, 121-158.

Hantke, R. (2006) Blatt 1151 Rigi - Geol. Atlas Schweiz 1:25.000 Erläut.116., Bundesamt für Landestopografie. Bern.

Häring, M.O., Schanz, U., Ladner, F. & Dyer, B.C. (2008) Characterisation of the Basel 1 Enhanced Geothermal System. *Geothermics*, 37, 469-495.

Harrison, T.M. & Zeitler, P.K. (2005) Fundamentals of Noble Gas Thermochronometry. *Reviews in Mineralogy and Geochemistry*, 58, 123-149.

Hasebe, N., Barbarand, J., Jarvis, K., Carter, A. & Hurford, A.J. (2004) Apatite Fission-Track Chronometry Using Laser Ablation Icp-Ms. *Chemical Geology*, 207, 135-145.

Haug, G.H. & Tiedemann, R. (1998) Effect of the Formation of the Isthmus of Panama on Atlantic Ocean Thermohaline Circulation. *Nature*, 393, 673-676.

Heidbach, O., Tingay, M., Barth, A., Reinecker, J., Kurfeß, D. & Müller, B. (2008) The 2008 Release of the World Stress Map *(available online at www.world-stress-map.org)*.

Heim, A. (1919) *Geologie Der Schweiz. Bd.1, Molasseland Und Juragebirge*, Leipzig.

Herb, R. (1988) Eocaene Paläogeographie Und Paläotektonik Des Helvetikums. *Eclogae Geol. Helv.*, 81, 611-657.

Herrmann, P., Draxler, I. & Müller, M. (1985) Erläuterungen Zu Blatt 83 Sulzberg *Geologische Karte der Republik Österreich 1:25.000*. G. Bundesanstalt, Geologische Bundesanstalt. Wien.

Hinsch, R. & Linzer, H.-G. (2010) Along-Strike Variations of Structural Styles in the Imbricated Molasse of Salzburg and Upper Austria: A 3-D Seismic Perspective. *EGU General Assembly 2010*, Geophysical Research Abstracts. Vienna, Ausrtia. 11**,** EGU2010-4966-2013.

Hodell, D.A., Curtis, J.H., Sierro, F.J. & Raymo, M.E. (2001) Correlation of Late Miocene to Early Pliocene Sequences between the Mediterranean and North Atlantic. *Paleoceanography*, 16, 164-178.

Homewood, P. (1983) Palaeogeography of Alpine Flysch. *Palaeogeography, Palaeoclimatology, Palaeoecology*, 44, 169-184.

Homewood, P.W. & Caron, C. (1982) Flysch of the Western Alps. In: *Mountain Building Processes* (Ed. by K. J. Hsü), 157-168. Academic Press, London.

Homewood, P.W., Allen, P.A. & Williams, G.D. (1986) Dynamics of the Molasse Basin of Western Switzerland. In: *Foreland Basins* (Ed. by P. A. Allen & P. W. Homewood), *Special Publications*, 8, 199-217. International Association of Sedimentologists, Oxford.

Hurford, A.J., Flisch, M. & Jäger, E. (1989) Unravelling the Thermo-Tectonic Evolution of the Alps: A Contribution from Fission Track Analysis and Mica Dating. *Geological Society, London, Special Publications*, 45, 369-398.

Husen, S., Bachmann, C. & Giardini, D. (2007) Locally Triggered Seismicity in the Central Swiss Alps Following the Large Rainfall Event of August 2005. *Geophysical Journal International*, 171, 1126-1134.

Husen, S., Kissling, E. & von Deschwanden, A. (2012) Induced Seismicity During the Construction of the Gotthard Base Tunnel, Switzerland: Hypocenter Locations and Source Dimensions. *Journal of Seismology*, 1-19.

Jin, J., Aigner, T., Luterbacher, H.P., Bachmann, G.H. & Müller, M. (1995) Sequence Stratigraphy and Depositional History in the South-Eastern German Molasse Basin. *Marine and Petroleum Geology*, 12, 929-936, IN923-IN928, 937-938, IN929-IN914, 939-940.

Jordan, P. & Nüesch, R. (1989) Deformational Behavior of Shale Interlayers in Evaporite Detachment Horizons, Jura Overthrust, Switzerland. *Journal of Structural Geology*, 11, 859-871.

Kälin, D. (1997) Litho- Und Biostratigraphie Der Mittel- Bis Obermiozänen Bois De Raube-Formation (Nordwestschweiz). *Eclogae Geol. Helv.*, 90, 97-114.

Kastrup, U., Zoback, M.L., Deichmann, N., Evans, K.F., Giardini, D. & Michael, A.J. (2004) Stress Field Variations in the Swiss Alps and the Northern Alpine Foreland Derived from Inversion of Fault Plane Solutions. *Journal of Geophysical Research-Solid Earth*, 109, -.

Kempf, O., Matter, A., Burbank, D.W. & Mange, M. (1999) Depositional and Structural Evolution of a Foreland Basin Margin in a Magnetostratigraphic Framework: The Eastern Swiss Molasse. *International Journal of Earth Sciences* 88, 253-275.

Kempf, O. & Pfiffner, O.A. (2004) Early Tertiary Evolution of the North Alpine Foreland Basin of the Swiss Alps and Adjoining Areas. *Basin Research*, 16, 549-567.

Ketcham, R.A., Donelick, R.A. & Carlson, W.D. (1999) Variability of Apatite Fission-Track Annealing Kinetics: Iii. Extrapolation to Geological Time Scales. *American Mineralogist*, 84, 1235-1255.

Ketcham, R.A. (2005) Forward and Inverse Modeling of Low-Temperature Thermochronometry Data. *Reviews in Mineralogy and Geochemistry*, 58, 275-314.

Ketcham, R.A., Carter, A., Donelick, R.A., Barbarand, J. & Hurford, A.J. (2007a) Improved Modeling of Fission-Track Annealing in Apatite. *American Mineralogist*, 92, 799-810.

Ketcham, R.A., Carter, A., Donelick, R.A., Barbarand, J. & Hurford, A.J. (2007b) Improved Measurement of Fission-Track Annealing in Apatite Using C-Axis Projection. *American Mineralogist*, 92, 789-798.

Ketcham, R.A. (2009) Refinements for Alpha Stopping Distances and Ft Corrections. *Ontrack* 16.

Krayenbuhl, T. & Steck, A. (2009) Structure and Kinematics of the Jungfrau Syncline, Faflertal (Valais, Alps), and Its Regional Significance. *Swiss Journal of Geosciences*, 102, 441-456.

Krijgsman, W., Hilgen, F.J., Raffi, I., Sierro, F.J. & Wilson, D.S. (1999) Chronology, Causes and Progression of the Messinian Salinity Crisis. *Nature*, 400, 652-655.

Kuhlemann, J. (2000) Post-Collisional Sediment Budget of Circum-Alpine Basins (Central Europe). *Mem Sci Geol Padova*, 52, 1-91.

Kuhlemann, J. & Kempf, O. (2002) Post-Eocene Evolution of the North Alpine Foreland Basin and Its Response to Alpine Tectonics. *Sedimentary Geology*, 152, 45-78.

Kuhlemann, J. (2007) Paleogeographic and Paleotopographic Evolution of the Swiss and Eastern Alps since the Oligocene. *Global and Planetary Change*, 58, 224-236.

Lacombe, O. & Mouthereau, F. (2002) Basement-Involved Shortening and Deep Detachment Tectonics in Forelands of Orogens: Insights from Recent Collision Belts (Taiwan, Western Alps, Pyrenees). *Tectonics*, 21, 1030.

Lammerer, B. & Weger, M. (1998) Footwall Uplift in an Orogenic Wedge: The Tauern Window in the Eastern Alps of Europe. *Tectonophysics*, 285, 213-230.

Lammerer, B., Gebrande, H., Lüschen, E. & Veselá, P. (2008) A Crustal-Scale Cross-Section through the Tauern Window (Eastern Alps) from Geophysical and Geological Data. *Geological Society, London, Special Publications*, 298, 219-229.

Laubscher, H.P. (1977) Fold Development in the Jura. *Tectonophysics*, 37, 337-362.

Lemcke, K. (1984) Geologische Vorgänge in Den Alpen Ab Obereozän Im Spiegel Vor Allem Der Deutschen Molasse. *Geologische Rundschau*, 73, 371-397.

Letouzey, J., Colletta, B., Vially, R. & Chermette, J.C. (1995) Evolution of Salt-Related Structures in Compressional Settings. In: *Salt Tectonics; a Global Perspective* (Ed. by M. P. A. Jackson, D. G. Roberts & S. Snelson), 65. American Association of Petroleum Geologists Memoir.

Lickorish, W.H., Ford, M., Bürgisser, J. & Cobbold, P.R. (2002) Arcuate Thrust Systems in Sandbox Experiments: A Comparison to the External Arcs of the Western Alps. *Geological Society of America Bulletin*, 114, 1089-1107.

Liddle, A.R. (2007) Information Criteria for Astrophysical Model Selection. *Monthly Notices of the Royal Astronomical Society: Letters*, 377, L74-L78.

Liniger, H. (1964) Beziehungen Zwischen Pliozän Und Jurafaltung in Der Ajoie. *Eclogae Geol. Helv.*, 57, 75-90.

Liu, C.C., Linde, A.T. & Sacks, I.S. (2009) Slow Earthquakes Triggered by Typhoons. *Nature*, 459, 833-836.

Lock, J. & Willett, S.D. (2008) Low-Temperature Thermochronometric Ages in Fold-and-Thrust Belts. *Tectonophysics*, 456, 147-162.

Lohrmann, J., Kukowski, N., Adam, J. & Oncken, O. (2003) The Impact of Analogue Material Properties on the Geometry, Kinematics, and Dynamics of Convergent Sand Wedges. *Journal of Structural Geology*, 25, 1691-1711.

Lüschen, E., Borrini, D., Gebrande, H., Lammerer, B., Millahn, K., Neubauer, F. & Nicolich, R. (2006) Transalp--Deep Crustal Vibroseis and Explosive Seismic Profiling in the Eastern Alps. *Tectonophysics*, 414, 9-38.

Macedo, J.M.B., Gottschalk, L.M.F. & Bon, E.P.S. (1999) Calcium Carbonate Mediates Higher Lignin Peroxidase Activity in the Culture Supernatant of Streptomyces Viridosporus T7a. *Brazilian Journal of Chemical Engineering*, 16, 163-169.

Madritsch, H., Schmid, S.M. & Fabbri, O. (2008) Interactions between Thin- and Thick-Skinned Tectonics at the Northwestern Front of the Jura Fold-and-Thrust Belt (Eastern France). *Tectonics*, 27, -.

Madritsch, H., Preusser, F., Fabbri, O., Bichet, V., Schlunegger, F. & Schmid, S.M. (2010) Late Quaternary Folding in the Jura Mountains: Evidence from Syn-Erosional Deformation of Fluvial Meanders. *Terra Nova*, 22, 147-154.

Malusa, M.G. & Vezzoli, G. (2006) Interplay between Erosion and Tectonics in the Western Alps. *Terra Nova*, 18, 104-108.

Mandal, N., Chattopadhyay, A. & Bose, S. (1997) Imbricate Thrust Spacing: Experimental and Theoretical Analyses. In: *Evolution of Geological Structures in Micro to Macro-Scales* (Ed. by S. Sengupta), 143–165. Chapman and Hall, London.

Matter, A., Homewood, P.W., Caron, C., Van Stuijvenberg, J., Weidmann, M. & Winkler, W. (1980) Flysch and Molasse of Central and Western Switzerland. In: *Geology of Switzerland, a Guide Book, Part B: Geological Excursions* (Ed. by S. G. Kommission), 261-293. Wepf & Co., Basel, New York.

Mazurek, M., Hurford, A.J. & Leu, W. (2006) Unravelling the Multi-Stage Burial History of the Swiss Molasse Basin: Integration of Apatite Fission Track, Vitrinite Reflectance and Biomarker Isomerisation Analysis. *Basin Research*, 18, 27-50.

Michalski, I. & Soom, M. (1990) The Alpine Thermo-Tectonic Evolution Ofthe Aar and Gotthard Massifs, Central Switzerland: Fission Track Ages on Zircon and Apatite and K-Ar Mica Ages. *Schweizerische mineralogische und petrographische Mitteilungen*, 70, 373-387.

Milnes, A.G. & Pfiffner, O.A. (1977) Structural Development of the Infrahelvetic Complex, Eastern Switzerland. *Eclogae Geol. Helv.*, 70, 83-95.

Milnes, A.G. & Pfiffner, O.A. (1980) Tectonic Evolution of the Central Alps in the Cross Section St. Gallen-Como. *Eclogae Geol. Helv.*, 73, 619-633.

Molnar, P. & England, P. (1990) Late Cenozoic Uplift of Mountain Ranges and Global Climate Change: Chicken or Egg? *Nature*, 346, 29-34.

Molnar, P. (2004) Late Cenozoic Increase in Accumulation Rates of Terrestrial Sediment: How Might Climate Change Have Affected Erosion Rates? *Annual Review of Earth and Planetary Sciences*, 32, 67-89.

Montgomery, D.R. & Brandon, M.T. (2002) Topographic Controls on Erosion Rates in Tectonically Active Mountain Ranges. *Earth and Planetary Science Letters*, 201, 481-489.

Moore, M.A. & England, P.C. (2001) On the Inference of Denudation Rates from Cooling Ages of Minerals. *Earth and Planetary Science Letters*, 185, 265-284.

Mosar, J. (1999) Present-Day and Future Tectonic Underplating in the Western Swiss Alps: Reconciliation of Basement/Wrench-Faulting and Decollement Folding of the Jura and Molasse Basin in the Alpine Foreland. *Earth and Planetary Science Letters*, 173, 143-155.

Mosbrugger, V., Utescher, T. & Dilcher, D.L. (2005) Cenozoic Continental Climatic Evolution of Central Europe. *Proceedings of the National Academy of Sciences of the United States of America*, 102, 14964-14969.

Müller, M., Nieberding, F. & Wanninger, A. (1988) Tectonic Style and Pressure Distribution at the Northern Margin of the Alps between Lake Constance and the River Inn *Geologische Rundschau*, 77, 787-796.

Nagra (2002) Projekt Opalinuston Synthese Der Geowissenschaftlichen Untersuchungsergebnisse. *Nagra Tech. Ber. NTB*, 02-03, 139-142.

Norton, K.P., von Blanckenburg, F., Schlunegger, F., Schwab, M. & Kubik, P.W. (2008) Cosmogenic Nuclide-Based Investigation of Spatial Erosion and Hillslope Channel Coupling in the Transient Foreland of the Swiss Alps. *Geomorphology*, 95, 474-486.

Norton, K.P., Abbuhl, L.M. & Schlunegger, F. (2010a) Glacial Conditioning as an Erosional Driving Force in the Central Alps. *Geology*, 38, 655-658.

Norton, K.P., von Blanckenburg, F. & Kubik, P.W. (2010b) Cosmogenic Nuclide-Derived Rates of Diffusive and Episodic Erosion in the Glacially Sculpted Upper Rhone Valley, Swiss Alps. *Earth Surface Processes and Landforms*, 35, 651-662.

Okaya, N., Cloetingh, S. & Mueller, S. (1996) A Lithospheric Cross-Section through the Swiss Alps—Ii. Constraints on the Mechanical Structure of a Continent-Continent Collision Zone. *Geophysical Journal International*, 127, 399-414.

Ortner, H., Thöny, W., Aichholzer, S., Pilser, R. & Tomek, C. (2009) Geometry and Sequence of Thrusting in the Alpine Foreland of Western Austria and Bavaria. *Geophysical Research Abstracts*, 11, EGU2009-12318.

Ortner, H., Fuegenschuh, B., Zerlauth, M. & von Hagke, C. (2011). *Geometry, Sequence and Amount of Thrusting in the Subalpine Molasse of Austria and Bavaria*. 10th Alpine Workshop, CorseAlp, Corsica, Universita de Pisa.

Persaud, M. & Pfiffner, O.A. (2004) Active Deformation in the Eastern Swiss Alps: Post-Glacial Faults, Seismicity and Surface Uplift. *Tectonophysics*, 385, 59-84.

Pfiffner, O.A. (1986) Evolution of the North Alpine Foreland Basin in the Central Alps. In: *Foreland Basins* (Ed. by P. A. Allen & P. W. Homewood), *Special Publications*, 8, 219-228. International Association of Sedimentologists, Oxford.

Pfiffner, O.A., Frei, W., Valasek, P., Stäuble, M., Levato, L., DuBois, L., Schmid, S.M. & Smithson, S.B. (1990) Crustal Shortening in the Alpine Orogen: Results from Deep Seismic Reflection Profiling in the Eastern Swiss Alps, Line Nfp 20-East. *Tectonics*, 9, 1327-1355.

Pfiffner, O.A., Erard, P.-F. & Stäuble, M. (1997a) Two Cross Sections through the Swiss Molasse Basin (Lines E4-E6, W1, W7-W110). In: *Deep Structure of the Swiss Alps: Results of Nrp 20* (Ed. by O. A. Pfiffner, P. Lehner, P. Heitzmann, S. Müller & A. Steck), 64-72. Birkhäuser Verlag, Basel.

Pfiffner, O.A., Heitzmann, P., Lehner, P., Frei, W., Pugin, A. & Felber, M. (1997b) Incision and Backfilling of Alpine Valleys: Pliocene, Pleistocene and Holocene Processes. In: *Deep Structure of the Swiss Alps: Results of Nrp 20* (Ed. by O. A. Pfiffner, P. Lehner, P. Heitzmann, S. Müller & A. Steck), 265-288. Birkhäuser Verlag, Basel.

Pfiffner, O.A., Lehner, P., Heitzmann, P., Müller, S. & Steck, A. (1997c) *Deep Structure of the Swiss Alps. Results of Nrp 20*. Birkhäuser Verlag, Basel.

Pfiffner, O.A., Sahli, S. & Stäuble, M. (1997d) Compression and Uplift of the External Massifs in the Helvetic Zone. In: *Deep Structure of the Swiss Alps: Results of Nrp 20* (Ed. by O. A. Pfiffner, P. Lehner, P. Heitzmann, S. Müller & A. Steck), 139-153. Birkhäuser Verlag, Basel.

Pfiffner, O.A., Schlunegger, F. & Buiter, S.J.H. (2002) The Swiss Alps and Their Peripheral Foreland Basin: Stratigraphic Response to Deep Crustal Processes. *Tectonics*, 21, -.

Pfiffner, O.A. (2005) The Alps. *Europe*, 125-135.

Pfiffner, O.A. (2010) *Geologie Der Alpen*, 2. erweiterte Auflage edn. UTB / Haupt Verlag, Bern.

Philippe, Y. (1994) Transfer Zone in the Southern Jura Thrust Belt (Eastern France): Geometry, Development, and Comparison with Analogue Modeling Experiments. *Hydrocarbon and Petroleum Geology in France, Spec. Publ. EAPG*, 4, 327–346.

Philippe, Y., Colletta, B., Deville, E. & Mascle, A. (1996) The Jura Fold-and-Thrust Belt: A Kinematic Model Based on Map-Balancing. In: *Peri-Tethys Memoir 2; Structure and Prospects of Alpine Basins and Forelands* (Ed. by P. A. Ziegler & F. Horvath), Memoires du Museum National d'Histoire Naturelle, vol.170, 235-261. Ed. du Museum National d'Histoire Naturelle, Paris.

Piller, W.E., Egger, H., Erhart, C., Gross, M., Harzhauser, M., Hubmann, B., van Husen, D., Krenmayr, H.-G., Krystyn, L., Lein, R., Lukeneder, A., Mandl, G., Rögl, F., Roetzel, R., Rupp, C., Schnabel, W., Schönlaub, H.P., Summesberger, H. & Wagreich, M. (2004) Die Stratigraphische Tabelle Von Österreich (Sedimentäre Schichtfolgen), Österreichische stratigraphische Kommission für die paläontologische und stratigraphische Erforschung Österreichs.

Rahn, M. & Selbekk, R. (2007) Absolute Dating of the Youngest Sediments of the Swiss Molasse Basin by Apatite Fission Track Analysis. *Swiss Journal of Geosciences*, 100, 371-381.

Ratschbacher, L., Frisch, W., Neubauer, F., Schmid, S.M. & Neugebauer, J. (1989) Extension in Compressional Orogenic Belts: The Eastern Alps. *Geology*, 17, 404-407.

Redfield, T.F. (2010) On Apatite Fission Track Dating and the Tertiary Evolution of West Greenland Topography. *Journal of the Geological Society*, 167, 261-271.

Reinecker, J., Danisik, M., Schmid, C., Glotzbach, C., Rahn, M., Frisch, W. & Spiegel, C. (2008) Tectonic Control on the Late Stage Exhumation of the Aar Massif (Switzerland): Constraints from Apatite Fission Track and (U-Th)/He Data. *Tectonics*, 27, -.

Reiners, P.W. & Farley, K.A. (2001) Influence of Crystal Size on Apatite (U-Th)/He Thermochronology: An Example from the Bighorn Mountains, Wyoming. *Earth and Planetary Science Letters*, 188, 413-420.

Reiners, P.W., Ehlers, T.A. & Zeitler, P.K. (2005) Past, Present, and Future of Thermochronology. *Reviews in Mineralogy and Geochemistry*, 58, 1-18.

Reiners, P.W. & Brandon, M.T. (2006) Using Thermochronology to Understand Orogenic Erosion. *Annual Review of Earth and Planetary Sciences*, 34, 419-466.

Reiners, P.W. & Nicolescu, S. (2006) Measurement of Parent Nuclides for (U-Th)/He Chronometry by Solution Sector Icp-Ms. *ARHDL Report 1*.

Reiners, P.W. (2007) Overview of Analytical Methods in the Arhdl. http://www.geo.arizona.edu/~reiners/arhdl/procs.htm,

Ripperger, J., Kästli, P., Fäh, D. & Giardini, D. (2009) Ground Motion and Macroseismic Intensities of a Seismic Event Related to Geothermal Reservoir Stimulation Below the City of Basel—Observations and Modelling. *Geophysical Journal International*, 179, 1757-1771.

Robert, X., van der Beek, P., Braun, J., Perry, C., Dubille, M. & Mugnier, J.-L. (2009) Assessing Quaternary Reactivation of the Main Central Thrust Zone (Central Nepal Himalaya): New Thermochronologic Data and Numerical Modeling. *Geology*, 37, 731-734.

Rosenberg, C.L. & Berger, A. (2009) On the Causes and Modes of Exhumation and Lateral Growth of the Alps. *Tectonics*, 28, TC6001.

Roth, P., Pavoni, N. & Deichmann, N. (1992) Seismotectonics of the Eastern Swiss Alps and Evidence for Precipitation-Induced Variations of Seismic Activity. *Tectonophysics*, 207, 183-197.

Rothé, J.P. (1970) Seismes Artificiels. *Tectonophysics*, 9, 215-238.

Ruffini, R., Polino, R., Callegari, E., Hunziker, J.C. & Pfeifer, H.R. (1997) Volcanic Clast-Rich Turbidites of the Taveyanne Sandstones from the Thônes Syncline (Savoie, France) : Records for a Teritary Postcollisional Volcanism. *Schweizerische mineralogische und petrographische Mitteilungen*, 77, 161-174.

Rybach, L. & Bodmer, P. (1980) Die Geothermischen Verhältnisse Der Schweizer Geotraverse Im Abschnitt Basel-Luzern. *Eclogae Geol. Helv.*, 73, 501-512.

Rybach, L. & Bodmer, P. (1983) Processing and Representation of Heat Flow Density Maps. Part Ii: Construction and Contouring of Heat Flow Density Maps. *Zbl. Geol. Paläont. Teil I*, 87-92.

Rybach, L. (1984) The Paleogeothermal Conditions of the Swiss Molasse Basin: Implications for Hydrocarbon Potential. *Revue de l'Institut Francais du Pétrole*, 39, 143-147.

Sachsenhofer, R.F. (2001) Syn- and Post-Collisional Heat Flow in the Cenozoic Eastern Alps. *International Journal of Earth Sciences*, 90, 579-592.

Schärli, U. & Rybach, L. (2002) Erstellung Einer Aktuellen Karte Der Temperaturgradienten Und Des Wärmeflusses Der Nordschweiz. *Nagra Int. Ber.*

Schegg, R. (1992) Coalification, Shale Diagenesis and Thermal Modelling in the Alpine Foreland Basin: The Western Molasse Basin (Switzerland/France). *Organic Geochemistry*, 18, 289-300.

Schegg, R. & Leu, W. (1998) Analysis of Erosion Events and Palaeogeothermal Gradients in the North Alpine Foreland Basin of Switzerland. *Geological Society, London, Special Publications*, 141, 137-155.

Schegg, R., Cornford, C. & Leu, W. (1999) Migration and Accumulation of Hydrocarbons in the Swiss Molasse Basin: Implications of a 2d Basin Modeling Study. *Marine and Petroleum Geology*, 16, 511-531.

Schlunegger, F., Burbank, D.W., Matter, A., Engesser, B. & Mödden, C. (1996) Magnetostratigraphic Calibration of the Oligocene to Middle Miocene (30-15 Ma) Mammal Biozones and Depositional Sequences of the Swiss Molasse Basin. *Eclogae Geol. Helv.*, 89, 753-788.

Schlunegger, F., Matter, A., Burbank, D.W. & Klaper, E.M. (1997a) Magnetostratigraphic Constraints on Relationships between Evolution of the Central Swiss Molasse Basin and Alpine Orogenic Events. *Geological Society of America Bulletin*, 109, 225-241.

Schlunegger, F., Matter, A., Burbank, D.W., Leu, W., Mange, M. & Màtyàs, J. (1997b) Sedimentary Sequences, Seismofacies and Evolution of Depositional Systems of the Oligo/Miocene Lower Freshwater Molasse Group, Switzerland. *Basin Research*, 9, 1-26.

Schlunegger, F. (1999) Controls of Surface Erosion on the Evolution of the Alps; Constraints from the Stratigraphies of the Adjacent Foreland Basins. *International Journal of Earth Sciences*, 88, 285-304.

Schlunegger, F., Melzer, J. & Tucker, G.E. (2001) Climate, Exposed Source-Rock Lithologies, Crustal Uplift and Surface Erosion: A Theoretical Analysis Calibrated with Data from the Alps/North Alpine Foreland Basin System *International Journal of Earth Sciences*, 90, 484-499.

Schlunegger, F. & Simpson, G. (2002) Possible Erosional Control on Lateral Growth of the European Central Alps. *Geology*, 30, 907-910.

Schlunegger, F., Rieke-Zapp, D. & Ramseyer, K. (2007) Possible Environmental Effects on the Evolution of the Alps-Molasse Basin System. *Swiss Journal of Geosciences*, 100, 383-405.

Schlunegger, F. (2010) Geologische Karte Schüpfheim Mit Erläuterungen, Unpubl. B. f. L. Swisstopo.

Schlunegger, F. & Mosar, J. (2011) The Last Erosional Stage of the Molasse Basin and the Alps. *International Journal of Earth Sciences*, 100, 1147-1162.

Schmid, S.M., Pfiffner, O.A., Froitzheim, N., Schönborn, G. & Kissling, E. (1996) Geophysical-Geological Transect and Tectonic Evolution of the Swiss-Italian Alps. *Tectonics*, 15, 1036-1064.

Schmid, S.M. & Kissling, E. (2000) The Arc of the Western Alps in the Light of Geophysical Data on Deep Crustal Structure. *Tectonics*, 19, 62-85.

Schmid, S.M., Fügenschuh, B., Kissling, E. & Schuster, R. (2004) Tectonic Map and Overall Architecture of the Alpine Orogen *Eclogae Geol. Helv.*, 97, 93-117.

Schott, B. & Koyi, H.A. (2001) Estimating Basal Friction in Accretionary Wedges from the Geometry and Spacing of Frontal Faults. *Earth and Planetary Science Letters*, 194, 221-227.

Schreurs, G., Hänni, R. & Vock, P. (2001) Four-Dimensional Analysis of Analog Models: Experiments on Transfer Zones in Fold and Thrust Belts. *Geological Society of America Memoirs*, 193, 179-190.

Shuster, D.L., Flowers, R.M. & Farley, K.A. (2006) The Influence of Natural Radiation Damage on Helium Diffusion Kinetics in Apatite. *Earth and Planetary Science Letters*, 249, 148-161.

Simoes, M. & Avouac, J.P. (2006) Investigating the Kinematics of Mountain Building in Taiwan from the Spatiotemporal Evolution of the Foreland Basin and Western Foothills. *J. Geophys. Res.*, 111, B10401.

Sinclair, H.D. & Allen, P.A. (1992) Vertical Versus Horizontal Motions in the Alpine Orogenic Wedge: Stratigraphic Response in the Foreland Basin. *Basin Research*, 4, 215-232.

Sinclair, H.D. (1997a) Tectonostratigraphic Model for Underfilled Peripheral Foreland Basins: An Alpine Perspective. *Geological Society of America Bulletin*, 109, 324-346.

Sinclair, H.D. (1997b) Flysch to Molasse Transition in Peripheral Foreland Basins: The Role of the Passive Margin Versus Slab Breakoff. *Geology*, 25, 1123-1126.

Sissingh, W. (1997) Tectonostratigraphy of the North Alpine Foreland Basin: Correlation of Tertiary Depositional Cycles and Orogenic Phases. *Tectonophysics*, 282, 223-256.

Sommaruga, A. (1999) Décollement Tectonics in the Jura Forelandfold-and-Thrust Belt. *Marine and Petroleum Geology*, 16, 111-134.

Spicher, A. (1980) Tektonische Karte Der Schweiz. B. f. W. u. Geologie, Bundesamt für Landestopographie. Bern.

Stampfli, G.M., Borel, G.D., Cavazza, W., Mosar, J. & Ziegler, P.A. (2001) Palaeotectonic and Palaeogeographic Evolution of the Western Tethys and Peritethyan Domain (Igcp Project 369). *Episodes*, 24, 222-228.

Stockli, D.F., Farley, K.A. & Dumitru, T.A. (2000) Calibration of the Apatite (U-Th)/He Thermochronometer on an Exhumed Fault Block, White Mountains, California. *Geology*, 28, 983-986.

Stockli, D.F. (2005) Application of Low-Temperature Thermochronometry to Extensional Tectonic Settings. *Reviews in Mineralogy and Geochemistry*, 58, 411-448.

Stockli, D.F. (2006) (U-Th)/He Laboratory. http://www.geo.ku.edu/programs/tectonics/helab.html,

Stüwe, K., White, L. & Brown, R. (1994) The Influence of Eroding Topography on Steady-State Isotherms. Application to Fission Track Analysis. *Earth and Planetary Science Letters*, 124, 63-74.

Suppe, J. (2007) Absolute Fault and Crustal Strength from Wedge Tapers. *Geology*, 35, 1127-1130.

Süsstrunk, A. (1968) Erdstösse Im Verzascatal Beim Aufstau Des Speicherbeckens, Vagorno. *Verhandlungen der Schweizerischen Naturforschenden Gesellschaft*, 89-92.

Tagami, T. & O'Sullivan, P.B. (2005) Fundamentals of Fission-Track Thermochronology. *Reviews in Mineralogy and Geochemistry*, 58, 19-47.

Thöny, W. (1999) A Review of Geochronological Data from the Eastern Alps. *Schweizerische mineralogische und petrographische Mitteilungen*, 79, 209-230.

Tomkin, J.H. & Roe, G.H. (2007) Climate and Tectonic Controls on Glaciated Critical-Taper Orogens. *Earth and Planetary Science Letters*, 262, 385-397.

Townend, J. & Zoback, M.D. (2000) How Faulting Keeps the Crust Strong. *Geology*, 28, 399-402.

Trümpy, R. (1960) Paleotectonic Evolution of the Central and Western Alps. *Geological Society of America Bulletin*, 71, 843-907.

Trümpy, R. (1980) Geology of Switzerland In: *Geology of Switzerland - a Guide Book, Part A: An Outline of the Geology of Switzerland* (Ed. by S. G. Kommission). Wepf & Co., Basel.

Ustaszewski, K., Schumacher, M.E., Schmid, S.M. & Nieuwland, D. (2005) Fault Reactivation in Brittle–Viscous Wrench Systems–Dynamically Scaled Analogue Models and Application to the Rhine–Bresse Transfer Zone. *Quaternary Science Reviews*, 24, 363-380.

Ustaszewski, K. & Schmid, S.M. (2006) Control of Preexisting Faults on Geometry and Kinematics in the Northernmost Part of the Jura Fold-and-Thrust Belt. *Tectonics*, 25, TC5003.

Ustaszewski, K. & Schmid, S.M. (2007) Latest Pliocene to Recent Thick-Skinned Tectonics at the Upper Rhine Graben – Jura Mountains Junction. *Swiss Journal of Geosciences*, 100, 293-312.

Valla, P.G., Herman, F., van der Beek, P.A. & Braun, J. (2010) Inversion of Thermochronological Age-Elevation Profiles to Extract Independent Estimates of Denudation and Relief History -- I: Theory and Conceptual Model. *Earth and Planetary Science Letters*, 295, 511-522.

Valla, P.G., Shuster, D.L. & van der Beek, P.A. (2011) Significant Increase in Relief of the European Alps During Mid-Pleistocene Glaciations. *Nature Geosci*, advance online publication.

Valla, P.G., van der Beek, P.A., Shuster, D.L., Braun, J., Herman, F., Tassan-Got, L. & Gautheron, C. (2012) Late Neogene Exhumation and Relief Development of the Aar and Aiguilles Rouges Massifs (Swiss Alps) from Low-Temperature Thermochronology Modeling and 4he/3he Thermochronometry. *J. Geophys. Res.*, 117, F01004.

Valley, B. & Evans, K. (2009) Stress Orientation to 5 km Depth in the Basement Below Basel (Switzerland) from Borehole Failure Analysis. *Swiss Journal of Geosciences*, 102, 467-480.

Vedova, B.D., Lucazeau, F., Pasquale, V., Pellis, G. & Verdoya, M. (1995) Heat Flow in the Tectonic Provinces Crossed by the Southern Segment of the European Geotraverse. *Tectonophysics*, 244, 57-74.

Vermeesch, P. (2004) How Many Grains Are Needed for a Provenance Study? *Earth and Planetary Science Letters*, 224, 441-451.

Vermeesch, P. (2008) Three New Ways to Calculate Average (U-Th)/He Ages. *Chemical Geology*, 249, 339-347.

Vermeesch, P. (2009) Radialplotter: A Java Application for Fission Track, Luminescence and Other Radial Plots. *Radiation Measurements*, 44, 409-410.

Vernon, A.J., van der Beek, P.A. & Sinclair, H.D. (2009a) Spatial Correlation between Long-Term Exhumation Rates and Present-Day Forcing Parameters in the Western European Alps. *Geology*, 37, 859-862.

Vernon, A.J., van der Beek, P.A., Sinclair, H.D., Persano, C., Foeken, J. & Stuart, F.M. (2009b) Variable Late Neogene Exhumation of the Central European Alps: Low-Temperature Thermochronology from the Aar Massif, Switzerland, and the Lepontine Dome, Italy. *Tectonics*, 28, TC5004.

Vesela, P., Lammerer, B., Wetzel, A., Sollner, F. & Gerdes, A. (2008) Post-Variscan to Early Alpine Sedimentary Basins in the Tauern Window (Eastern Alps). *Geological Society, London, Special Publications*, 298, 83-100.

Villa (1998) Isotopic Closure. *Terra Nova*, 10, 42-47.

Vollmayr, T. & Wendt, A. (1987) Die Erdgasbohrung Entlebuch 1, Ein Tiefenaufschluss Am Alpennordrand. *Bulletin der schweizerischen Vereinigung Petroleum-Geologen und -Ingenieure*, 53, 67-79.

Wagner, G.A. & Van den haute, P. (1992) *Fission Track-Dating*. Kluwer Academic Publishers, Dordrecht.

Walter, R. (1995) *Geologie Von Mitteleuropa*, 6 edn, Stuttgart.

Weisenberger, T.B., Rahn, M., van der Lelij, R., Spikings, R.A. & Bucher, K. (2012) Timing of Low-Temperature Mineral Formation During Exhumation and Cooling in the Central Alps, Switzerland. *Earth and Planetary Science Letters*, 327–328, 1-8.

Whipple, K.X. & Meade, B.J. (2006) Orogen Response to Changes in Climatic and Tectonic Forcing. *Earth and Planetary Science Letters*, 243, 218-228.

Whipple, K.X. (2009) The Influence of Climate on the Tectonic Evolution of Mountain Belts. *Nature Geoscience*, 2, 97-104.

Willett, S.D. (1999) Orogeny and Orography: The Effects of Erosion on the Structure of Mountain Belts. *J. Geophys. Res.*, 104, 28957-28981.

Willett, S.D., Schlunegger, F. & Picotti, V. (2006) Messinian Climate Change and Erosional Destruction of the Central European Alps. *Geology*, 34, 613-616.

Willett, S.D. & Schlunegger, F. (2009) The Last Phase of Deposition in the Swiss Molasse Basin: From Foredeep to Negative-Alpha Basin. *Basin Research*, no-no.

Willett, S.D. & Schlunegger, F. (2010) The Last Phase of Deposition in the Swiss Molasse Basin: From Foredeep to Negative-Alpha Basin. *Basin Research*, 22, 623-639.

Wittmann, H., von Blanckenburg, F., Kruesmann, T., Norton, K.P. & Kubik, P.W. (2007) Relation between Rock Uplift and Denudation from Cosmogenic Nuclides in River Sediment in the Central Alps of Switzerland. *J. Geophys. Res.*, 112, F04010.

Wolf, R.A., Farley, K.A. & Silver, L.T. (1996) Helium Diffusion and Low-Temperature Thermochronometry of Apatite. *Geochimica et Cosmochimica Acta*, 60, 4231-4240.

Wolf, R.A., Farley, K.A. & Kass, D.M. (1998) Modeling of the Temperature Sensitivity of the Apatite (U-Th)/He Thermochronometer. *Chemical Geology*, 148, 105-114.

Yin, A. (1993) Mechanics of Wedge-Shaped Fault Blocks 1. An Elastic Solution for Compressional Wedges. *J. Geophys. Res.*, 98, 14245-14256.

Zacher, W. (1995) Kompilation Geologische Manuskriptkarte Ök 112 Bezau, Geologische Bundesanstalt (GBA). Vienna.

Zhang, P.-Z., Molnar, P. & Downs, W.R. (2001) Increased Sedimentation Rates and Grain Sizes 2-4[Thinsp]Myr Ago Due to the Influence of Climate Change on Erosion Rates. *Nature*, 410, 891-897.

Zhang, P.-Z., Shen, Z., Wang, M., Gan, W., Burgmann, R., Molnar, P., Wang, Q., Niu, Z., Sun, J., Wu, J., Hanrong, S. & Xinzhao, Y. (2004) Continuous Deformation of the Tibetan Plateau from Global Positioning System Data. *Geology*, 32, 809-812.

Zhao, W.L., Davis, D., Dahlen, F.A. & Suppe, J. (1986) Origin of Convex Accretionary Wedges: Evidence from Barbados. *J. Geophys. Res.*, 91, 10246-10258.

Ziegler, P.A. (1990) *Geological Atlas of Western and Central Europe: Shell International Petroleum, Maatschappij, 239p*, Den Haag.

Zoback, M.D. & Townend, J. (2001) Implications of Hydrostatic Pore Pressures and High Crustal Strength for the Deformation of Intraplate Lithosphere. *Tectonophysics*, 336, 19-30.

Appendix

I. Helium production rate plots

Helium production rate plots for excluding single grain ages. X-axes are [He] in nmol/g and y-axes is the production rate calculated after formula 1-8. All samples must fit on a straight line going through the origin. Lines fitted by hand. Errors on [He] are 30% as suggested by Vermeesch (2008). Usually, the grains which are not falling on the suggested line could also be rejected due to other reasons (given in table 3-2)
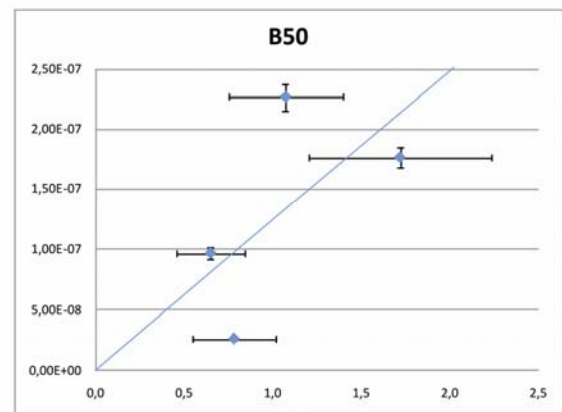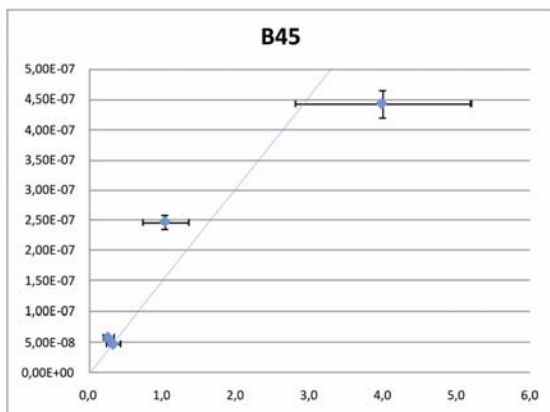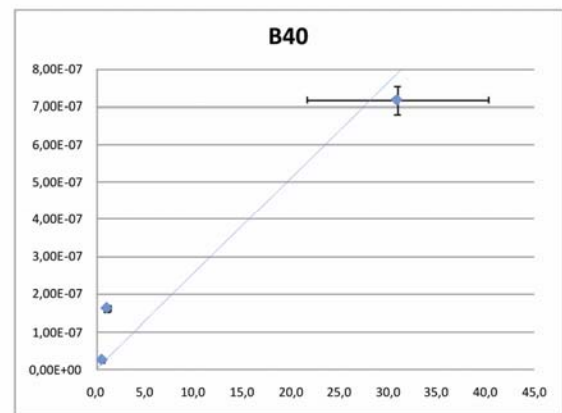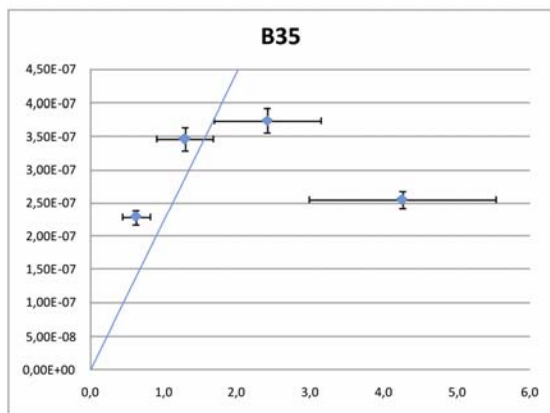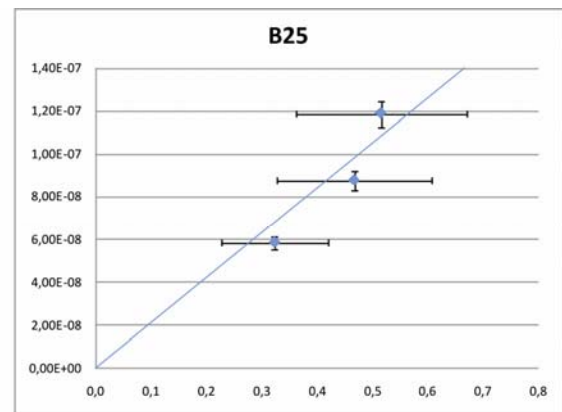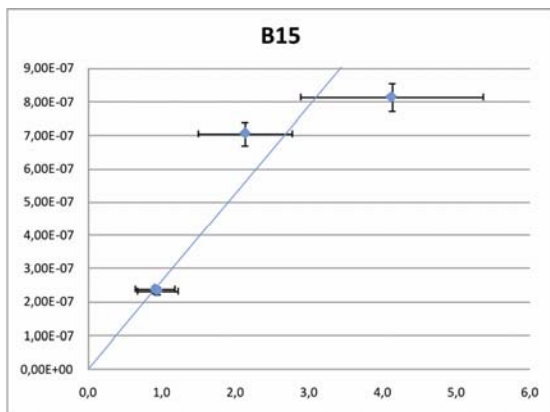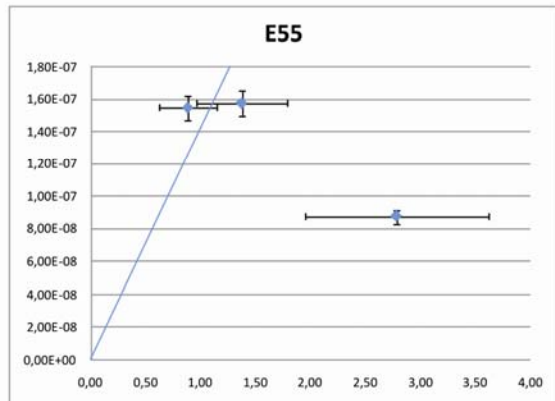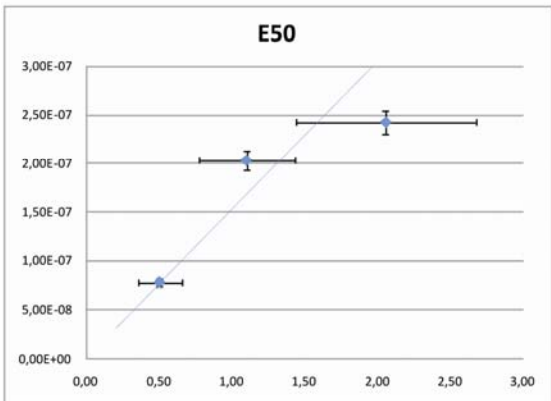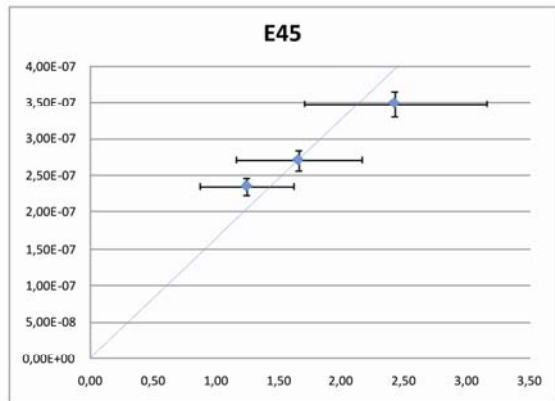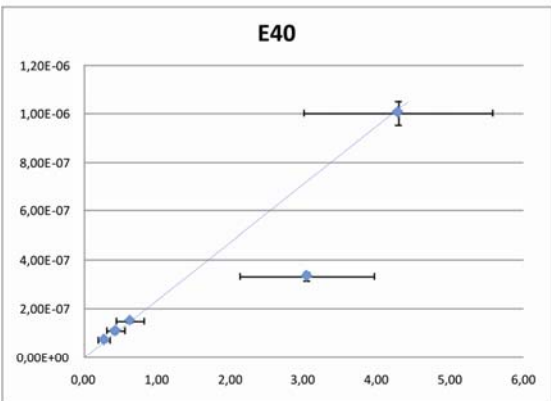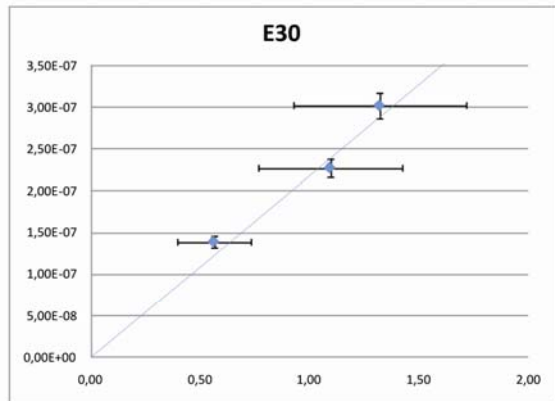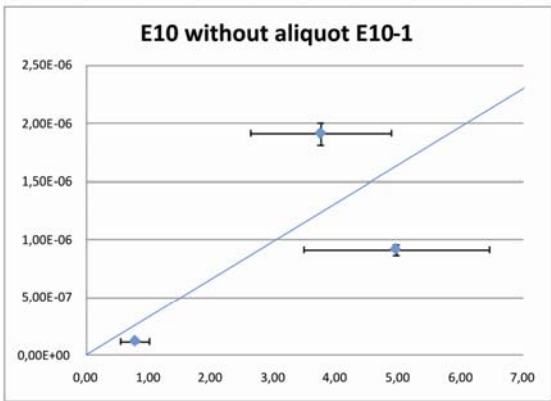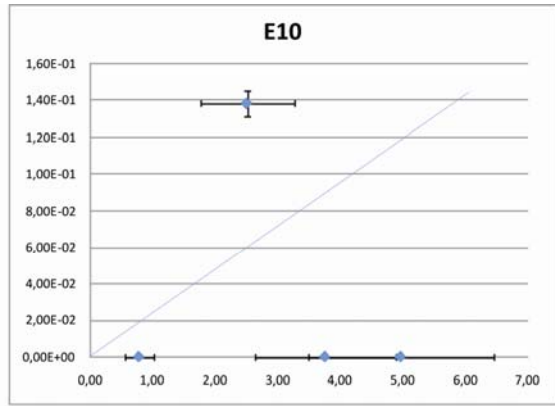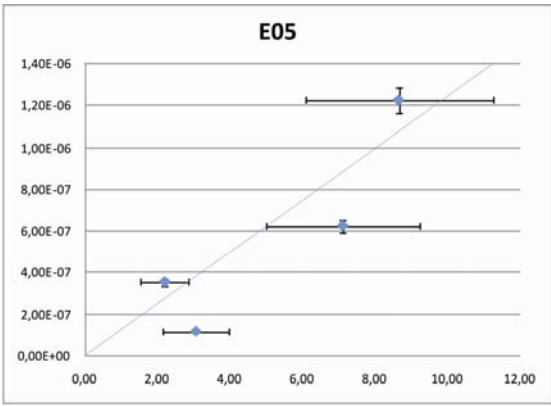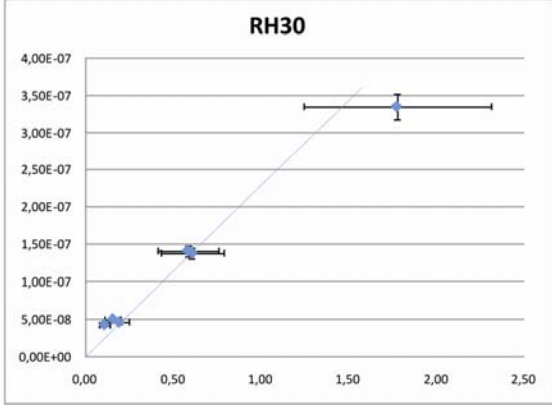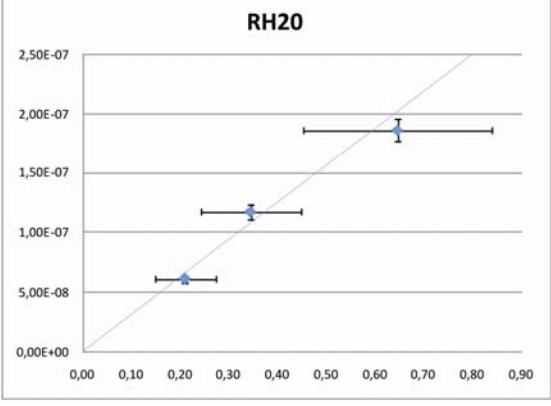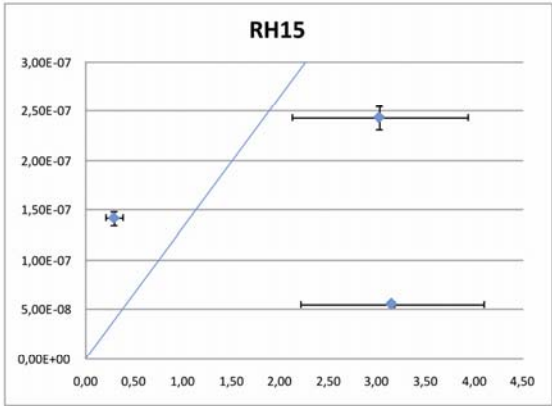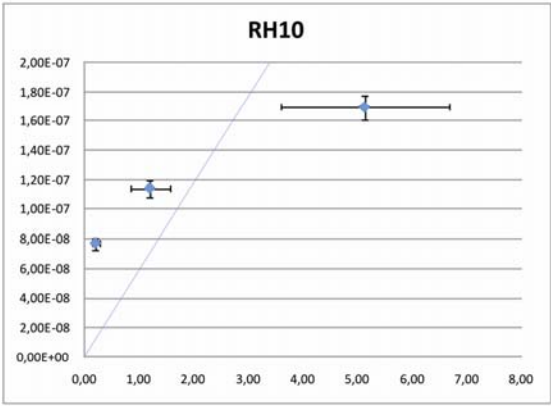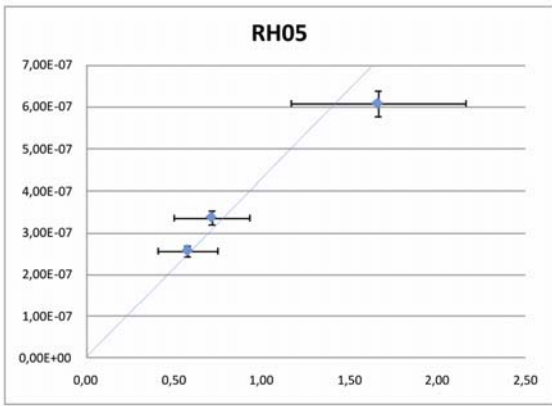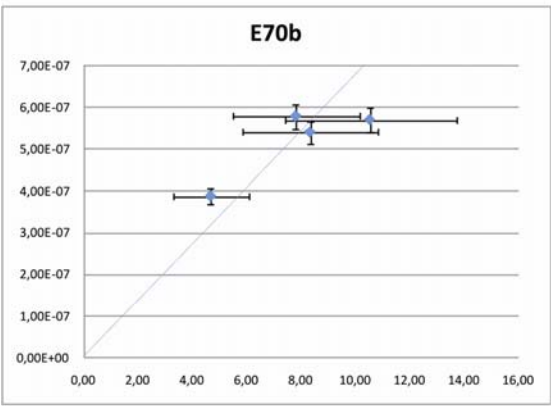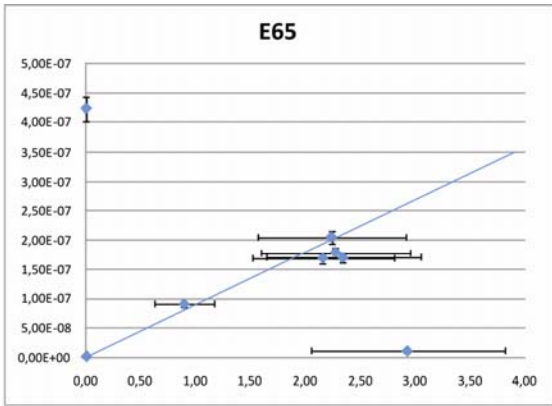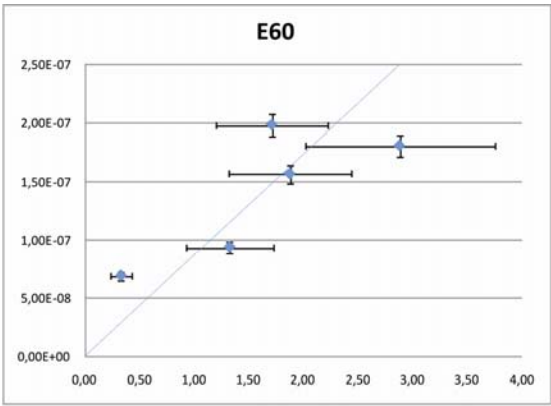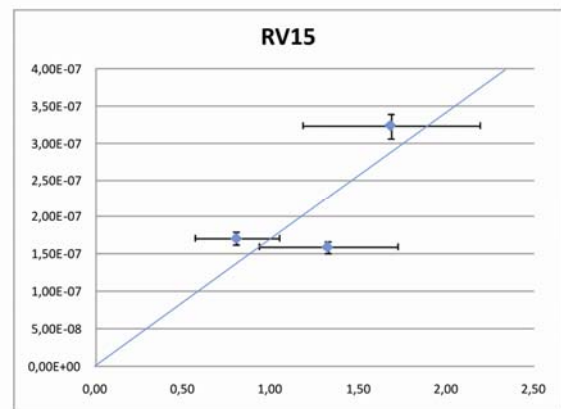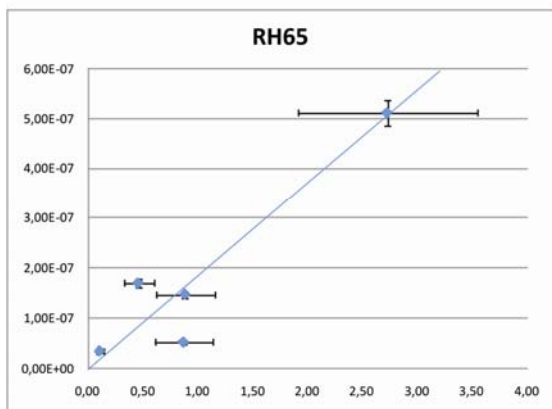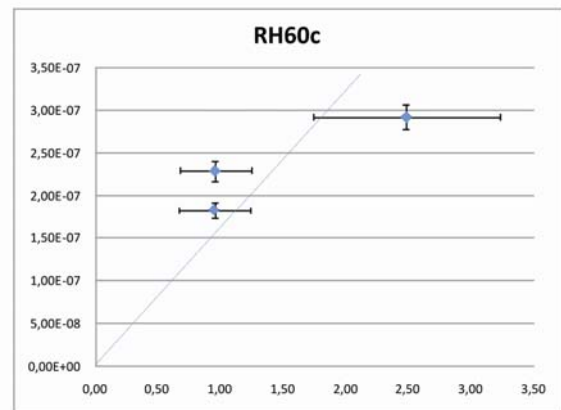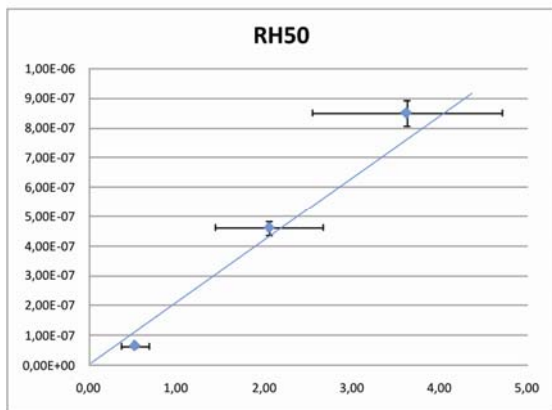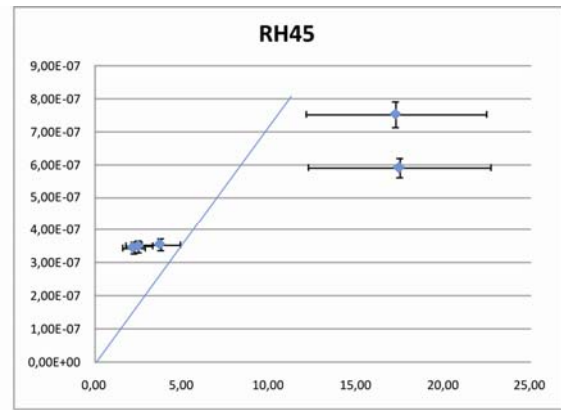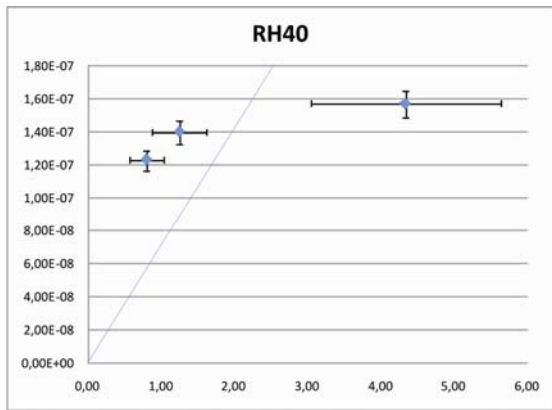
II. Forward modelling of thermochronological data

To quantify the impact of the cooling pulses detected from the thermochronological data, the data was forward modelled with the HeFTy software. As input parameters the depositional age (Schlunegger et al., 1996), the surface temperature at time of deposition (Mosbrugger et al., 2005) and at present day (ETHZ, 2004) and the sedimentation rate (Caron et al., 1989; Sinclair, 1997) were used. Four cooling scenarios were tested: (1) rapid cooling around 10 Ma, as suggested by the similarity of AHe and AFT data in some samples, (2) rapid cooling at 5 Ma, as suggested to have occurred in the Alps and world wide (e.g. Kuhlemann, 2000), (3) cooling after 2 Ma due to glacial erosion and (4) constant cooling to see whether the data require cooling pulses at all. The 1D forward modelling confirms that the observed strong cooling signal since the Middle Miocene cannot be explained by constant erosion, but requires increased uplift rates in distinct time windows. It is possible to quantify the maximum amount of section removed by the cooling events.
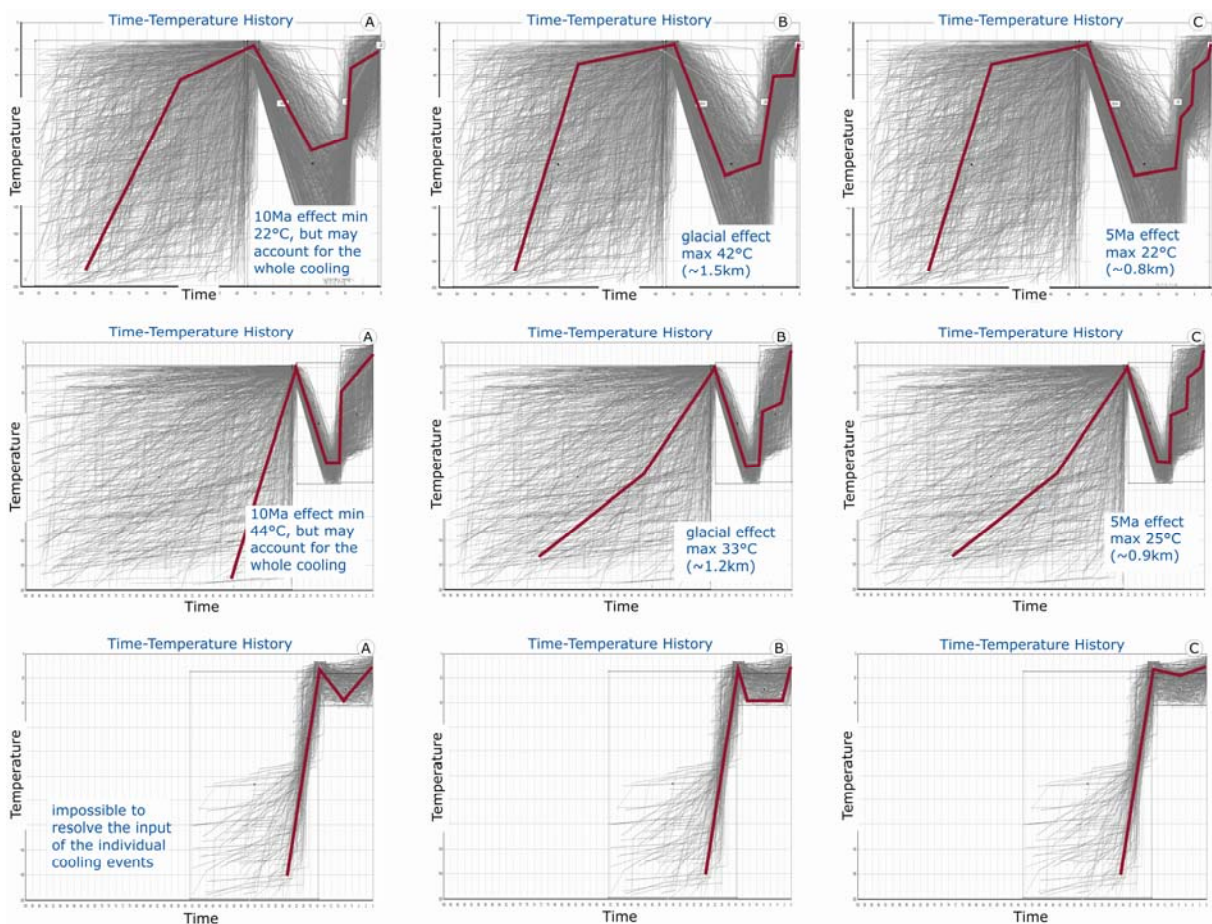

Figure II-1: quantifying the influence of different cooling pulses. The grey paths show inverse models with possible time-temperature histories, the red line shows a single forward model. First row: sample E05, second row: sample E45, third row: sample E70. First column: estimating the minimum amount of the 10 Ma cooling event, second column: maximizing the glacial cooling effect, third column: maximizing the 5 Ma cooling effect. See text for further explanations.

For the Entlebuch section, the modelling of E05 shows that the sample cooled from at least 100°C after c. 10 Ma (A-C). Initial rapid cooling is required for all scenarios. However, some of the cooling signal can be attributed to glacial activity (B) or a 5Ma event (C). Sample E45 is located in the triangle zone. A comparable pattern like for sample E05 is visible, with a required rapid cooling event at c. 10 Ma for all scenarios. It is also possible to quantify the maximum cooling at a potential 5 Ma event, which is like in E05 c. 20°C. Comparable maximum amounts of cooling can be attributed to glacial erosion. E70b is located north of the triangle zone. The data show that the sample has not been reheated over 40°C in the basin. Therefore, it can be considered as a detrital age and provides mainly information about the hinterland. Rapid uplift of the source area from 30-20 Ma can be inferred.
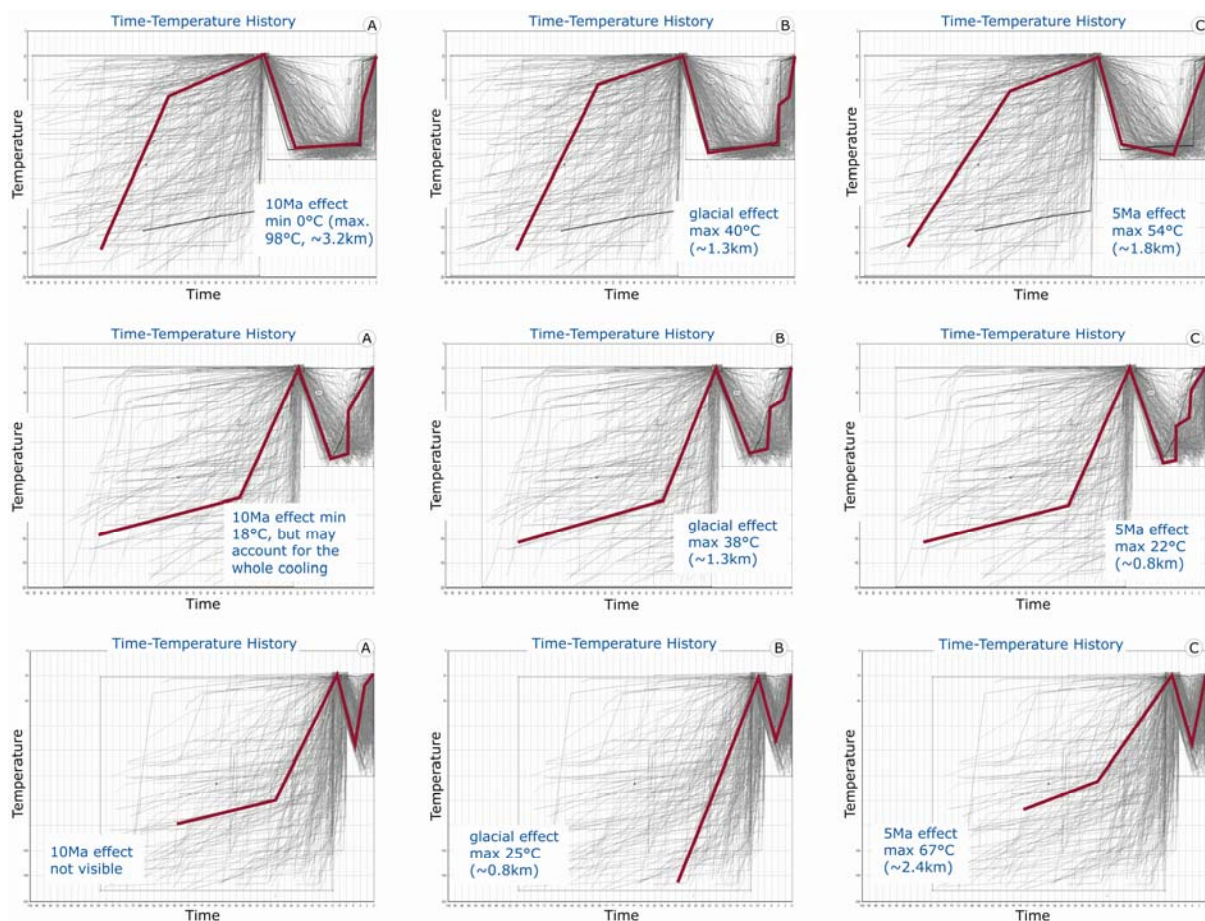

Figure II-2: quantifying the amount of cooling for different events in the Rigi area, analogous to the Entlebuch. First row: sample RH05, second row: sample RH45, third row: sample RH65. First column: estimating the minimum amount of the 10 Ma cooling event, second column: maximizing the glacial cooling effect, third column: maximizing the 5 Ma cooling effect.

Sample RH05 is located south of the triangle zone. In contrast to the Entlebuch section, no rapid cooling s required at c. 10 Ma. Either slow cooling starting at 10 Ma or rapid uplift at c. 5 Ma is also

possible. The influence of glacial erosion can be variable. It can be as much as 20 °C but is not required at all to explain the pattern. Sample RH45 stems from the triangle zone. Rapid cooling at c. 10 Ma is necessary to explain the observed age pattern. Interestingly, a 5 Ma event as observed in the southern sample RH05 is not required. The glacial impact on the data falls in the same range as observed in other samples and cannot exceed 20 °C/Ma. Sample RH65 was taken north of the triangle zone. In contrast to the corresponding sample in the Entlebuch profile, this sample was heated moderately after deposition. It is possible to model maximal temperatures of 70 °C. This sample requires rapid uplift between 5.6 and 3.9 Ma. These results are summarized in

Table II-1: summary of modelled maximum and minimum values for each cooling pulse. For the six chosen samples, first was tested whether constant cooling was possible and if so at which rate. Max temperature and max age denote the point in time and temperature since when the constant cooling may prevail to still produce a good fit of the data.

	unit	E05	RH05	E45	RH45	E70b	RH65
constant cooling	°C/Ma	no	9,5	no	6,7	no	no
max temperature	°C		167		98	42	
max age	Ma		18		15	5	
10 Ma, max	°C/Ma	220	89	954	180	no	no
	km/Ma	8	3	34	6		
min	°C/Ma	59	0	730	88		
	km/Ma	2	0	24	3		
5 Ma, max	°C/Ma	220	274	36	110		120
	km/Ma	8	9	1	4		4
min	°C/Ma	0	0	0	0		13
	km/Ma	0	0	0	0		0
2 Ma max	°C/Ma	21	20	17	18		16
	km/Ma	1	1	1	1		
min	°C/Ma	0	0	0	0		0
	km/Ma	0	0	0	0		0

In summary, the modelling shows that a 10 Ma cooling pulse is required in the Entlebuch but not in the Rigi and, maybe more important, that a 5 Ma event is not mandatory to explain the observed thermochronology age distribution. The glacial contribution cannot exceed c. 20 °C, also in the southern part of the study area, where the glaciers where massive.
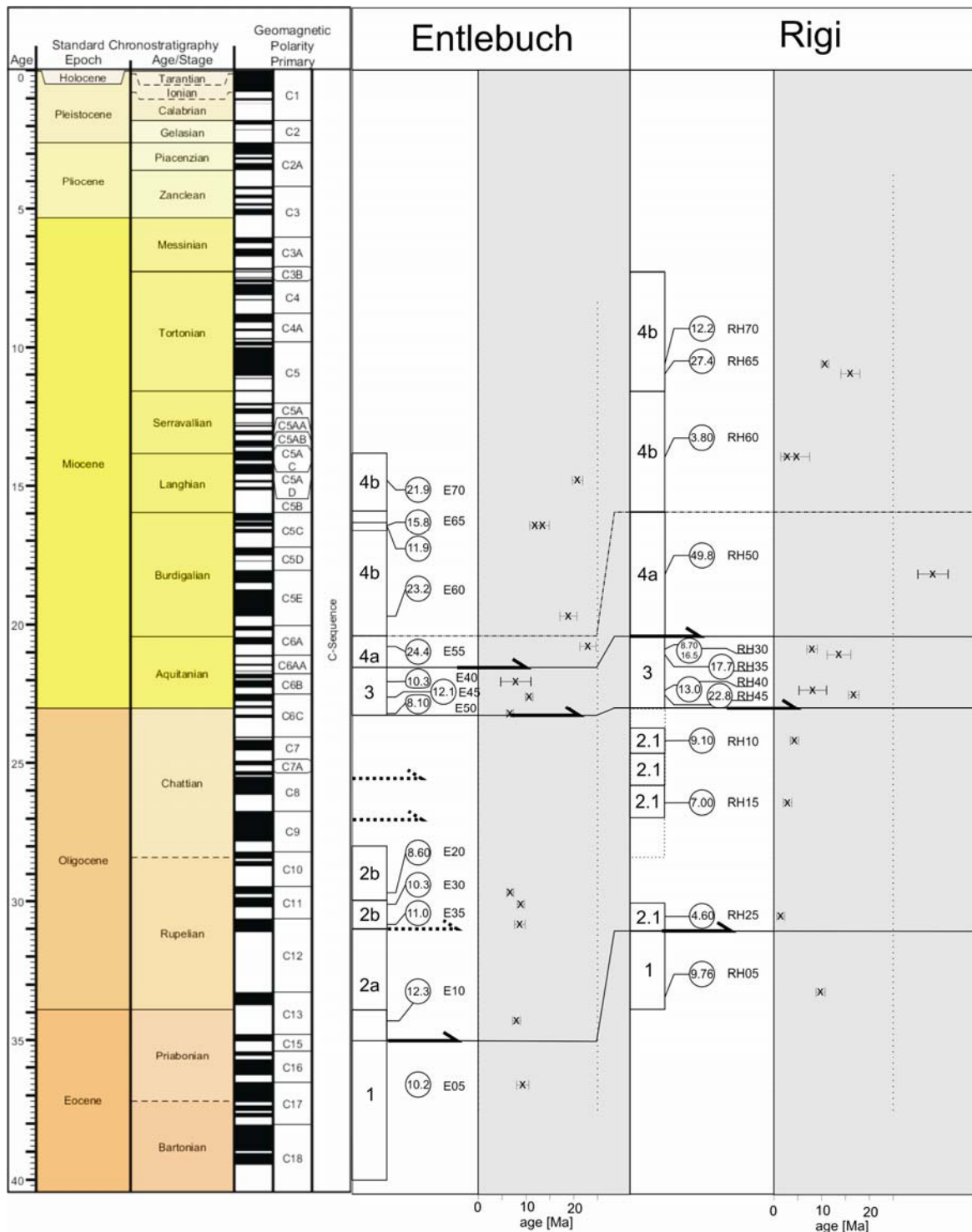
Figure III-1: Absolute and thermochronological ages of the samples in the Rigi and the Entlebuch area. Sample numbers are increasing from south to north. Note that between two thrusts sample numbers may decrease whereas stratigraphic ages increase. This shows the southward dip of the individual tectonic slices. Within the circles, the central apatite fission track age is given. In the grey area the fission track ages are plotted. This figure also illustrates that the section was eroded more deeply in the Entlebuch. For a detailed discussion see chapters 2 and 3.

IV.   Data modelling

In addition to the modelling with HeFTy, I modelled the data from Rigi and Entlebuch in collaboration with Matthew Fox, Frederic Herman and Pierre Valla from ETH Zurich. The models are run with the GLIDE software (Fox et al., in prep.), which estimates exhumation rates based on a one-dimensional thermal model. Each measurement is described with an independent thermal field but the solutions are linked by spatial correlation within individual tectonic slices. The presented time slices show preliminary results, which corroborate the findings discussed in chapters 2 and 3.
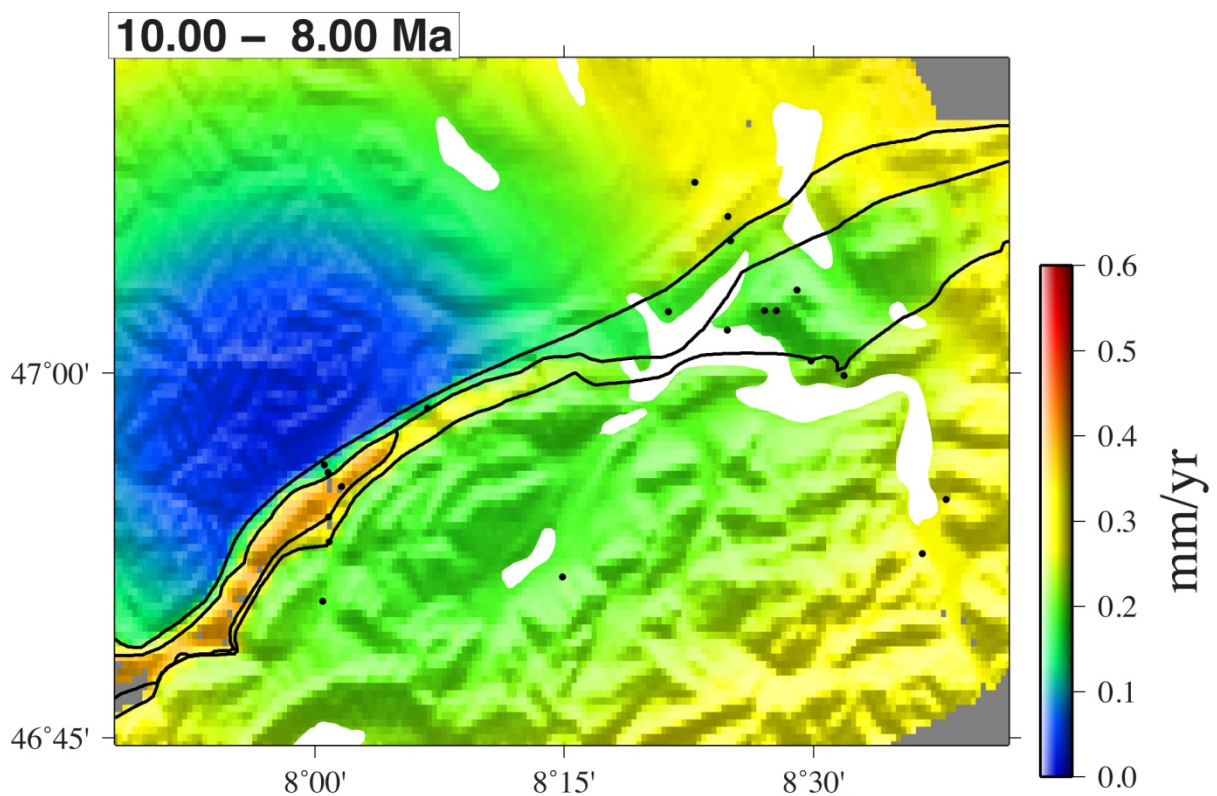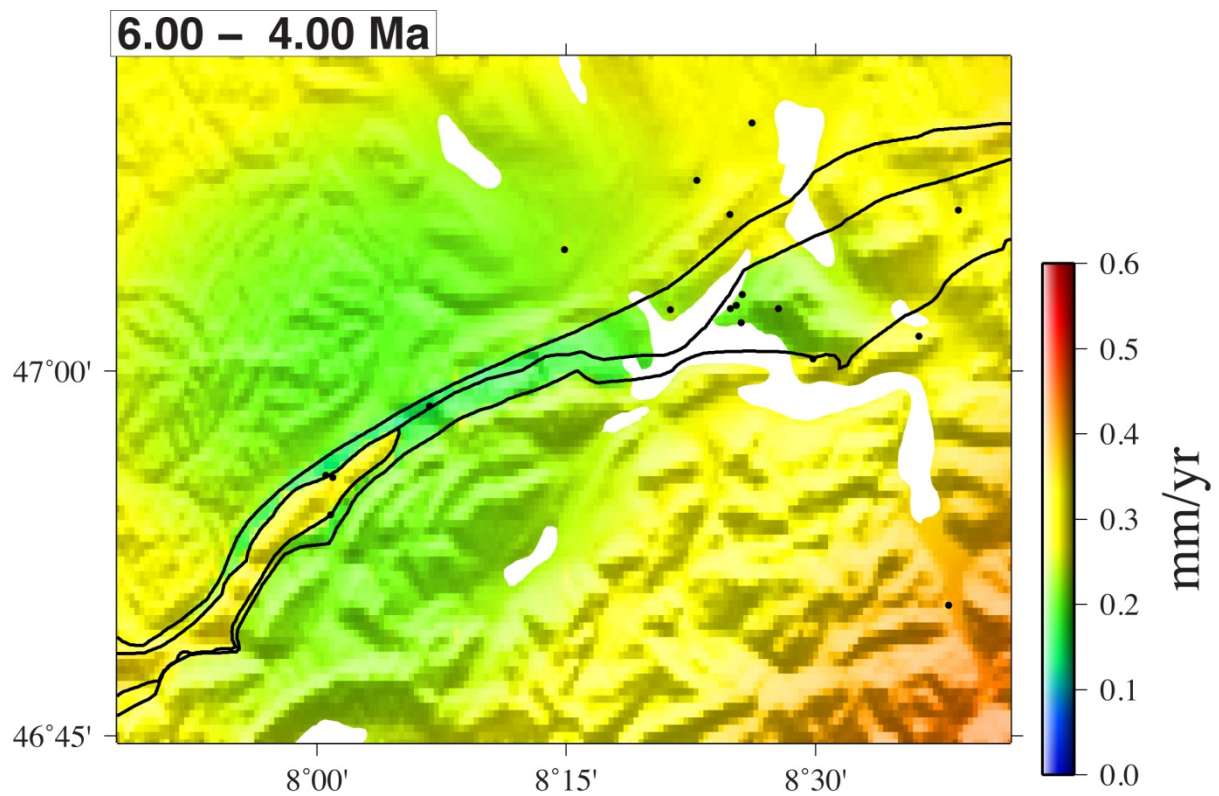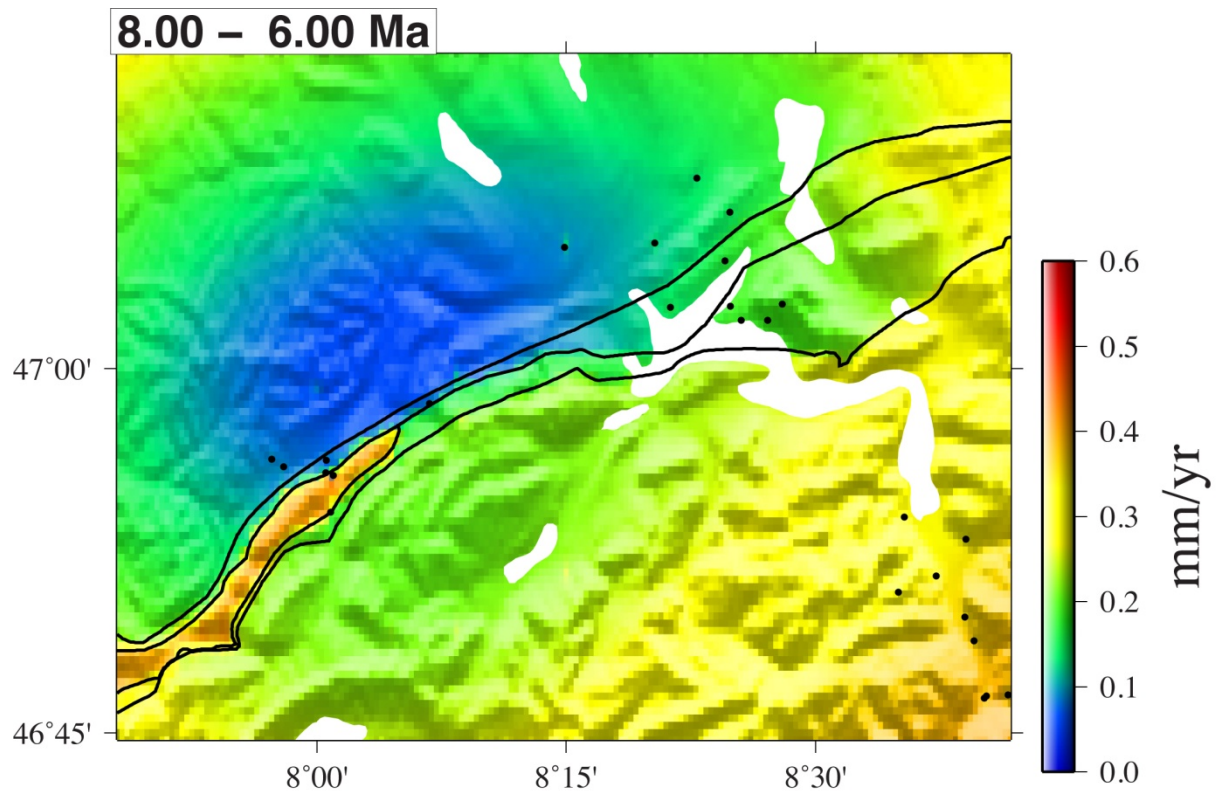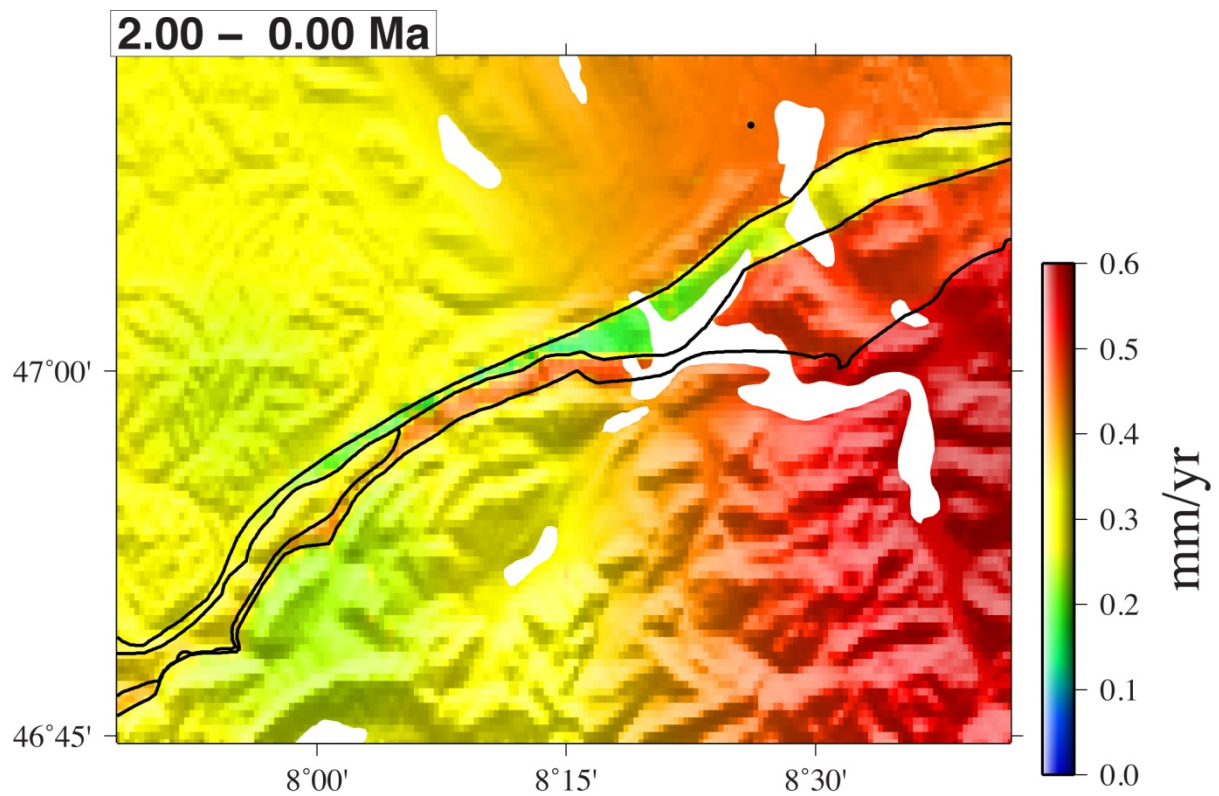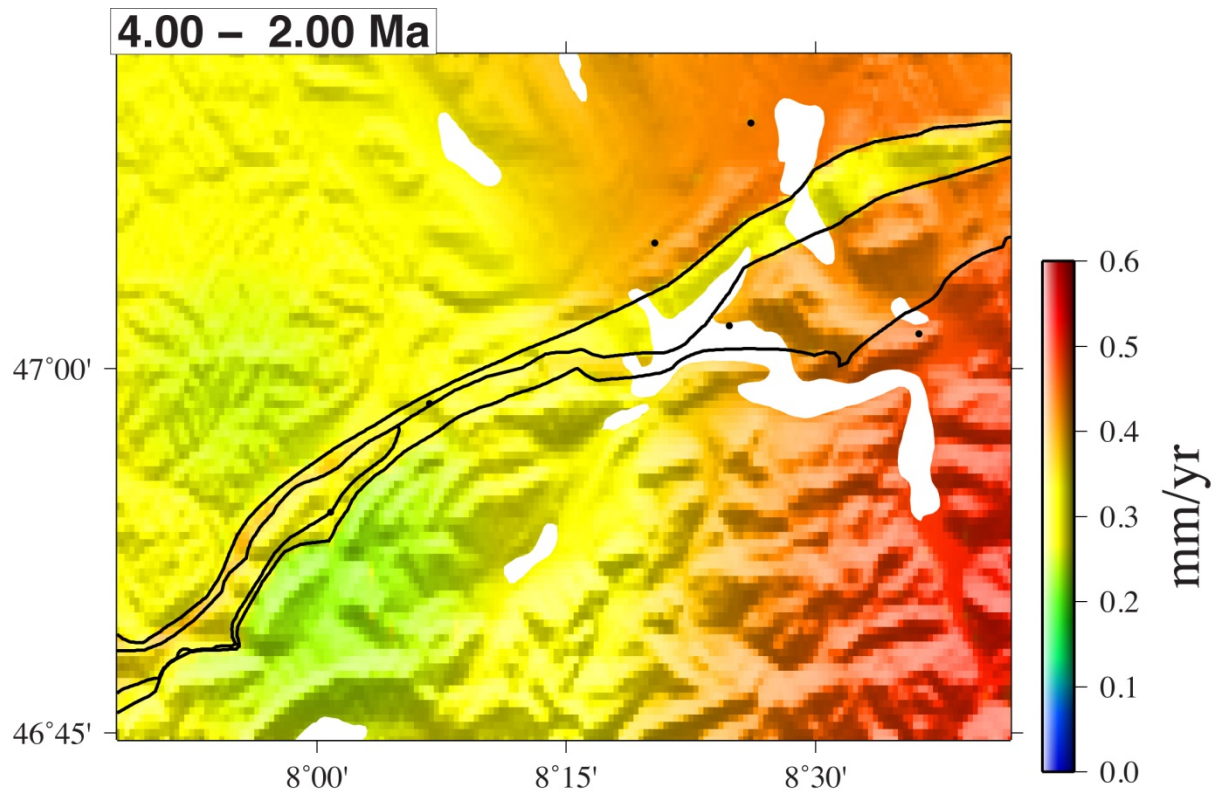
V. References

Caron, C., Homewood, P. & Wildi, W. (1989) The Original Swiss Flysch: A Reappraisal of the Type Deposits in the Swiss Prealps. *Earth-Science Reviews*, 26, 1-45.

ETHZ, I.f.K.u.G. (2004) Atlas Der Schweiz 2.0.2, Swisstopo. Zürich.

Fox, M.R., Herman, F. & Willett, S.D. (in prep.) Inferring Exhumation Rates in Space and Time from Spatially Distributed Thermochronological Data.

Kuhlemann, J. (2000) Post-Collisional Sediment Budget of Circum-Alpine Basins (Central Europe). *Mem Sci Geol Padova*, 52, 1-91.

Mosbrugger, V., Utescher, T. & Dilcher, D.L. (2005) Cenozoic Continental Climatic Evolution of Central Europe. *Proceedings of the National Academy of Sciences of the United States of America*, 102, 14964-14969.

Schlunegger, F., Burbank, D.W., Matter, A., Engesser, B. & Mödden, C. (1996) Magnetostratigraphic Calibration of the Oligocence to Middle Miocene (30-15 Ma) Mammal Biozones and Depositional Sequences of the Swiss Molasse Basin. *Eclogae Geol. Helv.*, 89, 753-788.

Sinclair, H.D. (1997) Tectonostratigraphic Model for Underfilled Peripheral Foreland Basins: An Alpine Perspective. *Geological Society of America Bulletin*, 109, 324-346.

Vermeesch, P. (2008) Three New Ways to Calculate Average (U-Th)/He Ages. *Chemical Geology*, 249, 339-347.

Presentations at conferences

Coupling between Climate & Tectonics? Insights from Low Temperature Thermochronology and Structural Geology applied to the Pro-Wedge of the European Alps

Presented at the 9th Workshop of Alpine Geological studies, Cogne Italy, 16.-18.09.09
von Hagke, C.[1], Cederbom, C.E.[1], Oncken, O.[1], Schlunegger, F.[2] Ortner, H.[3], Lindow, J.[1,4]

Post 5 Ma thrusting in the Northern Alpine Foreland Basin – insights from structural geology and new (U-Th)/He and Fission Track data

Presented at he EGU General Assembly 2010, 02.-07.05.2010, Vienna, Austria
von Hagke, C.[1], Cederbom, C.E.[2], Lindow, J.[3], Oncken, O.[1] Schlunegger, F.[4]

How tectonically active are the Central Alps?

Presented at the 12th International Conference on Thermochronology, 16.-20.08.2010 Glasgow, Scotland
von Hagke C., Cederbom C.E., O. Oncken, Stöckli D.F., Donelick R.A.

Coupling between Climate & Tectonics? Insights from Low Temperature Thermochronology and Structural Geology applied to the Pro-Wedge of the European Alps.

Presented at the ESF TopoEurope Workshop and Summer School on Detecting Landscape Change, 31.08-08.09 2010, Loen (Nordfjord), Norway

Did thrusting cease in the Northern Alpine Foreland Basin at 12 Ma? -Answers from low-temperature thermochronology.

Presented at he EGU General Assembly 2010, 02.-07.05.2010, Vienna, Austria
von Hagke, C., Onno Oncken, Charlotte E. Cederbom, Daniel F. Stöckli, Hugo Ortner

Geometry, Sequence and Amount of Thrusting in the Subalpine Molasse of Austria and Bavaria.

Presented at the 10th Workshop of Alpine Geological studies, St. Florent, Corsica, France, 10.-16.04.2011
Ortner H., Fügenschuh B., Zerlauth M., von Hagke, C.

How much material was eroded in the Northern Alpine Foreland Basin and why and when did it happen?

Presented at the 10th Workshop of Alpine Geological studies, St. Florent, Corsica, France, 10.-16.04.2011
von Hagke, C., Oncken, O., Stöckli, D.F, Ortner, H.

Timing of thrusting in the Subalpine Molasse, Northern Alps.

Presented at the 7th TOPO-EUROPE Workshop Davos, Switzerland, 06.-09.10.2011

Christoph v.Hagke, Charlotte Cederbom and Onno Oncken

A Multiple thermochronometer approach reveals post 12 Ma tectonic activity in the foreland basin of the Northern Alps,

Presented at the AGU Fall Meeting, 05.-09.12.2011, San Francisco, USA

Christoph v.Hagke, Charlotte Cederbom, Onno Oncken, Meinert Rahn and Daniel Stöckli

Post 12 Ma tectonic activity of the Subalpine Molasse resolved by combining thermochronology and critical wedge analysis

Presented at he EGU General Assembly 2012, 22.-77.04.2012, Vienna, Austria

Christoph v.Hagke*[1], Onno Oncken[1], Hugo Ortner[2] and Charlotte Cederbom[3]

Acknowledgements

I would like to thank my advisor Onno Oncken, who always had his door open and took great interest in my work. He helped with inspiring discussions, always impressing me with his sheer endless knowledge. I greatly acknowledge that he gave me all possible freedom to follow my ideas and supported all my plans. I whish to thank Charlotte Cederbom, who introduced me to the project, the field area and fission track dating. She helped making contacts with co-workers and other scientists and was great help during writing of the first manuscript. I am grateful to Daniel Stöckli and Ray and Margaret Donelick for explaining me the details of fission track and helium-dating and for dating many samples without charging. Special thanks go to Hugo Ortner, who was introducing me to the Molasse basin and who was always very helpful by sharing his knowledge. I would like to thank Pieter Vermeesch for answering all my questions about statistics in fission track dating and for modifying his software according to my needs. I am grateful to Fritz Schlunegger and Meinert Rahn who helped me with my first manuscript by providing additional maps and data, discussing the details and proof-reading the texts. Thanks go to Mark Handy, who was closely following my research and supported me during my entire time at GFZ and FU. Olaf Zielke, Christian Sippl and Nadaya Cubas are thanked for their help with coding issues. I want to thank my brother Alexander for helping me with mathematical problems. I thank Claudio Rosenberg, Bernd Schurr, Matias Rosenau, Marcos Moreno, Kamil Ustaszewski, Karen Leever, Peter van der Beek, Todd Ehlers, Roderick Brown, Ed Sobel, Jean-Philippe Avouac, John Suppe, Oliver Heidbach, Friedhelm von Blanckenburg, Kevin Norton, Adrian Pfiffner, Stefan Schmid, Bernd Lammerer and all other colleagues in and outside the GFZ, who were helping me a lot clarifying the picture. Thanks go to Johannes Glodny, who taught me how to separate minerals. I would like to thank Manuela Dziggel, Juliane Herwig, Gabi Arnold and Wilfried Herr for support during drafting, mineral separation and computer administration. Special thanks go to Franziska Alberg, who was invaluable help and made sure that I had my head free for doing science. I also want to thank Fang-Lin Wang, who was a great office mate. Jonathan Bedford and Cornelius Drautz are thanked for proof-reading the method and Molasse Basin sections. My colleagues and fellow students at GFZ and FU are thanked for the great time during coffee breaks and during the Eastern Alps field trip. This research was conducted in the framework of the ESF TopoEurope CRP "Thermo-Europe", which was a great opportunity. The German Research Foundation (DFG) provided funding. I want to thank my parents, brothers, in-laws, friends and of course Katharina for mental support. Last but not least I want to thank Katrin, who made this PhD project possible with her endless support, encouragement, endurance and understanding. To you I dedicate this thesis.